Ph. D. thesis

Disorder and crystallite size effects in weakly ferromagnetic system Ni_3Al and martensitic transformation in $Ni_{55}Fe_{20}Al_{20}$

Ashutosh C. Abhyankar

School of Physics
University of Hyderabad
Hyderabad – 500 046 India

Disorder and crystallite size effects in weakly ferromagnetic system Ni_3Al and martensitic transformation in $Ni_{55}Fe_{20}Al_{25}$

Thesis submitted for the degree of
Doctor of Philosophy

BY

Ashutosh C. Abhyankar

School of Physics
University of Hyderabad
Hyderabad – 500 046 India

August 2008

Declaration

I hereby declare that the matter embodied in this thesis is the result of investigations carried out by me in the School of Physics, University of Hyderabad, Hyderabad – 500 046, under the supervision of Prof. S. N. Kaul.

Place: Hyderabad

Date : **(Ashutosh C. Abhyankar)**

Certificate

This is to certify that the work contained in this thesis entitled, “Disorder and crystallite size effects in weakly ferromagnetic system Ni_3Al and martensitic transformation in $Ni_{55}Fe_{20}Al_{25}$” has been carried out by Mr. Ashutosh C. Abhyankar under my supervision and the same has not been submitted for the award of research degree of any university.

Place: Hyderabad

Date : **(Thesis Supervisor)**

With the Blessings of

Gurudev R. D. Ranade

To

Aai and Baba

Acknowledgements

It gives me immense pleasure to express my gratitude and respect to my mentor and thesis supervisor, Prof. Sharika Nandan Kaul for teaching me the research methodology and introducing me to this fascinating field of research. His meticulous planning, constant encouragement and support made it possible for me to achieve the aim of my research work. He provided excellent advice in preparing this thesis and helped to improve the presentation and explanation of the research results presented in the thesis.

I would like to thank Prof. H. Krönmuller (Max-Plank Institute for Metal Research, Stuttgart, Germany) and Prof. R. Birringer (University of Saarland, Germany) for permitting access to the sample preparation facilities at their institututions. I sincerely thank Prof. A. K. Nigam (Tata Institute of Fundamental Research, Mumbai) for allotting time on SQUID magnetometer for low temperature measurements and hosting me at TIFR. I wish to thank Dr. L. Fernández Barqúin (University of Cantabria, Spain) for rendering assistance in performing the Neutron diffraction measurements at ILL, Grenoble, France, and Dr. K. Muraleedharan for permitting the use of SEM and TEM facilities at DMRL, Hyderabad. I gratefully acknowledge the painstaking effort put in by Dr. D. V. Sridhar Rao for TEM measurements and his assistance in interpreting the results of these measurements. I thank Prof. V. Seshubai for allotting time on the optical microscope. I also thank Dr. R. Gopalan, Dr. V. Chandrasekaran and T. S. R. K. Sastry for their support and kind interest in my research work.

I thank the present and former Deans, School of Physics and all the faculty members of the School for their cooperation. I wish to thank Prof. Ashok Chatterjee and Dr. S. Srinath, my Doctoral Committee Members, for their valuable suggestions. I thank Abraham and the non-teaching staff of the School of Physics for their help and co-operation.

I cherish the motherly affection of Mrs. Manju Kaul and fond memories of my meetings with her that made some of my evenings special. I cannot forget the yearly celebrations of Holi.

I am thankful to my lab-mates Basheed, Sanjeev, Yugandhar, Shinto, Suresh and Srinivas for making my stay in the Lab joyful and memorable. I thank my seniors Dr. Vasu, Dr. Anita and Annie. Dr. Vasu has introduced me to Rietveld analysis. Dr. Anita Semwal and B. Annie'D Santhoshini made some of their data available for me to use in the present thesis.

I appreciate the concern shown, and encouragement given to me, by Dr. K. Suresh, Trivikram, Nihar, and Madan. My special thanks are due to my friends Vilas, Sandesh, Ravi, Swarjya and Manisha.

I thank Devendra, Sathish and Narasaiah for their timely help. I thank my colleagues Dr. Phani, Dr. A. Rajanikant, Dr. Subhajit, Abhilash, Prashant, Kiran, Laxmi, Sarvana, Ravi, Ramudu, Srinivas, Swarup, Manoj, Sai Santosh, Vijayan, Sendilkumar, Rajeeb, Joji, Sultan, Shankaraiah, Bheemalingam Siva, Saipriya, Juby, Thejal, Babita and N.V. Rama Rao. I thank my wing-mates Vishnu, Biju, Srinath, Samanta and Praveen.

I enjoyed playing cricket with Venkatesh, Balaraman, Selva, Armugam, Shiva, Ganavel, Prakash, Vijayan, Francis, Subbarao and also with 'quantum' team-mates Balmuralikrishna, Satyanarayana, Gopalkrishna, Anjan, Kurumurthy, Suman and others.

I thank CSIR and DST, New Delhi, for financially supporting my research work through the fellowship.

I am thankful to Prof. S. H. Pawar, Prof. R. N. Patil and Dr. S. Lotake and other faculty members of Shivaji University, Kolhapur, for their teaching and encouragement in my academic career. I must thank Prof. D. B. Devale, for his motivational lectures on Physics at the graduation level and his continued support. I have deepest regards for my school teacher, Shinde guruji.

I cannot express the gratitude in words toward my parents without whom I would not have been in a position to complete this work. They are my strength and power which enabled me to survive through thick and thin. My siblings Avinash and Gauri always supported and encouraged me when the things were not going well and made me believe that hard work pays sooner than later. My grandfather and grandmother have showered an unconditional love on me which cannot be appreciated in words. ARYAA, SANIKA and RAGHAV brought the happiness in our family and I love them all.

Table of contents

Chapter 1: Introduction

Chapter 2: Experimental techniques

Chapter 1

Introduction

1.1 Order and Disorder

In general, matter exhibits itself in different phases viz. solids, liquids, gases and plasma depending on the strength of interactions between the atoms. One may define a solid as any substance, which deforms elastically under small shear stresses. This definition evidently excludes gases and liquids; they exhibit only viscous resistance to shear. Viscosity opposes shear deformation but does not give rise to restoring forces that are at the origin of elasticity of the solids [1].

Crystalline order is the simplest way that atoms could possibly be arranged to form a macroscopic solid. Small basic units of atoms repeat endlessly, one placed next to the other, so that the whole solid can be described completely by studying a small number of atoms. It is remarkable that this simple structural model can be used to understand so much. But the world is built up of solids whose crystalline order is either defective, or absent altogether [2]. So, the study of disorder and its effect on physical properties of solids is important.

It is common to consider order and regularity as equivalent. But in actual practice something termed as regular is geometric and is based on the premise that one or more geometric objects are repeated whereas order is probabilistic [3] and leads to the idea of uniqueness in that a given macroscopic structure corresponds to a single microscopic configuration. The concept of disorder is intuitive and, to some extent, primitive. It is easier to define disorder as state of absence of, or departure from, the condition of order. In most cases, physical systems do not exhibit perfect order nor do they represent complete disorder. So, it is convenient to talk in terms of degree of order, which is quantified by

long-range or short-range order parameters. Crystals are ordered and regular since they can be obtained by periodic translation of an elementary (geometric) cell in space. *Long Range Order*, which extends throughout the structure is a characteristic of crystalline solids whereas *Short Range Order*, which involves shell of the first neighbours of any atom chosen to be the origin [3,4,5], depending on the spatial extension of the structure, is the one that describes non-crystalline, amorphous solids and also liquids. Thus, in amorphous or non-crystalline solids, crystalline-like order does exist but at very small length scales. In general, disorder is classified into three different categories, viz., site disorder, bond disorder and topological disorder [3,4,5]. The first two are relevant to crystalline solids whereas the last one pertains to non-crystalline solids. The experimental work carried out here mainly deals with the disorder in crystalline solids. In a perfect crystalline substance, the probability of finding an atom at a lattice site has the delta function form and this fixes the co-ordination number for the crystalline solids.

a. Site disorder: The fluctuation in the co-ordination number arising from the random occupation of sites on a regular crystalline lattice gives rise to site disorder. Thus, the point defects such as vacancies, di-vacancies, interstitials and substitutional impurity atoms, *F* centers, result in this type of disorder.

b. Bond disorder: Wild variations in the bond lengths and bond angles destroy the periodicity of the lattice or long-range atomic order leading to bond disorder.

c. Topological disorder: The fluctuations in bond lengths as well as in the bond coordination give rise to dangling bonds and topological disorder. Thus,

complete absence of translational symmetry and the fluctuations in the nearest-neighbour co-ordination number for a given atom constitutes topological disorder. This is the highest degree of disorder among the all the types of disorders, mentioned above [5].

d. Effect of disorder on magnetic properties: A magnetic moment exists on an atom whenever there are unpaired electrons. When such an atom becomes an ion in the solid, the existence and magnitude of its moment is decided by the extent of overlap of the wavefunctions of the electrons in different shells. The chemical and structural disorder present in a magnetic alloy affect the interaction coupling the magnetic moments as it depends on both the magnitude as well as the distance between the moments. It results in a distribution of the effective magnetic moments per atom thus affecting the magnetic properties of the materials in case of the localized picture. For an itinerant-electron ferromagnet, disorder smears out the otherwise sharp features of density of states curve and might even change the value of the density of states at the Fermi level leading to changes in the magnetic properties of the solids. However, it should be noted that inspite of the strong dependence of magnetic order on the distance and local environment, the structural disorder does not prevent the occurrence of the long range magnetic order such as ferromagnetism.

1.2 Itinerant magnetism

Since the discovery of loadstone (about 625-564 B.C.), that attracts iron, in Magnesia, a city in northern Greece, mankind has been intrigued and fascinated by magnets. Eventhough magnet was used in compass for terrestrial navigation for many centuries, extensive research on the development of

microscopic models of magnetic properties of solids started in the late 19th and early 20th century. P. Weiss [6] postulated the existence of an internal field, $H_m = \lambda M$, where M is the magnetization and λ is molecular field constant, to account for the spontaneous magnetic order in a ferromagnet but the origin of H_m was unknown at that time. Using classical mechanics and concept of local moments having a fixed size, Langevin [7] explained the Curie law of susceptibility. Miss Van Leeuwen [8] then showed that classical mechanics, which was used to explain both dia- and paramagnetism of free atoms and molecules, failed to explain ferromagnetism. With the advent of quantum mechanics, Heisenberg [9] formulated the exchange interaction between two spins, which, in turn, formed the theoretical basis for the existence of magnetic order starting with the Heisenberg Hamiltonian of the form

$$H = -2\sum_{i \neq j} \mathrm{J}_{ij}\, \vec{S}_i \cdot \vec{S}_j \qquad (1.1)$$

where spins located at different sites (i and j), represented by the spin operators, $\vec{S}_i$ and $\vec{S}_j$, interact via the exchange interactions of strength J_{ij}. Thus, he resolved the puzzle of Weiss molecular field interpreting it as an exchange field created by short-range exchange interactions between spins on the atomic sites. This picture, called the Heisenberg localized model, was successful in accounting for the ferromagnetic (antiferromagnetic) order when sign of the exchange integral J is positive (negative). When the magnetic anisotropies (of either dipolar or spin-orbit plus crystal-field origin) are taken into account adequately, Heisenberg Hamiltonian describes very well the ground state as well as finite-temperature properties of the localized-moment systems. In this model, the only form of collective excitations is the thermally-excited

propagating transverse spin fluctuations (spin waves) which have small energy dispersion and fill the entire Brillouin zone. Above the Curie temperature, T_C, the atomic moments are randomly oriented and change their directions with the average frequency of $\sim k_B T_C / h$, where k_B and h are the Boltzmann and Planck constants, respectively. Thus, the Curie-Weiss susceptibility is temperature-dependent and is given as

$$\chi_{CW} = \frac{J(J+1)Ng^2\mu_B^2}{3k_B(T-T_C)}. \tag{1.2}$$

In the above expression, J is the total angular momentum of an atom, N is the total number of magnetic atoms, g is the Landé splitting factor, and μ_B is the Bohr magneton. This microscopic model was thus able to explain the magnetism of magnetic insulator compounds like transition metal oxides and the majority of the rare earth metals where atomic moments are localized at lattice sites and have integral values that are temperature-independent.

However, the non-integral values of atomic moments (e.g., $2.2\,\mu_B$ for Fe, $1.7\,\mu_B$ for Co and $0.6\,\mu_B$ for Ni) and the temperature independence of exchange enhanced paramagnetic susceptibility of the transition metals and their alloys could not be explained on the basis of localized-electron picture [10]. This is so because, in these metals, the electrons responsible for the magnetism take part in atomic bonding and thus their wave functions, on the neighbouring sites, have appreciable overlap which allows these electrons to hop freely from one lattice site to the other. These electrons are called *itinerant* electrons. As the wave functions of *itinerant* electrons are *delocalized*, no truly localized magnetic moments exist [11]. The magnetism of these systems thus cannot be

explained by considering the magnetic degrees of freedom alone as is the case in the Heisenberg Hamiltonian. A separation of the magnetic degrees of freedom from the translational degrees of freedom is not possible in these itinerant systems. Therefore, Stoner [12] proposed a band model for itinerant magnetism where the magnetization is due to spontaneously spin-split bands. This spontaneous band-splitting is caused by the intra-atomic exchange interaction that originates from the *on-site Coulomb interaction* between the electrons with unsaturated spins of the narrow d-bands. This model is based on the following assumptions. (i) The carriers of magnetism are the unsaturated spins in the d-band. (ii) The effect of exchange interactions is treated within a molecular field framework. (iii) The Fermi-Dirac statistics has to be used. With these assumption, the Stoner equation [13, 14] is given by

$$n^{\pm} = \frac{1}{2} n\,(1 \pm \zeta) = \int_0^{\infty} N(E_F)\, f(E_F, \eta^{\pm})\, dE_F \tag{1.3}$$

where $f(E_F, \eta^{\pm}) = \dfrac{1}{\exp[(E_F - \eta^{\pm})/k_B T] + 1}$ is the Fermi-Dirac distribution function,

$$\eta^{\pm} = \mu \pm \frac{1}{2} n U \zeta \pm \mu_B H\,, \tag{1.4}$$

n the number of electrons per atom, $n^{\pm}$ the number with $\pm$ spin, ζ the relative magnetization, $N(E_F)$ the density of single-particle states per atom per magnetic moment, μ the chemical potential and U the effective intra-atomic Coulomb interaction between the itinerant electrons. U may be of short range

and corrected for the electron-correlation effects and is better known as the Stoner parameter. The criterion for the occurrence of ferromagnetism, in the Stoner model, is derived in the following way [15].

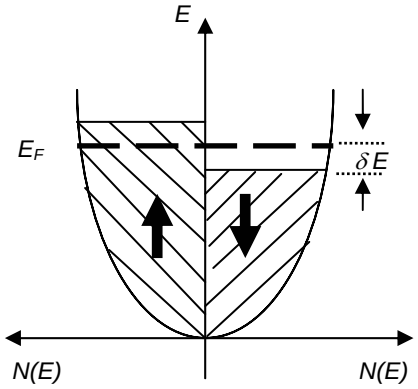

Figure 1.1: Density of states showing spontaneous spin-splitting of energy bands in the absence of an external field [15].

If, in the absence of an external magnetic field, we take a small number of electrons with energy in the range $E_F - \delta E$ from the spin-down band (where E_F is the Fermi energy) and flip their spin and then place them in the spin-up band within the energy range $E_F + \delta E$, as shown in figure 1.1, the number of electrons moved is $N(E_F)\,\delta E/2$ and they increase the energy by δE. Therefore, the total kinetic energy change is

$$\Delta E_{K.E.} = \frac{1}{2} N(E_F)(\delta E)^2. \tag{1.5}$$

This energy cost makes such a process seem unfavorable. However, the interaction of net magnetization with the exchange field gives an energy reduction which can overweigh this cost. The number density of up-spins is $n_\uparrow = [n + N(E_F)\delta E]/2$ and that of down-spins is $n_\downarrow = [n - N(E_F)\delta E]/2$. Hence, the magnetization is $M = \mu_B(n_\uparrow - n_\downarrow)$, assuming that each electron has

a magnetic moment of $1\mu_B$. The molecular field energy, which equivalent to the potential energy, is given by

$$\Delta E_{P.E.} = -\int_0^M (\lambda M')dM' = -\frac{1}{2}\lambda M^2 = -\frac{1}{2}\mu_B{}^2\lambda(n_\uparrow - n_\downarrow)^2 \tag{1.6}$$

Writing, $U = \mu_B{}^2\lambda$, where U is a measure of the Coulomb energy, we have

$$\Delta E_{P.E} = -\frac{1}{2}U(N(E_F)\delta E)^2 \tag{1.7}$$

So that the total change of energy, ΔE, is

$$\Delta E = \Delta E_{K.E} + \Delta E_{P.E} = \frac{1}{2}N(E_F)(\delta E)^2[1 - UN(E_F)] \tag{1.8}$$

Thus the spontaneous ferromagnetism is possible only if $\Delta E \le 0$, which implies that

$$UN(E_F) \ge 1 \tag{1.9}$$

This condition for ferromagnetism is known as the *Stoner criterion*. The ferromagnetic state is stable only when the Coulomb effects are strong and the density of states at the Fermi energy is large. If there is spontaneous ferromagnetism, the spin-up and spin-down bands will differ in energy by Δ, where Δ is the exchange-splitting in the absence of the external magnetic field. If the Stoner criterion is not satisfied, spontaneous ferromagnetism will not occur but the susceptibility gets altered. The Stoner enhancement in the

susceptibility can be calculated by the combined effect of an applied magnetic field, *H*, and the interactions. The spontaneous magnetization produced due to the energy shift δE is simply $M = \mu_B(n_\uparrow - n_\downarrow) = \mu_B N(E_F)\delta E$. The net change in energy ΔE, in the presence of magnetic field, is

$$\Delta E = \frac{1}{2} N(E_F)(\delta E)^2[1 - UN(E_F)] - M\,H$$
$$= \frac{M^2}{2\mu_B^2 N(E_F)}[1 - UN(E_F)] - M\,H\,. \qquad (1.10)$$

ΔE has the minimum value when

$$\frac{M}{\mu_B^2 N(E_F)}[1 - UN(E_F)] - H = 0 \qquad (1.11)$$

so that the magnetic susceptibility χ is given by

$$\chi = \frac{M}{H} = \frac{\mu_B^2 N(E_F)}{1 - UN(E_F)} = \frac{\chi_P}{1 - UN(E_F)}. \qquad (1.12)$$

where χ_P is the Pauli spin susceptibility in the absence of Coulomb interactions. Thus, χ is larger than χ_P by a factor $[1 - UN(E_F)]^{-1}$, a phenomenon known as the *Stoner enhancement*. This mechanism is responsible for the enhanced Pauli susceptibility [16] measured in the metals Pd and Pt, which can be considered to be on the verge of ferromagnetism. Pd and Pt have a large value for the parameter $UN(E_F)$ to cause significant enhancement in susceptibility but not close enough to unity to cause spontaneous ferromagnetism.

In the above discussion, the effect of temperature has been neglected completely. The Stoner theory was able to account for the rational values of the magnetic moments in the ground state but it had the following drawbacks [10,11]. (i) The values of Curie temperature, T_C, predicted by this model were higher by at least an order of magnitude. (ii) The temperature dependence of spontaneous magnetization could not be described correctly. (iii) It failed to account for the Curie-Weiss susceptibility for temperatures above the ferromagnetic-paramagnetic transition temperature. These inadequacies stem from the basic assumption of the Stoner theory that holds single-particle spin-flip excitations as solely responsible for the decline of magnetization with temperature [10, 17]. It neglects the collective excitations, such as the propagating and non-propagating spin fluctuations completely. Slater [18] was first to bring out clearly the importance of the interaction between the excited electrons and holes in his theory of spin waves, as excitons or bound collective modes in the ferromagnetic insulators. Later, Herring and Kittel [19] showed the importance of these excitations in itinerant-electron ferromagnetic transition metals using dynamical Hartree-Fock Approximation (HFA). But these theories were not able to explain the thermodynamic properties at finite temperatures [11].

Edwards and Wohlfarth [20] extended Stoner theory to explain the magnetism of weak itinerant-electron ferromagnets such as $ZrZn_2$ and Sc_3In with low T_C (25 K and 6 K) and low moments ($0.12\,\mu_B$ and $0.04\,\mu_B$) without much success especially for the Curie-Weiss susceptibility that persists over an extended temperature range, $T_C < T < 10\ T_C$. Curie-Weiss behaviour of susceptibility had been hitherto attributed solely to the local moments. Later, Murata and Doniach [21] developed a phenomenological theory for weakly

ferromagnetic materials in which mutually coupled modes of spin fluctuations were treated self-consistently with renormalized thermal equilibrium state. This theory was followed by a quantum statistical mechanical theory of self-consistent renormalization (SCR) of spin fluctuations put forward by Moriya and Kawabata [22]. The SCR theories were able to explain the discrepancy between the effective moment, deduced from the Curie constant, and the magnetic moment calculated from spontaneous magnetization at very low temperatures and provide a new mechanism for the Curie-Weiss susceptibility. Recent investigations on Ni_3Al and MnSi have given strong support to the SCR theory [23]. Detailed description of the SCR theory and its variants is given elsewhere [10, 11]. The itinerant magnets can be divided in to two categories such as weak itinerant-electron ferromagnets and strong itinerant-electron ferromagnets depending on the position of Fermi level in the spin-up and spin-down bands, as shown in figure 1.3. The following table shows the characteristic features of strong and weak itinerant-electron ferromagnets.

Weak itinerant-electron ferromagnets	Strong itinerant-electron ferromagnets
1. At Fermi energy level E_F, empty states exist in both the spin-up and spin-down bands.	1. At Fermi energy level E_F, empty states exist in only the spin-down band.
2. Low magnetic moment ($< 0.1\ \mu_B$) and low Curie temperature ($\leq$ 100 K).	2. Large magnetic moment ($> 0.1\ \mu_B$) and high Curie temperature ($\geq$ 300K).
3. Very large high-field susceptibility.	3. Small value of high-field susceptibility.
4. Thermal demagnetization occurs because of propagating and non-propagating spin fluctuations.	4. Thermal demagnetization is mainly due to Stoner single-particle excitations.

Next section gives a brief introduction to the magnetic excitations in itinerant- electron ferromagnets.

1.3 Magnetic excitations

1.3.1 Spin waves

In a wide variety of spin systems regardless of whether they are crystalline or amorphous, insulating (localized-electron) or metallic (itinerant-electron), ferromagnetic or antiferromagnetic, or even ferrimagnetic, spin waves exist as well-defined low-lying (in energy) collective magnetic excitations from the ground state. Spin wave excitations, involving energy transfer typically of the order of (~) 100 meV, are amenable to direct detection in the inelastic neutron scattering experiments on bulk samples [23, 17]. The transfer of an electron-hole pair excitation, which results from a spin-flip on an atom, from atom to atom gives rise to spin-wave excitations (figure 1.2). The typical spin wave energy is about ≈ 100 meV, nearly two orders of magnitude smaller than the band width and hence the time scale associated with this energy is $t_{sw} \approx 10^{-13}\, s$ [10]. In itinerant-electron ferromagnets, spin waves exist as well-defined collective excitations only in the small q and small $E_q = \hbar\omega_q$ region in the Brillouin zone (figure 1.4), where the Stoner single-particle excitations require high energies of the order of intra-atomic exchange splitting $\Delta = U(n_\uparrow - n_\downarrow)$; U is the intra-atomic exchange interaction and $n_\uparrow$ ($n_\downarrow$) is the population of the spin-up (spin-down) band (figures 1.2 and 1.3).

Regardless of the nature (localized or itinerant) of magnetic electrons, the spin wave dispersion relation has the form

$$E_{\mathbf{q}}(T) = \hbar\omega_{\mathbf{q}}(T) = \Delta_{SW} + D(T)\, q^2\, (1 - \beta q^2) \tag{1.13}$$

where $\beta = 1/k_B T$ and Δ_{SW} is an effective energy gap in the spin-wave spectrum originating from dipole-dipole interactions, magnetic anisotropy and

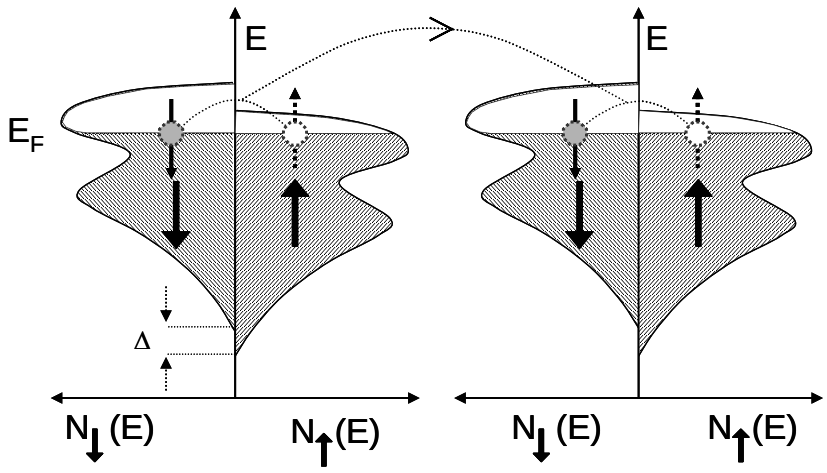

Figure 1.2: Schematic representation of spin-wave excitations in weak itinerant-electron ferromagnet [17].

external magnetic field (if present) and the spin-wave stiffness, D, renormalizes with temperature according to the relation

$$D(T) = D(0)\,(1 - D_2\,T^2 - D_{5/2}\,T^{5/2}) \tag{1.14}$$

for both localized-electron [24,25] and itinerant-electron [20,24] models. Within the framework of the Heisenberg model, the T^2 term is appreciable only when the localized spins interact with one another via the spin of conduction electrons and this term is normally several orders of magnitude smaller than the $T^{5/2}$ term, which arises from the magnon-magnon interactions. By contrast, the T^2 term in the band model results from the interaction between spin waves and single-particle excitations and dominates over the $T^{5/2}$ term, which originates from the magnon-magnon interactions, as in the localized-electron case. Thus, the expressions $D(T) = D(0)\,(1 - D_2\,T^2)$ and $D(T) = D(0)\,(1 - D_{5/2}\,T^{5/2})$ essentially denote the variation of the spin-wave stiffness with temperature for the itinerant- and localized-electron models, respectively.

1.3.2 Single particle excitations

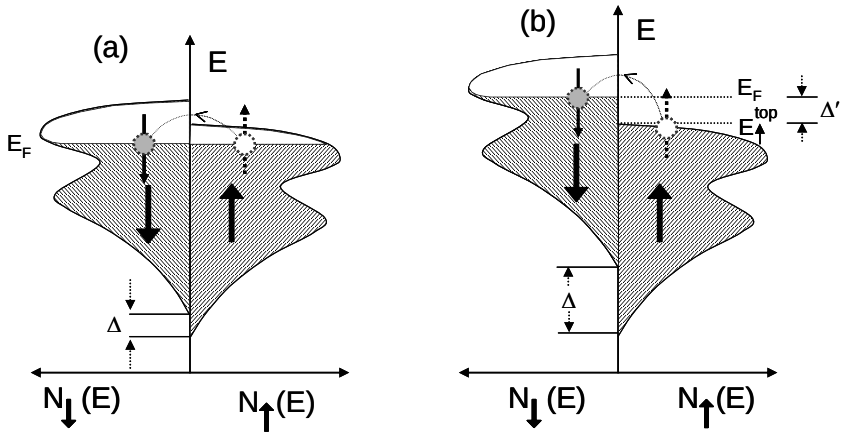

Figure 1.3: Schematic representation of spin-flip stoner single particle excitation in (a) weak itinerant electron ferromagnet and (b) strong itinerant electron ferromagnet [17].

At low temperatures, the spin-flip excitation spectrum consists of single-particle excitations and collective excitations. Spin-up holes and spin-down electrons are created by intra-atomic spin-flip transitions of electrons from a spin-up band to a spin-down band (as sketched in figure 1.3 for weak and strong itinerant-electron ferromagnets). These spin-up holes and spin-down electrons move independent of one another in a common mean (exchange) field and constitute the single-particle excitations. Such excitations form the Stoner continuum, which, at finite momentum transfer q, extends from $E_q = 0$ in figure 1.3(a) ($E_q = \Delta' = E_F\,(\textit{Fermi energy}) - E_\uparrow^{top}$ in figure 1.3(b)) to high

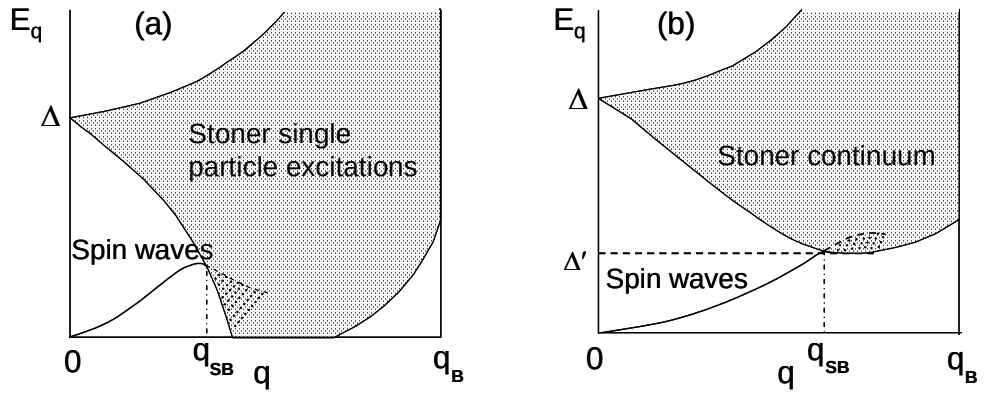

Figure 1.4: Schematic representation of magnetic dispersion and magnetic excitations in a (a) weak itinerant electron ferromagnet and (b) strong itinerant electron ferromagnet [17].

energies, as schematically depicted in figure 1.4(a) (1.4(b)) for weak (strong) itinerant-electron ferromagnets. Single-particle excitations with zero momentum transfer ($q = 0$) cost an energy equal to the exchange splitting Δ (figure 1.4).

1.3.3 Spin fluctuations

As the momentum transfer q increases from zero, the energy gap between the Stoner continuum and spin-wave spectrum reduces rapidly so much so that beyond a certain threshold value of $q = q_{SB}$, where SB is Stoner Boundary of the single particle excitations, the spin wave dispersion curve enters the Stoner continuum. For $q > q_{SB}$, the spin waves get damped with the result that the collective magnetic excitations in the Stoner continuum are the overdamped (non-propagating) modes of exchange-enhanced longitudinal and transverse spin-density fluctuations. For spin fluctuations of given q, in the longitudinal mode, the magnetic moments point in the same direction but their amplitude fluctuates from one lattice site to the other whereas in the transverse mode, amplitude of the magnetic moments remains nearly constant while their direction varies from site to site. Since spin wave modes of larger and larger q are excited as the temperature is raised from $T = 0$, the transition at $q = q_{SB}$, from well-defined spin waves to non-propagating exchange-enhanced transverse spin fluctuations should be observed at a certain finite value of temperature. By contrast, the thermally-excited non-propagating exchange-enhanced longitudinal spin-density fluctuations persist down to $q = 0$ and coexist with, but are swamped by, spin waves for $q \leq q_{SB}$ [26, 27].

Physical quantities that describe the equilibrium state of a macroscopic system are very close to their average values. However, there are always small

deviations from average values even at equilibrium, variables fluctuate and one has to deal with the probability distribution of these fluctuations that is generally taken into account using Gaussian statistics [28]. The probability distribution of frequency $\omega(x)$ is related to entropy though the Boltzmann formula

$$\omega(x) = const. \times \exp(S(x)) \tag{1.15}$$

Since the entropy $S(x)$ has to be maximum for the equilibrium, the first derivative of $S(x)$ with respect to x must vanish and second derivative should be negative. At equilibrium, $x = \langle x \rangle = 0$ (where $\langle x \rangle$ is the average value of x) and hence both the derivatives of $S(x)$ vanish while approaching the critical point. Therefore the Gaussian statistics for the fluctuations are restricted to those parts of the phase space that are far from critical points. To deal with fluctuations mathematically, one has to recognize the vector properties of both the magnetization and its fluctuations. For reasons of symmetry, it is postulated that the volume integral of odd powers in the fluctuation always vanishes. If now $\vec{m}(r)$ is the locally fluctuating magnetic moment, one assumes

$$\frac{1}{V}\int (\vec{m}(r))^n \, d\tau = \langle m^n \rangle \text{ for } n = 2k$$
$$= 0 \qquad n = 2k+1. \tag{1.16}$$

Fluctuations appear in all the three directions. The direction of $\vec{M}$ = *(0,0, M_z)* is taken as the z axis of a local co-ordinate system, so that there are two perpendicular fluctuations and one parallel fluctuation with respect to $\vec{M}$.

These three components of the fluctuations are denoted as $\vec{m}_i = m_i \vec{e}_i$ where $(m_1, m_2, m_3) \equiv (m_x, m_y, m_z)$ are the three components in the directions given by the unit vectors $\vec{e}_i$; m_z is parallel to $\vec{M}$, m_x and m_y perpendicular to $\vec{M}$. One now extends the original order parameter by the statistical average including the fluctuation terms in the Ginzberg-Landau expansion. The inherently small magnitude of the order parameter (local magnetization) $\vec{M} + \vec{m}(\vec{r})$ with mean $\vec{M}$ and fluctuation amplitude $\vec{m}(\vec{r})$, even at the lowest temperature, in weak itinerant-electron ferromagnets substantially enlarges the temperature domain over which the Ginzberg Landau expansion of the local free energy in the powers of the order parameter is valid. As a consequence, the total free energy and magnetic equation of the state hold [29] over the temperature range that spans both the ferromagnetic and paramagnetic regimes:

$$F(M) = F(0) + \frac{1}{2}[a(T) + b(< 3m_{\|}^2 > + 2 < m_{\perp}^2 >)]M^2 + \frac{b}{4}M^4 \tag{1.17}$$

$$F(0) = F_0 + \frac{1}{2}a(T)(< m_{\|}^2 > + 2 < m_{\perp}^2 >) + \frac{b}{4}(< m_{\|}^2 >^2 + 4 < m_{\perp}^2 >^2 + 4 < m_{\|}^2 >< m_{\perp}^2 > \tag{1.18}$$

and

$$\frac{1}{M}\frac{\partial F}{\partial M} = \frac{H}{M(T,H)} = a(T) + b[(3 < m_{\|}^2 > + 2 < m_{\perp}^2 >) + M^2(T,H)] \tag{1.19}$$

where F_0 is the contribution to the free energy which is independent of the order parameter, and the Landau coefficients of the Stoner theory [12, 30], *a* and *b*, are given by

$$a(T) = -[2\chi(0,0)^{-1}[1-(T/T_C^S)^2 - BST^4] \;\; ; \;\; b = [2\chi(0,0)M^2(0,0)]^{-1} \tag{1.20}$$

and

$$\chi(0,0) = N\mu_B^2 N(E_F)(T_F/T_C^S)^2 = N\mu_B^2 N(E_F)S = (\chi_P/2)S \tag{1.21}$$

$$M^2(0,0) = (N\mu_0\mu_B)^2 = (S\gamma)^{-1} \tag{1.22}$$

$$S = [IN(E_F)-1]^2 \tag{1.23}$$

$$\gamma = (1/2)\{N\mu_B N(E_F)\}^{-2}\{[N'(E_F)/N(E_F)]^2 - [N''(E_F)/3N(E_F)]\} \tag{1.24}$$

In the above expressions, $\chi(0,0)$ and μ_0 are the zero-field differential susceptibility and moment per alloy atom at 0 K, respectively, *H* stands for the external magnetic field (H_{ext}) corrected for demagnetization and the other anisotropy fields present, S is the Stoner enhancement factor, *U* (the Stoner parameter) is a measure of the exchange splitting of the bands, *N* is the number of atoms per unit volume, $N(E_F)$ is the density of single-particle states (DOS) at the Fermi level E_F and $N'(E_F)\,(N''(E_F))$ is its first (second) energy derivative, T_C^S is the Stoner Curie temperature, the coefficient B of the T^4-term in equation (1.20) involves derivatives of the DOS at E_F up to the fourth order and its explicit form is given elsewhere [31, 32], χ_P is the Pauli spin susceptibility and the thermal variances of the local magnetization parallel (||), $< m_{\|}^2 >$, and perpendicular ($\perp$), $< m_{\perp}^2 >$, to the average magnetization , $\vec{M}$, are related to the imaginary part of the dynamical wavevector dependent susceptibility, $\mathrm{Im}\,\chi_\nu(\vec{q},\omega)$, where $\nu(=\|,\perp)$ is the polarization index, through the well-known fluctuation dissipation relation [26, 29, 30, 33, 34]

$$< m_\nu^2 > = 4\hbar \int \frac{d^3 \vec{q}}{2\pi^3} \int \frac{d\omega}{2\pi} \left(n(\omega) + \frac{1}{2} \right) \mathrm{Im}\, \chi_\nu(\vec{q}, \omega) \tag{1.25}$$

with

$$n(\omega) = [\exp(\hbar\omega / k_B T) - 1]^{-1} \tag{1.26}$$

$$\mathrm{Im}\, \chi_\nu(\vec{q}, \omega) = \omega\, \chi_\nu(\vec{q})\, \frac{\Gamma_\nu(\vec{q})}{\omega^2 + \Gamma_\nu^2(\vec{q})} \tag{1.27}$$

$$\chi_\nu(\vec{q}) = \chi_\nu(\vec{q}, \omega = 0) = \chi_\nu(0)\, \frac{\kappa_\nu^2}{\kappa_\nu^2 + q^2} \tag{1.28}$$

$$\Gamma_\nu(\vec{q}) = \gamma_\nu\, q\, \chi_\nu^{-1}(\vec{q}) = \Gamma_\nu(0)\, q\, (\kappa_\nu^2 + q^2) \tag{1.29}$$

$$\chi_\nu(0) = \chi_\nu(\vec{q} = 0) = (c_\nu \kappa_\nu^2)^{-1} \tag{1.30}$$

$$\Gamma_\nu(0) = \Gamma_\nu(\vec{q} = 0) = c_\nu \gamma_\nu \tag{1.31}$$

where $n(\omega)$ is the Bose function, $\Gamma_\nu(\vec{q})$ is the relaxation frequency of a spontaneous spin fluctuation of wave vector $\vec{q}$ and polarization ν, $\chi_\nu(0)$ is the field- and temperature-dependent susceptibility (i.e., $\chi_\nu(0) \equiv \chi_\nu(T, H)$), c_ν is the coefficient of the gradient term in the Ginzburg-Landau expansion, and the quantity γ_ν depends [33] on the shape of the DOS curve near E_F. Equations (1.25-31), obtained by using self-consistent random-phase approximation

(RPA) or by making use of single-band model and assuming $\langle m_\nu^2 \rangle$, $\vec{q}$, and ω to be small [33], correctly describe the results of neutron scattering experiments on archetypical weak itinerant-electron ferromagnets. According to equation (1.25), spin fluctuations are made up of two components, the zero-point (ZP) spin fluctuations, $\langle m_\nu^2 \rangle^{ZP}$, and thermally-excited (TE) spin fluctuations, $\langle m_\nu^2 \rangle^{TE}$, represented in equation (1.25) by the factors ½ and $n(\omega)$, respectively. The importance of zero-point fluctuations in weak itinerant-electron ferromagnets was asserted by the theoretical treatments due to Kaul [26], Takahashi [35], Solontsov and Wagner [36] and experimental evidence for the same in bulk Ni_3Al was provided by Semwal and Kaul [37].

1.4 Magnetic phase transitions

In the zero external magnetic field, the ferromagnetic (FM)-to-paramagnetic (PM) phase transition at the critical point, T_C, is a second-order phase transition. In the critical region (whose extent depends on the type of material and is typically of the order of $|\varepsilon| = |(T - T_C)/T_C| \leq 0.01$, where T_C is the critical temperature) as the critical temperature is approached, the thermally-excited critical fluctuations of the local spin-density (order parameter) rapidly pick up in amplitude and get correlated in space over larger and larger distances with the result that they destroy the long-range magnetic order at T_C, where the spin-density-fluctuation-spin-density-fluctuation correlation length, $\xi(T = T_C)$, (henceforth referred to as spin-spin correlation length, for brevity) diverges and the magnetic order-disorder phase transition occurs. Experimental investigations in the critical region near a thermally-driven phase transition provide a unique and direct means of probing the type

of interactions present and the interplay between them, that finally decides the nature of magnetic order prevailing in the systems under study for temperatures below the transition temperature. This is so because the critical behaviour of a system is solely governed by the nature of the underlying interactions. For instance, an interplay between interactions such as crystal-field (leading to uniaxial anisotropy), isotropic short-range Heisenberg and long-range dipole-dipole interactions, in a localized-spin system gives rise to a series of crossovers from uniaxial dipolar critical regime (where both uniaxial anisotropy and dipolar interactions dominate) to isotropic dipolar critical regime (where anisotropy is negligibly small and isotropic dipolar interactions take over) to isotropic Heisenberg critical regime (where short-range isotropic Heisenberg interactions become prominent) and so on, as the temperature is raised above T_C in the critical region. To facilitate understanding of the magnetic phase transitions, the prerequisites such as the definition of the asymptotic critical exponents and amplitudes, which quantify the static critical behaviour near a magnetic order-disorder phase transition, are given below.

Static critical exponents and amplitudes

In the asymptotic critical region, the behavior of a magnetic system is characterized by a set of critical exponents and amplitudes [38, 39]. Critical exponents are the exponents in the power laws that define the deviations of various thermodynamic quantities from their values at the critical point T_C and the corresponding amplitudes are the forefactors in these power laws. The asymptotic critical exponents and amplitudes for the second-order ferromagnetic (FM) to paramagnetic (PM) phase transition are defined as follows.

Spontaneous magnetization

In the asymptotic critical region, spontaneous magnetization, M_S, the order parameter for the FM-PM phase transition, varies with the reduced temperature $\varepsilon = (T - T_C)/T_C$ as

$$M_S(T) = \lim_{H \to 0} M(T,H) = B(-\varepsilon)^{\beta}, \qquad \varepsilon < 0 \tag{1.32}$$

Initial susceptibility

Initial susceptibility, defined as $\chi_0 = \lim_{H \to 0} [\partial M / \partial H]_T$, diverges at T_C as

$$\chi_0(T) = \Gamma^{-} (-\varepsilon)^{-\gamma^{-}}, \qquad \varepsilon < 0 \tag{1.33}$$

$$\chi_0(T) = \Gamma^{+} \varepsilon^{-\gamma^{+}}, \qquad \varepsilon > 0 \tag{1.34}$$

Critical isotherm

At $T = T_C$, magnetization M varies with field H as

$$M(T_C, H) = A_0 \, H^{1/\delta} \qquad \text{or}$$

$$H = D \, M^{\delta} \qquad \varepsilon = 0 \tag{1.35}$$

Specific heat

Zero-field ($H = 0$) specific heat diverges at T_C as

$$C_{H=0}(T) = \frac{A^{-}}{\alpha^{-}}[(-\varepsilon)^{-\alpha^{-}} - 1] + B^{-}, \qquad \varepsilon < 0 \tag{1.36}$$

$$C_{H=0}(T) = \frac{A^{+}}{\alpha^{+}}[\varepsilon^{-\alpha^{+}} - 1] + B^{+}, \qquad \varepsilon > 0 \tag{1.37}$$

Specific heat exhibits a cusp at T_C when $\alpha < 0$ whereas for $\alpha = 0$ the singularity is logarithmic. B^- and B^+ represent the non-singular background for $\varepsilon < 0$ and $\varepsilon > 0$, respectively, in the asymptotic critical region.

Spin-spin correlation function

At T_C, the correlation function for the spin fluctuations at the points **0** and **r** in space, $G(\mathbf{r}) \equiv \langle [\mathbf{S}(\mathbf{r}) - \langle \mathbf{S} \rangle][\mathbf{S}(\mathbf{0}) - \langle \mathbf{S} \rangle] \rangle$, decays with distance, r, as

$$G(|\mathbf{r}|) = N \left|\mathbf{r}\right|^{-(d-2+\eta)} \qquad [\text{large} \left|\mathbf{r}\right|,\ \varepsilon = H = 0], \tag{1.38}$$

where d is the dimensionality of the lattice and η is a measure of the deviation from the mean-field behaviour.

Spin - spin correlation length

Correlation length, ξ, is the distance over which the order parameter fluctuations are correlated and is defined through the relation $G(|\mathbf{r}|) = e^{-|\mathbf{r}|/\xi(T)} / |\mathbf{r}|$, where $|\mathbf{r}| \to \infty$. In the critical region, ξ depends on temperature as

$$\xi(T) = \xi_0^- (-\varepsilon)^{-\nu^-} \qquad \varepsilon < 0, H = 0 \tag{1.39}$$

$$\xi(T) = \xi_0^+ \varepsilon^{-\nu^+} \qquad \varepsilon > 0, H = 0 \tag{1.40}$$

In equations (32)-(40), β, γ^-, γ^+, δ, α^-, α^+, η, ν^- and ν^+ are the asymptotic critical exponents and B, Γ^-, Γ^+, A_0 or D, A^-, A^+, N, ξ_0^- and ξ_0^+ are the corresponding asymptotic critical amplitudes. There are nine critical

exponents in total but only two of them are independent [38]. This is a consequence of the scaling relations between them, e.g., $\alpha^+ = \alpha^-$, $\gamma^+ = \gamma^-$, $\nu^+ = \nu^-$, $\beta\delta = \beta + \gamma$ (Widom equality), $\alpha + 2\beta + \gamma = 2$ (Rushbrooke equality), $\alpha + \beta(\delta + 1) = 2$ (Griffiths equality), $(2 - \eta)\nu = \gamma$ (Fisher equality) and $d\nu = 2 - \alpha$ (Josephson equality), to name a few.

The single power laws are strictly valid only at $T = T_C$. In practice, however, the power laws are fitted to the experimental data over a finite temperature range. Consequently, such an approach yields only average exponent values since, in general, the amplitudes as well as the exponents are temperature-dependent and they assume temperature-independent values only in the asymptotic critical region [39]. In order to tackle this problem effectively, the concept of effective critical exponent was introduced by Riedel and Wegner [40]. The effective critical exponents provide a local measure for the degree of singularity of physical quantities in the critical region. The effective critical exponent, $\lambda_{eff}(\mu)$, of a function $f(\mu)$, is defined by the logarithmic derivative $\lambda_{eff}(\mu) = d \ln f(\mu) / d \ln \mu$. In the limit $\mu \to 0$, $\lambda_{eff}(\mu)$ coincides with the asymptotic critical exponent λ.

1.5 Intermetallic compound Ni_3Al

1.5.1 Weak itinerant-electron ferromagnets

Before discussing the magnetic and electrical transport properties of intermetallic compound Ni_3Al in some detail, general properties of weak itinerant ferromagnets are described below. Transition metal-based intermetallic compounds such as MnSi, Ni_3Al, NiPt, Sc_3In and $ZrZn_2$ are the examples of weak itinerant electron ferromagnets [26]. They have

1) *low* saturation moment per transition metal atom (TM) at 0 K (< 0.4 μ_B/TM atom),
2) *low* magnetic order-disorder phase transition temperature (T_C < 45 K),
3) *large* high-field magnetic susceptibility at 0 K,
4) *very large* coefficient of the term *linear* in temperature in the specific heat at low temperatures,
5) *negative* magnetoresistance,
6) $T^{5/3}$-power law behaviour of the resistivity over a wide temperature range around T_C,
7) T^2 and $T^{4/3}$ temperature variations of the spontaneous magnetization squared in the intermediate temperature range and at temperatures just outside the critical region but below T_C, respectively, and
8) Curie-Weiss behaviour of the magnetic susceptibility in the paramagnetic state.

1.5.2 Magnetic properties

Among the weak itinerant-electron magnets mentioned above, intermetallic compound Ni_3Al has been extensively investigated mainly because it is comparatively easy to prepare and is an ideal candidate for testing and understanding the theoretical models of weak itinerant magnetism due to its low magnetic moment ($0.075\,\mu_B$) [41] and low Curie temperature ($T_C \cong 41$ - 43 K) [42]. Several investigations of the magnetic properties have been carried out to clarify the origin of the magnetism [41- 46, 37] but certain aspects of magnetism in this compound have eluded a complete understanding so far. According to the phase diagram [47] of binary Ni_xAl_{100-x} alloys, the intermetallic compound Ni_3Al has a homogeneity range which extends from x_l = 73.5 at.% to x_u = 76.5 at.%. The Curie temperature, T_C, where the

spontaneous magnetization vanishes, strongly depends on the Ni concentration in such a way that long range ferromagnetic order breaks down completely and thus T_C reduces to zero at the critical concentration x_c ~ 74.5% [41]. In addition, even for the stoichiometric compound, different groups have reported different values of T_C, e.g., for the sample with x = 75 at.%, T_C has values as different as 25 K [48], 40.6 K [45] 43.5 K [46], and 56.46 K [37]. While there is a general agreement [37, 41, 42, 45, 46] so far as the magnetic moment per Ni atom ($0.075\,\mu_B$) in Ni_3Al is concerned, the only exception [44] is the value 0.103 μ_B/Ni atom.

The results of magnetic measurements are normally discussed in the light of either the Stoner-Wohlfarth [30-32, 41-44] model or the spin fluctuation (SF) model [22, 26, 28, 29, 33-35, 44-46, 49-53]. On the one hand, de Boer et al. [31, 41] claim that the temperature dependence of spontaneous magnetization, M(T,0), in the temperature interval $0.1T_C \leq T \leq 0.75T_C$ is very well described by the expression $M(T,0) = M(0,0) - aT^2$, which is an outcome of the Stoner-Wohlfarth model [12, 13, 20, 30], according to which the Stoner *single-particle* spin-flip excitations are the sole cause for the thermal demagnetization of M(T,0). On the other hand, Sasakura et.al [45] assert that $M(T,0)$ decreases with increasing temperature in accordance with the relations $M^2(T,0) = M^2(0,0) - a'T^2$ and $M^2(T,0) = a''\,(T_C^{4/3} - T^{4/3})$, predicted by the spin fluctuation model [11, 21, 22, 26,29], in the temperature ranges $0.1T_C \leq T \leq 0.4T_C$ and $0.42T_C \leq T \leq T_C$, respectively. According to the spin fluctuation model, *non-propagating* thermally-excited longitudinal and transverse spin-density fluctuations are completely responsible for the decline of spontaneous magnetization with increasing temperature. On good quality single crystals of Ni_3Al with residual resistivity ratio greater than 40, small-angle neutron

scattering [54] and inelastic neutron scattering experiments [55] gave direct evidence for well-defined spin-wave excitations (*propagating* thermally excited *transverse* spin-density fluctuations) in the temperature range $0.1T_C \leq T \leq 0.8T_C$. This observation was in direct conflict with the Stoner-Wohlfarth model and earlier magnetic measurements. Though the existence of spin waves at low temperatures in itinerant-electron magnetic systems has been recognized [19] for a long time now, there has been *no indication* for such excitations in Ni_3Al from magnetization measurements. But in low temperature specific heat measurements, Dhar et al. [56] found an upturn (which could be progressively suppressed by magnetic fields) in the low-temperature region of the C/T-vs-T^2 plot and attributed it to an enhancement of the effective electronic mass due to spin fluctuations. They also found a crossover at a Ni concentration of 75.1 at.% from a spin fluctuator to a ferromagnet as Ni concentration increases [57]. The possibility of the presence of superparamagnetic clusters [58-60] or, at least, a magnetic inhomogeneity [42] in the samples was suggested among other conflicting opinions [61, 62].

Because of the aforementioned dispute, several theoretical investigations using the electronic-energy-band-structure calculations were undertaken in order to elucidate the origin of weak itinerant-electron ferromagnetism of the alloy [63-65]. Hackenbracht and Kübler [63] employed the linear-muffin-tin-orbital (LMTO) method with the atomic-sphere approximation (ASA) and arrived at the value for the magnetic moment $0.031\,\mu_B$/Ni atom, which is only 40% of the experimental value [41]. Later Buiting et al. [64] argued that Ni_3Al is a still in the fluctuation regime even though it is in a ferromagnetic state. The calculated magnetic moment almost vanished at the experimental lattice constant (a = 3.568 Å), while it was calculated to be $0.067\,\mu_B$/ Ni atom, which

is close to the experimental value, at a lattice constant of 3.583 Å. Min et al. [65] also investigated the electronic structure and magnetic properties of Ni_3Al. The calculated magnetic moment was 0.15 μ_B/ Ni atom and the authors argued that the spin-orbit interaction might reduce the calculated magnetic moment to 0.087 μ_B/ Ni atom, since the spin-orbit interaction would reduce the exchange splitting by ~ 40%. Recent electronic structure calculations due to Aguayo et al. [66] showed that the LDA results in the case of Ni_3Al are not satisfactory as this theoretical treatment ignores spin fluctuations. The SF theories proposed till now were, to some extent, limited in scope as they are unable to clarify the role of 'zero-point' (quantum) spin fluctuations and failed to yield an expression which quantifies the suppression of local spin-density fluctuations by external magnetic field, H_{ext}. Such theoretical limitations hamper the understanding of magnetism in weak itinerant-electron ferromagnets such as Ni_3Al. These deficiencies of the conventional spin fluctuation theories have been addressed and remedied by Kaul [26] using a self-consistent treatment of the spin fluctuation model, which makes use of the Ginzburg-Landau formalism. The zero-point and thermally-excited contributions to spin fluctuations in weak itinerant-electron ferromagnets in the presence and absence of H_{ext} have been explicitly calculated. The importance of 'zero-point' fluctuations in the thermal demagnetization of magnetization in Ni_3Al particularly in the intermediate temperature range was clearly brought out by the experimental investigations by Semwal and Kaul [37].

1.5.3 Electrical transport properties

The transport properties of Ni_3Al are as intriguing as its magnetic properties. For example, the temperature dependence of resistivity, $\rho(T)$, in Ni_3Al and its isostructural compound, Ni_3Ga, is very *strong* as compared with

that in other magnetic metals and alloys. The electron-phonon scattering contribution to the temperature-dependent part of the resistivity at low temperatures (only 1% at 10 K) is too small to account for the observed $\rho(T)$. In well-ordered annealed samples of Ni_xAl_{100-x} alloys, Fluitmann et al. [67] observed that the magnitude of temperature-dependent part of resistivity is two or three orders of magnitude larger than that expected from the usual T^2-power law behaviour due to electron-electron scattering. Moreover, as one approaches the critical concentration $x_c \approx 74.6$ at% of Ni, where long-range ferromagnetic order breaks down, from $x > x_c$, the exponent 'n' in the T^n variation of $\rho(T)$ deviates appreciably from 2. Fluitmann et al. [67] attributed these deviations to the scattering of conduction electrons from low-lying magnetic excitations, whose nature was obscure at that time. These experimental results are at variance with the temperature variation of resistivity predicted by the calculation of the electrical resistivity at low temperatures due to spin waves (SW), using the random phase approximation (RPA), by Mills and Lederer [68]. The theoretical investigations (based on RPA) due to Schindler and Rice [69] and Mathon [70] also could not explain the above experimental results since it was soon realized that RPA does not yield correct results particularly at high temperatures where the interactions between different spin fluctuation (SF) modes become important. The contributions due to spin waves and spin fluctuations to electrical resistivity in weakly ferromagnetic (WF) metals was calculated by Moriya and Ueda using the SCR theory [71] and the suppression of these excitations at low temperatures by external magnetic field, H_{ext}, was calculated by Ueda [72]. According to these calculations, at very low temperatures, spin-wave contribution to resistivity varies with temperature as $\rho_{SW}(T) \sim T^2$ for WF metals whereas at slightly higher temperatures, on both sides of the critical boundary (where the

ferromagnetic instability sets in), contribution from spin fluctuations is important and varies with T as $\rho_{SF}(T) \sim T^2$. The temperature region where the electrical resistivity is proportional to T^2, is narrow and the coefficient of T^2 becomes large when the substance lies near the critical boundary of ferromagnetism. For weakly ferromagnetic metals, the anomalies of the electrical and thermal resistivities at T_C are small. These observations were later confirmed experimentally by Sasakura [45] and Yoshizawa [73] et al. However, very recently, Niklowitz et. al [74] observed that in very high-purity single crystals (with a residual resistivity ratio of about 30) at low temperatures (50 mK to 7 K) and ambient pressure, the resistivity cannot be described in terms of the T^2 power law. In this temperature range, $\rho(T) \sim T^n$ with $n \cong 1.5$. Moreover, at the critical pressure, p_c, of 81 kbar, the long-range ferromagnetic order was destroyed completely with $T_C \rightarrow 0$ K. With the application of pressure (~ 32 kbar) < p_c, the resistivity, below 4 K, was best described by the power law $T^{5/3}$ and below 1 K, by the exponent $n = 2$. At temperatures well above 10 K, the exponent dropped down to unity. The physical significance of these exponents is as follows. For a metal on the border of ferromagnetism in three dimensions (3D), the mean-field spin fluctuation model predicts a $T^{5/3}$ temperature variation of resistivity, instead of the conventional T^2 temperature dependence of a normal metal at low temperatures. The $T^{5/3}$ variation of resistivity is a consequence of an underlying quasiparticle scattering rate that varies linearly with the excitation energy, E, of a quasi particle near the Fermi level. This is the behaviour associated not with a Fermi liquid, for which the quasiparticle scattering rate varies as E^2, but of a crossover state known as a the marginal Fermi liquid. The above-mentioned observed results are, at best, in agreement with the mean-field spin fluctuation model [70] but not with the results of small-angle neutron scattering experiments [54,55] and low-

temperature resistivity and magnetization data of Sasakura et al. [45] and Yoshizawa et al. [73].

1.5.4 Magneto-transport properties

Chang et al. [75] were first to study the effect of magnetic field on the resistivity of Ni_3Al and Ni_3Ga intermetallic compounds. The measurements were performed on the *well-annealed* polycrystalline samples at a few temperatures in the range from 1.5 K to 330 K with electrical current applied either parallel (longitudinal magnetoresistance) or perpendicular (transverse magnetoresistance) to the magnetic field direction, in magnetic fields up to 350 kOe. The main observations were that at any temperature, for all the samples, the difference between transverse and longitudinal magnetoresistance is positive and both longitudinal and transverse magnetoresistance exhibit the same general features. (I) At 4.2 K, the magnetoresistance, $\Delta\rho/\rho = [\rho_{||}(T,H) - \rho(T,H=0)]/\rho(T,H=0)$ has a three-stage behaviour. As the magnetic field increases, at low fields (0 - 50 kOe), $\Delta\rho/\rho$ is positive, goes through a maximum, and then decreases even to negative values in between 50 kOe to 100 kOe. It becomes a strictly monotonic increasing function of the field above 100 kOe. (II) In the case of Ni_3Al at 4.2 K, $\Delta\rho/\rho$ of paramagnetic compounds (near critical concentration) shows all the three-stage behavior mentioned earlier whereas in the case of ferromagnetic compounds, negative $\Delta\rho/\rho$ is observed at lower fields (< 100 kOe) and thereafter $\Delta\rho/\rho$, becomes positive at higher fields. By contrast, the stoichiometric compound, Ni_3Al shows a positive $\Delta\rho/\rho$ at all the fields. (II) At 77 K, $\Delta\rho/\rho$ is always *negative* but in a few samples, shows an upward turn at very high fields (> 250 kOe).

The interpretation of these observations was given on the basis of Mott two-band model [76] with the assumptions: (1) the electrons in the *s*-band are mainly responsible for carrying the electric current and their number is constant in the composition range, (2) the residual resistivity can be regarded as the sum of two terms; intra-band ($s \rightarrow s$) and inter-band ($s \rightarrow d$) scattering. (3) These transitions are induced by defects, impurities, phonons, etc. and their number is proportional to the density of states at the Fermi level, ε_F, in the *s* and *d* bands, $N_s(\varepsilon_F)$ and $N_d(\varepsilon_F)$ respectively. Hence, the respective relaxation times are inversely proportional to $N_s(\varepsilon_F)$ and $N_d(\varepsilon_F)$:

$$\tau_{s\to s} \propto 1/\mathrm{N}_s(\varepsilon_F);\ \tau_{s\to d} \propto 1/\mathrm{N}_d(\varepsilon_F) \quad \text{and}$$
$$1/\tau = 1/\tau_{s\to s} + 1/\tau_{s\to d} \tag{1.41}$$

With these assumptions and adjusting band parameter values, within the framework of two-band model, Chang et al. [75] could satisfactorily explain the magnetoresistivity data at low temperatures and high magnetic fields provided the non-spin-flip scattering processes are involved. However, in the ferromagnetic samples, the agreement between experiment and theory was good only at high fields (H >100 kOe) and low temperatures (T < 30 K) where the negative magnetoresistance (arising from the field-induced change in $N_d(\varepsilon_F)$ for the spin-up and spin-down d-sub-bands) was masked by the "conventional" positive magnetoresistance due to the orbital motion of the conduction electrons in a magnetic field.

Hambourger et. al. [48] showed that the agreement between theory and experiment is poor particularly at low fields and high temperatures where magnetoresistance is negative and magnetic effects dominate over the orbital

effects. They made an important observation that the temperature dependence of negative magnetoresistance shows pronounced peak near the Curie temperature. The transverse magnetoresistance, where magnetic field is applied in the plane of the sample and perpendicular to the flow of electric current, measured by Sasakura et al. [45] was positive up to 4.2 K and negative thereafter encompassing temperatures well above T_C. Total magnetoresistance was assumed to be the sum of two contributions, i.e.,

$$\Delta\rho = \Delta\rho_{orb} + \Delta\rho_{sf} \tag{1.42}$$

with $\Delta\rho_{orb} / \rho = C_1 \ (H / \rho)^2$ and $\Delta\rho_{sf}$ is the contribution due to spin fluctuations given by Ueda [72]. Yoshizawa et al. [73] obtained the suppression of the coefficient in the T^2-dependence of resistivity, by magnetic field, from their magnetoresistance data on annealed polycrystalline samples and found that at low temperatures, the results are consistent with the predictions based on the spin-fluctuation theory [72]. However, the theories that address the suppression of spin fluctuations by external magnetic field have some deficiencies. First, these theoretical formalisms make use of electron gas model to calculate the field- and temperature-dependent static susceptibility that is consistent with the magnetic equation of the state. The electron gas model forms an oversimplified description of the band structure in weak itinerant-electron ferromagnets. Second, a number of adjustable parameters were used to find an agreement between theory and experiment. Third, the theory completely neglects the contribution from the spin waves (which almost completely accounts for [37] the temperature dependence of magnetization observed in Ni_3Al at low temperatures and whose overwhelming presence in Ni_3Al is well-documented [54, 55] from neutron scattering

experiments) and exclusively deals with the spin-fluctuation contribution only at low temperatures. To remedy this situation, Kaul [27] has, recently, calculated the spin wave and exchange-enhanced spin-density fluctuation contributions to the electrical resistivity, $\rho(T)$, of weak itinerant-electron ferromagnets in the absence and presence of the magnetic field, H, employing two-band (s- and d- band) model and the version of spin-fluctuation theory that makes use of the Ginzberg-Landau formalism.

Considering that a varying degree of site disorder, resulting from different annealing treatments, is bound to be present in the samples studied previously in the literature, it is possible that the above discrepancy between the experimental observations and hence between experiment and theory is caused by an interplay between site disorder and compositional disorder. To address this issue, high-precision bulk magnetization and ac ('zero-field') susceptibility measurements were performed recently on well-characterised $Ni_{75}Al_{25}$ samples with varying degree of site-disorder. These investigations [77] revealed the presence of the thermally-excited propagating and non-propagating spin fluctuations as well as zero-point fluctuations. Moreover, the suppression of these magnetic excitations by external magnetic field, H_{ext}, was correctly described by the expressions predicted by the modified spin-fluctuation (MSF) [26] theory for weak itinerant-electron ferromagnets. The temperature dependence of magnetization, $M(T,H)$, in a few off-stoichiometric compositions in the alloy series $Ni_{75\pm x}Al_{25\mp x}$ (x = 0, 1) was at variance with the results of spin-fluctuations theories [11,26,29]. However, $M(T,H)$ data found a much better description [78] in terms of the percolation theory for magnon-to-fracton crossover [79]. Now that the percolation theory is based on local

moment picture, the departure from itinerant behavior in off-stoichiometric alloys is not understood at present and thus is intriguing.

With a view to ascertain how ternary Fe substitution modifies the magnetic properties of $Ni_{75}Al_{25}$, Ni-Fe-Al alloys with nominal composition as $Ni_{75-x}Fe_xAl_{25}$ (x = 0, 5, 10, 20) have been prepared [80] in different states of site disorder. The magnetic and structural investigations were intended to bring out the effect of substitutional site disorder on the magnetic properties of a given composition. In the above-mentioned alloy series, an elaborate procedure, detailed in Ref. [37], was used to accurately determine the temperature ranges over which spin waves (SW) and spin fluctuations (SF) are primarily responsible for thermal demagnetisation, the spin-wave stiffness at T = 0 K, D_0, T_C (Curie temperature, deduced from critical-point analysis [39]) and spontaneous magnetization at T = 0, M_0. Regardless the degree of site disorder present, M_0, D_0 and T_C for the composition x = 20 exhibit strong departure from the composition dependence of these parameters noticed in the range $0 \leq x \leq 10$. To elucidate this point further, while M_0 and D_0 vary linearly with increasing Fe concentration up to x = 10, the sample (of a given state of site disorder) with x = 20, does not follow the same trend [81].

Apart from the site- and compositional- disorder prevalent in the case of polycrystalline materials, a variety of other types of disorder and/or defects exist in nanocrystalline materials. In these materials, as the size of the crystallite becomes smaller, the number of atoms near the surface of the particle becomes comparable to that in the core volume of the particle. Thus, the ratio of the number of atoms at the surface to that within the core volume is very large in the nanocrystalline materials as compared to their polycrystalline

counterparts. A competition between the surface and bulk energies brought about by the size reduction can lead to drastic changes in the mechanical, electrical, optical and magnetic properties [82]. Recently, a detailed comparative bulk magnetization study [83] of the nanocrystalline and polycrystalline samples of Ni_3Al, revealed that the long-range ferromagnetic order prevalent in the crystalline Ni_3Al is completely absent in the nanocrystalline counterpart, which exhibits exchange-enhanced Pauli spin paramagnetism instead. Another intriguing feature is that this Pauli spin contribution to magnetic susceptibility is concomitant with the Curie-Weiss contribution (which arises from the antiferromagnetic spin correlations).

It is important to recognize that electrical and magneto-transport in a physical system are sensitive to changes taking place at the length scales of the electron mean free path. Degree of site-disorder and local compositional fluctuations are thus expected to get sensitively reflected in electrical and magneto-transport measurements. Thus, high-resolution resistivity and magnetoresistance measurements have been performed on (i) the off-stoichiometric Ni_3Al alloys, (ii) 20 at.% Fe substituted Ni_3Al alloys in different states of site disorder, and (iii) nanocrystalline Ni_3Al samples of distinctly different average crystallite size. The structural and magnetic properties are investigated and correlated with transport properties to understand the effect of site disorder, compositional disorder and the Fe-substitional disorder in Ni_3Al system.

1.6 Aim of thesis

Based on the exhaustive literature survey, the present investigation was undertaken with the following goals and with a view to seek answers to the pertinent questions.

a) To study the effect of site-disorder and compositional disorder on the magnetization, zero-field dc electrical resistivity and magnetoresistance of weak itinerant-electron ferromagnet Ni_3Al.
b) To determine the nature of magnetic excitations in different temperature regimes and to quantify the contribution of these excitations to magnetization and electrical resistivity in the presence and absence of the magnetic field.
c) To quantify the suppression of these collective excitations by magnetic field and to ascertain the role that the off-stoichiometry and site disorder in this suppression.
d) Do the site disorder and off-stoichiometry alter the values of critical exponents that characterize the critical behaviour near the ferromagnetic-to-paramagnetic phase transition in Ni_3Al?
e) What effect does the crystallite size have on resistivity, magnetoresistance, magnetization and ac susceptibility of nanocrystalline Ni_3Al?
f) To study the effect of thermoelastic martensitic transformation by electrical resistivity, magnetoresistance, magnetization and ac susceptibility in order to bring out the role of site-disorder on the thermoelastic martensitic phase transformation and shape memory effect in the $Ni_{55}Fe_{20}Al_{25}$ alloy.
g) To characterize and determine the crystal structures of the austenite and martensite phases by neutron diffraction.

h) To examine the microstructure of the martensite and austenite phases by transmission electron microscopy so as to refine and check the information obtained by neutron diffraction.

The thesis is divided into six chapters. The first chapter provides a brief introduction to itinerant magnetism and magnetic excitations in the itinerant-electron ferromagnets. It also furnishes a critical assessment of the relevant literature. Second chapter describes the experimental details. Third chapter is devoted to the contribution of spin waves and spin fluctuations in stoichiometric and off-stoichiometric polycrystalline alloys, $Ni_{75\pm x}Al_{25\mp x}$, as inferred from electrical transport, magnetoresistance. Fourth chapter details the effect of site- and compositional-disorder on magnetic and critical properties of polycrystalline $Ni_{75\pm x}Al_{25\mp x}$ alloys. Fifth chapter describes the effect of nanocrystallites size on magnetization, the 'zero-field' and 'in-field' electron-transport properties of Ni_3Al and introduces nanocrystallites size as a new control parameter to study novel properties like non-Fermi liquid behaviour and magnetically-mediated superconductivity near the quantum critical point. The role of substitutional site-disorder or anti-site occupancy in martensitic phase transition, magneto-transport and magnetic properties of Fe substituted Ni_3Al alloys forms the subject of the sixth chapter. The thesis ends with the future scope.

References

[1] F. J. Blatt, *Physics of electronic conduction in solids* (McGraw-Hill, New York, 1968).

[2] M. P. Marder, *Condensed Matter Physics* (John Wiley & Sons, New York, 2000).

[3] P. M. Ossi, *Disordered Materials* (Springer, Berlin, 2003).

[4] K. Moorjani and J.M.D. Coey, *Magnetic Glasses* (Elsevier, Amsterdam, 1984).

[5] S. N. Kaul, in *Lecture Notes*, Workshop on Glassy Materials, held at IUC-DAEF, Indore, India (1994).

[6] P. Weiss, J. Phys. Radium **6**, 661 (1907).

[7] P. Langevin, J. Phys. (Paris) **4**, 678 (1905), *Anu. Cim. Phys.* **5**, 70 (1905).

[8] J. H. van Leeuwen, J. de. Physique **2**, 361 (1921).

[9] W. Heisenberg, Z. Phys. **49**, 619 (1928).

[10] H. Capellmann and I. A. Campbell ed., *Metallic magnetism* (Springer-Verlag, 1987).

[11] T. Moriya, *Spin Fluctuations in Itinerant Electron Magnetism* (Springer-Verlag, Berlin, 1985).

[12] E. C. Stoner, Phil. Mag. **15**, 1080 (1933), Proc. R. Soc. A **165**, 372 (1938).

[13] E. P. Wohlfarth, Physica **91B**, 305 (1977).

[14] J. A. Blanco and J. Pisonero, Eur. J. Phys. **20**, 289 (1999).

[15] S. Blundell, *Magnetism in Condensed Matter*, (Oxford University Press, 2001).

[16] W. Pauli, Z. Physik **41**, 81(1927).

[17] S. N. Kaul, *Handbook of Magnetism and Advanced Magnetic Materials*, (Vol 1 edited by H. Kronmüller and S. Parkin, (John Wiely & Sons, New York, 2007), Vol 1.

[18] J. C. Slater, Phys. Rev. **49**, 537, 931 (1936), Phys. Rev. **52**, 198 (1937).

[19] C. Herring and C. Kittel, Phys. Rev. **81**, 869 (1951). C. Herring, Phys. Rev. **85**, 1003 (1952): ibid **87**, 60 (1952); Proc. Roy. Soc. London **A371**, 67 (1980)

[20] D. M. Edwards, E. P. Wohlfarth, Proc. Roy. Soc. **A 303**, 127 (1968).

[21] S. Doniach, S. Engelsberg, Phys. Rev. Lett. **17**, 750 (1966).

[22] T. Moriya, A. Kawabata, J. Phys. Soc. Jpn. **34**, 639 (1973); **35**, 69 (1973); Proc. ICM -73, Moscow IV p.5 (1973).

[23] Y. Ishikawa, J. Appl. Phys. **49**, 2125 (1978).

[24] T. Izuyama and R. Kubo, J. Appl. Phys. **35**, 1074 (1964).

[25] F. Kieffer, *Encyclopedia of Physics*, (Spinger-Verlag,) Vol XVIII/2 pp. 1-268 (1966).

[26] S. N. Kaul, J. Phys.: Condens. Matter, **11**, 7597 (1999).

[27] S. N. Kaul, J. Phys.: Condens. Matter, **17**, 5595 (2005).

[28] P. Mohn, *Magnetism in Solid State: An Introduction*,(Spriger-Verlag, Berlin, 2003).

[29] G. G. Lonzarich, J. Magn. and Magn. Mater. **45**, 43 (1984); G.G. Lonzarich and L. Taillefer, J. Phys. C **18**, 4339 (1985).

[30] E. P. Wohlfarth, Rev. Mod. Phys. **25**, 211 (1953).

[31] P. F. de Chatel and F. R. de Boer, Physica **48**, 331 (1970).

[32] E. P. Wohlfarth and P. F. de Chatel , Physica **48**, 477 (1970).

[33] G. G. Lonzarich, J. Magn. and Magn. Mater. **45**, 43 (1986)

[34] Y. Takahashi, J. Phys.: Condens. Matter **4**, 3611 (1992) and references cited therein.

[35] Y. Takahashi, J. Phys. Soc. Jpn **55**, 3353 (1986), J. Phys.: Condens. Matter **13**, 6323 (2001).

[36] A. Z. Solontsov and D. Wagner, Phys. Rev. B **60**, 12410 (1995).

[37] Anita Semwal and S. N. Kaul, Phys. Rev. B **60**, 12799 (1999).

[38] H.E. Stanley, *Introduction to Phase Transitions and Critical Phenomena* (Clarendon Press, Oxford, 1971).

[39] S. N. Kaul, J. Magn. Magn. Mater. **53**, 5 (1985).

[40] E. K. Riedel and F.J. Wegner, Phys. Rev. B **9**, 294 (1974).

[41] F. R. de Boer, C.J. Schinkel, J. Biesterbos and S. Proost, J. Appl. Phys. **40**, 1049 (1969).

[42] T. F. M. Kortekaas and J. J. M. Franse, J. Phys. F: Met. Phys. **6**, 1161 (1976).

[43] J. J. M. Franse, Physica **86-88B**, 283 (1977).

[44] N. Buis, J. J. M. Franse and P.E. Broumer, Physica **106B**, 1 (1981).

[45] H. Sasakura, K. Suzuki and Y. Masuda, J. Phys. Soc. Jpn. **53**, 352 (1984); J. Phys. Soc. Jpn. **53**, 754 (1984).

[46] S. Takahashi, A. Y. Takahashi and A. Chiba, J. Phys.: Condens. Matter. **6**, 6011 (1994).

[47] M. F. Singletone, J. L. Muray and P. Nash: in Binary Alloys phase diagrams, T.B. Massalski, ed., (ASM INTERNATIONAL, Ohio, 1986), pp.140-43.

[48] P. D. Hamourger, R. J. Olwert and C. W. Chu, Phys. Rev. B **11**, 3501 (1975).

[49] T. Moriya, J. Phys. Soc. Jpn. **40**, 933 (1976); J. Magn. Magn. Mater. **14**, 1 (1979); in *Electron Correlations and Magnetism in Narrow Band Systems*, ed. T. Moriya (Springer-Verlag, Berlin, 1981); J. Magn. Magn. Mater. **31-34**, 10 (1983).

[50] Y. Masuda, J. Magn. Magn. Mater. **31-34**, 259 (1983).

[51] T. V. Ramkrishnan, Solid State Commun. **14**, 449 (1974); Phys. Rev. B **10**, 4014 (1974).

[52] S. G. Mishra and T. V. Ramkrishnan, J. Phys. C.: Solid State Phys. **10**, L667 (1977).

[53] S. G. Mishra and T. V. Ramkrishnan, *Inst. Phys. Conf. Series* **39**, 528 (1978).

[54] N. R. Bernhoeft, I. Cole, G. G. Lonzarich and G. Scquires, J. Appl. Phys., **53**, 8204 (1982).

[55] N. R. Bernhoeft, G. G. Lonzarich, P. W. Mitchell and D. McK Paul, Phys. Rev. **28**, 422 (1983).

[56] S. K. Dhar and K. A. Gschneidner, Jr., Phys. Rev. B **39**, 7453 (1989).

[57] S. K. Dhar and K. A. Gschneidner, Jr., L. L. Miller and D. C. Johnston, Phys. Rev. B **40**, 11488 (1989).

[58] C. G. Robbins and H. Clauss, AIP Conf. Proc. **5**, 527 (1971).

[59] A. Parthasarathi and P. A. Beck, AIP Conf. Proc. **29**, 282 (1975).

[60] W. De Dood and F. De Chatel, J. Phys. F: Met. Phys. **3**, 1039 (1973).

[61] C. Stassis, F. X. Kayser, C. –K. Loong, and D. Arch, Phys. Rev. B **24**, 3048 (1981).

[62] G. P. Felcher, J. S. Kouvel, and A. E. Miller, Phys. Rev. B. 16, 2124. AIP Conf. Proc. **5**, 527 (1971).

[63] D. Hackenbracht and J. Kübler, J. Phys. F: Met. Phys. **10**, 427 (1980).

[64] J. J. M. Buiting, J. Kübler, and F. M. Mueller, J. Phys. F: Met. Phys. **13**, L179 (1983).

[65] B. I. Min, A. J. Freeman, and H. J. F. Jansen, Phys. Rev. B. 37, 6757 (1998).

[66] A. Aguayo, I. I. Mazin, and D. J. Singh, Phys. Rev. Lett. 92, 147201 (2004).

[67] J. H. J. Fluitmann, R. Boom, P. F. De Chatel, C. J. Schinkel, J. L. L. Tilanus and B. R. De Vries, J. Phys. F: Metal Phys. **3**, 109 (1973).

[68] D. L. Mills and P. Lederer, J. Phys. Chem. Solids **27**, 1805 (1966).

[69] A. I. Schindler, and M. J. Rice, Phys. Rev. **164**, 759 (1967).

[70] J. Mathon, Proc. Roy. Soc. A **306**, 355 (1968).

[71] K. Ueda and T. Moriya, J. Phys. Soc. Jpn. **39**, 605 (1975).

[72] K. Ueda, Solid state Commun. **19**, 965 (1976).

[73] M. Yoshizawa, H. Seki, K. Ikeda, K. Okuno, M. Saito and K. Shigematsu, J. Phys. Soc. Jpn. **61**, 3313 (1992).

[74] P. Niklowitz, F. Beckers and G.G. Lonzarich, G. Kneble, B. Salce, J. Thomsson, N. Bernhoeft, D. Braithwaite, and J. Flouquet, Phys. Rev. B **72**, 024424 (2005).

[75] K. H. Chang, R. H. van der Linde and E. G. Sieverts, Physica **69**, 467 (1973).

[76] N. F. Mott, Proc. Roy. Soc. **47**, 571 (1935); Adv. Phys. **13**, 139 (1964).

[77] A. Semwal and S. N. Kaul, J. Phys. : Condens. Matter **16**, 8675 (2004).

[78] S. N. Kaul and A. Semwal, J. Phys. : Condens. Matter **16**, 8695 (2004).

[79] S. N. Kaul and S. Srinath, Phys. Rev. B **63**, 0944101 (2001).

[80] B. Annie D'Santhoshini and S. N. Kaul, J. Phys. : Condens. Matter **15**, 4903 (2003).

[81] S. N. Kaul and B. Annie D'Santhoshini, J. Magn. Magn. Mater. **272-276**, 489 (2004).

[82] H. Gleiter, *Prog. Mater. Sci*. **33**, 223-315 (1989).

[83] S. N. Kaul, Anita Semwal, and H. –E. Schaefer, Phys. Rev. B. **62**, 13892 (2000).

Chapter 2

Experimental techniques

2.1 Introduction

According to Schulze [1], intermetallic compounds are defined as solid phases containing two or more metallic elements, with optionally one or more non metallic elements, in a fixed proportion to produce a different crystal structure from the individual metals. Intermetallic compounds tend to form when there is a strong solid solubility between the two component atoms, e.g., Cu-Zn, Ni-Al alloys. Alloys based on the Ni-Al binary system are one of the most important and well-exploited classes of intermetallic materials for practical applications. On the Ni-rich side of the Ni-Al phase diagram, several ordered phases are known to form [2]. Due to the increase in ductility Ni-Al system provides, the well-known γ (disordered fcc)/ γ' (ordered $L1_2$-type) phase combination which, in turn, leads to the development of Ni-based superalloys

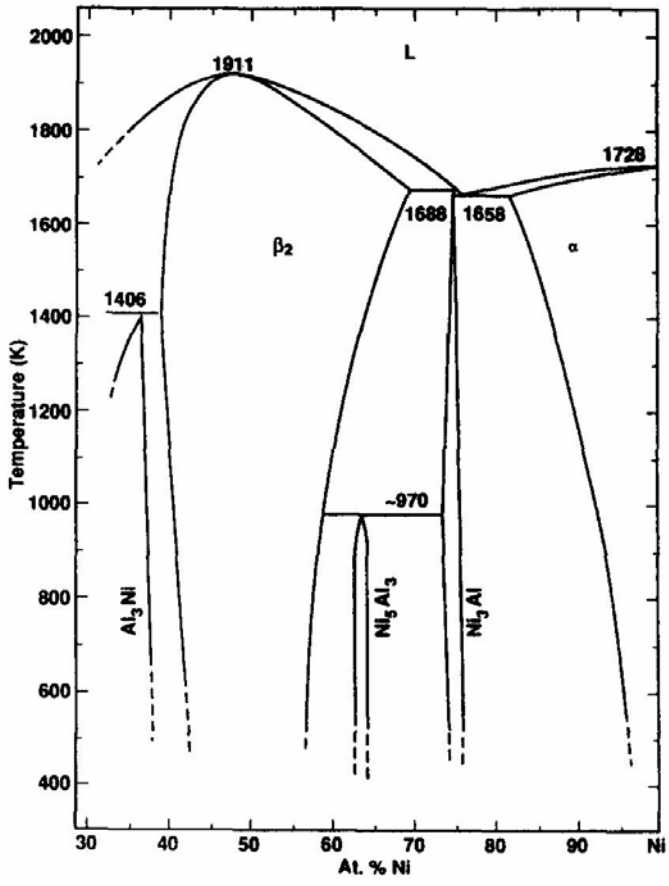

Figure 2.1: Portion of Ni-Al phase diagram [2].

[3]. Another example of the unique properties of Ni-Al alloys is the thermoelastic martensitic transition β (B2) → β′ ($L1_0$), which forms the basis for Ni-based shape memory alloy [4]. Due to their hard magnetic properties, Fe-Ni-Al alloys have been used as basis for the Alnico permanent magnets [5]. Finally, because of its high melting point (~1680 °C) and excellent oxidation resistance, the B2-NiAl ordered phase is of great interest in the development of high-temperature materials, though it is brittle at room temperature [6].

In the alloys made up of Ni and Al, as the concentration of Al is increased from 0 at.%, number of intermetallic phases are formed; for example, first Ni_3Al and then Ni_5Al_3, NiAl (B2 phase) and $NiAl_3$ etc. As observed in the phase diagram of Ni-Al alloys, Fig.2.1, Ni_3Al has a homogeneous phase-field of about 3 at.% around the stoichiometric composition. Ni_3Al has a Cu_3Au type face-centered-cubic (fcc) structure (γ′ phase), i.e., an $L1_2$ ordered crystal structure below the peritectic temperature of 1395 ^{0}C [7]. In a completely ordered Ni_3Al compound, Ni and Al atoms respectively occupy the face-

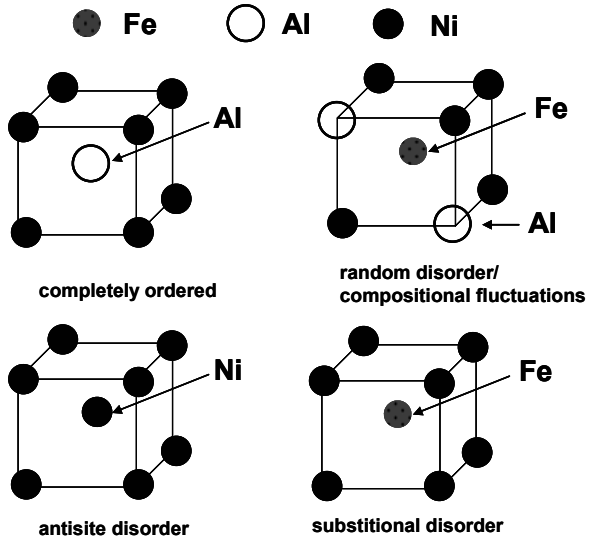

Figure 2.2: Schematic of different type of disorders present in B2 Ni-Al crystalline phase.

centered and corner sites of the cubic unit cell. The face-centered (corner) sites thus constitute the Ni (Al) sub-lattice. A complete atomic order in $Ni_{75}Al_{25}$ alloy exists only when probability of finding Ni (Al) atoms on Ni (Al) sub-lattice sites is 100% and 0% on Al (Ni) sublattice sites. A completely disordered state corresponds to the case if the probability of finding Ni and Al atoms on any type of lattice sites is the same [8]. As suggested by Guard and Westbrook [7], *off-stoichiometry* in both Ni_3Al as well as NiAl result in intrinsic site disorder/defects; i.e., Ni atoms substitute Al sub-lattice sites in Ni-rich alloys while Ni vacancies are formed in Al-rich alloys. Apart from this rapid solidification or melt spinning gives rise to site disorder, as shown in figure 2.2. First principle theoretical calculations predict, and experiments reveal, similar results for Ni-Al alloys as well [9]. In the rest of this chapter, a brief introduction to sample preparation, characterization techniques and various experimental set ups used for physical measurements is given.

2.2 Sample preparation and compositional characterization

2.2.1 'As-prepared' Ni_xAl_{100-x} alloys

99.998 % pure Ni and Al elements were taken in appropriate proportions by weight to form Ni_xAl_{100-x} with nominal composition given in table 2.1. An alloy of given composition was formed by melting the elements in a recrystallized alumina crucible under an inert atmosphere provided by high-purity (99.999) argon gas. After holding the melt for a couple of minutes in the crucible, it was poured into a cylindrical hole in a massive copper mould. The entire operation was carried out under high-purity argon gas pressure of >1 atm. Polycrystalline rods (100 mm in length and 10 mm in diameter) with the nominal composition $Ni_{74}Al_{26}$, $Ni_{74.5}Al_{25.5}$, $Ni_{75}Al_{25}$ and $Ni_{76}Al_{24}$ were formed in this way. Samples in the shape of a disc of 10 mm diameter and 5 mm

thickness, a rectangular strip of dimensions 10 x 2 x 0.5 mm^3 and a sphere of 2.5 mm diameter were spark-cut from these rods for x-ray diffraction, electrical and galvanomagnetic transport, and magnetic measurements, respectively. The actual chemical composition of the samples, as determined by the x-ray fluorescence technique and inductively coupled-plasma optical emission spectroscopy, is given in table 2.1. The compositional analysis also revealed that the total concentration of magnetic 3d transition metal impurities such as Mn, Cr, Fe and Co lies below 0.002 at. %. The 'as-prepared' alloy samples are henceforth referred to as *ap-*$Ni_{74.3}$, *ap-*$Ni_{74.8,}$ *ap-*$Ni_{75.1}$ and *ap-*$Ni_{76.1}$.

2.2.2 Annealed $Ni_{75}Al_{25}$ alloy

One set of spheres and strips of *ap-*$Ni_{75.1}$ was subjected to annealing treatment at 520 °C for 16 days in a quartz tube evacuated to a pressure of 10^{-7} torr, in order to reduce the degree of atomic site disorder in the stoichiometric sample. These samples are labeled as *an-*$Ni_{75.1}$.

2.2.3 Nanocrystalline $Ni_{75}Al_{25}$

Starting with 99.98% pure Ni and 99.998% pure Al, intermetallic compound Ni_3Al was prepared by induction-melting under an inert atmosphere of high-purity (99.999) argon gas. Nanocrystalline Ni_3Al was prepared in the powder form by the inert gas (helium) condensation technique wherein a portion of the polycrystalline sample was evaporated in the tungsten boat by an appropriate heating arrangement and condensed onto the stainless steel drum, which was maintained at liquid nitrogen temperature. An aluminum scrubber was used to scrub this condensed sample, which was collected in the dye placed just below the stainless steel vessel. The powder of $Ni_{75}Al_{25}$ thus obtained, was compressed *in-situ* under pressures > 1GPa to form discs of diameter 8 mm and thickness of 0.2 mm. Strips of the dimensions 7 x 2 x 0.2

mm^3 were spark-cut from the as-prepared discs and used for transport measurements. The discs of diameter 3 mm and thickness 0.2 mm were cut for magnetic studies.

2.2.4 Ni-Fe-Al alloy

Polycrystalline samples with nominal composition $Ni_{55}Fe_{20}Al_{25}$ were prepared by the method described earlier in the case of ap-Ni_xAl_{100-x}, in the form of rods of dimensions 100 mm in length and 10 mm in diameter. Rectangular strips of dimensions 40 x 2.5 x 0.5 mm^3 and discs of 10 mm diameter and 5 mm thickness were spark-cut from the rods. These strips were annealed at 520 °C for 16 days in a quartz tube evacuated to a pressure of 10^{-7} Torr and subsequently water quenched. The annealed samples are henceforth referred to as 'a-Fe_{20}'.

A portion of the polycrystalline rods was melt-quenched to form ribbons. In this preparation process, the molten alloy, contained in a quartz tube of 5 mm inner diameter, is ejected (at a temperature of 1500 °C and helium pressure of 200 mbar) out in the form of a jet through a rectangular slit of dimensions 3.2 x 0.49 mm^2 on one end of the quartz tube onto a rotating copper wheel of diameter 200 mm. The tangential velocity of the wheel, maintained at a temperature of 22 °C, was 30 m/s. Long thin ribbons of width 2 mm and thickness ~ 30 μm are thus formed when the melt comes in contact with the copper wheel. The samples, so produced, are labeled as 'q-Fe_{20}'.

2.2.4 Compositional analysis

The chemical composition of the samples was determined by x-ray fluorescence and inductively coupled plasma-optical emission spectroscopy.

Inductively Coupled Plasma - Optical Emission Spectroscopy (ICP-OES)

Inductively-coupled plasma optical emission spectroscopy (ICP-OES or ICP-AES) is a powerful technique for elemental analysis. The sample to be analyzed is dissolved in water before being fed into the plasma. The plasma temperature is sufficiently high to break chemical bonds, liberate elements present and transform them into a gaseous atomic state. A number of atoms pass into excited state and emit radiation. The light emitted by the atoms in the plasma is analyzed for the characteristic wavelengths of the elements present in the sample by optical spectrometers. The intensity of the radiation is proportional to the concentration of that element within the solution and so can be used for quantitative purposes. Calibration of the spectrometer based on the standards, enables a quantitative analysis of the samples. With this technique, even the trace impurities, if present, in the samples can be detected and their levels quantitatively determined.

Table 2.1: Elemental compositions for the samples and lattice parameters at room temperature.

Sample Label (NominalComposition)	Ni (at.%)	Al (at.%)	Fe (at.%)	Lattice parameter (Å)
ap-$Ni_{74.3}$ ($Ni_{74}Al_{26}$)	74.06(5), 74.26(9)	25.94(19), 25.74(11)	-	3.567(10)
ap-$Ni_{74.8}$ ($Ni_{75}Al_{25}$)	74.82(8)	25.18(12)	-	3.564(18)
ap-$Ni_{75.1}$ ($Ni_{75}Al_{25}$)	75.08(8)	24.92(10)	-	3.564(15)
an-$Ni_{75.1}$ ($Ni_{75}Al_{25}$)	75.08(8)	24.92(12)	-	3.564(15)
ap-$Ni_{76.1}$ ($Ni_{76}Al_{24}$)	76.13(5)	23.87(10)	-	3.560(5)
Nanocrystalline Ni_3Al (50 nm)	75.30(20)	24.70(15)	-	3.573(1)
Nanocrystalline Ni_3Al (3 nm)	75.24(20)	24.76(15)	-	a = 3.772(3) c = 3.236(4)
a-Fe_{20} (Annealed $Ni_{55}Fe_{20}Al_{20}$)	55.01(7)	24.94(9)	20.05(6)	$a(L1_2)$ = 3.586(2) a(B2) = 2.869(1)
q-Fe_{20} (Quenched $Ni_{55}Fe_{20}Al_{20}$)	55.01(7)	24.94(9)	20.05(6)	a(B2) = 2.867(2)

X-Ray Fluorescence (XRF)

X-ray fluorescence phenomenon is the emission of x-rays from excited atoms produced by the impact of high-energy electrons, other particles, or a primary beam of other x-rays. The wavelengths of the fluorescent x-rays can be measured by an x-ray spectrometer as a means of chemical analysis. X-ray fluorescence is used in such techniques as electron-probe microanalysis. The counts of fluorescent x-rays emitted by different elements present in the sample are calibrated against those emitted by the alloy standards with composition close to that of the samples under examination. This method was also used to ascertain the chemical composition of the samples. The outcome of a detailed compositional analysis of the samples using the ICP-OES method is given in table 2.1. The corresponding results obtained by the XRF technique tally with those of the ICP-OES method.

2.3 X-ray and Neutron diffraction

2.3.1 X-ray diffraction

The x-ray diffraction patterns were recorded on the INEL CPS 120 x-ray diffractometer. The x-rays of wavelength 1.7889 *Å* were generated using cobalt target at the voltage and current settings of 35 kV and 25 mA. In this diffractometer, it is possible to resolve the $K_{\alpha 1}$ and $K_{\alpha 2}$ lines and separate $K_{\alpha 2}$ visually using fluorescent screen and by tilting a flat monochromater. One of the advantages of this diffractometer is that the diffraction intensities can be simultaneously measured over the range of 2θ from 15 - 120 degree using Curved Position Sensitive (CPS) detector. Thus, a full x-ray pattern takes an order of magnitude lesser time than the conventional step-scan method and even the lowest intensity peaks can be detected with ease. The curved position

sensitive detector is filled with a mixture of argon gas and methane (C_2H_6), since the target is cobalt and this gas-mixture has reduced background noise than krypton-ethane mixture. The CPS operates in Steamer mode, which is known for its high stability, signal-to-noise ratio and gain. The detector assembly consists of one firm knife edge blade, anode and one cathode. The detector is filled with a gas mixture to increase quantum efficiency. The detector is placed under an intense electric field. When a photon collides with a gas atom, the gas atom gets ionized. This causes release of electrons, which are accelerated by electric field and ionize other atoms. The electric charges created by the aforementioned process are then collected by the cathode. The different sections of the cathode are connected by a delay line, which permits a determination of the position of the photons that have penetrated the interior of the detector. The alignment of the CPS and goniometer assembly is a crucial step for this instrument [10]. The instrument is calibrated with a standard silicon sample.

X-ray diffraction patterns of the disc-shaped polycrystalline samples of 'as-prepared' Ni_xAl_{100-x} were recorded at room temperature over the scattering angle, 2θ, range of $10^o \le 2\theta \le 120^o$, using $Co\ K_\alpha$ radiation, on Inel x-ray diffractometer with curved position-sensitive detector. Since the scattered x-ray intensity is measured simultaneously over the entire 2θ range, even the weakest Bragg peaks, which would have normally escaped detection in conventional x-ray diffractometers, can be detected with ease. The Bragg peaks of all the samples could be indexed using face centered cubic $L1_2$ structure. The lattice parameter values of these samples are given in table 2.1.

2.3.2 Neutron diffraction

Neutron beam coming out of a nuclear reactor (which is in thermal equilibrium with the moderator kept at a temperature ranging from 300 K to 400 K) have their kinetic energies distributed according to the Maxwell distribution law. The largest fraction of these so-called "thermal neutrons" with kinetic energy equal to k_BT, can be used for analyzing the unknown crystal structure when these thermal neutrons are diffracted from a single crystal to obtain a beam of mono-energetic (monochromatic) neutrons. The wavelength of such neutrons is given by

$$\lambda = \frac{h}{\sqrt{2mkT}} \tag{2.1}$$

For T = 300 K to 400 K, λ = 1 to 2 $\mathring{A}$, i.e., a wavelength of the same order as the interatomic spacings in solids. In neutron diffraction experiments, the intensity of the diffracted neutron beam from the sample is measured with a proportional counter filled with BF_3 gas. The neutron diffraction has following advantages over electron or x- ray diffraction technique [11].

A neutron beam is highly penetrating, e.g., a 1cm thick iron plate is opaque to electrons, virtually opaque to 1.5 $\mathring{A}$ x-rays, but transmits 35 percent of 1.5 $\mathring{A}$ neutrons. Thus, neutron diffraction (ND) gives structural details of not only the surface but also of the bulk. The intensity of neutron scattering varies quite irregularly with the atomic number, Z, of the scattering atom. Thus, neutrons can also distinguish in many cases elements differing by only one atomic number. Moreover, some light elements like hydrogen and carbon scatter neutrons more intensely than x-rays. Neutrons have a small magnetic moment. If the scattering atom also has a net magnetic moment, the two interact and modify total scattering. In the case of magnetic materials

(antiferromagnetic, ferromagnetic and ferromagnetic) neutron diffraction can disclose both the magnitude and direction of the magnetic moments. Only neutron diffraction can furnish such information and hence this technique has a major impact on the studies of magnetic structures.

In the present investigations, the neutron diffraction measurements are used to identify the crystal structure of the phases and to study the phase transformations in quenched and annealed samples of $Ni_{55}Fe_{20}Al_{25}$ alloy. The neutron diffraction measurements were performed at Institut Laue-Langevin, Grenoble, on D20 diffractometer. It is very high intensity 2-axis diffractometer equipped with a large microstrip curved position sensitive detector (CPSD). The complete diffraction pattern at 1536 positions, covering a scattering range up to 153.6°, can be obtained in a matter of seconds, and followed as a function of temperature, pressure or other parameter. A high resolution is obtained with a neutron flux of up to $10^7 – 10^8$ n s^{-1} cm^{-2}. The calibration of the instrument involves calibration of detector, wavelength and angle. Detailed experimental set up and diagrams are given in [12].

D20 detector consists in 1600 independent cells whose signal is transmitted to the data acquisition system through the same number of amplifiers which are adjusted individually. As the detection efficiency may vary slightly from cell to cell, one must normally correct patterns by multiplying the raw data by a correction factor α called efficiency coefficient:

$$I_i(\text{corr.}) = \alpha_i * I_i(\text{raw}) \; [i = 0 \text{ to } 1599] \qquad (2.2)$$

Efficiency coefficients are calculated from the measured diffraction patterns of a vanadium (constant wavelength), or plexiglass rod (some inelastic scattering

contribution due to hydrogen, so no constant wavelength). Before starting the experiment one normally uses the calibration files for angle calibration and efficiency correction those are stored on d20sgi.ill.fr in `~lambda/CALIBRATION`. Relative efficiencies (so the efficiency correction coefficients) of some detection cells may change if these are not exactly geometrically equivalent. As the total detection efficiency changes with wavelength, the position of neutron capture in the detection gap changes as well. This would not change relative efficiencies if all detection cells are geometrically totally equivalent.

The wavelength calibration includes the offset or zero-shift that depends on the adjustment of 2θ encoders of the detector. It is normally refined from a diffraction pattern of a standard sample (e.g. NBS-Al_2O_3 or Silicon). The angle calibration is required as the PSD is curved and the 50 microstrip plates of each 32 detector cells are arranged polygonally. The electrical field within this bunch of cell is not constant in 2θ over the whole detection gap of 5 cm. Close to the Aluminum entrance window detector cells of the mid of microstrip plates covers a slightly larger angular range because they are closer to that window, whilst detector cells near the plate junctions are farther away and covering less angular range. Closer to the microstrip plates this effect becomes less important, it might even be inverted at last due to a parallax effect of projection. So not only the width of each cell is slightly different and so their position deviated slightly from the ideal one, supposing each cell to cover 0.1 deg in 2 Theta, but also this deviation is wavelength-dependent: If detection appears closer to the entrance window (high efficiency - high wavelength) the deviation is more important than for detection in the mid of the detection gap (low efficiency - low wavelength).

In the present case, the measurements were performed on ductile ribbons q-Fe_{20} and a-Fe_{20} samples. The strips (ribbons) of length 50 (40) mm, width 2 (2.5) mm and thickness 0.5 mm (~ 30 μm) were mounted in a vanadium can in a bath-type helium cryostat. Neutron diffractions pattern were recorded on a-Fe_{20} (q-Fe_{20}) while cooling (heating) at various (a few) fixed temperatures in the range of 10 K ≤ T ≤ 300 K. The thermal neutrons of wavelength 1.297 Å were used for diffraction and diffraction intensities were recorded in the step size of 0.1° over the scattering angle range of 10°- 150°. These data were analyzed using FULLPROOF Rietveld refinement program. The data and results of these refinements are discussed in detail in chapter 5.

2.4 Microscopic techniques

2.4.1 Optical microscopy

Microstructures of the polycrystalline 'as-prepared' Ni_xAl_{100-x} samples were examined by 'Carl Zeiss' model Axiovert 40 MAT Inverted Metallurgical optical microscope. This microscope has the options of bright-field and dark-field imaging with polarizer and the magnification from 100 to 1000. As noticed in figure 2.3, the samples *ap-$N_{74.3}$* and *ap-$Ni_{74.8}$* show two-phase like contrast in microstructure and black spots are the voids while *ap-$N_{75.1}$* and *ap-$Ni_{76.1}$* have single-phase microstructure.

The compositional analysis of the major (lighter regions) and minor (darker regions) phases was performed using EDAX. Ni concentration in the darker regions (minor phase) is found to be 0.2 at.% less than in the major

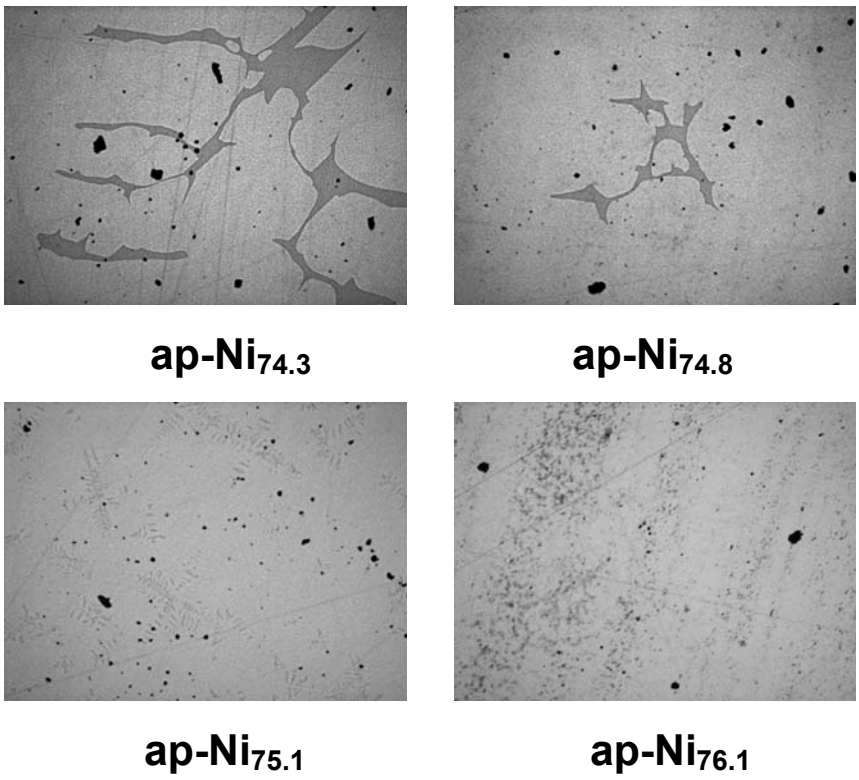

*Figure 2.3 Optical polarizing microscope pictures of the 'as-prepared' samples taken at a magnification of 100*x*, revealing the presence of dark regions (minor crystalline phase) in ap-$Ni_{74.3}$, ap-$Ni_{74.8}$, ap-$Ni_{75.1}$ and ap-$Ni_{76.1}$.*

phase in *ap-*$N_{74.3}$ while the difference in the composition between the major and minor phases in the sample *ap-*$N_{74.8}$ was below the resolution limit (≈ 0.1at. %) of the EDAX technique. Thus, the samples *ap-*$N_{74.3}$ and *ap-*$Ni_{74.8}$ have large compositional fluctuations as compared to *ap-*$N_{75.1}$ and *ap-*$Ni_{76.1}$. With increasing Ni concentration, this compositional fluctuation (iso-structural minor phase) reduces, as inferred from Fig. 2.2. Thus all the samples are actually single phase but local inhomogenities or compositional fluctuations do exist in *ap-*$N_{74.3}$ and *ap-*$Ni_{75.8}$ samples.

2.4.2 Scanning electron microscopy (SEM)

In SEM, a focused beam of electrons is accelerated to moderately high energy (<100 keV) and positioned onto a sample by electromagnetic fields under high vacuum. The electron beam gets elastically as well as inelastically scattered from atoms in the specimen when they impinge on the sample

surface. In inelastic scattering, energy is transferred to the sample from the beam while elastic scattering involves only a change in the trajectory of the electron beam without any loss of energy.

Backscattered electrons (BSE's) are the electrons from the incident beam that undergo elastic scattering from the sample, change trajectory, and escape the sample surface. These make up the majority of the electrons emitted from the sample surface (with an average energy of the BSE's of the order of a few keV). The intensity of the BSE signal is a function of average atomic number (Z) of the sample; higher the Z, higher is the intensity. Thus, it forms a useful signal for generating compositional images, in which higher Z phases appear brighter than lower Z phases. Secondary electrons, generated by inelastic scattering, are of low energy (typically < 50 eV), and are influenced by surface properties rather than by the atomic number. The secondary electrons are emitted by an outer-shell of a sample atom upon impact of the incident electron beam. The secondary-electron sampling volume is, therefore, smaller than that of the back-scattered electrons and hence provides a high-resolution image of the specimen surface. Secondary-electrons intensity is a function of the surface orientation with respect to the beam and the secondary-electron detector and thus produces an image of the surface morphology. Characteristic x-rays and Auger electrons are generated by inelastic scattering of the probe electrons in which an inner-shell electron is emitted from a sample atom (ionization). These signals can be used for the identification of elements within the sample volume and by comparing them with standards, a quantitative compositional analysis can be performed. The spatial resolution of conventional SEM is around 100 nm (using field-emission guns, this resolution improves to ~ 1

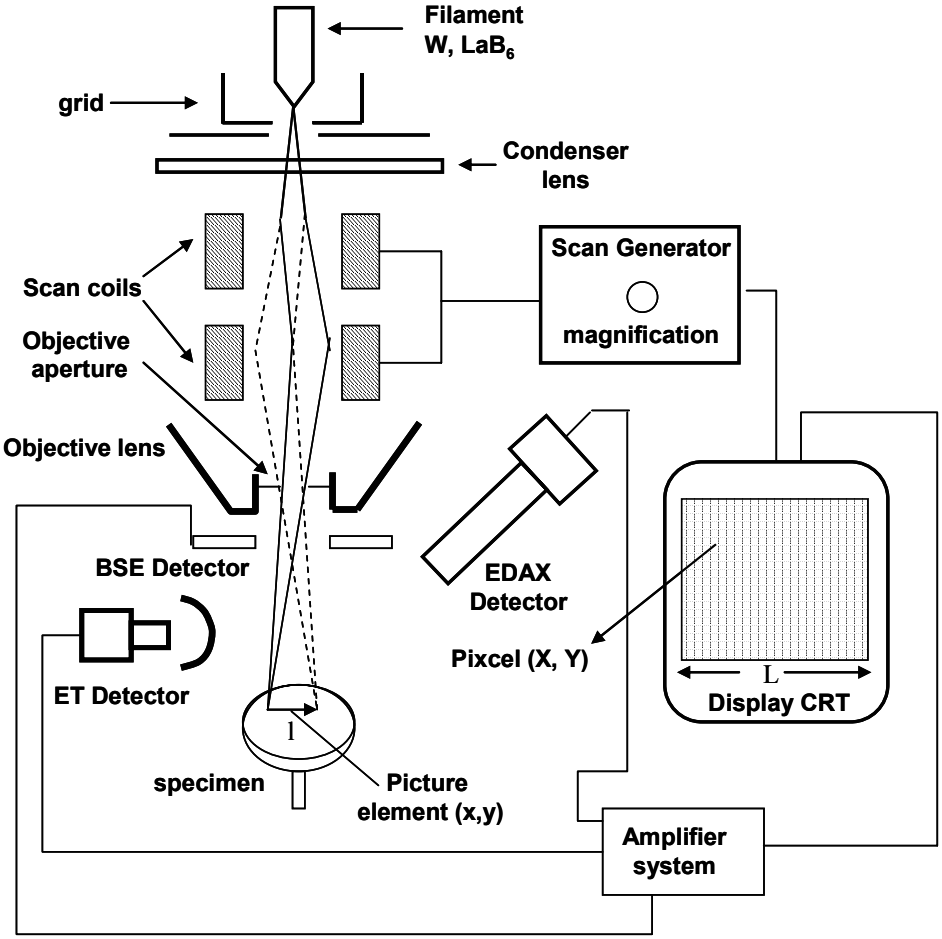

Figure 2.4: Schematic of image formation system of the SEM. The electron beam is shown at two positions in time, scanned in the X-direction to define the distance 'l' on the sample surface. Reproduction of this scan on the CRT with a width 'L', gives the magnification, M = L / l. The picture element is an area on the sample surface, its location is given by (x, y). Signal from this area (Secondary electrons, BSE or x-ray) is transferred to the CRT and converted to an intensity value for pixel (X, Y, I) [13].

nm). Resolution of SEM depends mainly on the electron beam size or sampling volume [13]. The image formation system along with block diagram of SEM is shown in figure 2.4.The morphology and microstructure of the melt-spun ribbons and annealed sample of the $Ni_{55}Fe_{20}Al_{25}$ alloy have been observed using LEO 440i scanning electron microscope (SEM) with an OXFORD ISIS300 ultracool energy dispersive x-ray silicon (EDS) crystal doped with lithium [Si(Li)] as detector. The annealed sample was mounted on a bakelite mold and polished with emery papers, and finally with cloth and diamond paste

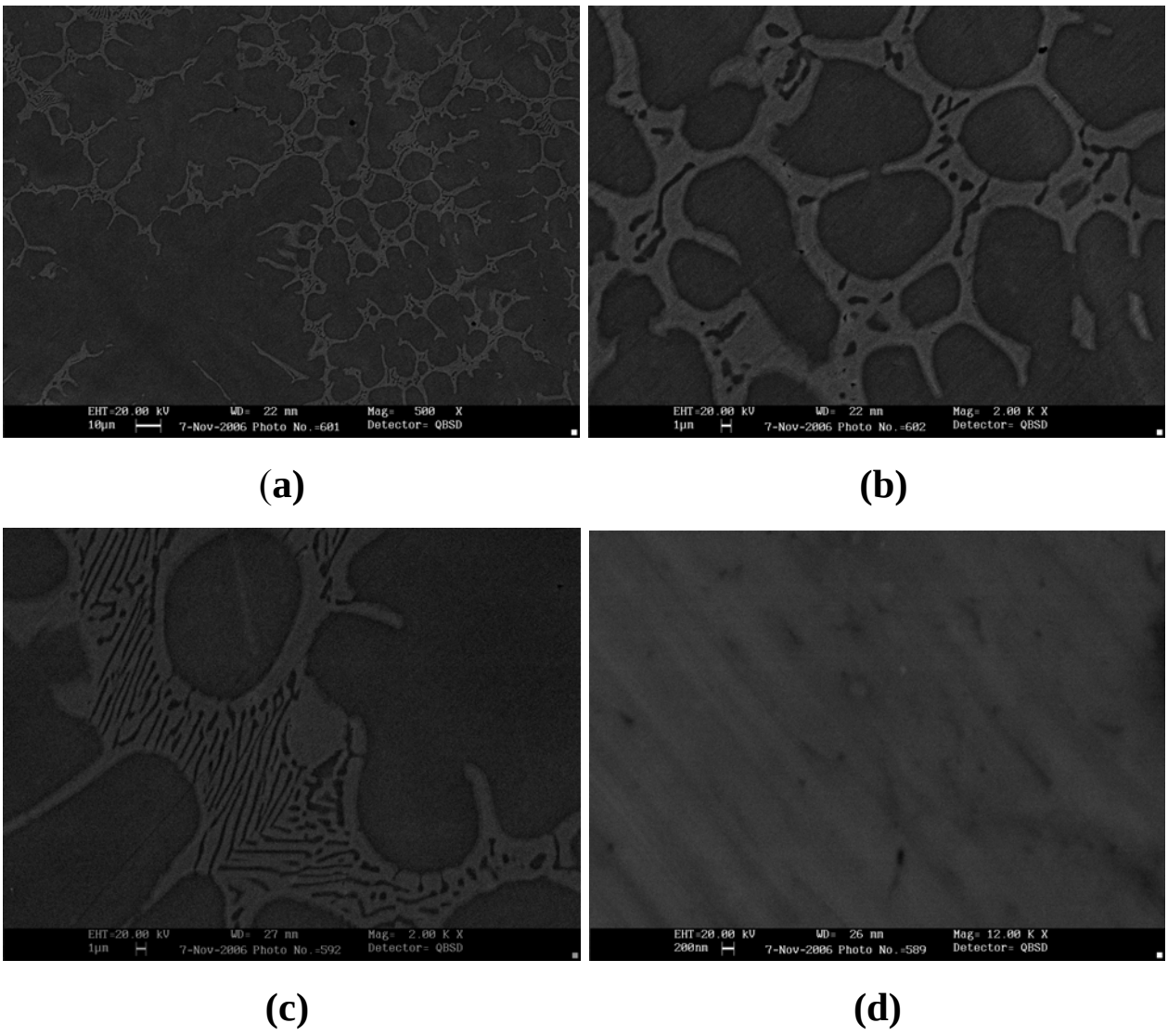

*Figure 2.5 Scanning electron microscope pictures of the $Ni_{55}Fe_{20}Al_{25}$ alloys taken in Back-Scattered-Electron mode at T = 300 K; (a) a-$F_{20,}$ 500*x; *(b) a-$F_{20,}$ 2000*x; *(c) a-$Fe_{20,}$ 2000*x *revealing two-phase microstructure in a-Fe_{20} and (d) q-$Fe_{20,}$ 12000*x; *shows a single phase microstructure.*

with particle size of 1µm to get mirror polish with even surface. The observations were carried out after ultrasonic-cleaning of the sample surface in the unetched condition. The melt-spun ribbons were directly mounted on a conducting Cu stub. Qualitative analysis was carried out on individual phases to know the chemical composition of the phase followed by a quantitative analysis for the estimation of the phase composition. Figure 2.5 (a), (b) and (c) show micrographs of different regions of the a-Fe_{20} sample at different magnifications, taken in BSE mode, at room temperature. These micrographs

indicate two-phase contrast with dark regions corresponding to the Al-rich phase and light regions to the Al-poor phase. Detailed EDAX analysis of different regions is presented in the table 2.2 below. A typical EDAX graph is shown in figure 2.6.

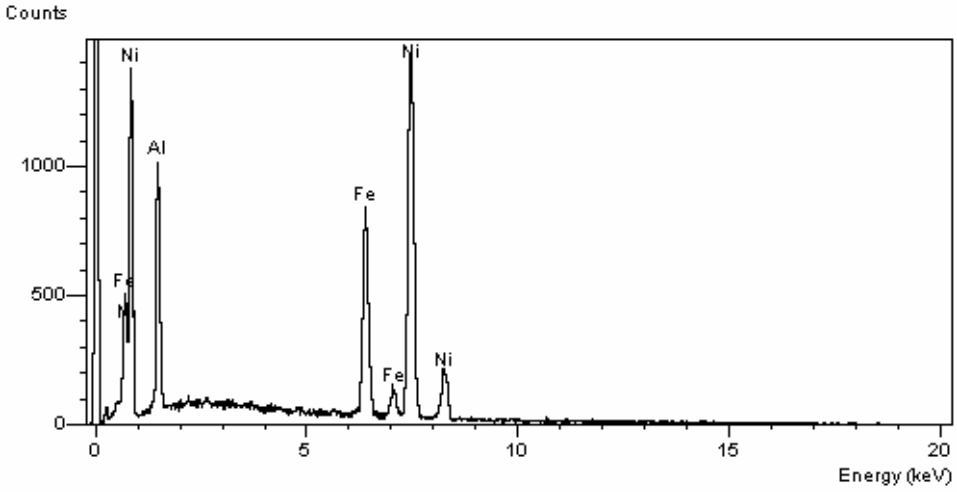

Figure 2.6: Typical EDAX spectrum shown for quenched $Ni_{55}Fe_{20}Al_{25}$ sample at room temperature.

Table 2.2: Elemental compositions for the annealed and quenched samples of $Ni_{55}Fe_{20}Al_{25}$ alloy.

Sample	Ni (at.%)	Al (at.%)	Fe (at.%)
a-Fe_{20} (Global)	55.0(1)	24.0(5)	21.0(4)
a-Fe_{20} (Dark phase)	55.3(6)	27.7(4)	17.0(1)
a-Fe_{20} (Bright phase)	55.3(2)	15.4(1)	29.3(3)
q-Fe_{20} (Global)	55.6(4)	23.8(2)	20.6(3)

The global composition of both the samples matches well with the nominal composition and also with the results of the ICP-OES analysis given in table 2.2. By contrast, fig.2.4 (d) represents the micrograph for the quenched sample at 12000x magnification; no second phase is observed in this case; the grains are equiaxed and elongated. The results of the EDAX analysis

in this case also match well with the nominal composition and those of the ICP-OES analysis. Thus, q-F_{20} is a single-phase material while a-Fe_{20} is at least a two-phase one. It will be shown later that using the Transmission electron microscopy (TEM) and neutron diffraction techniques that q-Fe_{20} crystallizes into B2 structure while a-Fe_{20} has crystalline phases with B2 and $L1_2$ crystal structures. Thus, long duration annealing at 520 °C results in phase-segregation because of thermal diffusion of atoms leading to Ni-poor B2 and Ni-rich $L1_2$ phases.

2.4.3 Atomic force microscopy

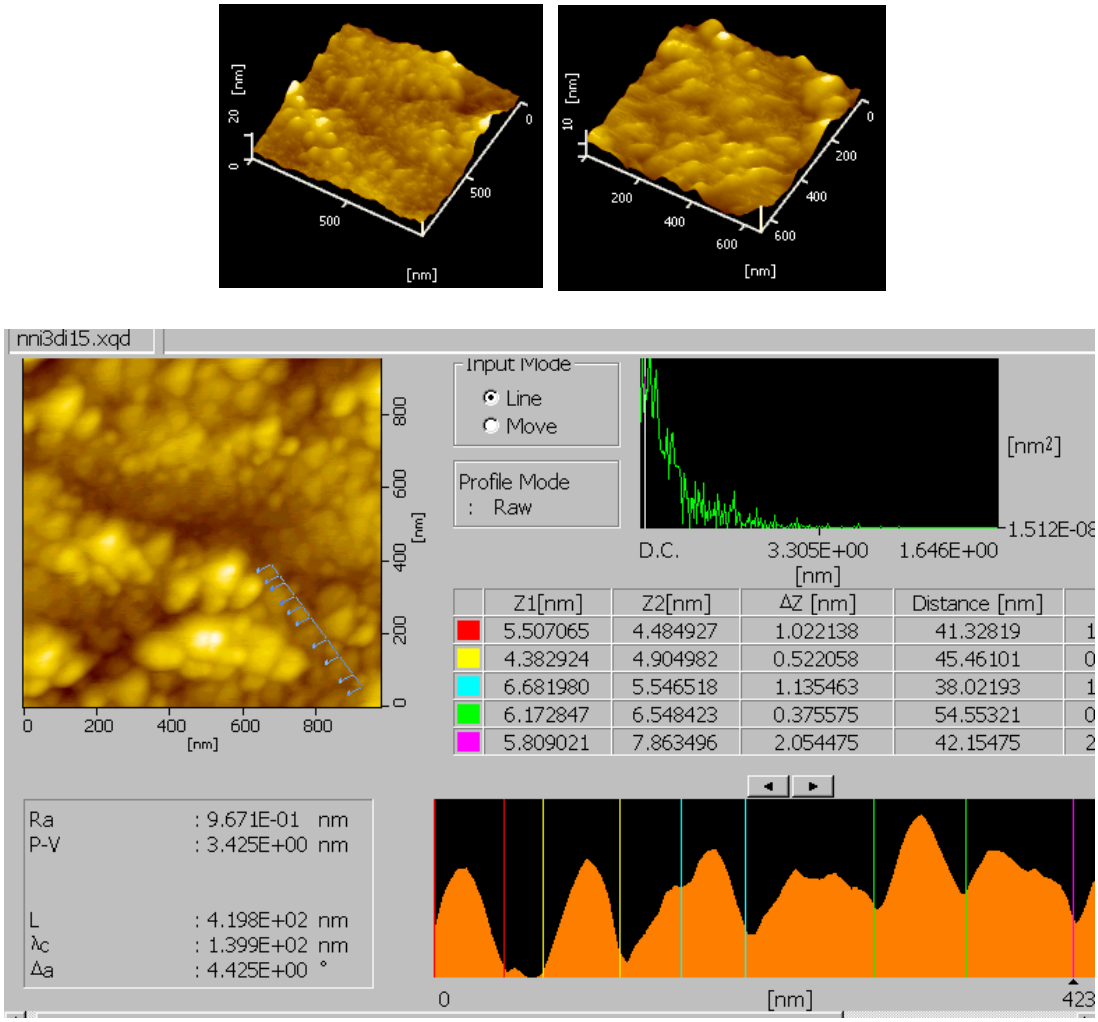

Figure 2.7: (a) AFM pictures of nanocrystalline Ni_3Al in 3-dimensional topography. (b) Line profile analysis is shown for the grain size determination.

Atomic Force Microscope (AFM) is an extremely high-resolution type of scanning-probe microscope for the manipulation of the matter at the nano-scale. AFM consists of a cantilever (probe) with a sharp tip at one of its ends that is used to scan the specimen surface. The probe is typically silicon or silicon nitride with a tip diameter less than 100 Å. The probe is attached to the piezoelectric scanner tube. When the tip is brought in the close proximity of the sample surface, the Van der Waals force between the tip and sample leads to deflection of cantilever in accordance with the Hook's law. A laser light reflected from the back of the cantilever tip measures the deflection of the cantilever. This information is fed back to a computer, which generates a map of topography and/or other properties of the interest. The information gathered from the probe's interaction with the surface can be as simple as physical topography or as diverse as measurement of materials mechanical, magnetic, electrical or chemical properties. The AFM has several advantages over SEM. AFM can produce images of materials as small as 1 nm while SEM is limited to 100 nm. AFM provides true three-dimensional surface profiles. Additionally, sample does not require special treatments that would irreversibly change or damage the sample.

AFM of SEIKO make was used for microstructure determination and grain size analysis of nanocrystalline Ni_3Al in the dynamic force mode. It is a non-contact technique in which AFM cantilever is vibrated with resonant frequency near the surface of the sample. Fig 2.7(a) shows a three-dimensional view of the microstructure/surface morphology where consolidation of nanoparticles is seen because of high pressure > 1 GPa applied in inert gas condensation method. Fig 2.7(b) demonstrates that the crystallite size is around

40 to 60 nm, as revealed by the line-profile analysis. These values match well with the average crystallite size determined by x-ray diffraction.

2.4.4 Transmission electron microscopy

Transmission electron microscopy (TEM) is a premier tool for understanding the internal microstructure of materials at the nanometer level. In TEM, the electrons are emitted from the source and accelerated to high energy (100 - 400 keV) that gives a spatial resolution of about ~ 0.2 nm. The electron beam can transmit through the sample provided the sample is ~ 100 nm thick. Preparation of samples in such thickness is both an art as well as

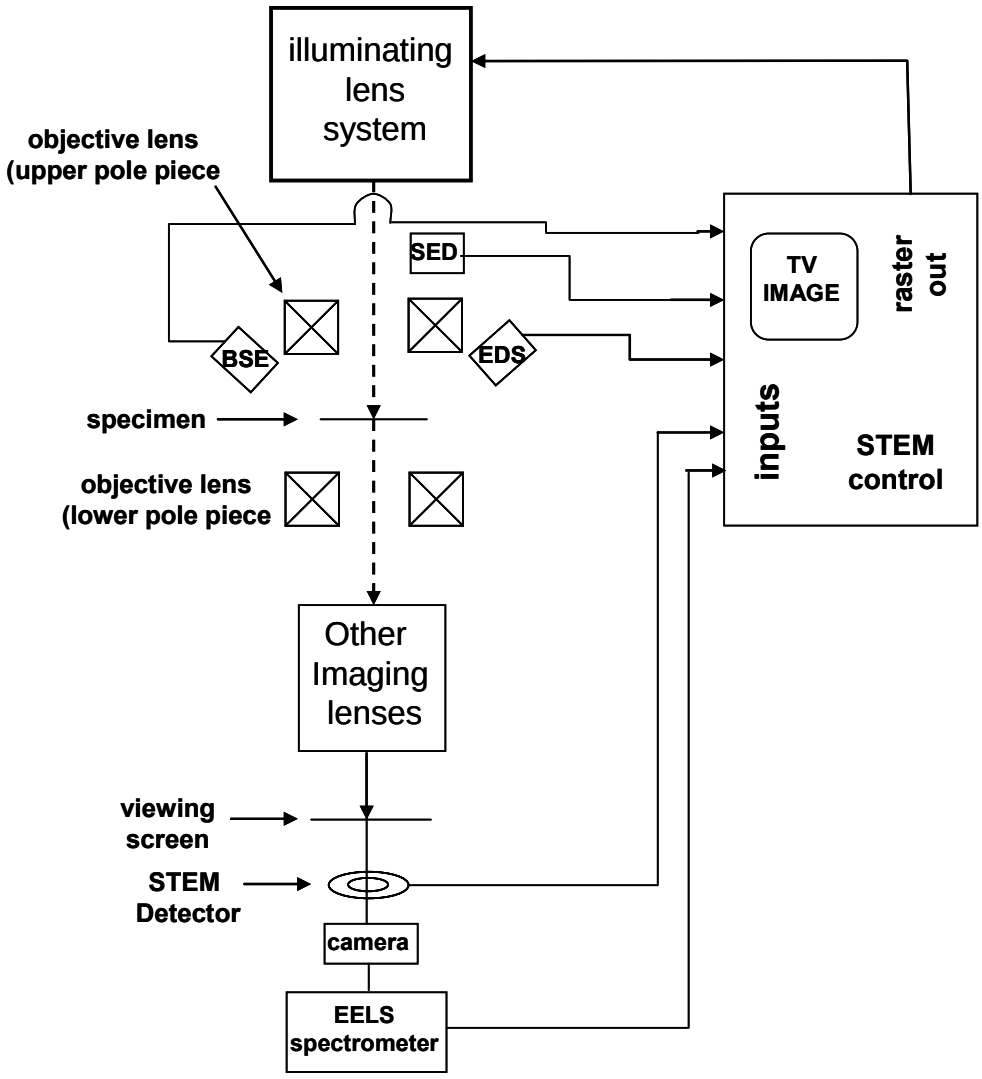

Figure 2.8: Typical schematic diagram of a transmission electron microscope with scanning (STEM) capability (adapted from [13]).

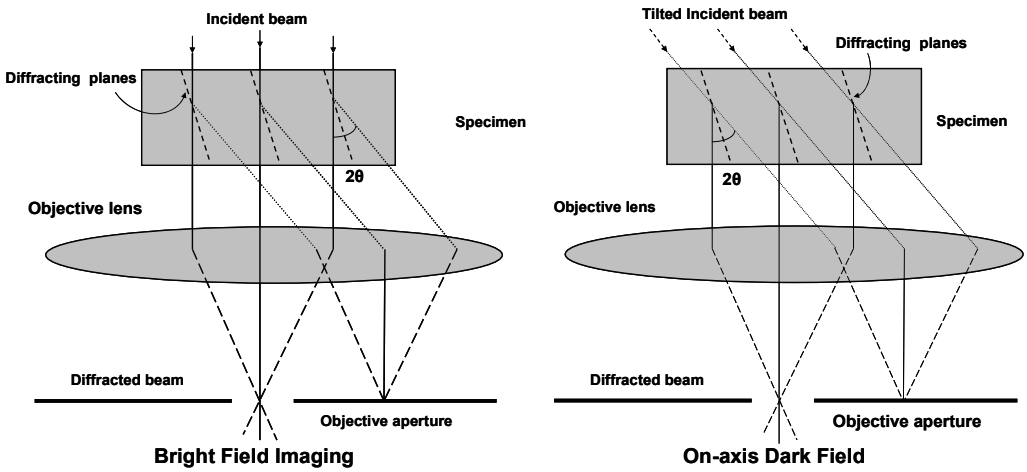

Figure 2.9: Image modes for transmission electron microscope a) Bright field b) Dark field.

science. Although x-rays generally provide better quantitative information than electron diffraction, electrons have an important advantage over x-rays in that they can be focused using electromagnetic lenses [14]. That allows one to obtain real-space images of the materials with high resolution, and simultaneously obtain diffraction information from the specific regions in the images as small as 1 nm. In addition to diffraction and imaging, the high-energy electrons in TEM cause electronic excitations of atoms in the sample. Two important spectroscopic techniques make use of these excitations by incorporating suitable detectors into TEM. I) Energy-dispersive x-ray spectroscopy (EDS); characteristic x-rays of each element are used to determine the concentrations of the different elements present in the sample. II) Electron energy loss spectroscopy (EELS); magnetic prism is used to separate the electrons according to their energy losses after having passed through a specimen. Energy loss such as plasmon excitations and core-electron excitations cause distinct features in EELS. These can be used to quantify the elements as well as provide information about atomic bonding and variety of useful phenomena. Figure 2.8 shows schematic of typical TEM that has a facility of STEM and EELS.

Another important aspect of TEM is to record the variations in the image intensity across the sample using mass thickness or diffraction contrast, theoretical basis for which is given by the kinematical theory of diffraction [13, 14]. Conventional TEM provides three modes of image formation; a) bright-field (BF) imaging b) dark-field (DF) imaging and c) lattice imaging (selective area diffraction). When the objective aperture is positioned to pass only the transmitted (undiffracted) electrons, a BF image is formed as illustrated in Fig. 2.9(a). When the objective aperture is positioned to pass only diffracted electrons by tilting the beam, a DF image is formed. To obtain lattice image or Selective Area Diffraction (SAD) pattern a large objective aperture is used and diffracted beams along with transmitted beam is allowed to pass through it. The image is formed by the interference of diffracted beams with the transmitted beam (phase contrast). If the point resolution of the microscope is sufficiently high and a suitable sample oriented along a zone axis, high-resolution SAD images are obtained. The spherical aberration of the objective lens limits the techniques to regions less than micrometer or so in diameter. For regions much smaller than this small probe technique such as convergent beam electron diffraction is used.

2.5 Measurement techniques

2.5.1 Resistivity and magnetoresistance measurement setup

The schematic block diagram of the resistivity and magnetoresistance setup is shown in Fig. 2.10. Cryogenic Limited UK-make stainless steel low boil-off cryostat was equipped with 8 tesla superconducting magnet and variable temperature insert. The cryostat is fitted with high-purity aluminum radiation shields for improving thermal conductivity. 8 Tesla (80 kOe) superconducting magnet is placed inside a 60 liter expanded liquid He

reservoir which is enclosed by 55 liter of liquid nitrogen can. Outer jacket of the cryostat is super-insulated. The space between the two insulations is evacuated to diffusion vacuum to ensure minimum losses of liquid N_2 and therefore of liquid He. Sample space is connected to helium reservoir by a needle valve (not shown in Fig. 2.10) which controls the flow of cold helium exchange gas and/or liquid He. By controlling this valve, it is possible to achieve a temperature, at the sample site, as low as 1.6 K by evaporating liquid He by low speed rotary pump. Two samples are measured simultaneously using Variable Temperature Insert that contains all the necessary electrical connections for measurements. Superconducting magnet is made up of Nb-Ti alloy and controlled by SMS series superconducting controllers. In the present

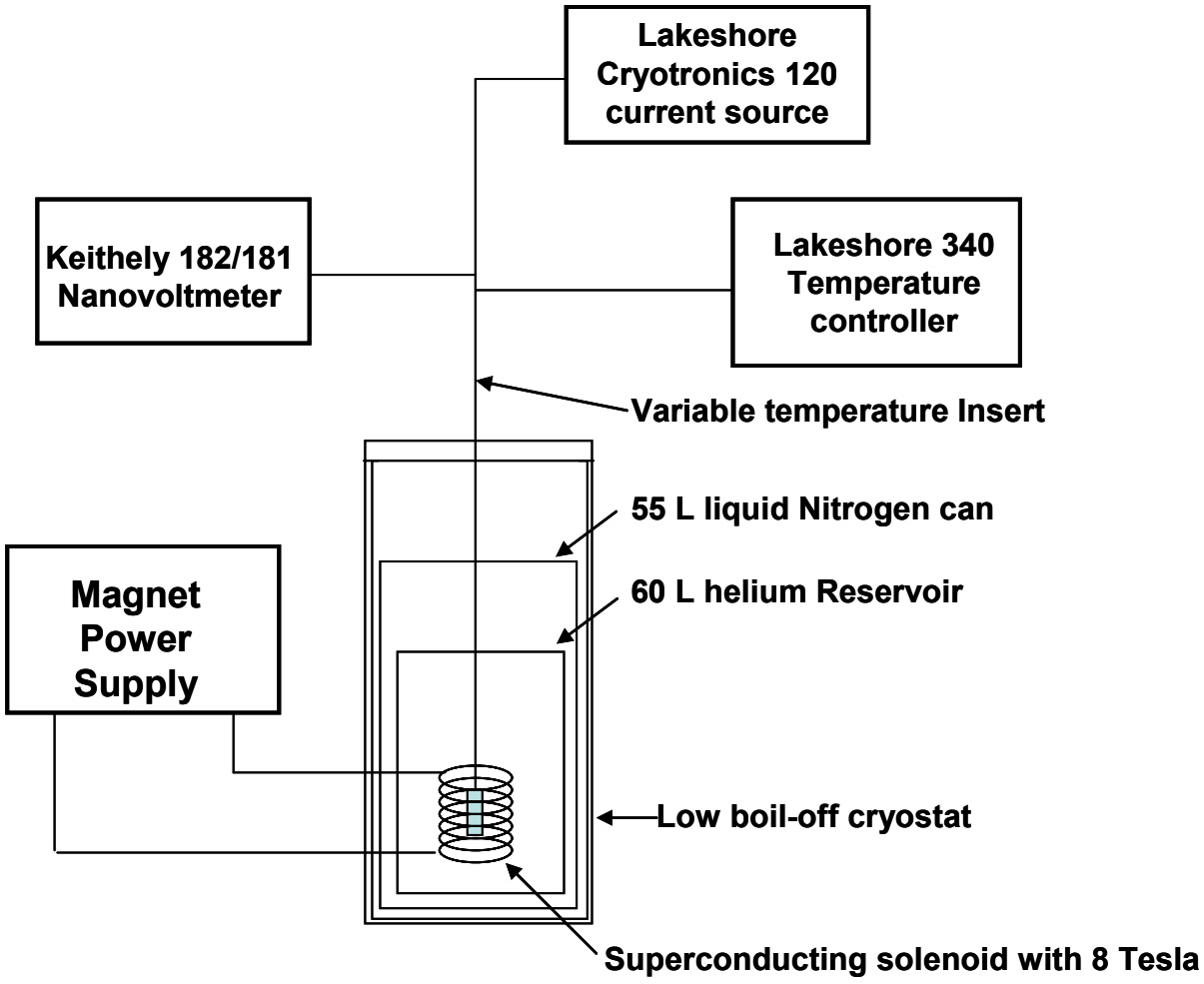

Figure 2.10: Schematic block diagram of 8T superconducting magnet set up for resistivity and magnetoresistance measurement.

system, longitudinal magnetoresistance is measured, as the direction of applied magnetic field is parallel to the direction of the electric current flowing through the sample.

All the samples in the present study have been measured using standard four-probe measurement technique. The metallic samples were coated by apeizon grease to have good thermal contact with the sample holder. The electrical receptivity measurements over a wide temperature range extending from 300 K down to 1.7 K were carried out on 'as prepared' polycrystalline Ni_xAl_{100-x} alloys, nanocrystalline Ni_3Al, q-Fe_{20} and a-Fe_{20} samples. The resistance was measured as a function of temperature at 0.1 K intervals at low temperatures (below 12 K) and also near the Curie temperatures and at 0.5 K steps outside these temperature ranges (up to 300 K). At every setting, temperature was stabilized to within ± 10 mK using DRC 93C, Lakeshore, PID temperature controller. A current of 100 mA was passed through the sample and the voltages of the order of ~ 1 mV were measured with a resolution of 1 nV using Keithley 182 nanovoltmeters. The sample current at each temperature was reversed in order to correct the measured voltage for the thermo-emf generated due to small temperature gradients, if present across the sample, and also for the zero-drift of the nanovoltmeter. The longitudinal magnetoresistance (MR), $\Delta\rho_{||}/\rho = [\rho_{||}(T,H) - \rho(T,H=0)]/\rho(T,H=0)$, was measured as a function of magnetic field in steps of 1 kOe up to 10 kOe, 5 kOe up to 3 kOe and 10 kOe to the maximum available field of 80 kOe. During each isotherm, the voltage drop in zero-field was corrected for thermo-emf by reversing the direction of current though sample and the same correction was used for all the field values since this correction was almost constant in magnetic fields up to

80 kOe. The temperature remained constant to within ± 20 mK during the recording of each isotherm. Such isotherms were measured at 1 K intervals at low temperatures and in the temperature range $T_C - 5\ \text{K} < T < T_C + 5\ \text{K}$ near T_C and at 10 K intervals otherwise. The longitudinal magnetoresistance (MR) versus field isotherms were later converted into MR as a function of temperature at different but fixed values of the field, H.

2.5.2 Vibration Sample Magnetometer (VSM)

The working principle of VSM is based on the Faraday's law of induction. When a dipole is made to undergo sinusoidal motion in a homogenous magnetic field, there is an induced voltage in its neighborhood which is proportional to the magnetic moment possessed by the dipole and also to the frequency and amplitude of vibration of the dipole [15].

There is a direct relationship between the induced voltage in a suitably designed set of pick-up coils and the magnetic moment of the vibrating sample positioned inside them. The VSM measures the total magnetic moment, m, of the sample in emu, which can be converted to Gauss by using the following expression

$$M\ (\text{Gauss}) = [m\ (\text{emu}) / \text{mass (g)}] \times \text{density (g/cc)} \qquad (2.3)$$

The EG&G Princeton Applied Research (PAR) model 4500 VSM, which we used for performing the measurements, was calibrated using a small standard highly pure (99.999%) nickel sample. Model 4500 PAR VSM is capable of measuring magnetic moment in the range from 5×10^{-5} emu to 2×10^{3} emu. The sample to be studied is inserted into the sample cup made up of

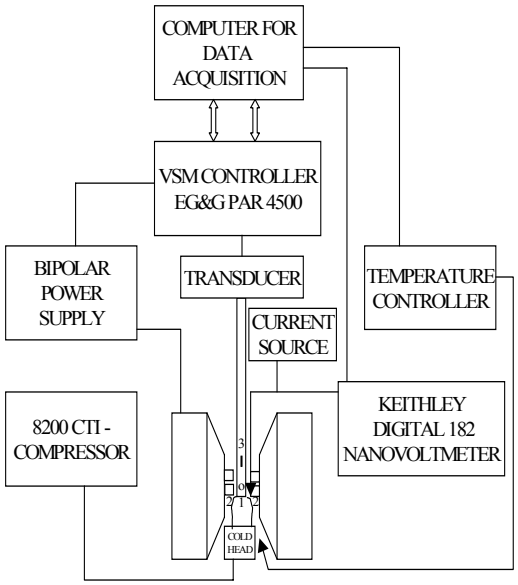

Figure 2.11: Block Diagram of Vibrating Sample Magnetometer.

perspex and positioned on the sample holder in such a way that it rests at the centre of the pair of specially designed sensing or pick-up coils housed between the poles of the electromagnet. The optimum sample position is at the center of symmetry of the pick coil system and in the homogeneous magnetic field, where the pick-up signal is minimum along x-direction (parallel to field direction) but maximum along y- and z-directions. In order to ensure an accurate monitoring of the sample temperature, the sample holder is so designed that the platinum sensor is in direct thermal contact with the sample. It consists of a brass tube, 75 cm in length connected to a hylam tube of 15 cm length (4 mm O.D. and 2mm. I.D.), which is attached to a perspex adopter at the other end. In this adopter is housed a precalibrated platinum (PT 103) sensor whose tip comes in body-contact with the sample when the perspex sample cup containing the sample is screwed onto this adopter. Tiny holes have been drilled at the bottom of the sample cup as well as on its sides at different locations close to the sample site so that the sample comes in direct contact with the helium exchange gas present in the sample chamber. In order to

perform measurements at low temperatures, a two-stage Janis Closed Cycle Refrigerator (CCR) has been used in conjunction with the VSM. This arrangement provides a convenient means of attaining a temperature as low as 12 K. The proportional, integral and differential (PID) temperature controller (Model DRC- 93 CA, Lake Shore Cryogenics, USA), facilitates the temperature control over the range 12 K ≤ T ≤ 300 K. Sample temperature is monitored by sending an excitation current of 1mA through the precalibrated platinum sensor and the sensor voltage is measured with the help of a nanovoltmeter (Model 182, Keithley USA).

Magnetization measurements on Ni_xAl_{100-x} alloy samples were performed on spheres of diameters 3 mm / 2.5 mm and ribbon strips of length 2.5 mm and 2 mm width stacked one above the other after a thin layer of apeizon grease was applied in between them to ensure a good thermal contact between them. The sample, to be investigated, was placed in the sample holder assembly and rotated such that the field lies within the ribbon plane and is directed along their length in case of ribbon strips. This arrangement leads to minimization of the demagnetizing effects. For polycrystalline samples of spherical shape, the field can be applied along any direction since the demagnetizing factor is the same in all directions of the field. M versus H_{ext} isotherms were taken on polycrystalline ap-Ni_xAl_{100-x} samples, at 60 different field values ranging from 0 to 15 kOe at temperature intervals of 0.5 K, 0.1 K, 0.05 K and 0.025 K in the ranges 12 K ≤ $T \leq 0.5T_C$, $0.5T_C \leq T \leq T_C$ - 10 K, T_C - 10 K ≤ $T \leq T_C - 3$ K, $T_C - 3$ K ≤ $T \leq T_C + 3$ K, respectively. Above $T_C + 3$ K, the temperature interval was slowly increased to 0.1 K, 0.5 K, 1 K, 5 K and 10 K till the room temperature was reached. The isotherms, so obtained, were corrected for demagnetizing field. The Curie temperature, T_C, was measured by the kink-point method. The

details about this method and the calculation as well as the experimental determination of demagnetization factors are described in reference [16].

*2.*5.3 ac susceptibility measurement setup

Susceptibility is defined as the change in magnetization of the sample corresponding to the infinitesimal change in the externally applied magnetic field. If a time-varying external magnetic field, say a sinusoidal field, is applied, magnetization lags in phase with respect to the applied field and the susceptibility becomes complex, i.e., $\chi = \chi' - i\,\chi''$, where χ' and χ'' are the real and imaginary components of susceptibility.

The ac susceptibility measurement, as an experimental technique, is very useful in studying the magnetic properties of materials, especially of the magnetic phase transitions where the response of magnetic moments in low field is of great importance. The method is based on the fact that mutual inductance of two coils (and therefore the induced voltage) changes if a magnetic sample is placed inside them. The ac susceptometer generally consists of the primary coil and two coaxially placed exactly identical secondary (pick-up) coils, which are connected in series-opposition (their induced voltages subtract) so that, without a sample, their resultant induced voltage is nearly zero. If a (magnetic) sample is placed in one of the secondary coils, it causes the imbalance in the voltages as a consequence of the redistribution of flux lines over the cross-section of that secondary coil. This voltage is related to the susceptibility of the sample [17]. Ideally, if the sample is very long so that the influence of edges on the distribution of flux lines can be neglected, the induced voltage is

$$v(t) = -\mu_0 N_s A_s dM / dt\,. \tag{2.4}$$

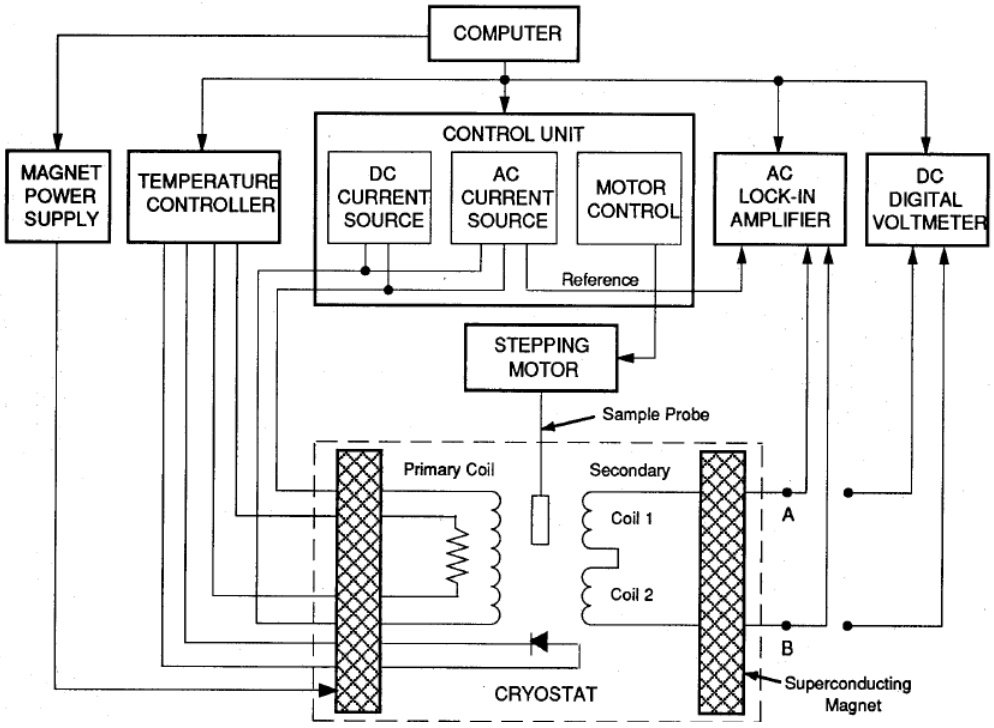

Figure 2.12: Block Diagram of ac susceptometer with the facility of DC extraction magnetometer [18].

Here N_s is the number of turns of either secondary coil and A_s is the cross-sectional area of the sample. The change of the magnetic field induces the change of the magnetization. If the magnetizing field is harmonic ($H = H_0 \exp(i\omega t)$), we have

$$v(t) = -i\omega\mu_0 N_s A_s \frac{dM}{dH} e^{i\omega t} \tag{2.5}$$

i.e., the induced voltage is proportional to the ac susceptibility, $\chi_{ac} = dM / dH$. In reality, the relation between the ac susceptibility and the induced voltage is not so straightforward. It depends on the shape of the sample, its dimensions and inhomogeneities (demagnetizing effect), the dimensions of the secondary coils, filling fraction, etc. Finding out the relation between the induced voltage and ac susceptibility (calibration of the susceptometer) can be a very hard task. But the proportionality between the induced voltage and ac susceptibility

permits an evaluation of many valuable physical properties. Figure 2.12 shows the block diagram with essential components of commercial ac susceptometer in physical property measurement system. The details are given in reference 18.

2.5.4 SQUID Magnetometer

A SQUID is a device which makes use of flux quantization and Josephson tunneling to measure magnetic moment to a very high precision. This device operates at temperatures as low as a few Kelvin and is a magnetic-flux detector.

In the case of two Josephson junctions connected in parallel, as the magnetic flux Φ threading a superconducting loop is changed, the critical current of two junctions oscillates with a period equal to the flux quantum Φ_0. These oscillations arise due to the interference between macroscopic wavefunctions at the two junctions. This phenomenon of "superconducting quantum interference" forms the basis of a SQUID (Superconducting Quantum Interference Device) magnetometer.

A Josephson junction is made up of a thin insulating layer sandwiched between two superconducting loops. Hence, only a tunnel current is able to flow through it. Let $\psi = \psi_0 e^{i\theta_i}$ be the superconducting order parameter and θ_i are the phases on the two sides of the junction. Then the relative phase $\delta = \theta_1 - \theta_2$ is the relevant quantity. The current I through the ideal junction is given by the dc Josephson equation:

$$I = I_0 \sin\delta \tag{2.6}$$

while the voltage V across the ideal junction is given by the ac Josephson equation:

$$V = \hbar / 2e\left(d\delta / dt\right) \tag{2.7}$$

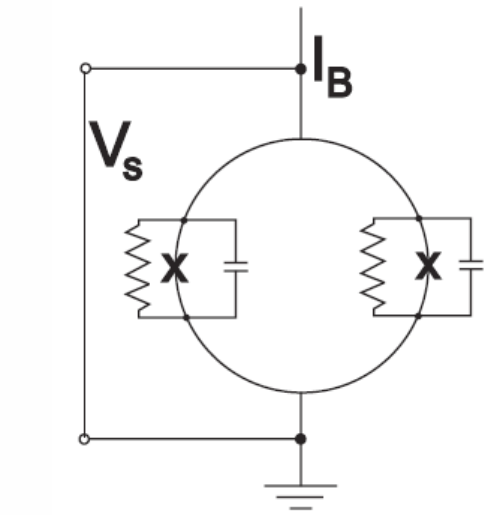

Fig. 2.13: Schematic of dc SQUID Josephson junctions, marked by 'X'. dc SQUID is biased with dc current I_B.

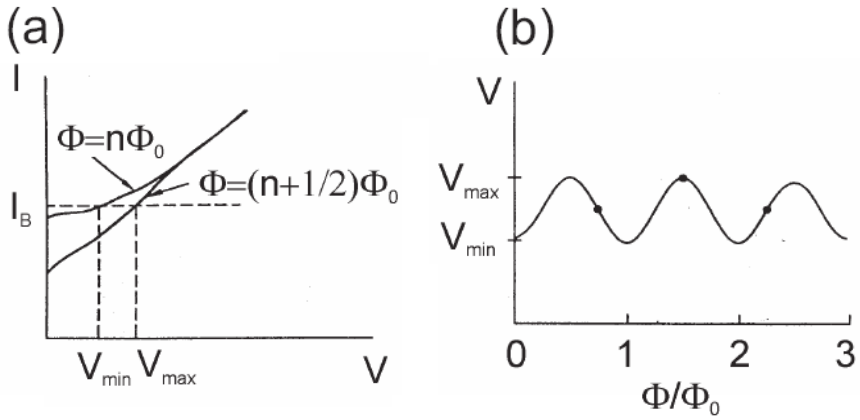

Figure 2.14: (a) The $I-V$ characteristics of a dc-SQUID. The amount of flux Φ_0 determines the output voltage V for a particular value of the bias current I_B. As the applied flux varies between $n\Phi_0$ and $(n+1/2)\Phi_0$ the output voltage changes between V_{min} and V_{max}. (b) The resulting $V-\Phi$ curve of a dc-SQUID at a given bias current [19].

A real junction has its own physical capacitance and is shunted by a resistor, both joined in parallel to the junction, as indicated in Fig. 2.13. The parallel arrangement of Josephson junctions must be considered in an accurate model of the electrical properties of the SQUID [19]. A superconducting loop contains flux only in integral multiples of the flux quantum

$$\Phi_0 = 2\pi\hbar / 2e = 2.07 \times 10^{-15}\ Wb. \qquad (2.8)$$

A change in flux applied to the loop will cause currents to oppose that change leading to a change in the relative phase, which according to eq. (2.2) gives rise to a voltage leading to a typical $I - V$ characteristic sketched in Fig. 2.14(a) for a dc-SQUID. The voltage oscillates between V_{min} and V_{max} when Φ changes by Φ_0, as indicated in Fig. 2.14 (b). Thus the SQUID acts as a nonlinear flux-to-voltage transducer. The $V - \Phi$ curve is linearized with the help of the so-called flux-locked loop (FLL). The basic idea is to keep the system at a constant flux of $(n/2)\Phi_0$, i.e., one of the extrema in the $V - \Phi$ curve. Then the change is magnetic flux is directly measured as change in SDUID voltage through the pick-up coil. The pick-up coil is wound in a second-order gradiometer configuration (Fig.2.14(c)) so as to measure only $\partial^2 H/\partial z^2$ and higher gradients. This configuration rejects any response due to change in uniform field or change in its first derivative. A typical SQUID voltage response as the specimen is moved through the SQUID coils is shown in Fig.2.14(c). The magnetic moment of the specimen is then obtained from this SQUID response curve with the help of various algorithms. The SQUID magnetometer used in the present work is a completely automated, computer-controlled and software-driven commercial system (Quantum Design Model MPMS7).

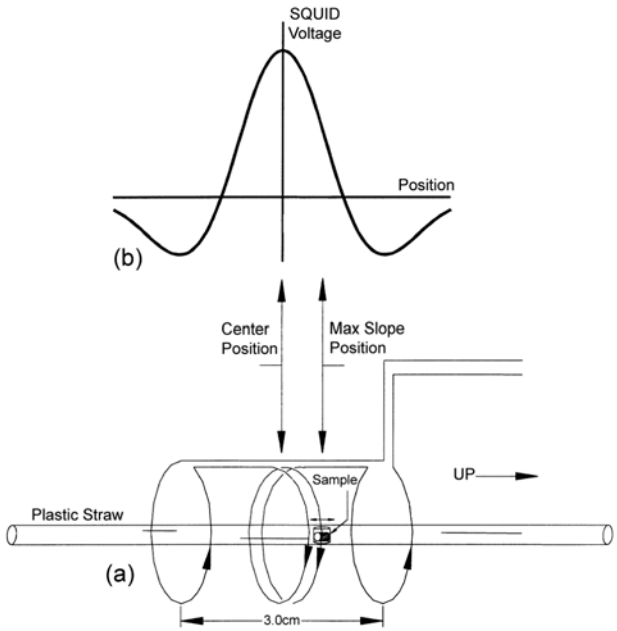

Figure 2.14(c): Second-derivative coil-configuration and pick-up coil response as the sample is moved through the coils.

References

[1] G. E. R. Schulze: Metallphysik, Akademie-Verlag, Berlin 1967.

[2] M. F. Singleton, J. L. Muray and P. Nash: in Binary Alloys phase diagrams, T.B. Massalski, ed., ASM INTERNATIONAL, Meatals Park, OH, 1986, pp.140-43.

[3] D Letzig, J Klöwer and G. Sauthoff, Z. Metallkd. **90**, 712 (1990).

[4] R. Kainuma, N Ono and K. Ishida, Mat. Res. Soc. Symp. Proc. **360**, 467 (1995).

[5] S. M. Hao, K. Ishida and T. Nishizawa, Metall. Trans. A **16**, 179 (1985).

[6] H. Bitterlich, W. Löser and L. Schultz, J. Phase Equilib. **23**, 301 (2002).

[7] R. W. Guard and J. H. Westbrook, Trans. MS AMIE **215**, 807 (1959).

[8] Anita Semwal and S. N. Kaul, J. Phys. : Condens. Matter **16**, 8675 (2004).

[9] C. T. Liu, C. L. Fu, M. F. Chisholm, J. R. Thompson, M. Kremar and X. –L. Wang, Prog. Mat. Sci. **52**, 352 (2007).

[10] INEL, X-ray diffractometer instruction manual, Artenay, France (1998).

[11] B. D. Cullity, *Elements of x-ray diffraction*, Addision-Wesley Publishing Company, Inc., London (1978).

[12] http://www.ill.edu/D20

[13] E. N. Kaufmann, *Characterization of Materials*, (Wiley-Interscience, New Jersey, 2003.

[14] Williams, DB., and Carter, CB., *Transmission Electron Microscopy: a Textbook for Materials Science*, New York (1996),

[15] S. Foner, Rev. Sci. Instr. **27**, 548 (1956); ibid 30, 548 (1959).

[16] A. Semwal, *Ph.D. Thesis* (University of Hyderabad, 2002); P. D. Babu *Ph.D. Thesis* (University of Hyderabad, 1995).

[17] S. Srinath, *Ph.D. Thesis* (University of Hyderabad, 2000).

[18] Đ. Drobac and Z. Marohnić, FIZIKA A **8**, 165 (1999).

[19] John K. Krause, IEEE trans. magn. **28**, 3066 (1992).

[20] W. G. Jenks, S. S. H. Sadeghi, and J. P. Wikswo, J. Phys. D: Appl. Phys. **30**, 293 (1997).

Chapter 3

Effect of off-stoichiometry and site-disorder on electrical- and magneto-transport properties of Ni_3Al

3.1 Introduction

Substantial progress has been made in understanding electrical and thermal transport in nearly ferromagnetic (NF) and weakly ferromagnetic (WF) metals since Mills and Lederer [1] calculated electrical resistivity at low temperatures due to spin waves (SW) using the random phase approximation (RPA) within the framework of a simple model in which the conduction electrons (s-electrons) are scattered by the spin fluctuations (SF) of the d-band electrons via s-d exchange interaction. Subsequently, Schindler and Rice [2] (Mathon [3]) applied this model to NF (both NF and WF) metals to investigate electrical and thermal resistivity (electrical resistivity) at low temperatures near the critical boundary, which separates the nearly and weakly ferromagnetic regimes, by employing RPA for calculating the dynamical susceptibility due to spin fluctuations. Schindler and Rice [2] found that electrical resistivity, $\rho(T)$, varies with temperature as T^2 at low temperatures, and as the critical boundary is approached from the NF side, the coefficient of the T^2 term becomes large while the temperature range over which $\rho(T)$ follows this power law behavior narrows down. By contrast, Mathon [3] obtained the result that $\rho_{SF}(T) \sim T^{5/3}$ at very low temperatures on either side, but in the immediate vicinity, of the critical boundary. However, it was soon realized that RPA does not yield correct results particularly at high temperatures where the interactions between different spin fluctuation modes become important. Ueda and Moriya [4] (UM), thus, used the self-consistently renormalized (SCR) spin fluctuation theory [5] (which provides a correct description for the main attributes of weak itinerant-electron ferromagnets, including the Curie-Weiss behavior of susceptibility for temperatures above the Curie temperature, T_C), instead of RPA, to calculate the dynamical susceptibility and thereby the SF (SW) contributions to the electrical and thermal resistivity in NF and WF (WF)

metals over an extremely wide temperature range. In summary, their results pertaining to resistivity are: (i) at very low temperatures, $\rho_{SW}(T) \sim T^2$ ($\rho_{SF}(T) \sim T^2$) for WF metals (on both sides of the critical boundary, where the ferromagnetic instability sets in), (ii) as the critical boundary is approached either from below (nearly ferromagnetic side) or from above (weakly ferromagnetic side), the coefficient of the T^2 term in $\rho_{SF}(T)$ increases steeply while the temperature range over which this power law holds becomes narrow, and (iii) a crossover from the T^2 variation to $T^{5/3}$ variation occurs as the temperature is raised from low temperatures in NF metals whereas $\rho_{SF}(T) \sim T^{5/3}$ ($\rho_{SF}(T) \sim T$) at temperatures just below and above (well above) T_C in WF metals. Ueda [6] extended the UM formalism [4,5] to ascertain the effect of external magnetic field (*H*) on the SF contribution to $\rho(T)$ at low temperatures in weak itinerant-electron ferromagnets but neglected the SW contribution. Pai and Mishra [7] were first to investigate the influence of disorder (caused by either impurities or off-stoichiometry or both) on electrical and thermal conductivity of NF metals at very low temperatures using the Keldysh-diagram technique. Recently, the self-consistent calculations, due to Kaul [8], of the SW and SF contributions to $\rho(T)$ of weak itinerant-electron ferromagnets in the absence and presence of H at temperatures up to T_C overcame the main weakness of the UM [4,5] and Ueda [6] theoretical treatments by completely dispensing with the unrealistic electron-gas approximation used by UM and Ueda to arrive at the final expression for the dynamical susceptibility.

Out of the weak itinerant-electron ferromagnets known in the literature [9], the intermetallic compound Ni_3Al has attracted the maximum attention.

The ordered Ni_3Al phase has a homogeneity range that extends from 73 at.% Ni to 77 at.% Ni and as the Ni concentration (x) increases from 73 at.%, long-range ferromagnetic order sets in at the critical concentration (boundary) $x_c \approx 74.5$ at%. Early investigations of electrical resistivity [10], $\rho(T)$, in the temperature range $1.2\,K \le T \le 20\,K$ and magnetoresistance (MR) at 4.2 K in magnetic fields [11] $H \le 350\ kOe$ (MR at $H \le 23\ kOe$ and temperatures in the range [12] $1.2\,K \le T \le 90\,K$) in the polycrystalline samples of Ni_xAl_{100-x} alloys with x ranging from $73.5\ at.\%$ to $76.0\ at.\%$ revealed the following. (I) In the temperature interval $1.2\,K \le T \le 4.2\,K$, $\rho(T)$, for all the compositions in the range specified above, is described by the expression [10] $\rho(T,x) = \rho(0,x) + A(x)\,T^{\alpha(x)}$. As a function of x, the exponent (coefficient) starts with a value $\alpha = 2.0$ ($A \cong 1.5\ n\Omega\,cm\ K^{-2}$) at $x = 73.5\ at.\%$, goes through a minimum, $\alpha = 1.5$, (peak, $A \cong 12.0\ n\Omega\,cm\ K^{-\alpha(x_c)}$) at x_c and assumes the value of $\alpha = 2.0$ ($A \cong 7.0\ n\Omega\,cm\ K^{-\alpha(x)}$) at $x = 75.7$ and 76.0 *at.*%; at the stoichiometric composition $x = 75.0\ at.\%$, $\alpha = 1.75$ while A exhibits a discontinuous jump. Note that the observed variation of the exponent α with Ni concentration does not conform to that predicted by the above-mentioned theories [2-4]. (II) However, so far as the MR is concerned, the agreement between the experimental observations and the theoretical predictions, based on a two (s-d) band model [11], is remarkably good [11,12] over wide ranges of temperature and field in the strongly exchange-enhanced paramagnetic samples with $x < x_c$; a similar agreement between theory and experiment is observed [11,12] in the weakly ferromagnetic compositions ($x > x_c$) only at low temperatures $T < 30\,K$ and high fields $H > 100\ kOe$, where the negative MR (arising from the field-induced change in the density of states at the Fermi level of the d sub-bands) is masked by the 'conventional' positive MR due to

the orbital motion of the conduction (s) electrons in a magnetic field (the so-called the Lorentz force contribution). Subsequent studies [13-15] of electrical resistivity and magnetoresistance in this alloy system yielded results that are not only in conflict with one another but also with the previous ones [10-12]. For instance, Sasakura et al. [13] observe a crossover from the T^2 variation of $\rho(T)$ in the range $1.2\,K \le T \le 2.5\,K$ to the $T^{5/3}$ variation for temperatures $10\,K \le T \le T_C$ in polycrystalline ordered Ni_3Al, Yoshizawa et al. [14] find that irrespective of the Ni concentration (within the range $72.91\ at.\% \le x \le 77.17\ at.\%$), $\rho(T) \sim T^2$ at temperatures in the range $4.2\,K \le T \le 10\,K$ in polycrystalline Ni_xAl_{100-x} alloys while Fuller et al. [15] report that $\rho(T) \sim T^{5/3}$ from 1.2 K to $T = T_C$ in $Ni_{76.6}Al_{23.4}$ single crystal. Though these observations are at variance with one another, it is claimed that the temperature variations of magnetization, ρ and MR [13, 14] (ρ and magnetization [15]) are consistent with the predictions of the SCR spin fluctuation theory [4,5].

Considering that a varying degree of site disorder, resulting from different annealing treatments, is bound to be present in the samples studied previously in the literature, it is possible that the above discrepancy between the experimental observations and hence between experiment and theory is caused by an interplay between site disorder and compositional disorder. We have, thus, undertaken a systematic experimental study, which aims at ascertaining the influence of off-stoichiometry and site disorder on the variation of resistivity (magnetoresistance) with temperature (temperature and external magnetic field) in $Ni_{75}Al_{25}$. To this end, polycrystalline samples of Ni_xAl_{100-x} alloys with x ranging from 74 at.% to 76 at.% were prepared out of a

specific batch of high-purity Ni and Al under identical conditions without subjecting them to any thermal treatment. The observed compositional dependence of the transport and magneto-transport properties is thus governed by the compositional disorder (off-stoichiometry) and the site disorder introduced by the preparation protocol. The terms compositional disorder and site disorder are defined in section 3.3. A comparison between the results obtained on as-quenched samples (which have both site disorder and compositional disorder) and annealed/completely-ordered counterparts (which have only compositional disorder) of a given composition is expected to bring out the effect of only the site disorder.

3.2 Experimental details

Polycrystalline rods of 100 mm length and 10 mm diameter with nominal composition $Ni_{74}Al_{26}$, $Ni_{74.5}Al_{25.5}$, $Ni_{75}Al_{25}$ and $Ni_{76}Al_{24}$ were prepared by first melting the proper proportions of the 99.998 % pure Ni and Al starting materials using a radio-frequency induction-melting technique and then quenching the melt following a procedure detailed elsewhere [16]. Samples in the shape of a disc of 10 mm diameter and 5 mm thickness, a rectangular strip of dimensions 9 x 2 x 0.5 mm^3 and a sphere of 2.5 mm diameter were spark-cut from these rods for x-ray diffraction, electrical and galvanomagnetic transport, and magnetic measurements, respectively. The actual chemical composition of the samples, as determined by the x-ray fluorescence technique and inductively coupled plasma optical emission spectroscopy, is given in table 3.1. The compositional analysis also revealed that the total concentration of magnetic 3d transition metal impurities such as Mn, Cr, Fe and Co lies below 0.002 at. %. The 'as-prepared' alloy samples are henceforth labeled as *ap-$Ni_{74.3}$*, *ap-$Ni_{74.8,}$* *ap-$Ni_{75.1}$* and *ap-$Ni_{76.1}$*. Optical polarizing micrographs (figure 3.1) and scanning electron micrographs of *ap-$Ni_{74.3}$*, *ap-$Ni_{74.8,}$* *ap-$Ni_{75.1}$* revealed the

existence of a *trace* second *isostructural* crystalline phase. EDAX (energy dispersive absorption of x-rays) analysis showed that (i) in the alloy *ap-*$Ni_{74.3}$, the second (minor) phase is *poorer* in Ni concentration (by $\cong 0.2$ at. %) compared to the matrix (major) phase (which has the same composition as that given in table 3.1) and (ii) this difference in the composition of the minor and major crystalline phases diminishes very fast as the Ni concentration increases beyond 74.3 at. % so much so that it falls within the uncertainty limits of the EDAX technique ($\cong \pm 0.05\ at.\%$) for the alloys with $x \geq 74.8\ at.\%$.

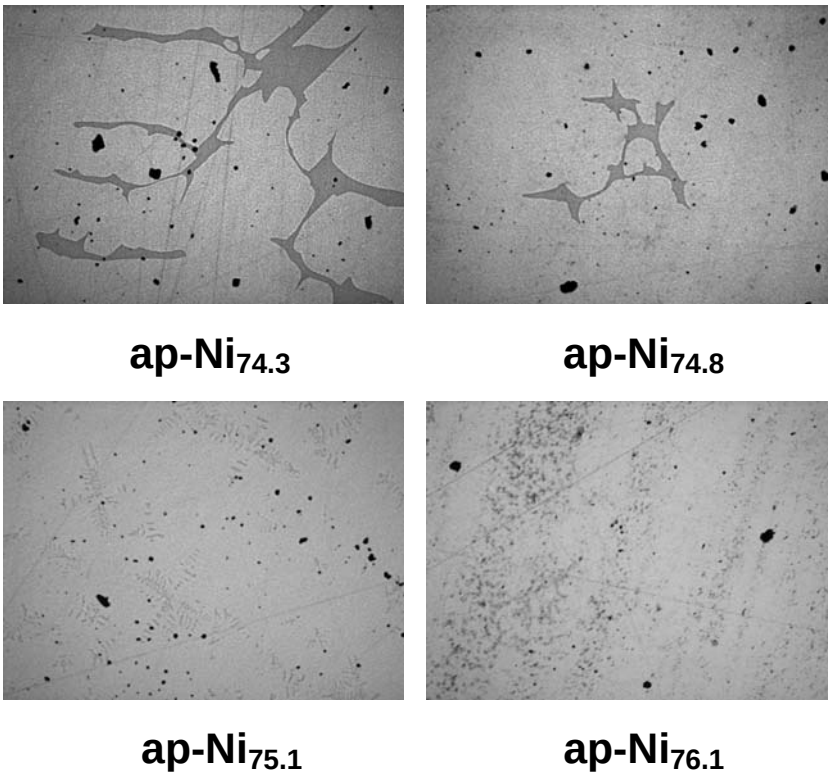

*Figure 3.1: Optical polarizing microscope pictures of the 'as-prepared' samples taken at a magnification of 100*x, *revealing the presence of dark regions (minor second crystalline phase) in ap-*$Ni_{74.3,}$ *ap-*$Ni_{74.8,}$ *ap-*$Ni_{75.1}$ *and ap-*$Ni_{76.1}$.

Electrical resistivity, $\rho(T)$, and longitudinal magnetoresistance, $\Delta\rho_{\|} / \rho = [\rho_{\|}(T,H) - \rho(T,H=0)] / \rho(T,H=0)$, were measured to a relative accuracy of better than 10 ppm on rectangular strips of 10 mm length, 2 mm width and 0.5 mm thickness, at temperatures in the range $1.7\,K \leq T \leq 300\,K$,

using four-probe dc method; $\Delta\rho_{\|}/\rho$ measurements were carried out in the above temperature range in external magnetic fields, *H*, up to 80 *kOe*. In this chapter, the magnetoresistance versus magnetic field isotherms taken on the Ni_xAl_{100-x} alloys in different temperature regimes have been analyzed in terms of the relevant theoretical expressions yielded by the self-consistent spin fluctuation theory [8] using the magnetization, $M(T,H)$, data taken on the samples coming from the same batch as that used in this work. The results of an elaborate analysis of the $M(T,H)$ data and their discussion in terms of the spin fluctuation theory [19] form the subject of the next chapter.

3.3 X-ray diffraction

X-ray diffraction patterns of the disc-shaped samples were recorded at room temperature over the scattering angle, 2θ, range of $10^o \le 2\theta \le 120^o$, using $Co\ K_\alpha$ radiation, on Inel x-ray diffractometer with curved position-sensitive detector. Since the scattered x-ray intensity is measured simultaneously over the entire 2θ range, even the weakest Bragg peaks, which would have normally escaped detection in the conventional x-ray diffractometers, can be detected with ease. Figure 3.2 compares the x-ray diffraction (XRD) patterns observed for the samples *ap-*$Ni_{74.3}$, *ap-*$Ni_{74.8,}$ *ap-*$Ni_{75.1}$ and *ap-*$Ni_{76.1}$ with that generated for a completely ordered Ni_3Al compound using the space group $L1_2$ and the reported value [17, 18] of the lattice parameter '*a*' in the Rietveld program. In a completely ordered Ni_3Al compound, Ni and Al atoms respectively occupy the face-centered and corner sites of the cubic unit cell. The face-centered (corner) sites thus constitute the Ni (Al) sub-lattice. A complete atomic order in $Ni_{75}Al_{25}$ alloy exists only when 100% of Ni (Al) sub-lattice sites are occupied by Ni (Al) atoms. By the same token, *the maximum atomic order permitted by the chemical composition* in $Ni_{74}Al_{26}$ ($Ni_{76}Al_{24}$) alloy

is realized only when 98.7%, 1.3% (100%, 0%) of Ni sub-lattice sites and 0%, 100% (4%, 96%) of Al sub-lattice sites are occupied by Ni, Al atoms. Antisite atoms, e.g., Ni (Al) atoms on Al (Ni) sub-lattice sites, on either of, or both, the sub-lattices give rise to site disorder in atomic arrangement on the underlying face-centered-cubic (f.c.c.) lattice. Thus, a *residual site disorder* (e.g., 1.3%

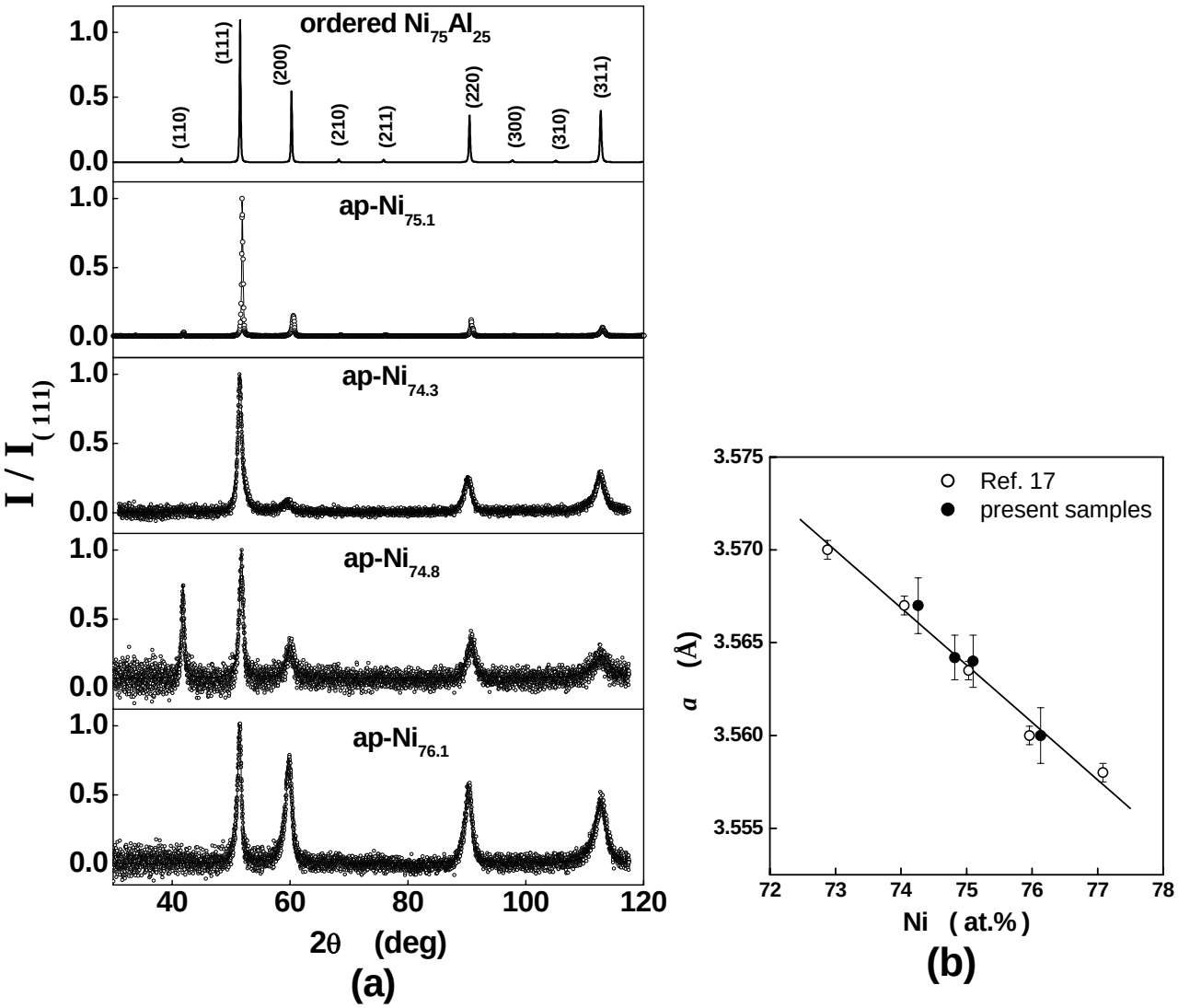

Figure 3.2 (a) X-ray diffraction patterns taken at room temperature on the 'as-prepared' Ni_xAl_{100-x} alloys with x = 74.3, 74.8, 75.1 and 76.1 at. % . The top panel shows the x-ray pattern for a completely ordered Ni_3Al compound generated by the Rietveld program. In order to facilitate a direct comparison between different compositions, the scattered x-ray intensities are normalized to the peak intensity of the (111) Bragg reflection. (b) The variation of the lattice parameter 'a' with Ni concentration. Similar data on well-ordered Ni_xAl_{100-x} alloys reported previously in reference [17] are also included for comparison.

(4%) of Ni (Al) sites occupied by Al (Ni) atoms in $Ni_{74}Al_{26}$ ($Ni_{76}Al_{24}$) alloy) is *intrinsic* to off-stoichiometric alloys that exhibit maximum possible atomic order. This type of residual site disorder that depends on chemical composition will henceforth be referred to as the *compositional disorder*. Additional site disorder brought about by the variation in the population of antisite atoms on Ni and Al sub-lattices in an alloy of given composition due to preparation technique (as-prepared state) will be simply termed as the *site disorder*.

Existence of well-defined Ni and Al sub-lattices in an ordered Ni_xAl_{100-x} alloy gives rise to the superstructure Bragg peaks corresponding to the reflections (110), (210), (211), (300), (310), ..., besides the fundamental Bragg reflections (111), (200), (220), (222), (311), … that are characteristic of the f.c.c. structure. The ratio of the integrated intensities of the superstructure and fundamental Bragg peaks is a direct measure [16] of the atomic order (or disorder) present in a given alloy. The comparison between the observed and generated XRD spectra in Fig. 3.2(a) brings out the following features. Except for the appearance of the (110) reflection in the sample *ap-*$Ni_{74.8}$ presumably due to the texture effects, the superstructure Bragg peaks are completely absent. A complete absence of the superstructure Bragg peaks reflects a large population of antisite atoms on Ni and Al sub-lattices and hence the presence of a substantial amount of site disorder in all the samples. Alternatively, this observation implies that Ni and Al atoms occupy the Ni or Al sub-lattice sites with equal probability with the result that a distinction between the two sub-lattices disappears. The XRD linewidths are considerably broad compared to those in the ordered stoichiometric compound. The extra broadening possibly originates from a large local internal strain at the grain boundaries and / or local compositional inhomogeneity / site disorder. For a given Bragg peak, the

linewidth decreases as the Ni concentration increases. This observation is consistent with the expected progressive enhancement in the compositional disorder as the critical concentration [16] $x_c \approx 73.5$ at.% is approached from above. The analysis of the observed XRD patterns reveals that the lattice parameter '*a*' decreases linearly with increasing Ni concentration (Fig.3.2(b)) much the same way as that reported previously [17] on well-ordered Ni_xAl_{100-x} alloys. The finding that the functional form of $a(x)$ is the same for site-disordered and ordered Ni_xAl_{100-x} alloys asserts that site disorder has essentially no effect on the lattice parameter and that the observed variation of '*a*' with *x* is solely governed by the compositional disorder.

3.4 Theoretical considerations

In this section a brief introduction is given to the theoretical formalism which deals with the spin wave and spin fluctuation contribution to the electrical resistivity and magnetoresistance and suppression of these collective excitations by magnetic field. With a view to resolve the controversial issues concerning the electrical and galvanomagnetic transport in weakly ferromagnetic metals detailed in the introduction section, a quantitative comparison between theory (whose details are furnished in reference 8) and experiment is made in the next section. To facilitate unraveling the physical phenomena that are responsible for our main observations from such a comparison, we provide here a brief summary of the *self-consistent* calculation [8] of spin-wave and exchange-enhanced spin-density fluctuation contributions to the electrical resistivity of weak itinerant-electron ferromagnets in the absence and presence of the external magnetic field. This calculation makes use of the two-band (*s*- and *d*-band) model and the version of spin-fluctuation theory for *d*-band that employs the Ginzburg-Landau formalism. The scattering

of conduction (*s*) electrons by the spin density fluctuations of the d-electrons via the *s-d* exchange interaction yields the following expression [8] for the electrical resistivity

$$\rho(T) = \frac{3}{4}\left(\frac{m}{ne^2}\right)\Im_{s-d}^2\left(\frac{E_F^s}{\hbar}\right)N(E_F^s)\,N(E_F^d)\left(\frac{k_F^d}{k_F^s}\right)^4\left(\frac{E_F^d}{E_F^s}\right)r(T) \tag{3.1}$$

with

$$r(T) = \frac{1}{T}\int_0^{2k_F^s/k_F^d} dq\, q^3 \int_{-\infty}^{\infty} d\omega\, \omega\, n(\omega)\left[n(\omega)+1\right]\mathrm{Im}\,\chi_r(q,\omega) \tag{3.2}$$

$$n(\omega) = \left[\exp(\omega/T)-1\right]^{-1} \tag{3.3}$$

$$\chi_r(q,\omega) = \left[\chi_{\|}(q,\omega) + 2\,\chi_{\perp}(q,\omega)\right]/3 \tag{3.4}$$

In the above expressions, m and n are the effective mass and number density of the s-electrons, respectively, E_F^s (E_F^d) is the Fermi energy of the s (d)-band measured from the bottom of the band, k_F^s (k_F^d) and $N(E_F^s)$ $(N(E_F^d))$ respectively are the Fermi wavevector and the density of states at the Fermi energy per spin per atom of the s (d)-band, $\Im_{s-d}$ is the *s-d* exchange coupling constant, $n(\omega)$ is the Bose function, $\chi_{\|}(q,\omega)$ and $\chi_{\perp}(q,\omega)$ are the *dynamical wavevector-dependent* longitudinal and transverse susceptibilities [19]. As elucidated below, spin waves and exchange-enhanced spin-density fluctuations give dominant contributions to electrical resistivity, $\rho(T)$, and magneto-resistance (MR) in different temperature ranges so that the calculation of $\rho(T)$ and MR basically boils down to inserting the relevant expressions [19] for the reduced dynamical wavevector-dependent susceptibility, $\chi_r(q,\omega)$, in Eq.(3.2).

3.4.1 Low temperatures

At T = 0, the energy dispersion, $E(q)$, of magnetic excitations in a weakly ferromagnetic metal reveals that (i) in a small region around $q = 0$ in the Brillouin zone, the bound states for electron-hole pairs, representing spin-wave excitations, have lower energy and are separated by an energy gap from the energy continuum, corresponding to the Stoner single-particle spin-flip excitations, and (ii) this energy gap reduces as q increases such that beyond a certain threshold value of $q = q_0$, the spin-wave dispersion curve enters the Stoner excitation continuum with the result that *propagating transverse* spin fluctuations (spin waves) get damped. For $q > q_0$, the magnetic excitations in the continuum are the overdamped (*non-propagating*) modes of exchange-enhanced longitudinal and transverse spin-density fluctuations. Since spin-wave modes of larger and larger q are excited as the temperature is raised from T = 0, the transition at $q = q_0$ from well-defined spin waves to *non-propagating* exchange-enhanced *transverse* spin fluctuations manifests itself at a certain finite value of temperature in the measurement of $\rho(T)$ and MR. By contrast, the thermally-excited *non-propagating* exchange-enhanced *longitudinal* spin-density fluctuations persist down to $q = 0$ and coexist with, but are swamped by, spin waves for $q \le q_0$.

At low temperatures ($T << T_C$), the main contribution to $\rho(T)$ arises from long-wavelength $(q \le q_0)$ low-frequency spin wave (*SW*) modes. This contribution is obtained by inserting the following expression [19] for $\mathrm{Im}\,\chi_r(q,\omega)$ in Eq.(3.2) and then evaluating the integrals:

$$\mathrm{Im}\,\chi_r(q,\omega) = 2\,\mathrm{Im}\,\chi_\perp(q,\omega)/3 \tag{3.5}$$

with

$$\mathrm{Im}\,\chi_{\perp}(q,\omega) = (\pi/2)\,\omega\,\chi_{\perp}(q)\left[\delta(\omega-\omega(q)) + \delta(\omega+\omega(q))\right] \tag{3.6}$$

and the spin-wave propagation frequency $\omega(q)$ given by [8, 19]

$$\hbar\omega(q) = g\,\mu_B\,M(T,H)\;\chi_{\perp}^{-1}(q) = g\,\mu_B\,M(T,H)\,(\chi_{\perp}^{-1}(0) + c_{\perp}\,q^2 + ...)$$

$$= g\,\mu_B\,H + D(T,H)\;q^2 + ... \tag{3.7}$$

where $\chi_{\perp}^{-1} = H/M(T,H)$, the *effective* field H is the external magnetic field, H_{ext}, corrected for the demagnetizing field, H_{dem}, and other anisotropy fields, H_A, i.e., $H = H_{ext} - H_{dem} + H_A = H_{ext} - 4\pi\,N\,M(T,H_{ext}) + H_A$, N is the demagnetizing factor, g is the Landé splitting factor, and $D(T,H) = g\,\mu_B\,M(T,H)\,c_{\perp}$ is the spin-wave stiffness. Combining Eqs.(3.2), (3.3), (3.5) – (3.7) yields finally the following expressions [8] for the spin-wave contributions to the 'zero-field' resistivity, $\rho_{SW}(T,H=0)$, and magnetoresistance, $(\Delta\rho/\rho)_{SW}$, at low temperatures

$$\rho_{SW}(T,H=0) = \frac{\pi}{3}\,\rho_0\,\Gamma(3)\,\zeta(2)\left(\frac{g\mu_B M}{\hbar}\right)\left(\frac{k_B T}{D}\right)^2 \tag{3.8}$$

with

$$\rho_0 = \frac{3}{4}\left(\frac{m}{ne^2}\right)\,\Im_{s-d}^2\;\;N(E_F^d)\;N(E_F^s)\;(k_F^s)^{-4} \tag{3.9}$$

and

$$\left(\frac{\Delta\rho}{\rho}\right)_{SW} = \frac{\rho_{SW}(T,H)}{\rho_{SW}(T,H=0)} - 1$$
$$= \left[\Gamma(3)\zeta(2)\right]^{-1}\left[h\,\ln(e^h - 1) + 2\sum_{n=1}^{\infty}\frac{(-1)^n\,(e^h-1)^n}{n^2}\right] \qquad (3.10)$$

for $(e^h - 1) < 1$, where the *reduced field*, $h = (g\,\mu_B\,H/k_BT)$. In order to make the variations of $(\Delta\rho/\rho)_{SW}$ with *h* more transparent, the $(e^h - 1)$ term, appearing in Eq.(3.10), is *approximated* by *h* for $h << 1$ and only the first two (leading) terms in the sum over *n* are retained, with the result that

$$\left(\frac{\Delta\rho}{\rho}\right)_{SW} \cong 0.304\left[\,h\,\ln h - 2\,h + \frac{1}{2}\,h^2\,\right] \qquad (3.11)$$

3.4.2 Intermediate temperatures

At intermediate temperatures, which lie well below T_C, the spin-fluctuation contribution to resistivity or magnetoresistance becomes more important than the spin- wave contribution. For temperatures below T_C, the longitudinal and transverse spin- fluctuation contributions to resistivity, and hence to magnetoresistance, have to be treated differently since the imaginary part of the dynamical wavevector-dependent spin susceptibility has different lower bounds $(q_\perp = q_0,\ \omega = 0)$ and $(q_\parallel = 0,\ \omega = 0)$ in the (q,ω)- plane for the transverse and longitudinal spin fluctuations. This theoretical approach leads to the result [8]

$$\rho_\perp(T,H) = \frac{2\pi^2}{9}\,\gamma_\perp\left(\frac{\rho_0}{q_0}\right)\left(\frac{k_B\,T}{\hbar\,\Gamma_\perp}\right)^2$$
$$\left\{\left(\frac{q_0}{\kappa_\perp}\right)\left[\frac{\pi}{2} - \tan^{-1}\left(\frac{q_0}{\kappa_\perp}\right) + \frac{(q_0/\kappa_\perp)}{1+(q_0/\kappa_\perp)^2}\right]\right\} \qquad (3.12)$$

and

$$\rho_{\parallel}(T,H) = \frac{\pi^3}{18}\,\gamma_{\parallel}\left(\frac{\rho_0}{q_0}\right)\left(\frac{k_B\,T}{\hbar\,\Gamma_{\parallel}}\right)^2\left\{\frac{q_0}{\kappa_{\parallel}}\right\} \tag{3.13}$$

In the above expressions, the field dependence basically originates from the inverse spin correlation length κ_ν (where the subscript ν denotes the transverse $\perp$ or longitudinal $\parallel$ case) which is related to the temperature- and field-dependent transverse (longitudinal) susceptibility $\chi_\perp = M/H$ ($\chi_{\parallel} = \partial M/\partial H$) as $\kappa_\nu^2 = [c_\nu\,\chi_\nu]^{-1}$. Using the expressions

$$\chi_\perp^{-1}(T,H) = \frac{H}{M} = A + b\,M^2 = b\,(M^2 - M_0^2) \tag{3.14}$$

$$\chi_\perp^{-1}(T,H=0) = 0 \tag{3.15}$$

$$\chi_{\parallel}^{-1}(T,H) = \frac{\partial H}{\partial M} = A + 3\,b\,M^2 = b\,(3\,M^2 - M_0^2) \tag{3.16}$$

$$\chi_{\parallel}^{-1}(T,H=0) = 2\,b\,M_0^2 \tag{3.17}$$

For $\chi_{\parallel}$ and $\chi_\perp$ (where the spontaneous magnetization, $M_0 \equiv M(T,H=0) = (-A(T)/b)^{1/2}$ and 'in-field' magnetization, $M \equiv M(T,H)$) that are *consistent* with the *magnetic equation of state* $H = A\,M(T,H) + b\,[M(T,H)]^3$ (the detailed expressions for the coefficients $A(T)$ and b are given in reference [19]) in Eqs. (3.12) and (3.13), we finally

arrive at the following expressions [8] for the total spin-fluctuation (SF) contributions to magnetoresistance and 'zero-field' resistivity

$$\left(\frac{\Delta\rho}{\rho}\right)_{SF} = \frac{\rho(T,H)}{\rho(T,H=0)} - 1 = \left[\frac{\pi}{2\sqrt{2}}\sqrt{\frac{c}{b}}\,M_0^{-1} + \frac{2}{q_0}\right]^{-1} \left[\frac{\pi}{2}\sqrt{\frac{c}{b}}\,\frac{1}{\sqrt{3M^2 - M_0^2}} + \frac{2}{q_0}\left\{x\left(\frac{\pi}{2} - \tan^{-1}x + \frac{x}{1+x^2}\right)\right\}\right] - 1 \tag{3.18}$$

with

$$x = \frac{q_0}{\kappa_\perp} = q_0\sqrt{\frac{c}{b}}\,\frac{1}{\sqrt{M^2 - M_0^2}} \tag{3.19}$$

and

$$\rho(T,H=0) = \rho_{\parallel}(T,H=0) + \rho_{\perp}(T,H=0) = \frac{\pi^2}{9}\,\rho_0\,\gamma\left(\frac{k_B T}{\hbar\Gamma}\right)^2\left[\frac{\pi}{2\sqrt{2}}\sqrt{\frac{c}{b}}\,\frac{1}{M_0} + \frac{2}{q_0}\right] \tag{3.20}$$

In order to bring out the field dependence of magnetoresistance clearly and thereby facilitate a direct comparison with the experiments, we make use of the experimental result that the quantity $(q_0/\kappa_\perp)$ is *greater* than unity for weak itinerant-electron ferromagnets. Expanding the function $\tan^{-1}(x)$ in Eq.(3.12) in powers of $(1/x)$, retaining the terms up to x^{-7} only and using Eq.(3.14), the expressions (3.20) and (3.18) finally assume the form

$$\rho_{SF}(T,H=0) = \frac{\pi^2}{9}\,\rho_0\,\gamma\left(\frac{k_B T}{\hbar\Gamma}\right)^2\left[\frac{\pi}{2\sqrt{2}}\sqrt{\frac{c}{b}}\,\frac{1}{M_0} + \frac{4}{q_0}\right] \tag{3.21}$$

and the magnetoresistance at *low* and *intermediate* temperatures assumes the form

$$\left(\frac{\Delta\rho}{\rho}\right)_{SF} = \frac{\rho_{SF}(T,H)}{\rho_{SF}(T,H=0)} - 1 = \left[\frac{\pi}{2\sqrt{2}}\sqrt{\frac{c}{b}}\,M_0^{-1} + \frac{4}{q_0}\right]^{-1}\left[\frac{\pi}{2}\sqrt{\frac{c}{b}}\left(3M^2 - M_0^2\right)^{-1/2}\right.$$

$$\left. + \frac{4}{q_0}\left(1 - \frac{2}{3a}\left[b\,(M^2 - M_0^2)\right] + \frac{3}{5a^2}\left[b^2\,(M^2 - M_0^2)^2\right]\right)\right] - 1 \qquad (3.22)$$

3.4.3 Temperatures around T_C but outside the critical region

At temperatures just outside the critical region but on either side of the Curie point, T_C, (henceforth referred to as 'for temperatures close to T_C', for brevity), an analytical solution is possible only when the *classical approximation* is used. In this approximation, the spin fluctuation cut-off wavevector q_c is chosen such that the spatially varying local magnetization, $m(r)$, is *classical*, which, in turn, implies that each local spin-density mode $m_\nu(q)$ for $q < q_c$ is thermally excited such that the part of the integrand in Eq. (3.2) involving the Bose function $n(\omega)$, i.e., $n(\omega)[n(\omega)+1]$ can be approximated by $(T/\omega)^2 - (1/12)$ for those values of ω for which $\mathrm{Im}\,\chi_r(q,\omega)$ makes an appreciable contribution to the integral over ω in Eq.(3.2). Taking into account the functional dependences of the cut-off wavevector q_c on temperature and field, the spin fluctuation contributions to the 'in-field' and 'zero-field' resistivity are given by [8]

$$\rho_{SF}(T,H) = \frac{\pi}{2}\,\eta\,\rho_0\,\gamma\left(\frac{k_B T}{\hbar\Gamma}\right)^{5/3}\left[1 - \alpha\left\{b\left(3M^2 - M_0^2\right) + 2\left(\frac{H}{M}\right)\right\}\right.$$

$$+ \beta \left\{ b^2 \left(3 M^2 - M_0^2\right)^2 + 2 \left(\frac{H}{M}\right)^2 \right\} \Bigg] \tag{3.23}$$

$$\rho_{SF}(T, H = 0) = \frac{\pi}{2} \eta \ \rho_0 \ \gamma \left(\frac{k_B T}{\hbar \Gamma}\right)^{5/3} \left[1 - 2 \alpha \ b \ M_0^2 + 4 \beta \ b^2 \ M_0^4\right] \tag{3.24}$$

$$\eta = 1 - \frac{1}{15\pi} + \frac{1}{48} \tag{3.25}$$

$$\alpha = \frac{1}{27 \ \eta \ c} \left(25 - \frac{1}{\pi}\right) \left(\frac{\hbar \Gamma}{k_B T}\right)^{2/3} \tag{3.26}$$

$$\beta = \frac{1}{81 \ \eta \ c^2} \left(\frac{337}{4} - \frac{2}{\pi}\right) \left(\frac{\hbar \Gamma}{k_B T}\right)^{4/3} \tag{3.27}$$

A simplified expression for the spin fluctuation contribution to magnetoresistance, given below, is obtained when, in accordance with Eq.(3.14), (H / M) in Eq.(23) is set *equal to* $b\,(M^2 - M_0^2)$.

$$\left(\frac{\Delta\rho}{\rho}\right)_{SF} = \frac{\rho_{SF}(T, H)}{\rho_{SF}(T, H = 0)} - 1$$

$$= \frac{1 - \psi[(3M^2 - M_0^2) + 2(M^2 - M_0^2)] + \phi[(3M^2 - M_0^2)^2 + 2(M^2 - M_0^2)^2]}{1 - 2 \ \psi \ M_0^2 + 4 \phi \ M_0^4} - 1 \tag{3.28}$$

where $\psi = \alpha b$ and $\phi = \beta b^2$.

The detailed definitions of various quantities appearing in equations (3.1) – (3.28), are furnished in reference [8].

The above-mentioned parameters are specific to a given weakly ferromagnetic metal and hence they will sensitively depend on the Ni concentration, *x*, in the present case. Another important point to note is that with increasing compositional disorder or increasing external pressure (i.e., as $x \to x_c$ or $p \to p_c$), $T_C \to 0$ and the energy gap at $q = 0$ between the Stoner energy continuum and the bound states, representing spin-wave excitations, narrows down tremendously so much so that the spin-wave dispersion region near $q = 0$ in the Brillouin zone progressively shrinks to an extremely small size. Consequently, near $x = x_c$, the spin-wave dispersion curve enters the Stoner excitation continuum at $q_0 \approx 0$ and a transformation from the *propagating transverse* spin fluctuations (spin waves) to overdamped (*non-propagating*) modes of exchange-enhanced longitudinal and transverse spin-density fluctuations occurs as soon as q exceeds $q_0 \approx 0$. Thus, strong departures from the spin wave behavior are expected at low temperatures as *x* nears x_c. Though the theoretical calculations detailed in reference 8 do not explicitly take into account the effect of site disorder, site disorder is expected to enhance the above-stated effect of compositional disorder.

3.5 Electrical resistivity and magnetoresistance: Temperature and magnetic field dependence

With a view to resolve the controversial issues concerning the electrical and galvanomagnetic transport in weakly ferromagnetic metals detailed in the introduction section, a quantitative comparison between theory [8] and

experiment is made in this section. To facilitate such a comparison, we quoted the relevant results of the *self-consistent* calculation [8] of spin-wave and exchange-enhanced spin-density fluctuation contributions to the electrical resistivity, $\rho(T)$, and magnetoresistance (MR) of weak itinerant-electron ferromagnets, in the preceding section.

Electrical resistivity, $\rho(T)$, is plotted against temperature from 1.7 *K* to 300 *K* in figure 3.3. The inset of figure 3.3 displays the temperature variation of the temperature derivative of resistivity, $d\rho(T)/dT$. $d\rho(T)/dT$ goes through a peak (two peaks) at a temperature, $T = T_{peak}$, for the alloys with $x = 76.1$, 75.1 and 74.8 *at. %* ($x = 74.3$ *at.*%). Identifying T_{peak} with the Curie temperature, T_C, yields the values of T_C for different compositions given in table 3.1. Consistent with the EDAX results, in the case of *ap-*$Ni_{74.3}$ sample alone,

Table 3.1: Actual composition, Curie temperature, resistivity values at 1.7 K and 300 K, and residual resistivity ratio (RRR).

Sample Label	Actual Ni (at.%)	T_C (K)		ρ(1.7 K) (μΩ - cm)	ρ(300 K) (μΩ - cm)	RRR= ρ(300K) / ρ(1.7 K)
		ρ(T)	$\Delta\rho_{\|\|}$(T)/ ρ(T)			
ap-$Ni_{74.3}$	74.26(9)	41(1); 48.5(9)	41(1); 48(2)	7.62	41.30	5.42
ap-$Ni_{74.8}$	74.82(8)	59(1)	60(1)	9.11	44.89	4.93
ap-$Ni_{75.1}$	75.08(8)	55.5(8)	55(1)	6.83	45.24	6.62
an-$Ni_{75.1}$	75.08(8)	56.1(9)	56(1)	7.08	51.97	7.34
ap-$Ni_{76.1}$	76.13(5)	71(1)	70(1)	14.80	70.68	4.77

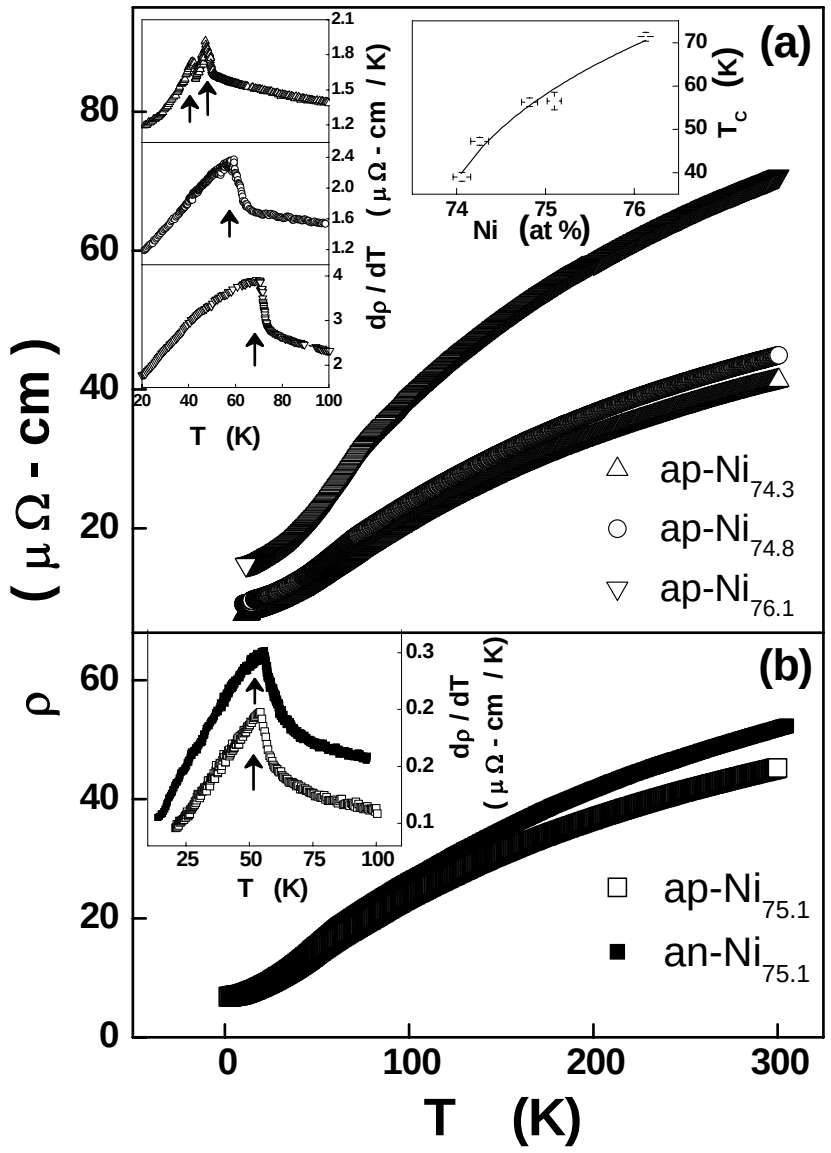

Figure 3.3: Electrical resistivity, ρ, as a function of temperature from 1.7 K to 300 K. Insets show the temperature derivative of resistivity, $d\rho/dT$, plotted against temperature. The arrows indicate approximate locations of the peak temperature, which is identified with the Curie temperature, T_C Top right insert highlights the Ni concentration dependence of T_C.

presence of a minor second crystalline phase with Ni concentration $x = 74.06(5)$ (table 3.1) is reflected in a satellite peak at $T_C = 41K$ in $d\rho(T)/dT$ (top inset of figure 3.3(a)); the main peak at $T_C = 48K$ corresponds to the major crystalline phase with $x = 74.3\ at.\%$. Residual resistivity ratio, $\rho(300K)/\rho(1.7K)$, (RRR) and residual resistivity at 1.7 K, $\rho(0)$, as functions of Ni concentration are displayed in table 3.1 and figure 3.4.

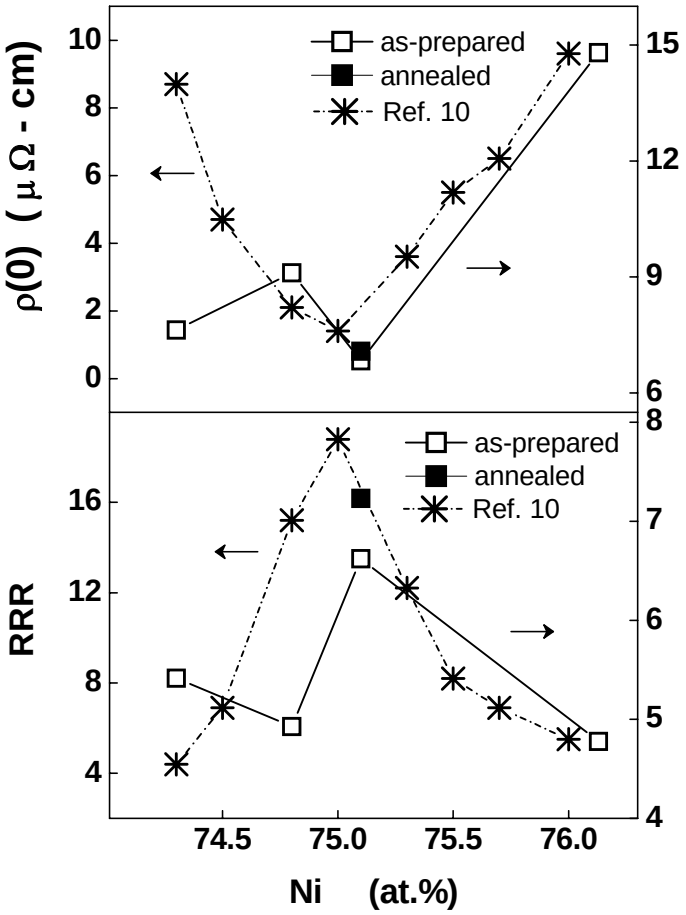

Figure 3.4: Variation of the residual resistivity, $\rho(0)$, and residual resistivity ratio (RRR) with Ni concentration. The corresponding data on well-ordered samples, previously reported in reference [10], are also included for comparison.

Of all the 'as-prepared' (*ap*-) samples, the sample of stoichiometric composition ($x = 75.1\,at.\%$) has the lowest (highest) residual resistivity (RRR). Annealing the *ap-*$Ni_{75.1}$ sample at 520 ^{o}C for 16 days, improves the atomic order from 75 % to nearly [16] 85 %, leaves the residual resistivity essentially unaltered but increases the RRR appreciably. A much lower annealing temperature, T_A = 520 ^{o}C (as against $T_A = 1150$ ^{o}C, used in the literature [10] to achieve $\approx 100\%$ atomic order), was chosen to avoid a significant loss of Al in the alloy during annealing so that no shift in the composition occurs and a comparison between the physical properties of the 'as-prepared' and 'annealed' samples brings out clearly the role of site disorder. Comparison with the data reported by Fluitman et al. [10] on *completely-ordered* samples in the alloy

series Ni_xAl_{100-x} (note the widely different sensitivities of the ordinate scales for different sets of data in figure 3.4), indicates that the as-prepared samples in the present study have considerable amount of site-disorder. The variations of longitudinal magnetoresistance, $\Delta\rho_{\|}(T,H)/\rho(T,H=0)$, with temperature at various fixed values of the external magnetic field, *H*, in the temperature interval $3K \le T \le 200K$, are shown in figure 3.5. Magnetoresistance (MR) is *negative* in the entire temperature range extending from 3 *K* to 300 *K* and goes through a *maximum* as a function of temperature at $T = T_{\max}$. The values of $T_{\max}$ are also tabulated in table 3.1. For a given alloy composition, $T_{\max} \cong T_C$.

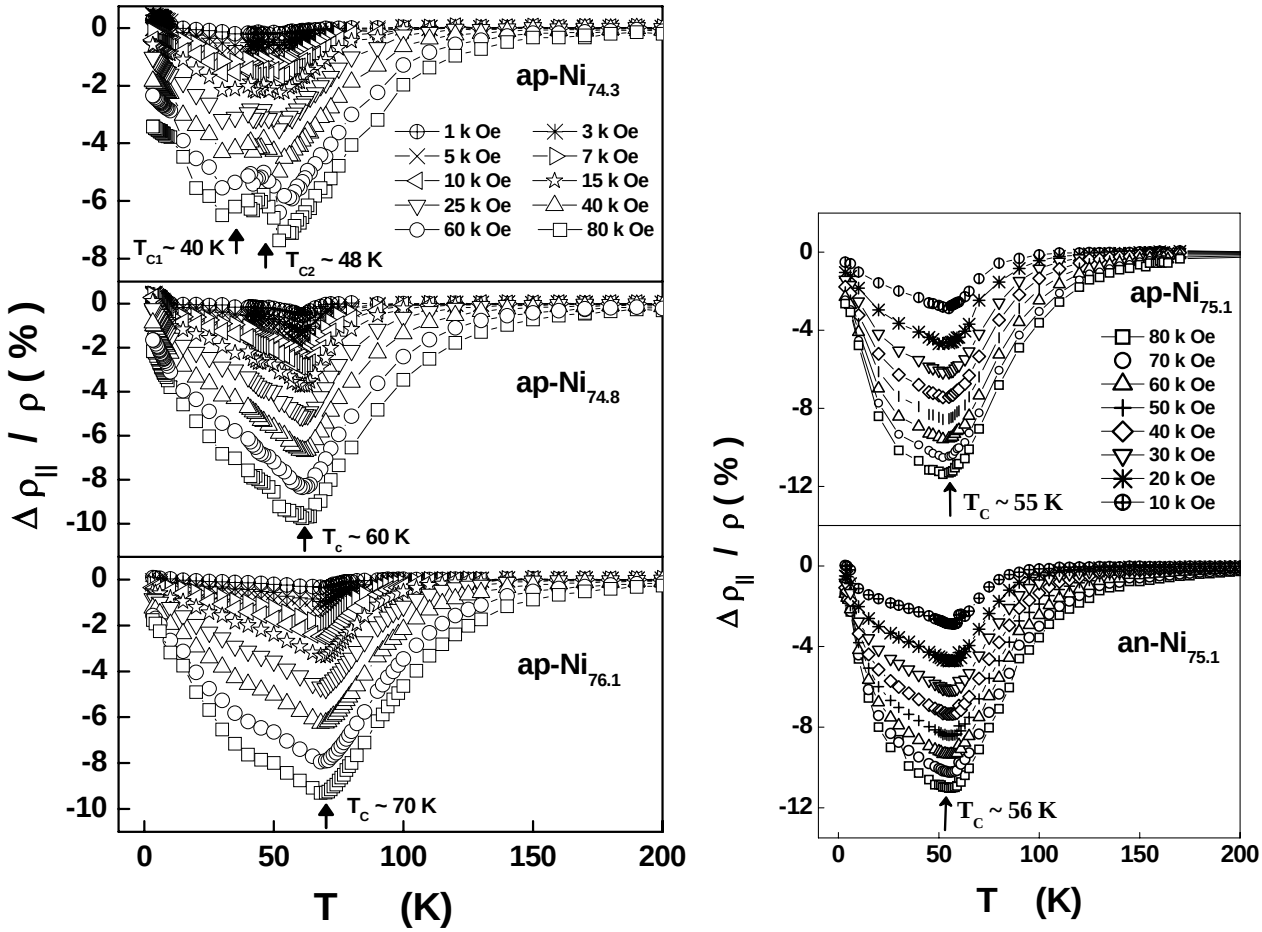

Figure 3.5: Longitudinal magnetoresistance, $\Delta\rho_{\|}/\rho$, as a function of temperature at fixed values of the external magnetic field. The arrows indicate the approximate location of the Curie temperature, T_C, where $\Delta\rho_{\|}(T,H)/\rho(T,H=0)$ goes through a dip at low fields.

3.5.1 Low temperatures ($T << T_C$)

Figure 3.6 clearly demonstrates that at low temperatures $1.7\ K \le T \le T_x$ (where T_x depends on the Ni concentration, *x*), electrical resistivity varies with temperature as $\rho(T) \sim T^n$ with *n* = 1.50(1), 1.66(1) and 1.64(3) for the samples *ap-Ni*$_{74.3}$, *ap-Ni*$_{74.8}$ and *ap-Ni*$_{75.1,}$ respectively (Fig.3.5). These samples exhibit a *strong departure* from the *Fermi liquid behavior* at low temperatures in that the above values of the exponent '*n*' are significantly different from that ($n = 2$)

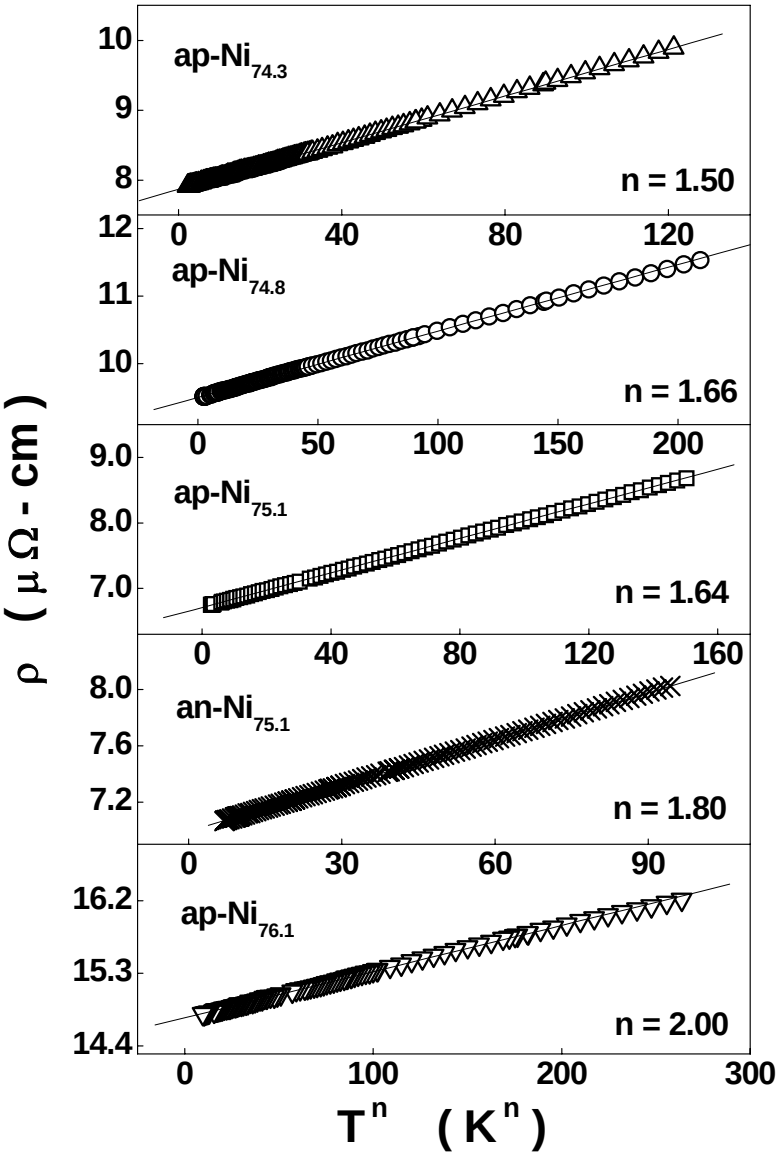

Figure 3.6: Non-Fermi (Fermi) liquid behavior of resistivity at low temperatures in ap-Ni$_{74.3}$*, ap-Ni*$_{74.8}$*, ap-Ni*$_{75.1}$ *and an-Ni*$_{75.1}$ *(ap-Ni*$_{76.}$*).*

predicted by the Fermi liquid theory. By contrast, $\rho(T)$ in the *ap-Ni*$_{76.1}$ follows the T^2 law (the Fermi liquid behavior) over a narrow temperature range $1.7\,K \le T \le 16\,K$. As the critical concentration [16] $x_c \cong 73.5$ at.% (site-disorder reduces the critical concentration from $x_c \cong 74.5$ at.% to $x_c \cong 73.5$ at.%, see below) is approached from above, the *deviations* from the Fermi liquid behavior become *more prominent* and the temperature range [$1.7\ K \le T \le T_x$ with $T_x = 25\,K$ ($T_x = 21K$) for *ap-Ni*$_{74.3}$ and *ap-Ni*$_{74.8}$ (*ap-Ni*$_{75.1}$)] over which the non-Fermi liquid behavior persists *widens*. The values of the exponent *n* and coefficient $A_n(0) \equiv A_n(H=0)$ are determined by the 'range-of-fit' analysis, in which the values of the parameters $\rho(0) \equiv \rho(T=0, H=0)$, $A_n(0)$ and n are monitored as the temperature range of the fit (based on the expression $\rho(T, H=0) = \rho(T=0, H=0) + A_n(H=0)\,T^n$) is varied. The values of $\rho(0)$, $A_n(0)$ and n, so determined over the specified temperature ranges, are given in table 3.2. At this stage, it is interesting to note the following observations. (a) The $T^{1.65}$ variation of $\rho(T)$ at $T \le 7\,K$ and ambient pressure has also been reported [20] in single crystals of Ni_3Al. (b) The value of the exponent '*n*' falls below [21] *n* = 2 and goes on decreasing continuously, when the upper bound T_m of the temperature interval $0.05\,K \le T \le T_m$, at a given external pressure in the range $32\,kbar \le p \le 99\,kbar$, is increased from 1 *K* to 5 *K* or when at a fixed value of T_m, the external pressure is increased from 32 *kbar* to 99 *kbar*. The presently determined values of the ratio $A_n(0)/\rho(0)$ and the exponent *n* for different Ni concentrations, *x*, are compared in figure 3.7 with those reported earlier [10] for similar compositions. The quantities $A_n(0,x)/\rho(0,x)$ and *n(x)* exhibit the same trend in the present case as that observed previously [10]; however, our values for $A_n(0,x)/\rho(0,x)$ are lower by nearly a factor of two, particularly for *x* close to

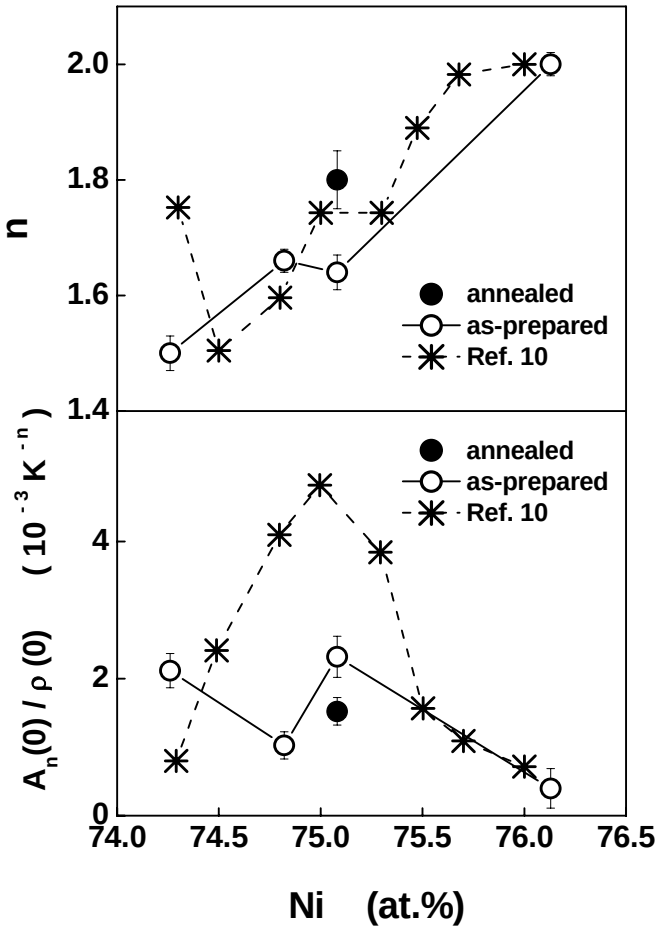

Figure 3.7: The variations of the exponent 'n' and the ratio $A_n(0)/\rho(0)$ *with Ni concentration at low temperatures. The corresponding data on well-ordered samples, previously reported in reference 10, are also included for comparison.*

the stoichiometric composition. Considering that the samples used in the reference 10 had been subjected to prolonged annealing at elevated temperatures so as to ensure complete atomic ordering in them, the reduced $A_n(0,x)/\rho(0,x)$ (or RRR) in our 'as-prepared' samples can be attributed to a high degree of site disorder present in them. The exponent '*n*' increases from *n* = 1.64(3) to 1.80(5) when the *ap-Ni*$_{75.1}$ sample is annealed. An excellent agreement between the value *n* = 1.80(5) for the annealed (ordered) *Ni*$_{75.1}$ and that [10] (*n* = 1.75) for the completely ordered Ni_3Al compound leads to the obvious conclusion that site disorder tends to enhance the deviations from the Fermi liquid behavior at the stoichiometric composition. Fluitman et al. [10]

report the critical nickel concentration x_c for the onset of long-range ferromagnetic order as $x_c = 74.6\ at.\%$, which is well above $x_c = 73.5\ at.\%$ obtained in the present case when the $T_C(x)$ data are fitted to the simple power law $T_C(x) = t_p\ (x - x_c)^p$ with $p = 0.33$, where T_C is the ferromagnetic-to-paramagnetic transition (Curie) temperature (inset of Fig. 3.3) for a given composition *x*. The site disorder thus lowers the critical Ni concentration.

From a close comparison of the non-Fermi liquid behavior in the single crystals, completely-ordered and site-disordered polycrystalline samples with *Ni* concentration close to the critical concentration x_c, we infer that the effect of site disorder is (i) to make the non-Fermi liquid behavior more prominent particularly in the stoichiometric composition by increasing the extent of deviation of the exponent '*n*' from the value *n* = 2 and (ii) to stabilize the non-Fermi liquid behavior in any given composition over a much wider temperature range.

Before discussing the present results in the light of the existing theories, the following remarks about a comparison between theory and experiment are in order. For $x \cong x_c$ (or equivalently, externally applied pressures, *p*, in the immediate vicinity of the critical pressure [21], p_c), $T_C \approx 0$ so that at ultra low temperatures, the conditions same as those for temperatures close to T_C prevail. Thus, by predicting the variation $\rho(T) \sim T^{5/3}$ at temperatures $T \approx T_C$, the theoretical treatment [8] outlined in the previous section, like the self-consistently renormalized (SCR) spin fluctuation theory [4] of Ueda and Moriya, adequately describes the non-Fermi liquid behavior observed for concentrations $x \cong x_c$ (figures 3.6 and 3.7) or pressures $p \cong p_c$ [21]. For $x > x_c$

or $p < p_c$, T_C has an appreciable magnitude and these theories [4,8] predict a T^2 variation of resistivity at low (intermediate) temperatures arising from the scattering of conduction electrons from *propagating transverse* spin fluctuations, i.e., spin waves, SW (exchange-enhanced longitudinal and transverse spin fluctuations). The electron-electron (EE) scattering too gives rise to the T^2 variation of resistivity at low temperatures but, unlike the SW scattering, the EE scattering is *insensitive* to *H*. A T^2 dependence of $\rho(T)$ (which could be attributed to either EE or SW scattering mechanism) has been observed in a Ni_3Al single crystal [21] at low temperatures $0.05\,K \le T \le 1K$ and low pressures $p << p_c$ and presently in *ap-*$Ni_{76.1}$ (Fig.3.6) at ambient pressure and temperatures $1.7\,K \le T \le 16\,K$. However, the theoretically predicted [4,8] T^2 variation of $\rho(T)$ at low temperatures (basically originating from the spin wave dispersion which is *quadratic* in the wavevector *q*, Eq.(3.7)) is *at variance* with the observed values 1.5 – 1.66 of the exponent '*n*' in the Ni concentration range $x_c < x \le 75.1\,at.\%$ (Figs. 3.6 and 3.7). In view of the above remarks, the non-Fermi liquid behavior observed at low temperatures when *x* falls below $76.1\,at.\%$ (Fig.3.7), most likely, reflects that the increased compositional disorder (or increased external pressure) as the critical concentration, x_c (critical pressure, p_c) is approached from above (below) alters the spin-wave dispersion at *finite q* such that as *q* increases from $q = 0$, the SW dispersion becomes increasingly similar to the spin-fluctuation dispersion prevalent at temperatures close to T_C.

The above proposition provides the following explanation for the monotonous reduction in the exponent '*n*' from $n = 2$ to $n = 1.66$ observed [21] in Ni_3Al when the upper bound, T_m, of the temperature range $0.05\,K \le T \le T_m$

increases from 1 *K* to 5 *K*. At sub-Kelvin temperatures, only long-wavelength ($q \approx 0$) spin wave modes get excited. In the long-wavelength ($q \to 0$) limit, the SW dispersion is quadratic in *q* and hence it is not surprising that $n = 2$ in the temperature range $0.05K \le T \le 1K$. As the temperature increases above 1 *K*, SW modes of larger and larger *q* (compared to $q = 0$) get thermally excited with the result that the modified SW dispersion at such q values causes *n* to decline from the value $n = 2$. Magnetic field introduces a gap ($E_g = g\,\mu_B\,H_{eff}$; $H_{eff} = H - H_{dem} + H_A$) in the spin-wave energy spectrum (Eq.(3.7)) and enters the resistivity expression (Eq.(3.2)) via the Bose function (Eq.(3.3)). Creation of a gap makes it energetically more difficult to excite spin waves (or equivalently, at a given temperature, the spin-wave stiffness, *D*, increases

Table 3.2: Temperature ranges and the parameters values corresponding to the fits in the low temperature (spin wave) region, based on the relation $\rho(T) = \rho(0) + A_n(0)\ T^n$ and Eq. (3.29) of the text.

Sample Label	Temperature range (K)	ρ(0) (μΩ-cm)	n	$A_n(0)$ (nΩ - cm K^{-n})	$A_n^*(0)$ (nΩ - cm K^{-n})	a_λ (10^{-4} $Oe^{-\lambda}$)	λ
ap-$Ni_{74.3}$	1.7 – 24 (0.04 T_C – 0.5 T_C)	7.85(2)	1.50 (1)	16.6(6)	16.5(2)	3.9(5)	0.52 (2)
ap-$Ni_{74.8}$	1.7 – 25 (0.03 T_C – 0.42 T_C)	9.50(1)	1.66 (1)	9.74(6)	9.6(1)	2.8(3)	0.60 (3)
ap-$Ni_{75.1}$	1.7 – 21 (0.03 T_C – 0.38 T_C)	6.68(3)	1.64 (3)	15.5(5)	14.8(9)	2.4(4)	0.65 (5)
an-$Ni_{75.1}$	1.7 – 12.5 (0.03 T_C – 0.22 T_C)	7.00(1)	1.80 (5)	9.0(6)	8.3(3)	2.4(6)	0.65 (3)
ap-$Ni_{76.1}$	1.7 – 16.25 (0.02 T_C – 0.23 T_C)	14.73(3)	2.00 (2)	5.88(5)	5.80(9)	2.6(6)	0.80 (1)

steeply at low fields and tends to saturate at high fields in accordance with the relation $D(T,H) = g\,\mu_B\,M(T,H)\,c_\perp$; see section 3.4.1 for details [8,19]). Consequently, an increase in H progressively suppresses the SW scattering contribution, thereby reduces the resistivity and gives rise to *negative magnetoresistance*, in agreement with our observations (Fig.3.5). However, H does not alter the q-dependence in the SW dispersion relation and hence field has no effect on the temperature dependence of resistivity. This theoretical prediction [8] is clearly corroborated by the data, presented in figure 3.8, which are representative of all the compositions studied in this work. The coefficient $A_n(H)$ of the T^n term in the expression $\rho(T,H) = \rho(0,H) + A_n(H)\,T^n$ is calculated from the slope of the $\rho(T,H)$ versus T^n straight lines displayed in

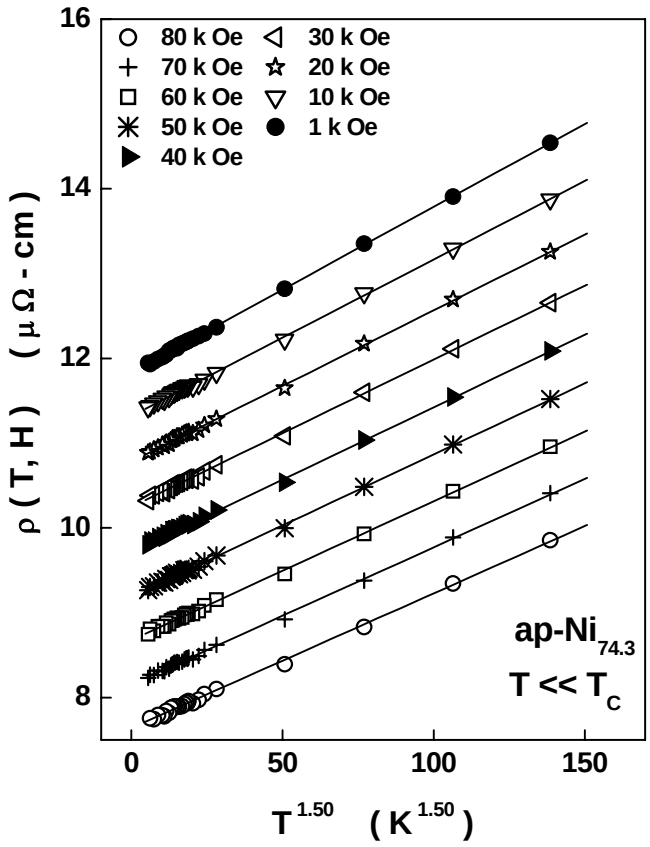

Figure 3.8: $T^{1.5}$ variation of $\rho(T,H)$ for the sample ap-$Ni_{74.3}$ at different fixed fields at low temperatures. For the sake of clarity, a constant upward shift of $0.5\,\mu\Omega - cm$ has been given to the successive $\rho(T,H)$ data starting from that taken at H = 80 kOe.

Fig. 3.8. That the functional dependence of A_n on H is accurately described by the empirical relation

$$A_n(H) = A_n^*(0)\ [1 - a_\lambda\ H^\lambda], \tag{3.29}$$

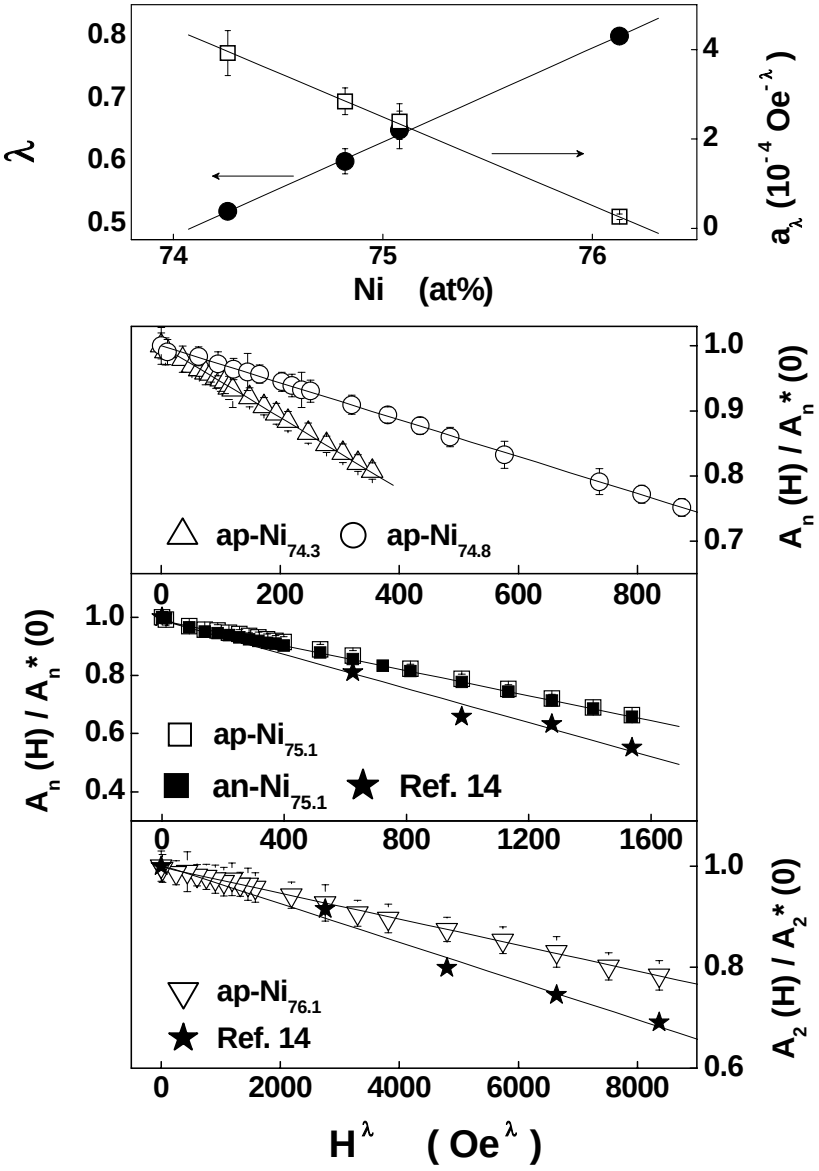

Figure 3.9: H^λ power law field dependence of the normalized coefficient, $A_n(H)/A_n^*(0)$, of the T^n term in the expression of resistivity at low temperatures. The corresponding data on well-ordered samples, previously reported in reference 14, are also included for comparison. Linear composition dependence of the exponent λ and coefficient a_λ of the magnetic field-dependent term in equation (3.29) of the text is shown in top panel.

is clearly borne out by the $A_n(H)/A_n^*(0)$ versus H^λ plots shown in figure 3.9 for all the samples . While $A_n(H)$ is a quantitative measure of the suppression of SW scattering at a given field strength over a specified temperature range (table 3.2) at low temperatures, the term $a_\lambda H^\lambda$ gives how such a suppression varies with *H*. The optimum values of $A_n^*(0)$, a_λ and the exponent λ obtained from these plots for various compositions are given in table 3.2. The values of $A_n^*(0)$, so obtained, are the same as those ($A_n(0)$) directly determined from the 'zero-field' resistivity, $\rho(T)$, data (cf. $A_n^*(0)$ and $A_n(0)$ listed in table 3.2). The $A_n(H)$ and $A_n(0)$ data with *n* = 2, reported by Yoshizawa et al. [14] on well-ordered samples of similar composition (*an-Ni*$_{75.1}$ and *an-Ni*$_{76.1}$), are plotted in Fig. 3.9 as $A_n(H)/A_n(0)$ versus H^λ, using the presently determined values of the exponent λ (which are found to be consistent with their data), so as to facilitate a direct comparison with our data. While comparing the two sets of data, proper allowance has to be made for the change in $A_n(H)$ and $A_n(0)$ with *n* (the exponent of the T^n term in the expressions for $\rho(T,H)$ and $\rho(T,H=0)$). Such a comparison reveals that at any specified field value, site disorder reduces the extent of suppression by field and this reduction in suppression (by site disorder) becomes more pronounced as *H* increases. Alternatively, for a *fixed* value of λ, *site disorder*, in a sample of given composition, *reduces* a_λ. The coefficient a_λ (exponent λ) decreases (increases) *linearly* with Ni concentration, as evidenced from figure 3.9.

Contrasted with the above empirical relation, i.e., Eq.(3.29), which quantifies the suppression of SW scattering at a *given field strength over a specified temperature range* at low temperatures, the self-consistent treatment [8] calculates the suppression of SW scattering with *varying magnetic field at a*

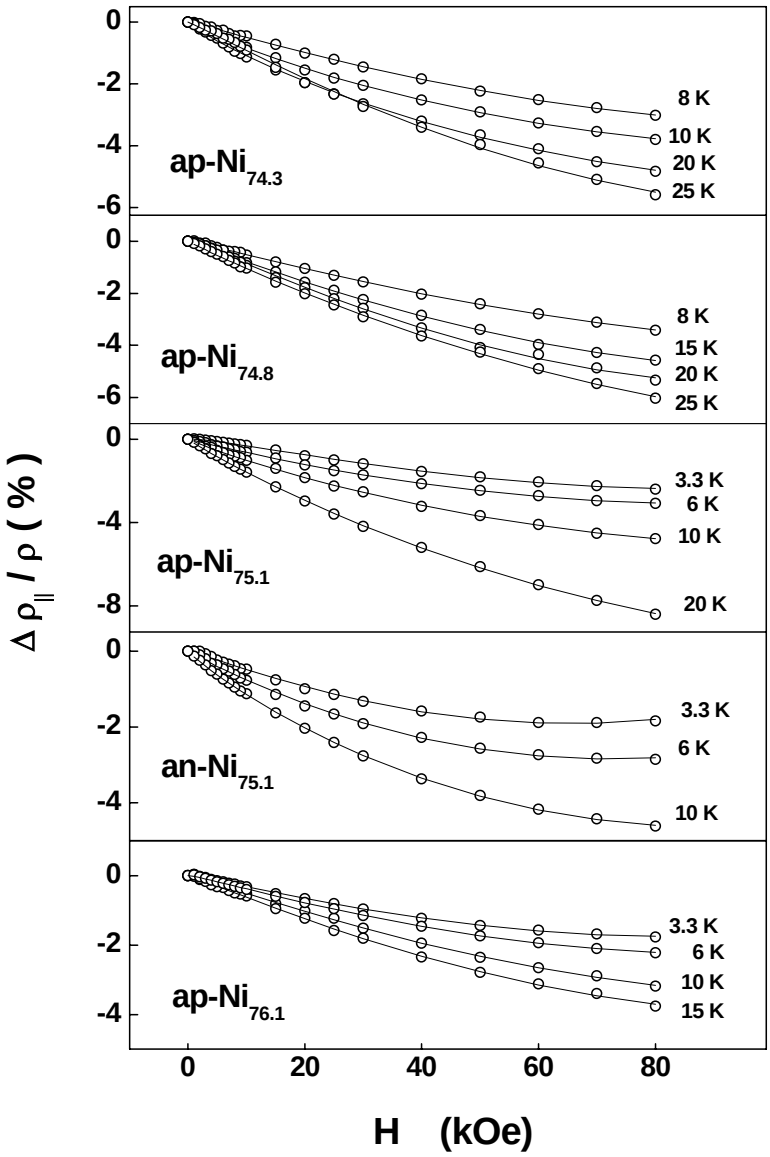

Figure 3.10: Longitudinal magnetoresistance, $\Delta\rho_{||}/\rho$, as a function of magnetic field at a few representative values of temperature in the spin wave region. Open circles denote the $\Delta\rho_{||}/\rho$ data while the continuous curves through the data points are the theoretical fits based on Eq.(11) of the text.

fixed temperature in the low temperature region. Thus, in order to verify the theoretical predictions [8], the fits to the longitudinal magnetoresistance, $\Delta\rho_{||}/\rho = [\rho_{||}(T,H) - \rho(T,H=0)]/\rho(T,H=0)$ versus H isotherms taken in the spin-wave temperature region (the actual temperature range depends on the composition, see table 3.2) are attempted based on Eq.(3.11) by varying the coefficients of the $h \ln h$, h and h^2 terms so as to optimize agreement between

the theory and experiment. That the theoretical fits (continuous curves), based on Eq.(3.11), accurately reproduce the experimentally observed (open circles) field variations of magnetoresistance is evident from figure 3.10. The coefficients of various terms have the same values as those predicted by equation (3.11) but the prefactor 0.304 is exactly one order of magnitude less ($\cong 0.031$) with the result that equation (3.11) predicts MR values that are nearly 10 times the observed ones.

3.5.2 Intermediate temperatures ($T < T_C$)

In the (intermediate) temperature range that partly overlaps the spin-wave region but falls well below T_C, the spin-fluctuation (SF) scattering contribution to the resistivity, $\rho(T)$ and magnetoresistance (MR) becomes more important than that arising from the SW scattering as the thermally-excited exchange-enhanced longitudinal and transverse spin-density fluctuations dominate over propagating transverse spin fluctuations (i.e., spin waves). At these temperatures, the theory [8] predicts a *quadratic temperature dependence* (i.e., $n = 2$) for both $\rho(T)$ and MR, as in the spin-wave region, but with a totally different value for the coefficient $A_n(0)$ (cf. Eqs.(3.8) and (3.20)) and for the suppression of the SF contribution, and hence for the variation of MR with field (cf. Eqs.(3.11) and (22)). A comparison of figures 3.6 and 3.11(a) reveals that the exponent '*n*' in $\rho(T) \sim T^n$ increases (decreases) from *n* = 1.50(1) and 1.66(1) (*n* = 1.64(3), 1.85(5) and 2.00(5)) to *n* = 1.81(1) and 1.96(1) (*n* = 1.50(1), 1.50(1) and 1.90(1)) for *ap-Ni*$_{74.3}$ and *ap-Ni*$_{74.8}$ (*ap-Ni*$_{75.1}$, *an-Ni*$_{75.1}$ and *ap-Ni*$_{76.1}$), respectively, as the sample temperature increases from low to intermediate temperatures. With the exception of the 'as-prepared' (-*ap*) and 'annealed' (-*an*) samples of *Ni*$_{75.1}$, all the samples (i.e., *ap-Ni*$_{74.3}$, *ap-Ni*$_{74.8}$ and *ap-Ni*$_{76.1}$) have exponent values that do not differ appreciably from the

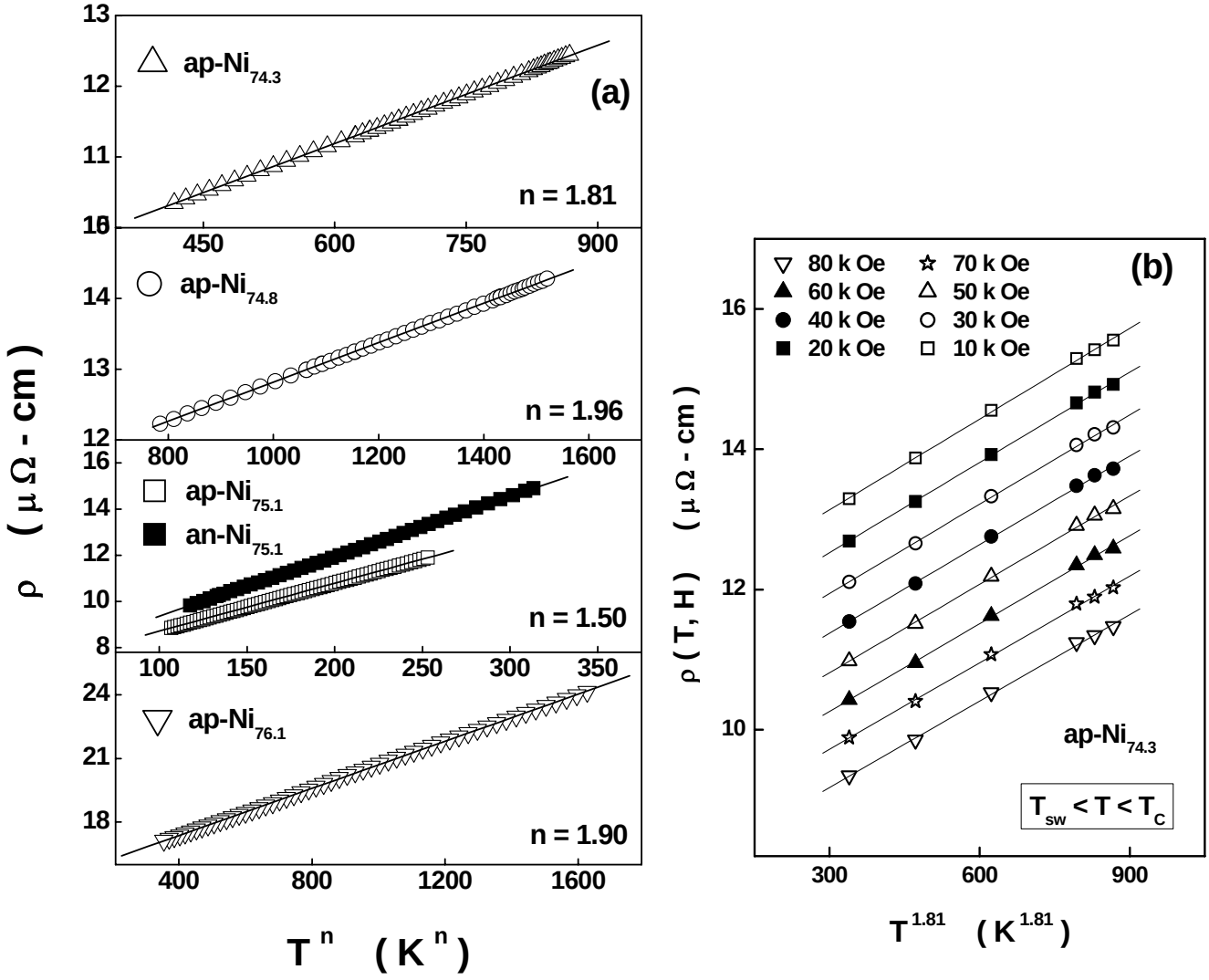

Figure 3.11: (a)T^n power law variation of resistivity with temperature in the intermediate temperature range for all the samples. (b) $T^{1.8}$ power law variation of $\rho(T,H)$ for the sample ap-$Ni_{74.3}$ at different fixed fields at intermediate temperatures. For the sake of clarity, a constant upward shift of 0.5 $\mu\Omega - cm$ has been given to the successive $\rho(T,H)$ data starting from that taken at H = 80 kOe.

theoretical value, *n* = 2. Another remarkable observation is that the *site disorder* in *ap-$Ni_{75.1}$* has *no discernible influence* on the exponent value (1.50(1)). At this stage, it is not clear as to why in the case of the stoichiometric composition alone, (i) a serious discrepancy exists between the predicted and observed values of *n*, and (ii) the exponent '*n*' is insensitive to site disorder. Like in the spin-wave region, at intermediate temperatures, the field *H* does not affect the temperature variation of resistivity (as illustrated by

figure 3.11(b)), the empirical relation, Eq.(3.29), is obeyed (figure 3.12) with the values of $A_n^*(0)$, a_λ and the exponent λ given in table 3.3, and $A_n(0) \cong A_n^*(0)$ within the uncertainty limits (see, table 3.3).

In order to ascertain whether or not Eq.(3.22) describes correctly the functional dependence of $\Delta\rho_{\|} / \rho = [\rho_{\|}(T,H) - \rho(T,H=0)] / \rho(T,H=0)$ on H at a given T in the intermediate temperature range, which depends on the composition (table 3.3), we have adopted the following approach. In accordance with the magnetic equation of state (MES), $[M(T,H)]^2$ versus $H / M(T,H)$ (Arrott) plots at different but fixed values of temperature are

Table 3.3: Temperature ranges and the parameters values corresponding to the fits in the intermediate temperature (spin-density fluctuation) region, based on the relation $\rho(T) = \rho(0) + A_n(0)\ T^n$ and Eq.(3.29) of the text.

Sample Label	Temperature range (K)	ρ(0) (μΩ - cm)	n	$A_n(0)$ (nΩ-cm K^{-n})	$A_n^*(0)$ (nΩ-cm K^{-n})	a_λ (10^{-4} $Oe^{-\lambda}$)	λ
ap-$Ni_{74.3}$	28 – 42 (0.59 T_C – 0.88 T_C)	8.30(3)	1.81 (1)	4.65(5)	4.70(2)	3.9(1)	0.47 (3)
ap-$Ni_{74.8}$	30 – 42 (0.5 T_C – 0.71 T_C)	10.0(1)	1.96 (1)	2.71(4)	2.73(4)	1.57(4)	0.60 (2)
ap-$Ni_{75.1}$	22 – 40 (0.4 T_C – 0.72 T_C)	6.65(5)	1.50 (1)	20.7(2)	21.0(5)	1.81(2)	0.61 (1)
an-$Ni_{75.1}$	24 – 46 (0.45 T_C – 0.8 T_C)	6.82(4)	1.50 (1)	25.7(3)	25.6(7)	1.75(2)	0.60 (1)
ap-$Ni_{76.1}$	22 – 48 (0.31 T_C – 0.68 T_C)	15.2(2)	1.90 (1)	5.70(5)	5.69(2)	0.91(1)	0.66 (1)

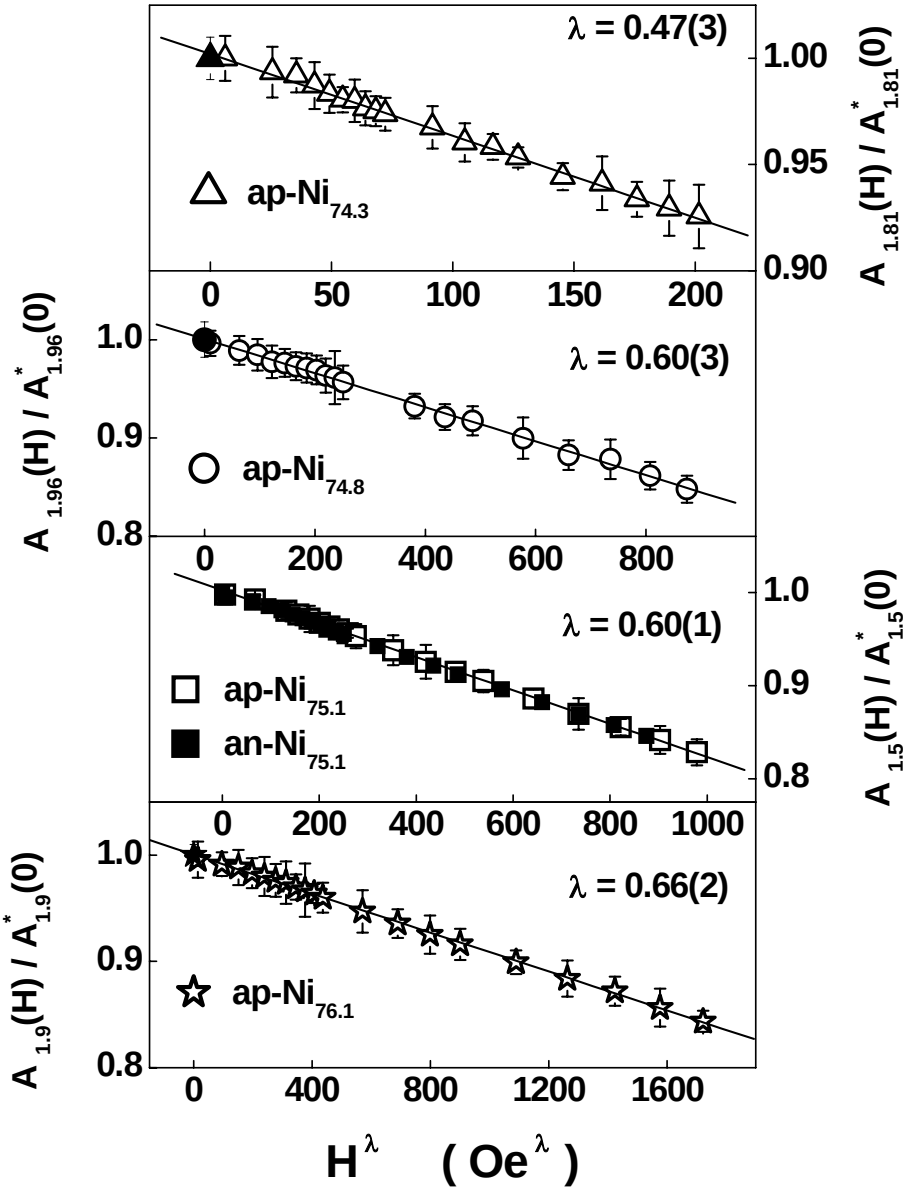

Figure 3.12: H^{λ} power law field dependence of the normalized coefficient, $A_n(H)/A_n^*(0)$, of the T^n term in the expression of resistivity at intermediate temperatures.

constructed out of the magnetization versus field, $M - H$, isotherms measured on the same samples as those used in the present work. The high-field linear portions of the Arrott plot isotherms are extrapolated to H = 0 to yield the values of spontaneous magnetization, M_0, at different temperatures, from the intercepts on the ordinate axis. Inserting the values for the quantities M_0, $[b\,(3M^2 - M_0^2)]^{-1/2}$, $b\,(M^2 - M_0^2)$ and $b^2\,(M^2 - M_0^2)^2$, obtained from Arrott

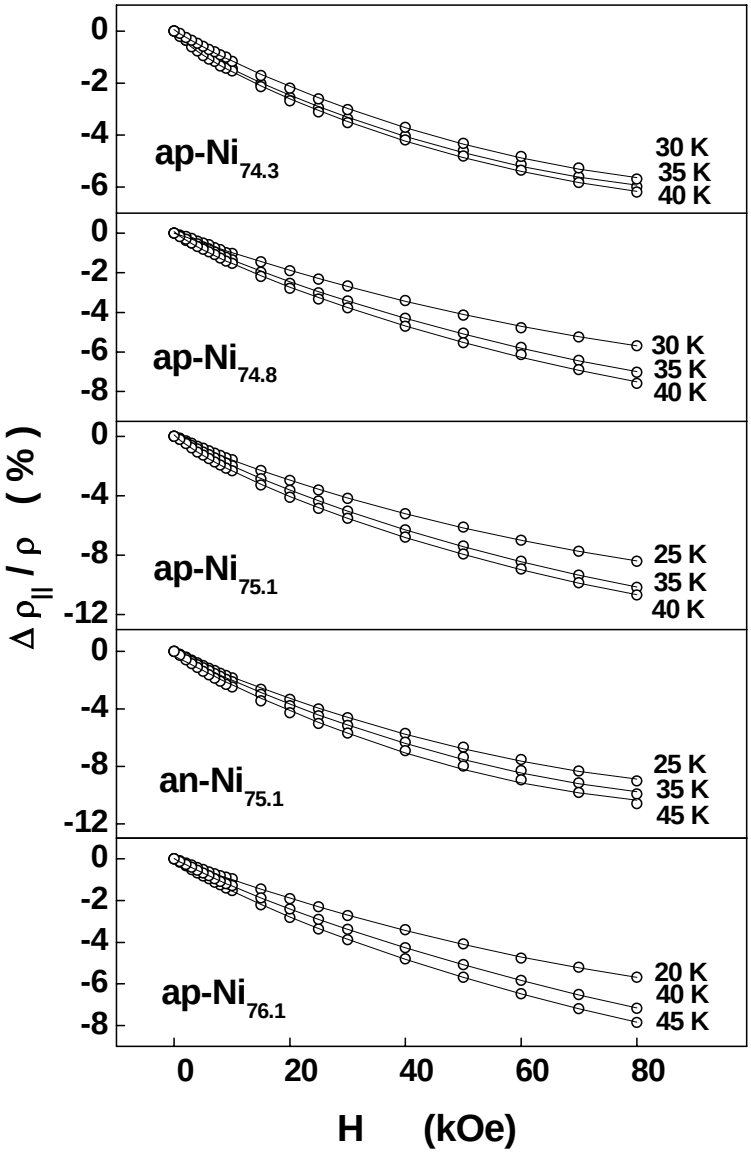

Figure 3.13: Longitudinal magnetoresistance, $\Delta\rho_{||}/\rho$, as a function of magnetic field at a few representative values of temperature in the intermediate temperature region. Open circles denote the $\Delta\rho_{||}/\rho$ data while the continuous curves through the data points are the theoretical fits based on Eq.(3.22) of the text.

plots and MES, in Eq.(3.22) and varying the coefficients of various terms in Eq.(3.22) so as to minimize the least-squares deviations from the measured $(\Delta\rho_{||}/\rho) - H$ isotherms, we arrive at the theoretical fits (continuous curves) to the $(\Delta\rho_{||}/\rho) - H$ data (open circles) at various temperatures shown in figure 3.13. Evidently, like in the spin-wave region, a perfect agreement between the theoretically predicted [8], Eq.(3.22), and experimentally observed

variations of MR with field exists at intermediate temperatures as well but equation (3.22) predicts one order of magnitude higher values for MR. We have also verified whether or not Eq.(3.22) forms a unique description of MR at intermediate temperatures by fitting the spin-wave expression, Eq.(3.11), (spin-fluctuation expression, Eq.(3.22)) to the MR data in the intermediate (low) temperature region, with the result that Eqs.(3.11) and (3.22) are indeed obeyed only at low and intermediate temperatures only. This observation thus confirms that spin-wave excitations and non-propagating spin-density fluctuations make dominant contributions at low and intermediate temperatures, respectively.

3.5.3 Temperatures close to T_C

Consistent with the predictions (Eq.(3.24)) of the spin-fluctuation theory [8], the observed temperature variation of resistivity for all the samples is closely reproduced by the expression $\rho(T) = \rho(0, H = 0) + A_{5/3}(H = 0)\ T^{5/3}$ at temperatures close to T_C $(0.7T_C \le T \le T_C)$, as is evident from figure 3.14(a). In this temperature range, the scattering of conduction electrons from the longitudinal and transverse non-propagating spin-density fluctuations completely accounts for the electrical resistivity. The coefficient $A_{5/3}(0) \equiv A_{5/3}(H = 0)$ is a direct measure of this spin-fluctuation (SF) contribution to resistivity. The composition dependence of $A_{5/3}(0)$, displayed in the top panel of figure 3.15, depicts the growth of the SF scattering with increasing Ni concentration. As the Curie temperature increases with Ni concentration, spin fluctuation modes of larger and larger q (higher energy) get thermally excited for temperatures close to T_C and contribute to the integral in Eq.(3.2) and hence to resistivity.

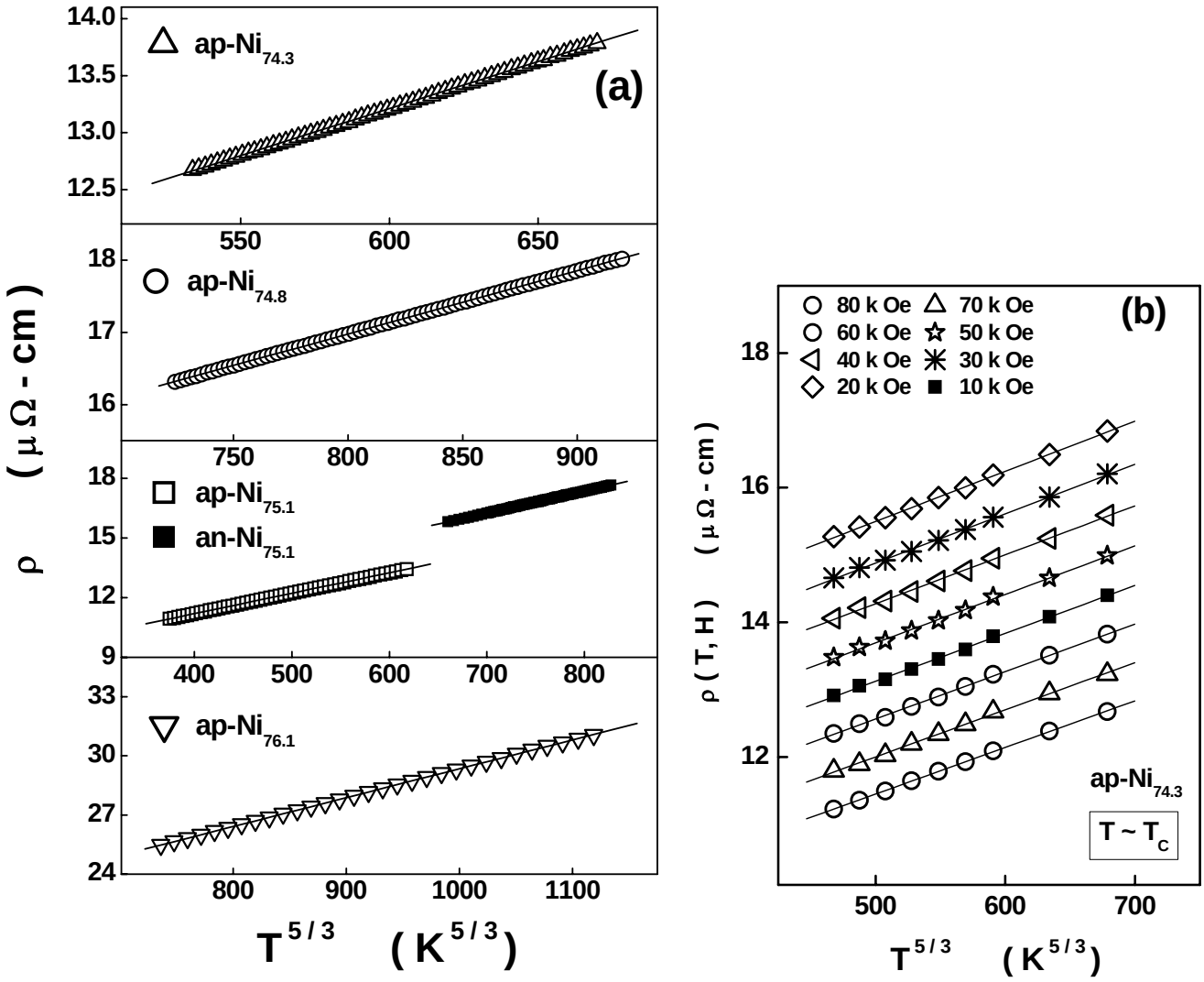

Figure 3.14: (a) $T^{5/3}$ power law variation of resistivity for temperatures close to the Curie temperature close to the Curie point. (b) $T^{5/3}$ power law variation of $\rho(T,H)$ for the sample ap-$Ni_{74.3}$ at different fixed fields at temperatures close to the Curie point. For the sake of clarity, a constant upward shift of 0.5 $\mu\Omega - cm$ has been given to the successive $\rho(T,H)$ data starting from that taken at H = 80 kOe.

As in the case of low and intermediate temperatures, (i) the theoretical result [8] that the field *H* leaves the temperature variation of resistivity *unaltered* is validated by the behavior of 'in-field' resistivity, $\rho(T,H)$, observed (figure 3.14(b)) at temperatures close to T_C, (ii) the empirical relation, Eq.(3.29), holds (figure 3.16) at these temperatures with the values of $A^*_{5/3}(0)$, a_λ and the exponent λ given in table 3.4,and (iii) $A_{5/3}(0) \cong A^*_{5/3}(0)$

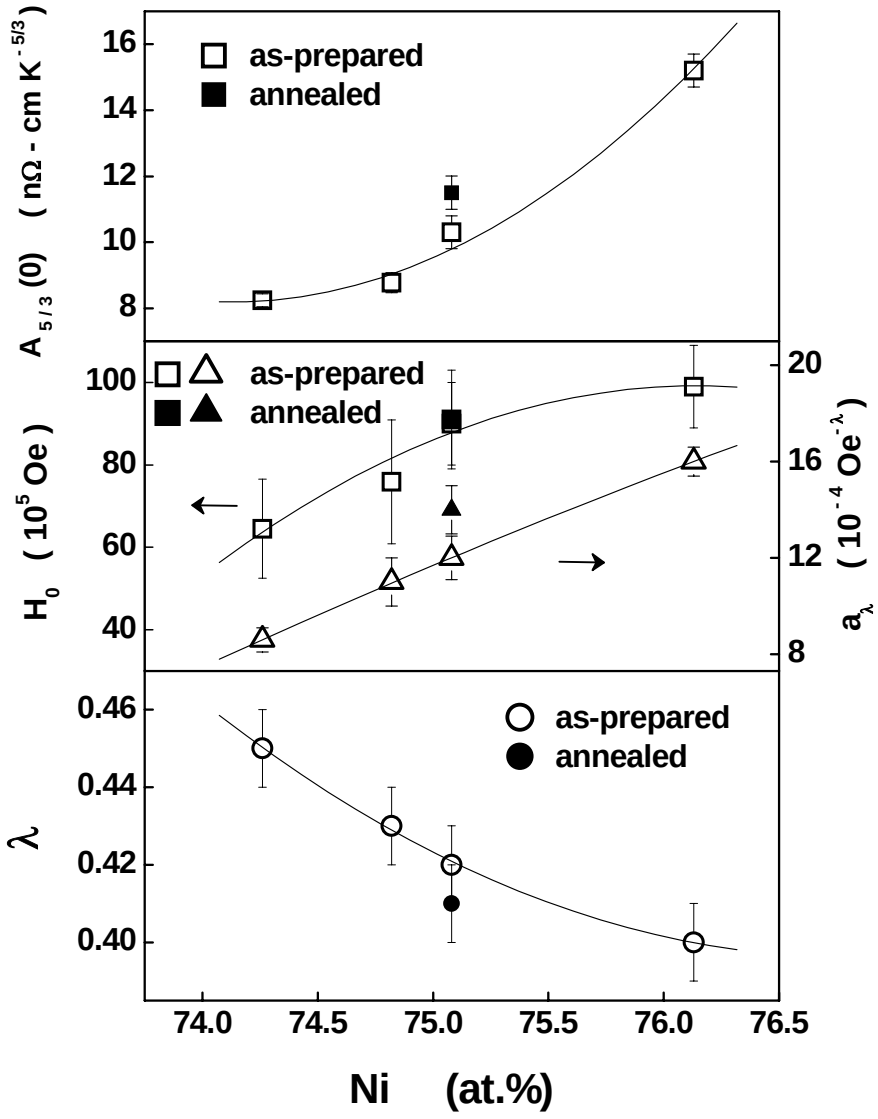

Figure 3.15: Variations with Ni concentration of the coefficient of the $T^{5/3}$ term in the expression for resistivity, $A_{5/3}(0)$, the exponent λ and the coefficient a_λ of the magnetic field-dependent term in Eq. (3.29) as well as of the critical field H_0 in Eq.(3.32) at temperatures.

within the error bars (see, table 3.4). The quantities a_λ and λ are plotted as functions of Ni concentration, *x*, in Fig. 3.15 so as to highlight the increasing (decreasing) trend of a_λ (λ) with *x*. The finding that, at $T \approx T_C$, $\rho(T,H)$ follows the *same* power law ($T^{5/3}$) for *all the compositions* enables us to put Eq.(3.29) into the scaling form

$$[A_{5/3}(H)/A_{5/3}(0)] = 1-(H/H_0)^{\lambda} \qquad (3.30)$$

Table 3.4: Temperature ranges and the parameters values corresponding to the fits at temperatures close to the Curie point (spin-density fluctuation region), based on the relation $\rho(T) = \rho(0) + A_n(0)\ T^n$ and Eq.(3.29) of the text.

Sample Label	Temperature range (K)	ρ(0) (μΩ - cm)	n	$A_n(0)$ (nΩ - cm K^{-n})	$A_n^*(0)$ (nΩ - cm K^{-n})	a_λ (10^{-4} $Oe^{-\lambda}$)	λ
ap-$Ni_{74.3}$	43.3 – 49.6 (0.91 T_C – 1.04 T_C)	8.27(2)	1.66 (1)	8.24(2)	8.25(2)	8.6(1)	0.45 (1)
ap-$Ni_{74.8}$	52 – 60 (0.89 T_C – 1.01 T_C)	9.96(7)	1.66 (1)	8.77(7)	8.81(4)	11(1)	0.43 (1)
ap-$Ni_{75.1}$	36 – 51 (0.65 T_C – 0.92 T_C)	7.09(6)	1.66 (3)	10.4(4)	10.4(1)	12(1)	0.42 (2)
an-$Ni_{75.1}$	45 – 56 (0.80 T_C – 1.00 T_C)	8.1(1)	1.66 (3)	11.5(4)	11.48(5)	14(1)	0.41 (1)
ap-$Ni_{76.1}$	47 – 65 (0.67 T_C – 0.93 T_C)	14.8(6)	1.66 (2)	15.2(5)	15.2(2)	15.9(6)	0.40 (1)

in which H_0 denotes the *critical field* at which the spin-density fluctuations get completely quenched. An extremely good collapse of the $A_{5/3}(H)/A_{5/3}(0)$ versus $(H/H_0)^\lambda$ data for all the compositions onto a single universal curve, demonstrated in figure 3.16(b), testifies to the validity of the scaling relation, Eq.(3.30). This type of scaling could not be attempted at low and intermediate temperatures because the exponent '*n*' depends on composition in those temperature ranges. The values of H_0, calculated using the relation $H_0 = a_\lambda^{-1/\lambda}$, are plotted in Fig. 3.15 as a function of *x*. The increase in H_0 with the Ni concentration is consistent with the above inference (drawn based on the

$A_{5/3}(0)$ vs. *x* plot, shown in Fig. 3.15) that higher-energy spin fluctuation modes contribute to resistivity as *x* increases because higher fields are required to quench high-frequency spin fluctuations.

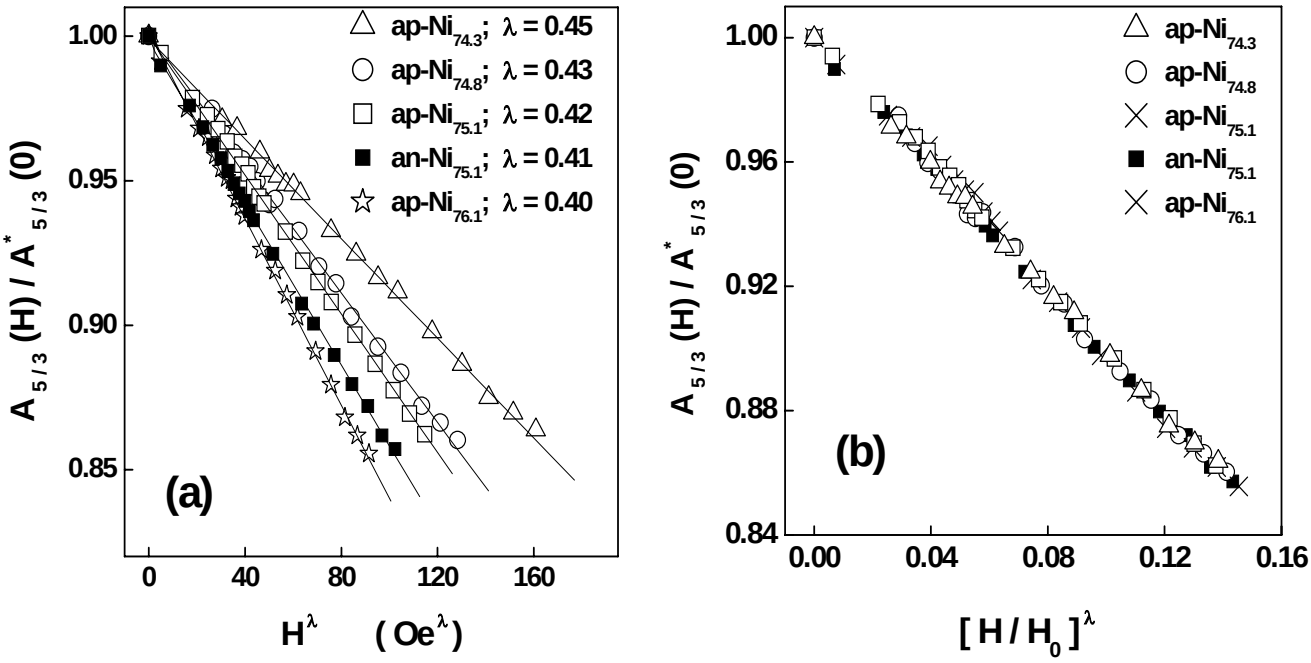

Figure 3.16:(a) H^{λ} *power law field dependence of the normalized coefficient,* $A_{5/3}(H)/A^{*}_{5/3}(0)$*, of the* $T^{5/3}$ *term in the expression of resistivity at temperatures close to the Curie point. (b) Scaling of the normalized coefficient,* $A_{5/3}(H)/A^{*}_{5/3}(0)$*, of the* $T^{5/3}$ *term in the expression of resistivity with* $(H/H_0)^{\lambda}$ *at temperatures close to the Curie point (*T_C*), in accordance with the Eq.(3.30) of the text. In this scaling plot,* H_0 *is the critical field strength required to completely quench the spin-density fluctuations for* $T \approx T_C$*.*

Next, a quantitative comparison is made between the observed and calculated [8] (based on Eq.(3.28)) variations of MR with *H* at fixed temperatures in the vicinity of T_C**.** We follow the same procedure as that detailed in the previous sub-section to arrive at the values for the quantities M_0^2, M_0^4, $[b\,(3M^2 - M_0^2)]$, $[b\,(3M^2 - M_0^2)]^2$, $b\,(M^2 - M_0^2)$ and $b^2\,(M^2 - M_0^2)^2$ appearing in Eq.(3.28) and optimize the coefficients of these terms so as to achieve the best agreement with the measured $(\Delta\rho_{\|}/\rho)$ versus *H* isotherms

using the non-linear least-squares-fit method. The data presented in figure 3.17 clearly demonstrate that the self-consistent theoretical calculations [8] yield the variations of MR with field (continuous curves, based on Eq.(3.28)) that conform well, in *quantitative* terms, with the observed ones (open circles) at temperatures close to T_C, as was the case at low and intermediate temperatures as well. Yet another important observation made in this work is that the

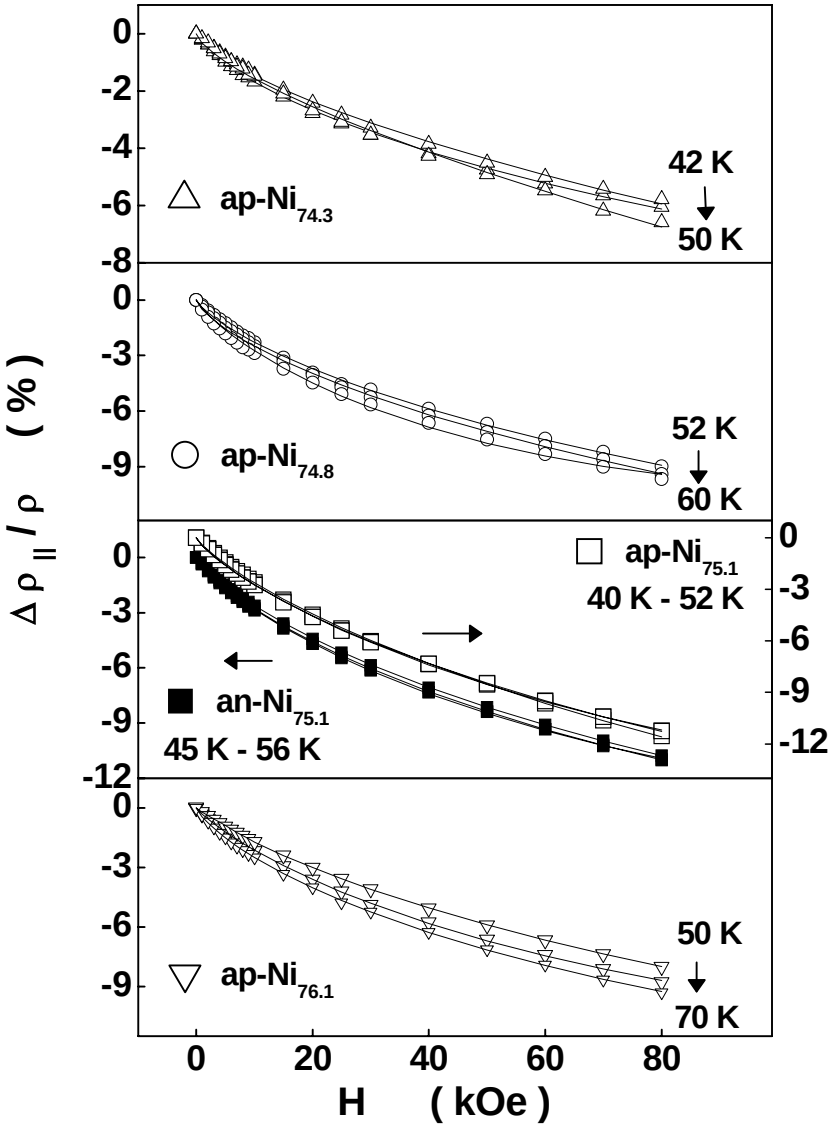

Figure 3.17: Longitudinal magnetoresistance, $\Delta\rho_{\|}/\rho$, as a function of magnetic field at afew representative values of temperature in the intermediate temperature region. Open circles denote the $\Delta\rho_{\|}/\rho$ data while the continuous curves through the data points are the theoretical fits based on Eq.(3.22) of the text.

$(\Delta\rho_{\|}/\rho)$ versus H isotherms at $T = T_C$ (the *critical isotherms*) for all the samples have the unique feature that $(\Delta\rho_{\|}/\rho) \sim H^{0.66}$ (see, figure 3.18). This power law behavior can be understood as follows in terms of the theory, due to Balberg [22], which takes into account the critical fluctuations of the order parameter (spontaneous magnetization) and yields the expression

$$(\Delta\rho_{\|}/\rho) \sim h^{(1-\alpha)/\beta\delta} \tag{3.31}$$

for the field dependence of magnetoresistance in the critical region ($T \cong T_C$) for a ferromagnet. In Eq.(3.31), $h = g\,\mu_B H / k_B T$ is the reduced field, and α, β and δ are the critical exponents for the 'zero- field' specific heat, spontaneous magnetization and the M versus H isotherm at $T = T_C$, respectively**.** An extensive study of critical phenomena in the 'as-prepared' and 'annealed' samples of the stoichiometric composition have previously yielded [16,23] *mean-field* values for the critical exponents β, γ (the critical exponent for initial susceptibility) and δ, i.e., $\beta = 0.500(3)$, $\gamma = 1.000(5)$ and $\delta = 3.000(4)$. Similar exponent values have been obtained (see chapter 4, for details) for the present samples as well [24]. Inserting these mean-field values for the exponents β and γ in the Rushbrooke equality $\alpha + 2\beta + \gamma = 2$, yields the value for the exponent α as $\alpha = 0$. Using the values $\alpha = 0$, $\beta = 0.5$ and $\delta = 3.0$, Eq.(3.31) reduces to exactly the same form, $(\Delta\rho_{\|}/\rho) \sim h^{2/3}$, as that observed in this work. Interestingly, Eq.(3.28) provides as good a quantitative description of the critical $(\Delta\rho_{\|}/\rho)$ versus H isotherms for all the compositions as Eq.(3.31) does. This is so because the theoretical formalism [8] leading to Eq.(3.28) makes use of the mean-field equation of state, which is consistent with the above values for the critical exponents.

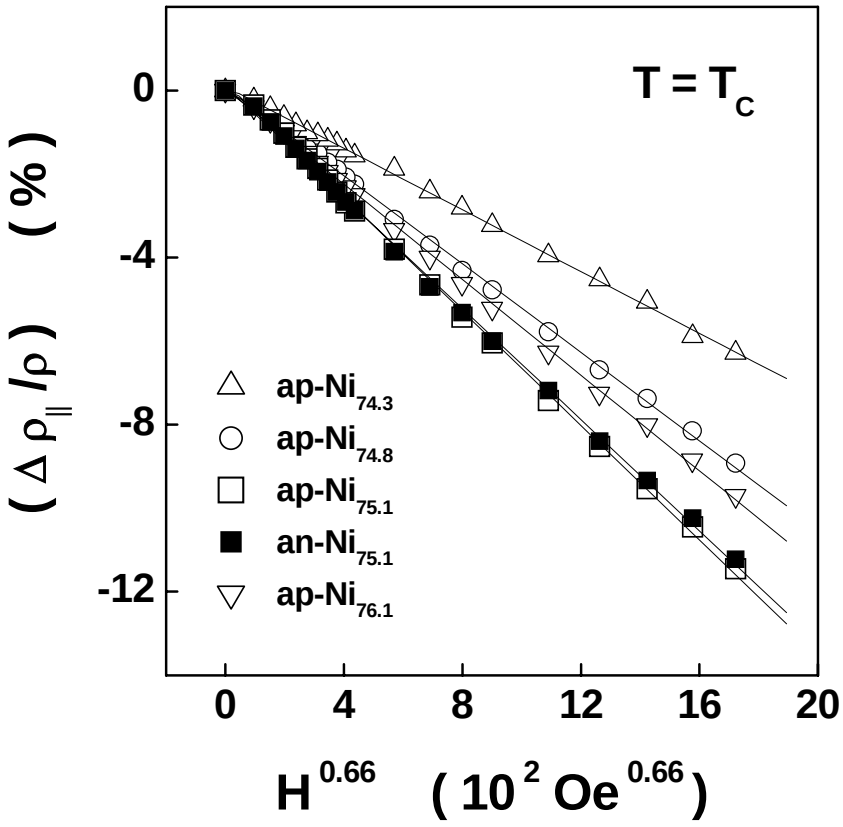

Figure 3.18: $H^{0.66}$ power law field dependence of the longitudinal magnetoresistance, $\Delta\rho_{||}/\rho$, at $T = T_C$.

Finally, in order to clearly bring out the composition dependence of negative MR, the $(\Delta\rho_{||}/\rho)$ versus H isotherms for different compositions taken at the reduced temperatures $T/T_C = 0.2$, 0.5 and 0.9 (that fall within the low, intermediate and near T_C, temperature regions, respectively) are compared in figure 3.19. In this figure, the continuous curves through the data points (symbols) are the theoretical fits for the alloys in question, based on Eqs.(3.11), (3.22) and (3.28), at the fixed temperatures $T/T_C = 0.2$, 0.5 and 0.9, respectively. The insets of Fig. 3.19 demonstrate that: (i) at any fixed value of H (shown only for $H = 8$ *Tesla* but is true for other fields as well), the *negative* magnetoresistance (MR) goes through a *peak* at the stoichiometric composition at all temperatures and (ii) regardless of composition, the negative MR

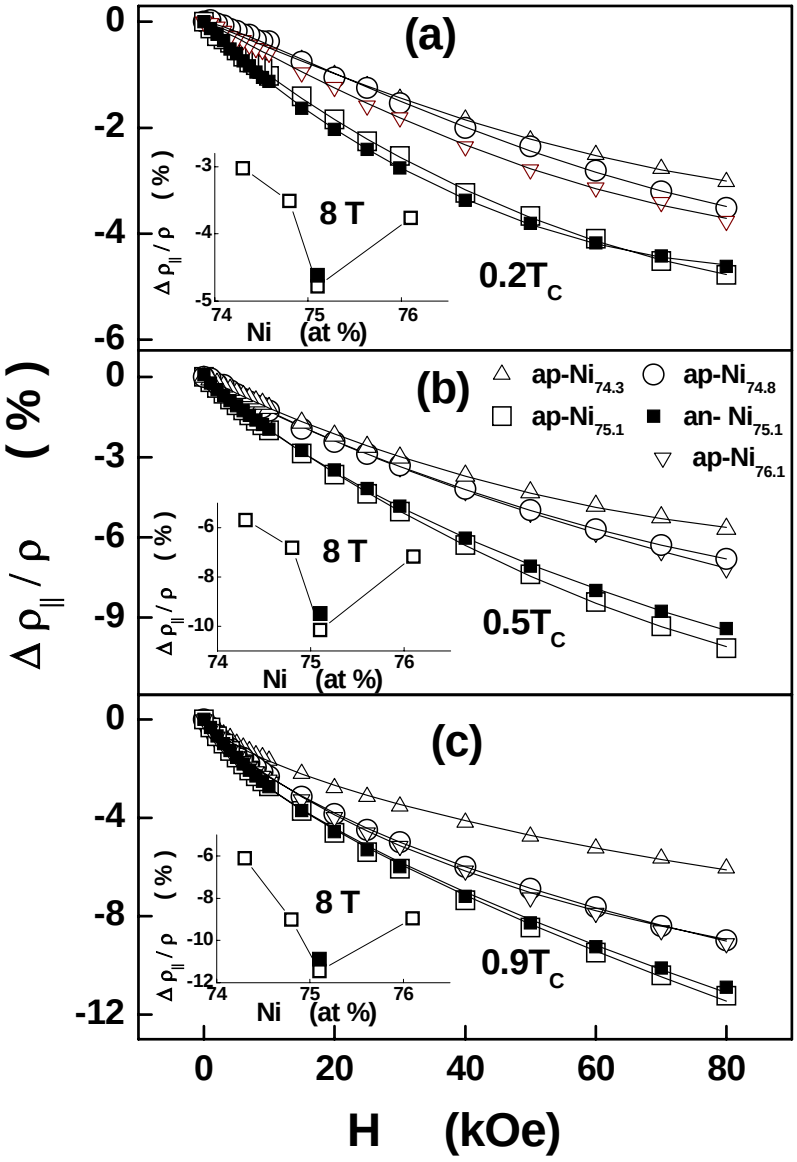

Figure 3.19: Longitudinal magnetoresistance, $\Delta\rho_{\|}/\rho$, of all the compositions as a function of magnetic field at $T = 0.2T_C$, $0.5T_C$ and $0.9T_C$. Open symbols denote the $\Delta\rho_{\|}/\rho$ data while the continuous curves through the data points at $T = 0.2T_C$, $0.5T_C$ and $0.9T_C$ are the theoretical fits based on the Eqs.(3.11), (3.22) and (3.28) of the text, respectively. Insets show that the longitudinal magnetoresistance, $\Delta\rho_{\|}/\rho$, at $H = 80\,kOe$ (or in SI units, $H = 8$ Tesla) and $T = 0.2T_C$, $0.5T_C$ and $0.9T_C$ goes through a dip at the stoichiometric composition as a function of Ni concentration.

increases as the temperature is progressively raised from low temperatures so as to approach T_C from below. These observations imply that irrespective of the temperature range (low, intermediate or close to T_C), the maximum

suppression of the dominant magnetic excitation by magnetic field occurs for the stoichiometric composition, and that the amplitude of the thermally-excited spin fluctuation modes picks up rapidly as T_C is approached with the result that at any field strength, the suppression is maximum at T_C.

3.6 Summary and conclusion

Extensive high-resolution electrical resistivity, $\rho(T)$, and longitudinal magneto-resistance, (MR), $\Delta\rho_{\|}/\rho = [\rho_{\|}(T,H) - \rho(T,H=0)]/\rho(T,H=0)$, measurements have been carried out on well-characterized 'as-prepared' Ni_xAl_{100-x} alloys with x = 74.3, 74.8, 75.1 and 76.1 at.% and on the 'annealed' $Ni_{75.1}Al_{49.9}$ alloy at temperatures in the range $1.7\,K \le T \le 300\,K$ and in magnetic fields, H, up to 80 *kOe*. In the following text, we briefly summarize the most important observations made based on the $\rho(T)$ and $\Delta\rho_{\|}/\rho$ data and the inferences drawn from them.

In the temperature range $1.7\,K \le T \le 25K$ and, electrical resistivity exhibits *non-Fermi liquid* behavior in that it varies with temperature as $\rho(T) \sim T^n$ with n = 1.50(1), 1.66(1) and 1.64(3) (1.80(5)) for the samples *ap-$Ni_{74.3}$*, *ap-$Ni_{74.8}$* and *ap-$Ni_{75.1}$* (*an-$Ni_{75.1}$*), respectively. On the other hand, $\rho(T)$ in *ap-$Ni_{76.1}$* follows the T^2 law (the Fermi liquid behavior) over a narrow temperature range $1.7\,K \le T \le 16\,K$. As the critical concentration, $x_c \cong 73.5$ *at.%*, is approached from above, i.e., as the *compositional disorder* increases, *stronger deviations* from the Fermi liquid behavior occur and the temperature range over which the *non-Fermi liquid behavior* persists *widens*. By contrast, the *site disorder* makes the non-Fermi liquid behavior *more prominent* particularly in the *stoichiometric* composition (Ni_3Al) and stabilizes the non-

Fermi liquid behavior in any given composition over a *much wider* temperature range. Based on plausible arguments, it is proposed that the non-Fermi liquid behavior observed at low temperatures when *x* falls below $76.1\,at.\%$ reflects that the increased compositional disorder *alters the spin-wave dispersion* at *finite q* such that as *q* increases from $q = 0$, the spin-wave dispersion becomes increasingly similar to the non-propagating spin-fluctuation dispersion prevalent at temperatures close to T_C (Curie temperature).

The expression $\rho(T,H) = \rho(0,H) + A_n(H)\ T^n$ with $H = 0$ and $H \neq 0$ forms an excellent description of the 'zero-field', $\rho(T, H = 0)$, and 'in-field', $\rho(T,H)$, resistivities at all temperatures below T_C. The values of the quantities $\rho(0) \equiv \rho(0, H = 0)$, $\rho(0,H)$, $A_n(0)$, $A_n(H)$ and the exponent '*n*' *depend on* the sample composition and on the choice of the temperature range (see, tables 3.2 – 3.4) but in any given temperature range, '*n*' is *independent* of *H*. The observation that the exponent '*n*' does not depend on *H* vindicates the theoretical approach, recently proposed by Kaul [8]. The functional dependence of A_n on *H* is accurately described by the empirical relation $A_n(H) = A_n(0)\ [1 - a_\lambda\ H^\lambda]$ over the entire temperature range $T \leq T_C$ but with the coefficient a_λ and the exponent λ varying from sample to sample and from one temperature regime to the other (for actual values, refer to tables 3.2 – 3.4). For temperatures close to T_C, where, in accordance with the theoretical predictions [8], the exponent '*n*' has the *universal* value (the same value for all the compositions) of $n = 5/3$, the above empirical relation has been put into the scaling form $[A_{5/3}(H)/A_{5/3}(0)] = 1 - (H/H_0)^\lambda$. The validity of this scaling form has been demonstrated by a perfect collapse of the $A_n(H)$ data for all the samples onto the *universal plot* (Fig.3.16(b)) of $A_{5/3}(H)/A_{5/3}(0)$ versus

$(H/H_0)^{\lambda}$; the critical field, H_0, required to completely quench the spin-density fluctuations, increases with the Ni concentration, *x*.

Contrasted with the above empirical relation, which quantifies the suppression of the dominant magnetic excitations at a *given field strength over a specified temperature range* (low temperatures or intermediate temperatures or temperatures close to T_C), the self-consistent theoretical treatment [8] calculates the suppression of such excitations with *varying magnetic field at a fixed temperature* in a particular temperature range. Thus, a quantitative comparison between the theoretical predictions [8] and the longitudinal magnetoresistance $\Delta\rho_{\parallel}/\rho = [\rho_{\parallel}(T,H) - \rho(T,H=0)]/\rho(T,H=0)$ versus H isotherms taken in different temperature regimes is sought by making use of the magnetization, $M(T,H)$, data taken on the same samples as the present ones at temperatures $5K \le T \le 300K$ and magnetic fields $0 \le H \le 70kOe$. Such a comparison reveals that the self-consistent spin fluctuation theory [8] predicts the observed variations of $\Delta\rho_{\parallel}/\rho$ with H at fixed temperatures in different temperature regimes (i.e., at low temperatures, intermediate temperatures and temperatures close to, or even equal to, T_C) correctly. The $(\Delta\rho_{\parallel}/\rho)$ versus H isotherms taken at $T = T_C$ (the *critical isotherms*) for all the samples have the *common feature* that $(\Delta\rho_{\parallel}/\rho) \sim H^{2/3}$. The theory, due to Balberg [22], is shown to provide a straightforward explanation for the observed power law behaviour.

Other important observations that deserve a mention are: (i) at any fixed value of *H*, the *negative* magnetoresistance (MR) goes through a *peak* at the stoichiometric composition at all temperatures and (ii) regardless of

composition, the negative MR increases as the temperature increases from low temperatures to $T = T_C$. These observations imply that irrespective of the temperature range (low, intermediate or close to T_C), the maximum suppression of the dominant magnetic excitation by magnetic field occurs for the stoichiometric composition, and that the amplitude of the thermally-excited spin fluctuation modes picks up rapidly as T_C is approached with the result that at any field strength, the suppression is maximum at T_C.

References

[1] D. L. Mills and P. Lederer, J. Phys. Chem. Solids **27**, 1805 (1966).

[2] A. I. Schindler and M. J. Rice, Phys. Rev. **164**, 759 (1967).

[3] J. Mathon, Proc. Roy. Soc. A **306**, 355 (1968).

[4] K. Ueda and T. Moriya, J. Phys. Soc. Jpn. **39**, 605 (1975).

[5] T. Moriya and A. Kawabata, J. Phys. Soc. Jpn. **34**, 639, 669 (1973).

[6] K. Ueda, Solid State Commun. **19**, 965 (1976).

[7] R. V. Pai and S. G. Mishra, Phys. Rev. B **48**, 10292 (1993).

[8] S. N. Kaul, J. Phys. : Condens. Matter **17**, 5595 (2005).

[9] T. Moriya, *Spin Fluctuations in Itinerant Electron Magnetism* (Springer, Berlin, 1985), Springer series in Solid State Sciences Vol. **56**.

[10] J. H. J. Fluitman, R. Boom, P. F. De Chatel, C. J. Schinkel, J. L. L. Tilanus and B. R. De Vries, J. Phys. F: Metal Phys. **3**, 109 (1973).

[11] K. H. Chang, R. H. van der Linde and E. G. Sieverts, Physica **69**, 467 (1973).

[12] P. D. Hambourger, R. J. Olwert and C. W. Chu, Phys. Rev. B **11**, 3501 (1975).

[13] H. Sasakura, K. Suzuki and Y. Masuda, J. Phys. Soc. Jpn. **53**, 352 (1984).

[14] M. Yoshizawa, H. Seki, K. Ikeda, K. Okuno, M. Saito and K. Shigematsu, J. Phys. Soc. Jpn. **61**, 3313 (1992).

[15] C. J. Fuller, C. L. Lin, T. Mihalisin, F. Chu and N. Bykovetz, Solid State Commun. **3**, 863 (1992).

[16] A. Semwal and S. N. Kaul, J. Phys. : Condens. Matter **14**, 5829 (1999).

[17] K. Aoki and O. Izumi, Phys. Stat. Sol. **32**, 657 (1975).

[18] Anita Semwal and S. N. Kaul. Phys. Rev. B **60**, 12799 (1999).

[19] S. N. Kaul, J. Phys. : Condens. Matter **11**, 7597 (1999).

[20] M. J. Steiner, F. Beckers, P. G. Nilkowitz, and G. G. Lonzarich, Physica B **329-333**, 1079 (2003).

[21] P. G. Niklowitz, F. Beckers and G.G. Lonzarich, G. Kneble, B. Salce, J. Thomsson, N. Bernhoeft, D. Braithwaite, and J. Flouquet, Phys. Rev. B **72**, 024424 (2005).

[22] I. Balberg, Physica **91B**, 71 (1977).

[23] Anita Semwal and S. N. Kaul. Phys. Rev. B **64**, 014417 (2001).

[24] A. C. Abhyankar and S. N. Kaul, Accepted for publication in J. Phys. : Condens. Matter.

Chapter 4

Effect of off-stoichiometry and site-disorder on the magnetic properties of Ni_3Al

4.1 Introduction

A recent appraisal [1] of the previously reported [2-9] results on the magnetic behaviour of binary Ni_xAl_{100-x} alloys with $73.5\,at.\,\% \le x \le 76.5\,at.\,\%$ highlighted the controversies that surround the nature of magnetism in this weakly ferromagnetic alloy system. Attributing the disagreement between the results of earlier investigations to a complex interplay between the compositional disorder and site disorder, and to a complete neglect of the spin-wave contribution to magnetization at low temperatures, Kaul and Semwal made an attempt to unravel the individual roles of compositional disorder [4] and site disorder [13,14]. To this end, the study of magnetization in the 'as-prepared' Ni_xAl_{100-x} alloys [4] with $74\,at.\,\% \le x \le 76\,at.\,\%$ (the Ni concentration range that includes the critical concentration [5-10] $x_c \approx 74.5\,at.\%$ below which long-range ferromagnetic order ceases to exist) and in the alloy of stoichiometric composition, Ni_3Al, 'prepared' in different states of site disorder [13,14], revealed the following. (i) Regardless of the degree of site disorder present, spin waves, at low temperatures ($0.09T_C \le T \le 0.28T_C$), zero-point and thermally-excited local spin-density fluctuations, at intermediate temperatures ($0.32T_C \le T \le 0.62T_C$), and non-propagating thermally-excited spin fluctuations, at temperatures close to the Curie point, T_C, ($0.65T_C \le T \le 0.95T_C$), completely account for [13,14] the thermal demagnetization of spontaneous magnetization, $M(T,0)$, and 'in-field' magnetization, $M(T,H)$. By contrast, the spin fluctuation theories [12 – 14], that predict precisely this behaviour of $M(T,0)$ and $M(T,H)$ for a weak itinerant-electron ferromagnet *in the absence of any disorder*, failed [1] to describe the decline in $M(T,H=1kOe)$ with increasing temperature observed in the Ni_xAl_{100-x} alloys that have substantial compositional disorder. Instead, the

functional form of $M(T, H = 1kOe)$ observed in these alloys could be closely reproduced over the entire temperature range, $T \leq T_C$, by the temperature variation predicted by the percolation (*localized-spin*) theories [15 – 17] that invoke a crossover in the spin dynamics on a three-dimensional ferromagnetic percolating network from a hydrodynamic (magnon) regime at low temperatures to a critical (fracton) regime at high temperatures. Moreover, the power laws, $M_0(x) \sim (x - x_c)^{\beta_P}$, $D_0(x) \sim (x - x_c)^{\theta_P}$ and $T_C(x) \sim (x - x_c)^{\phi}$ with $x > x_c$, which, according to the percolation theories [15,16], characterize the percolation critical behaviour (second order phase transition) at $x = x_c$ in three-dimensional percolating networks, described very well the Ni concentration dependences of the spontaneous magnetization at 0 K, $M_0 \equiv M(0,0)$, the spin wave stiffness at 0 K, D_0, and the Curie temperature, T_C. (ii) Like compositional disorder, site disorder smears out the sharp features in the density of states (DOS) curve near the Fermi level, E_F, and reduces the DOS at E_F, $N(E_F)$, M_0, D_0, and T_C. (iii) Site disorder affects the magnitude of suppression of the low-lying magnetic excitations (spin waves and spin fluctuations) by external magnetic field (*H*) but does not alter the functional form of the suppression with *H*.

Though the above observations (i) – (iii) facilitated characterizing the roles of site disorder and compositional disorder in influencing the magnetic properties of the weakly ferromagnetic alloy system, Ni_xAl_{100-x}, they concomitantly raised the following basic questions. (1) Why do the spin fluctuation theories [12 – 14], which otherwise enjoy the distinction of providing correct explanation for the characteristic attributes of weak itinerant-electron magnets, fail to describe the magnetic behaviour of weak itinerant-

electron ferromagnets with compositional disorder? (2) How does one reconcile to the fact that weak *itinerant-electron* ferromagnets with compositional disorder follow closely the predictions of a *localized-spin* (percolation) theory? As a reconciliatory measure, Kaul and Semwal [1] conjectured that quenched random disorder in such systems could cause localization of the otherwise itinerant magnetic moments. This conjecture, however, does not explain as to why site disorder cannot be as effective in localizing the magnetic moments as compositional disorder supposedly is. The non-Fermi liquid behaviour of resistivity at low temperatures in the same alloy system, Ni_xAl_{100-x}, reported in the preceding chapter [18], adds a new dimension to the problem.

To seek answers to these fundamental queries, extensive high-resolution bulk magnetization, $M(T,H)$, measurements were undertaken on well-characterized samples of Ni_xAl_{100-x} alloys, in the 'as-prepared' state. An elaborate analysis of the present $M(T,H)$ data not only resolves the issues (1) and (2), mentioned above, by bringing out clearly the effect of compositional disorder and/or site disorder on the contributions to $M(T,0)$ and $M(T,H)$, arising from spin waves at low temperatures and non-propagating thermally-excited longitudinal and transverse spin fluctuations at intermediate temperatures and for temperatures close to T_C, but also quantifies the suppression of these contributions by H. At low temperatures, $M(T,0)$ and $M(T,H)$ exhibit non-Fermi liquid behaviour in the alloys with $x_c \cong 73.5\,at.\% \le x < 75.1\,at.\%$ much the same way as the resistivity and magnetoresistance do, as reported in chapter 3. The present results also demonstrate that the compositional disorder and site disorder (for a precise definition of the terms compositional disorder and site disorder, see section 3.2

of chapter 3) change T_C drastically but have practically no effect on the magnetic behaviour in the critical region since, irrespective of the amount or type of disorder present, mean-field critical exponents characterize the ferromagnetic-to-paramagnetic phase transition at T_C.

4.2 Magnetic measurements

For magnetic measurements, spherical-shaped samples (2.5 mm in diameter) of *ap-*$Ni_{74.3}$, *ap-*$Ni_{74.8}$, *ap-*$Ni_{75.1}$ and *ap-*$Ni_{76.1,}$ were spark-cut from the 'as-prepared' (*ap-*) rods, as already mentioned in chapter 3. Note that the magnetization, resistivity and magnetoresistance samples come from the *same* batch. Though the composition of these alloys is not very different from those used previously in reference [1], the x-ray diffraction patterns of the corresponding compositions are distinctly different (cf. Fig.1 of chapter 3 with Fig.1 of reference [1]) in that the substantial (200) texture, present in the earlier samples, is completely absent in the new ones.

Magnetization, $M(T, H_{ext})$, of polycrystalline $Ni_x Al_{100-x}$ samples was measured in external static magnetic fields (H_{ext}) up to 15 *kOe* on a vibrating sample magnetometer (VSM). These measurements cover a temperature range of $15\,K \le T \le 300\,K$ that embraces the critical region near the ferromagnetic (FM) - paramagnetic (PM) phase transition. *M* versus H_{ext} isotherms were taken at 60 predetermined but fixed values of H_{ext} (each stable to within ±1 *Oe*) ranging from 0 to 15 *kOe*, at the temperature intervals of 0.5 *K*, 0.1 *K*, 0.05 *K* and 0.025 *K* within the ranges $15\,K \le T \le 0.5T_C$, $0.5T_C \le T \le T_C - 10\,K$, $T_C - 10\,K \le T \le T_C - 3\,K$, $T_C - 3\,K \le T \le T_C + 3\,K$ and then the temperature interval was slowly increased to 0.1 *K*, 0.5 *K*, 1 *K*, 5 *K* and 10 *K* while

increasing the temperature to $300\,K$. Demagnetizing factor, *N*, was computed from the inverse slope of the linear $M - H_{ext}$ isotherm (i.e., $4\pi N = (slope)^{-1} = H_{ext}/M$) taken at the lowest temperature T = 15 *K* in field range $-20\,Oe \le H_{ext} \le 20\,Oe$. To construct the Arrott ($M^2(T,H)$ versus $H/M(T,H)$) plots out of the $M(T,H_{ext})$ data, the external magnetic field was corrected for the demagnetizing field, i.e., $H = H_{ext} - 4\pi N M(T,H_{ext})$. The spontaneous magnetization at different temperatures, $M(T,H=0)$, was computed from the intercepts on the ordinate obtained by extrapolating the high-field (also the low-field) portion of the Arrott plot isotherms to $H = 0$ (in the case of *ap-$Ni_{74.3}$*) for $T \le T_C$, as elucidated in sub-section 4.3.4. The $M - H$ isotherms, used for constructing Arrott plots, were converted into the $M - T$ data at 16 different but fixed values of *H* in the interval $0.3\,kOe < H < 15\,kOe$. Note that the above-mentioned detailed magnetization measurements were not performed on the *ap-$Ni_{75.1}$* sample when the preliminary measurements revealed a magnetic behaviour that was not significantly different from the one reported earlier [10, 11] on the annealed counterpart of this sample. However, magnetization was measured on all the samples, including *ap-$Ni_{75.1}$*, as a function of H_{ext} for $H_{ext} \le 70\,kOe$ at $T = 5\,K$ (and at a few specific temperatures so that a quantitative comparison between the magnetoresistance data and the spin-fluctuation theory could be made in chapter 3) and as a function of temperature in the range from 5 *K* to 150 *K* at $H_{ext} = 1\,kOe$, using a SQUID magnetometer

4.3 Temperature and magnetic field dependence of magnetization

The Curie temperature, T_C, and spontaneous magnetization at 0 K, $M_0 \equiv M(0,0)$, determined from the Arrott plots by the following procedure, are

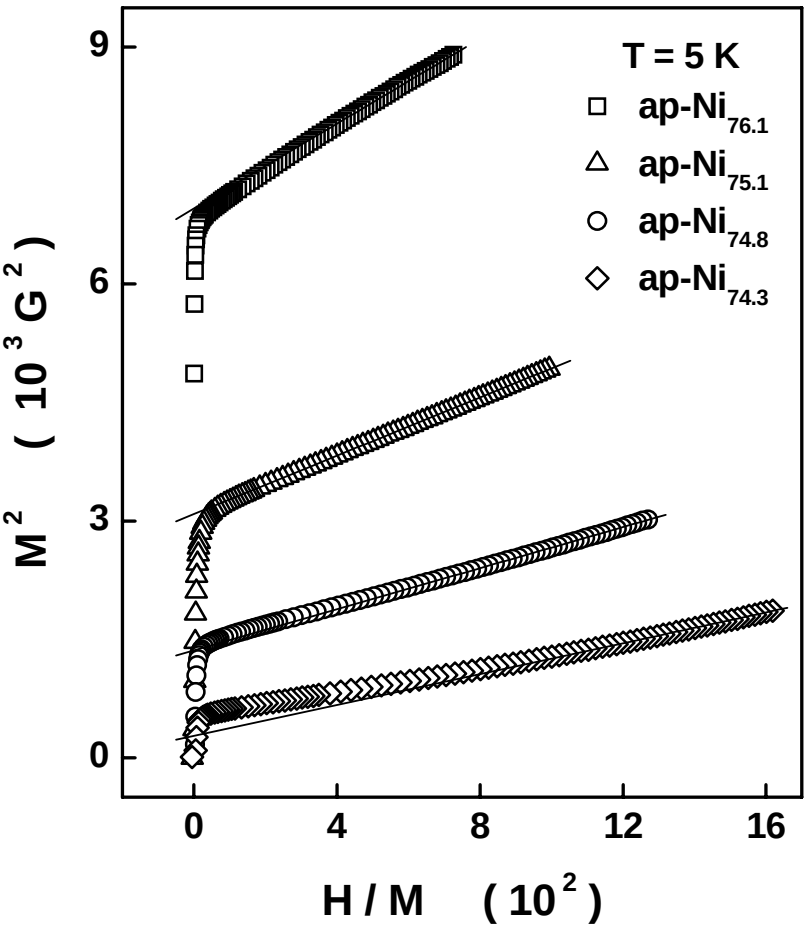

Figure 4.1: Arrott (M^2 versus H/M) plots constructed out of the M(H) isotherms taken at T = 5 K. The solid lines represent the linear extrapolation from high field data. The value of intercept to M^2-axis at H = 0 gives square of spontaneous magnetization at 5 K.

displayed in the top and bottom panels of figure 4.3. While T_C corresponds to the temperature at which the *linear* Arrott plot isotherm passes through the origin (as shown in the figure 4.13 in the sub-section **4.3.4**), M_0 is computed from the intercept on the ordinate yielded by a linear extrapolation [1] of the high-field portion of the $M^2(T,H)$ versus $H/M(T,H)$ plot at $T = 5K$ to $H = 0$(figure 4.1). Alternatively, M_0 is extracted from the optimum fit to the $M(T = 5K, H)$ isotherm for fields above the technical saturation, i.e., over the range $2kOe \le H \le 70kOe$, based on the expression [4,13] $M(T = 5K, H) = M_0 + \lambda\sqrt{H} + \chi_{hf} H$, where the $\sqrt{H}$ term accounts for the

suppression of spin waves by the field H [19] and the high-field susceptibility, χ_{hf}, is related to the exchange-enhanced Pauli spin susceptibility [1,10]. The continuous curves through the $M(T = 5K, H)$ data, shown in figure 4.2, represent the best least-square fits to the data based on the above expression. Both the determinations yield the same value (within the uncertainty limits) for

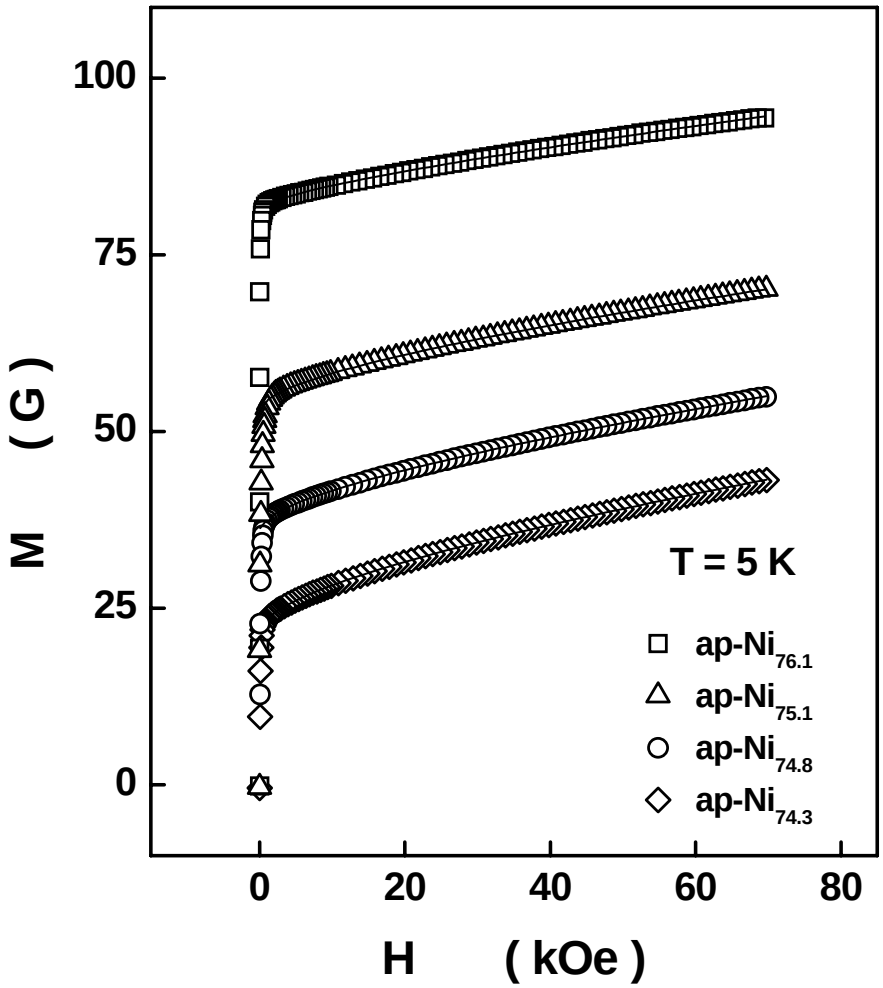

Figure 4.2: M(H) isotherms at T = 5 K. Continuous solid lines represent the best least square fits based on the equation mentioned in the text below.

M_0 for a given composition. Figure 4.3 compares the values of T_C and M_0, so obtained, for the samples *ap-Ni*$_{74.3}$, *ap-Ni*$_{74.8}$, *ap-Ni*$_{75.1}$ and *ap-Ni*$_{76.1}$, with those determined for the same samples (samples of similar composition) from resistivity and magnetoresistance in chapter 3 or [18] (in the literature [1-

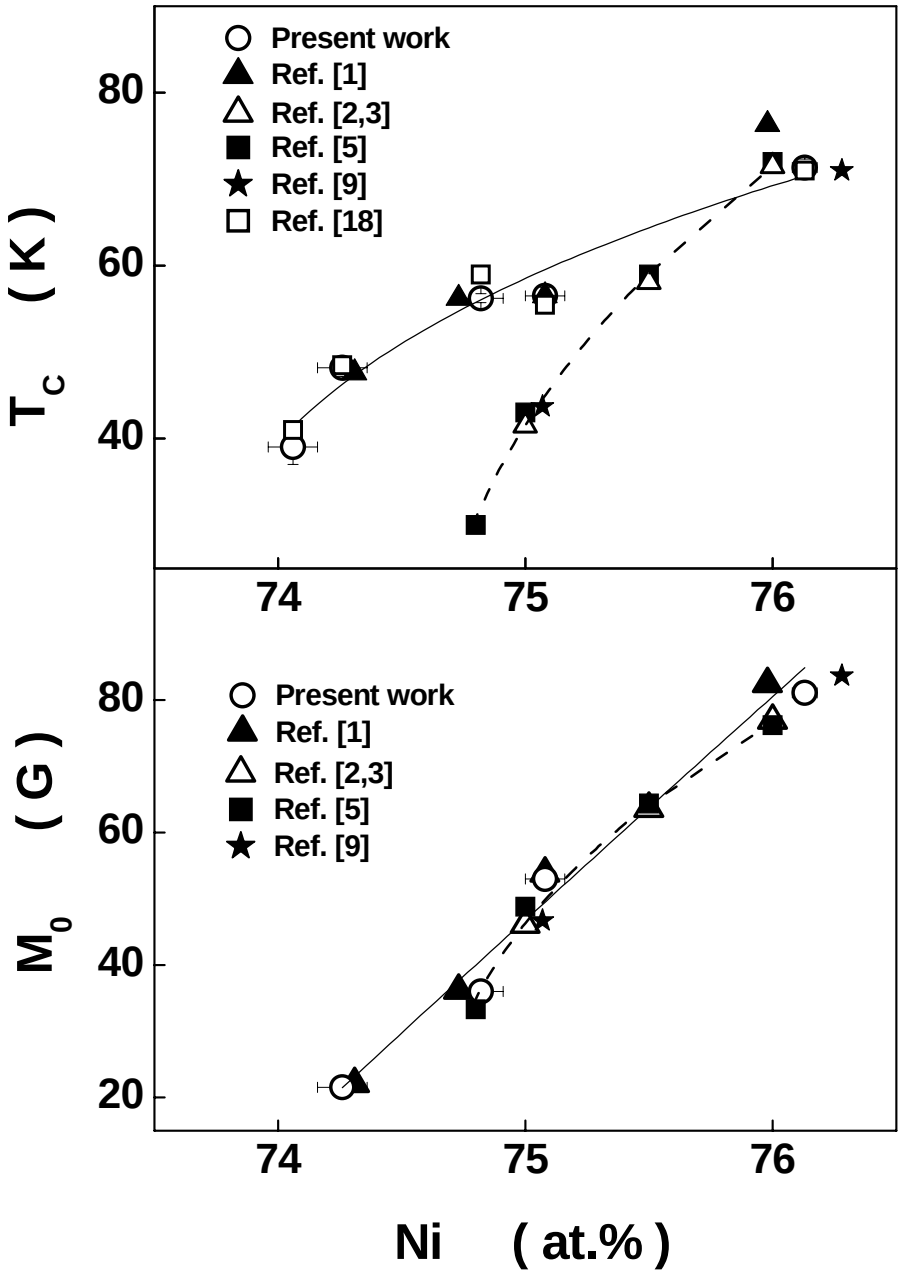

Figure 4.3: Variations of T_C and M_0 with Ni concentration, x, compiled from the values of T_C and M_0 obtained in the present work and those reported previously on the alloys with the same or similar composition. Continuous (dashed) curves represent the best least-squares fits to our (those reported in references 2, 3, 5 and 9) $T_C(x)$ and $M_0(x)$ data based on the power laws mentioned in the text.

4,5,9]). Note that only the *Ni* atoms carry magnetic moment in the alloys in question and hence compositional and/or site disorder in the *Ni* sublattice alone is of direct relevance so far as the magnetic properties are concerned.

Considering that the *'as-prepared' samples* used in the present magnetization, resistivity and magnetoresistance [18] measurements and in the previous study [1] have *both compositional disorder and site disorder* whereas the *well-annealed* (and hence completely ordered) *counterparts* used in earlier investigations [2,3,5,9] have *only compositional disorder*, the following unambiguous conclusions about the roles of compositional disorder and site disorder can be drawn from the comparison made in Fig. 4.3. (i) With increasing compositional disorder, i.e., as $x \to x_c$, T_C and M_0, in the alloys with compositional disorder alone, decrease in accordance with the power laws (dashed curves) $T_C(x) = t_x\ (x - x_c)^{\tau}$ and $M_0(x) = m_x\ (x - x_c)^{\psi}$ with $x_c = 74.60(6)\,at.\%$, $\tau = 0.43(5)$ and $\psi = 0.40(8)$. (ii) The effect of site disorder is to slow down the variations (continuous curves) of T_C and M_0 with *x* such that the above power laws still hold but with $x_c = 73.6(1)\ at.\%$, $\tau = 0.33(3)$ and $\psi = 1.00(5)$. Alternatively, compared to the values of T_C for the Ni_xAl_{100-x} alloys with compositional disorder alone, site disorder enhances T_C for a given composition (leaves T_C essentially unaltered) and this enhancement grows rapidly as $x \to x_c$ (for $x \geq 76\,at.\%$). In sharp contrast with this behaviour, except for $x \approx x_c$, M_0 is relatively *insensitive* to site disorder. Why $T_C(x)$ is more sensitive to site disorder than $M_0(x)$, can be understood [1,10], as follows, in terms of the spin fluctuation theories [12 – 14] that yield the expressions for T_C and M_0

$$T_C = \left(\frac{2\pi^2}{5\alpha}\right)^{3/4} \left(\frac{c_v}{k_B}\right) (\hbar\gamma_v)^{1/4}\ {M_0}^{3/2} \qquad (4.1)$$

$$M_0 = N\,\mu_B\,2^{1/2}\left\{[N'(E_F)]^2 - [N''(E_F)\,N(E_F)/3]\right\}^{-1/2}[N(E_F)]^2\,[I\,N(E_F)-1]^{1/2} \tag{4.2}$$

In equations (4.1) and (4.2), the coefficient of the gradient term in the Ginzburg-Landau expansion, c_ν, is a measure of the spin-fluctuation stiffness, while γ_ν and the quantity within the curly brackets in Eq. (4.2) depend on the shape of the density of states (DOS) curve near the Fermi level, E_F, as well as on the DOS at E_F, $N(E_F)$. According to these expressions, M_0 is sensitive to both $N(E_F)$ and the shape of DOS curve near E_F whereas, apart from these factors, T_C is also depends on c_ν. Thus, the insensitivity of M_0 to site disorder implies that site disorder has essentially no effect on $N(E_F)$ and the shape of DOS curve near E_F (except for $x \approx x_c$, where site disorder tends to primarily enhance $N(E_F)$ and thereby stabilize long-range ferromagnetic order for *Ni* concentrations below the threshold concentration, $x_c \cong 74.6\,at.\%$, dictated by compositional disorder). It immediately follows that as $x \to x_c$, site disorder increases the concentration of Ni atoms on the Al sub-lattice beyond that allowed by the compositional disorder and thereby enhances c_ν (and hence T_C) because of the increase in the number of Ni nearest neighbours for a given Ni atom. Site disorder, thus, lowers the critical concentration, x_c, by nearly one $at.\%\ Ni$.

Having discussed the influence of compositional disorder and site disorder on M_0 and T_C, we now focus our attention on their effect on the temperature and magnetic field dependences of magnetization in the

temperature regimes where different kinds of low-lying magnetic excitations dominantly contribute to $M(T,H)$.

4.3.1 Low temperatures (T << T_C)

In weak itinerant-electron ferromagnets without any disorder, spin-wave modes of wavevector q, in the region around $q=0$ in the Brillouin zone, exist as well-defined excitations at low temperatures, $T << T_C$. According to the spin fluctuation theory [14], this spin wave (SW) contribution to magnetization is given by

$$[M(T,0)]_{SW} = M(0,0) - g\,\mu_B\,\xi(3/2)\,[k_BT/4\pi D(T,0)]^{3/2}, \qquad H=0 \quad (4.3a)$$

$$[M(T,H)]_{SW} = M(0,H) - g\,\mu_B\,Z(3/2,t_H)\,[k_BT/4\pi D(T,H)]^{3/2}, \quad H\neq 0 \quad (4.3b).$$

In these equations, the Bose function $Z(3/2,t_H)=\sum_{n=0}^{\infty} n^{-3/2}e^{-nt_H}$ with the reduced field $t_H = g\mu_B H/k_BT$ allows for the energy gap in the spin wave spectrum, introduced by H_{ext} and anisotropy fields, and D is the spin-wave stiffness. In the case of weak itinerant-electron ferromagnets, D renormalizes with temperature as $D(T)=D(0)\,(1-D_2\,T^2)$ where the spin-wave stiffness at 0 K, $D_0 \equiv D(0) = g\,\mu_B\,c_\perp\,M(0,0)$, is independent of field. An attempt has been made to determine D_0, the thermal-renormalization coefficient, D_2, $M_0 \equiv M(0,0)$ and 'in-field' magnetization at 0 K, $M(0,H)$, from the fits to the $M(T,0)$ and $M(T,H)$ data based on equations (4.3a) and (4.3b), respectively, using the 'range-of-fit' analysis in which the variation in the above-mentioned parameters is monitored as the temperature range ($T << T_C$) of the fit is varied. Due to the extra temperature variations introduced by the thermal

renormalization of spin wave stiffness and the presence of the function $Z(3/2,t_H)$ in Eq. (4.3b), Eqs. (4.3a) and (4.3b) predict a *concave-downward* curvature in the $M(T,0)$ versus $T^{3/2}$ and $M(T,H)$ versus $T^{3/2}$ plots. In sharp contradiction with this prediction, the $M(T,H=1kOe)$ versus $T^{3/2}$ plots for *ap-Ni*$_{74.3}$ and *ap-Ni*$_{74.8}$ alloys, shown in the insets of figure 4.4(a) and 4.4(b), exhibit a *concave-upward* curvature, which is more pronounced in the alloy *ap-Ni*$_{74.3}$ whose composition is closer to the critical concentration $x_c \cong 73.6 at.\%$. Exactly the same behaviour was observed previously [1] in the alloys of similar composition. Thus, Eqs. (4.3a) and (4.3b) cannot describe the

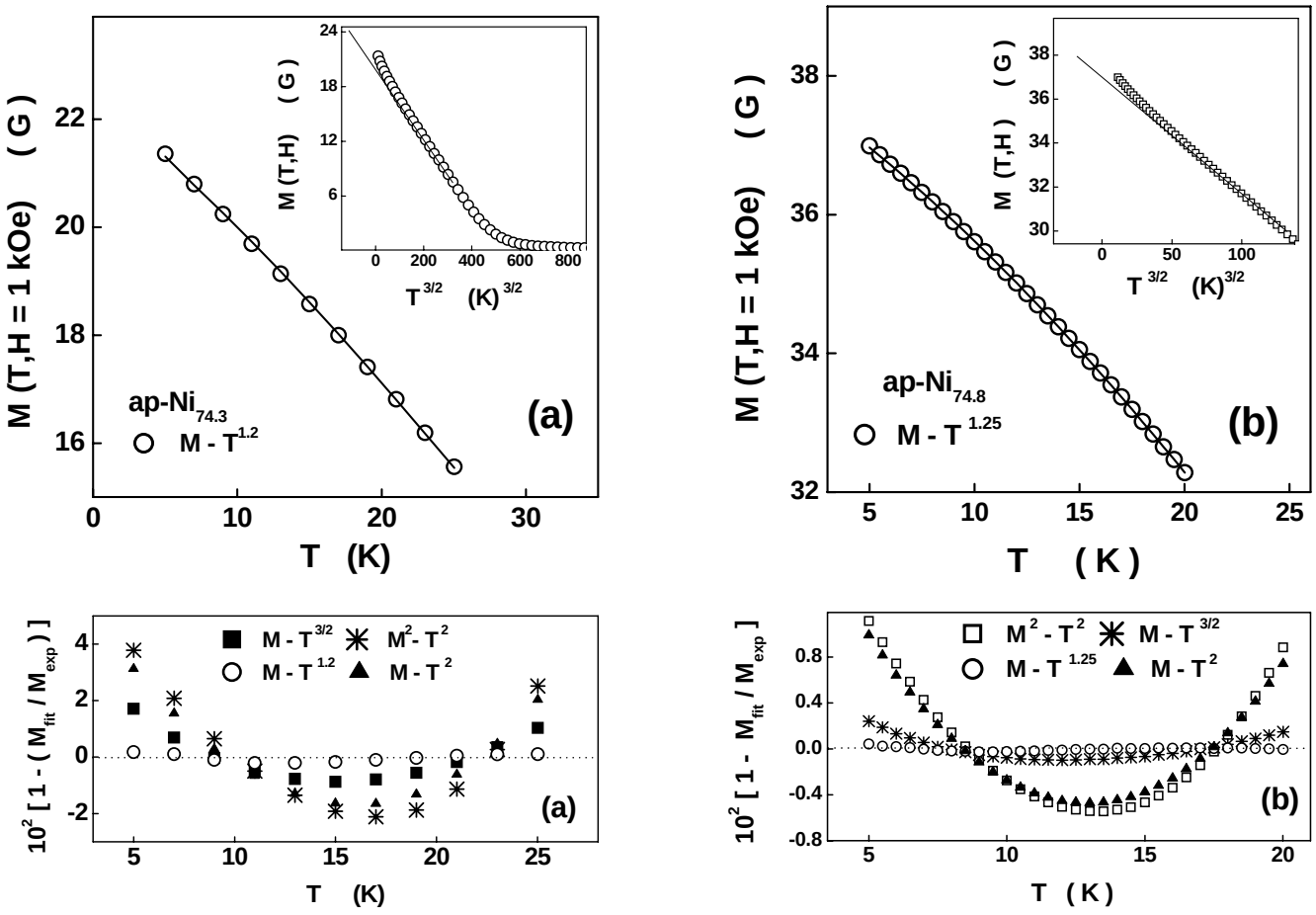

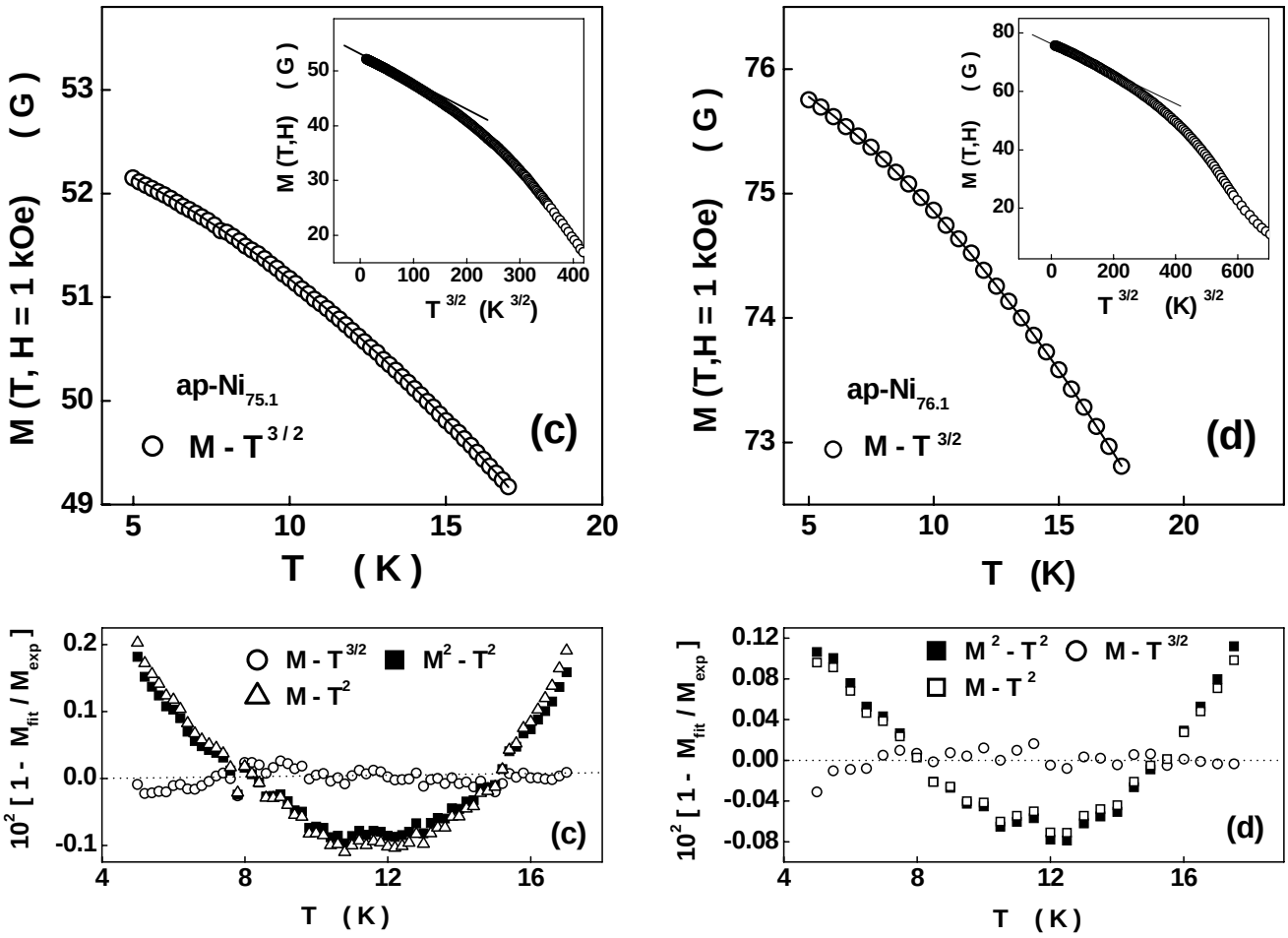

Figure 4.4: The upper panels (a), (b), (c) and (d) display M(T,H =1 kOe) as a function of temperature at low temperatures for the samples ap-$Ni_{74.3}$, ap-$Ni_{74.8}$, ap-$Ni_{75.1}$ and ap-$Ni_{76.1}$ along with the best least-squares fits (continuous curves) through the data (open circles) based on the equations (4.3b) and (4.4) of the text, while the lower panels show the corresponding percentage deviations of the data from the fits based not only on the equations (4.3b) and (4.4) but also on the other expressions used previously in the literature. The insets in the upper panels serve to highlight the concave-upward deviations of the data from the spin-wave $T^{3/2}$ law in the case of the samples ap-$Ni_{74.3}$ and ap-$Ni_{74.8}$.

temperature dependence of magnetization in the alloys *ap-$Ni_{74.3}$* and *ap-$Ni_{74.8}$*. By contrast, the $M(T, H = 1kOe)$ versus $T^{3/2}$ plots for the *ap-$Ni_{75.1}$* and *ap-$Ni_{76.1}$* alloys, displayed in the insets of figure 4.4(c) and 4.4(d), show the expected curvature and Eq.(4.3b) does indeed closely reproduce (continuous curves through the data points, represented by symbols) the observed temperature dependence of magnetization at 1 *kOe*, as is evident from Fig.

4.4(c) and 4.4(d). The percentage deviations of the data from the best least-squares (LS) fits based on Eq.(4.3b), shown in the bottom panels of 4.2(c) and 4.2(d), do not exceed ± 0.02 in the temperature range $5K \le T \le 18K$. These LS fits yield the values for D_0 as 67.5(5) meV Å^2 and 70(1) meV Å^2 for the alloys *ap-Ni$_{75.1}$* and *ap-Ni$_{76.1}$*, respectively. Lower magnitude of D_0 in 'as-prepared' *Ni$_{75.1}$* (*Ni$_{76.1}$*) compared to $D_0 = 69.6(14)$ meV Å^2, from the magnetization data [10,11] or $D_0 = 85(15)$ meV Å^2 ($D_0 = 95(5)$ meV Å^2), from inelastic neutron scattering results [20] ([21]), for well-annealed, and hence completely ordered, counterpart, basically reflects a reduction in the coefficient $c_\perp$ by site disorder. That this is indeed the case is obvious from the relation $D_0 = g\,\mu_B\,c_\perp\,M_0$ and our observation that site disorder has essentially no effect on M_0 in this concentration range (Fig.4.3).

The deviation plots, shown in the lower panels of Fig. 4.4(a) and 4.4(b), clearly demonstrate that the functional form

$$M(T,H) = M(0,H)\left(1 - A_n(H)\,T^n\right) \tag{4.4}$$

with $n = 1.20(1)$ and $n = 1.25(1)$ describes the $M(T, H = 1kOe)$ data in the temperature ranges $5K \le T \le 25K$ and $5K \le T \le 20K$ for the samples *ap-Ni$_{74.3}$* and *ap-Ni$_{74.8}$* far better than either Eq.(4.3b) or other forms $M \sim T^2$ [2,4,5] and $M^2 \sim T^2$ [6,7] used in the literature for completely ordered samples. Spin fluctuation theories [19, 20] of non-Fermi liquid behaviour, that do not include any kind of disorder, predict $n = 4/3$ for a three-dimensional weak itinerant-electron ferromagnet. The finding that the values of the exponent *n* for the samples *ap-Ni$_{74.3}$* and *ap-Ni$_{74.8}$* are closer to this value (1.33) than $n = 1.5$,

expected for the normal spin-wave behaviour at low temperatures, asserts that these samples, with composition close to the critical concentration $x_c = 73.6(1)\ at.\%$, exhibit non-Fermi liquid behaviour. This inference is not only consistent with the similar behaviour observed in the resistivity [18] (specific heat [8]) of these samples (the samples with similar composition) in nearly the same temperature ranges but also with the premise that the non-Fermi liquid behaviour for $x \approx x_c$ is a consequence of the alteration in the spin-wave dispersion, leading to severe damping of spin waves, brought about primarily by compositional disorder (with site disorder only tending to enhance the effect of compositional disorder); for details, see the paragraph following Eq.(3.7) in chapter 3.

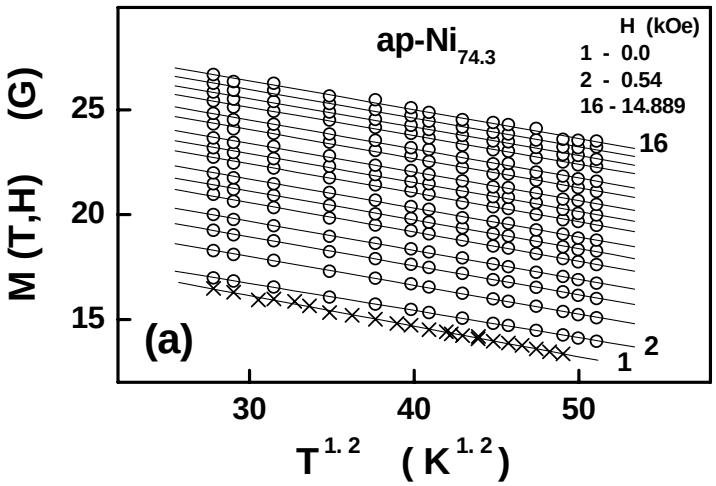

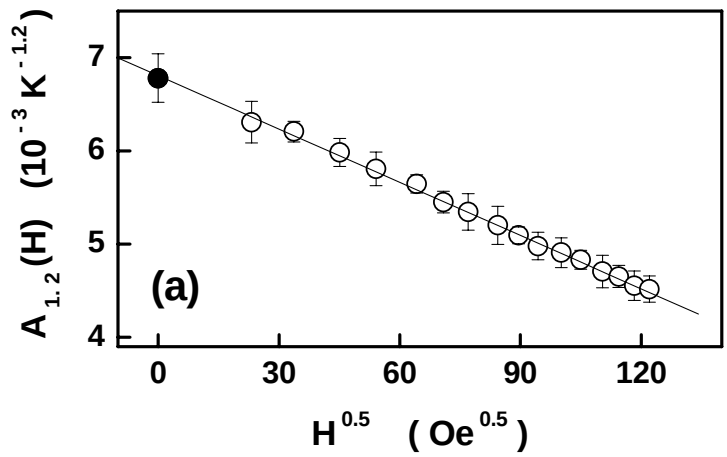

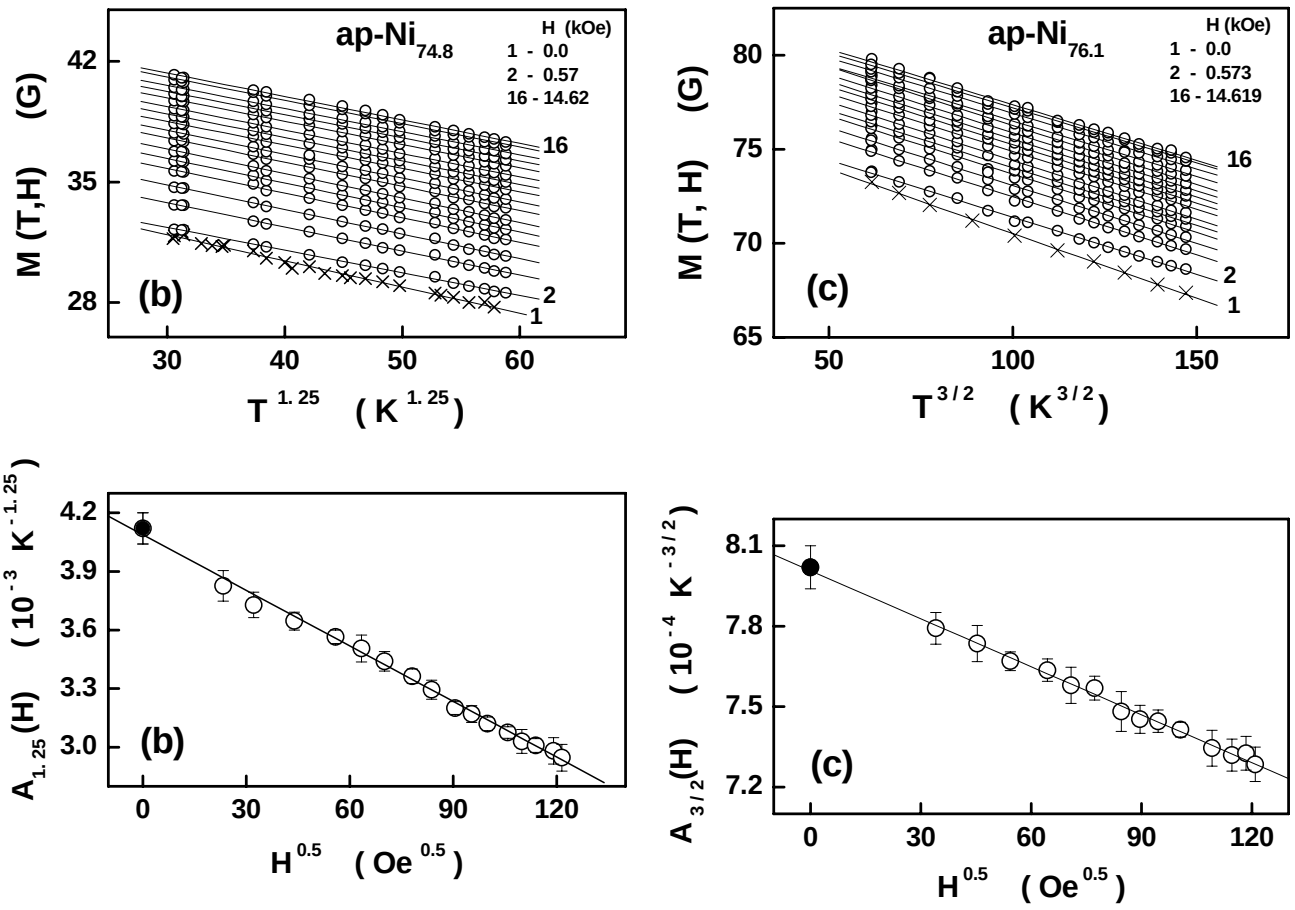

Figure 4.5: The upper panels (a), (b) and (c) display the low-temperature M - T^n plots with n = 1.2, 1.25 and 1.5 at a few representative but fixed values of H for the samples ap-$Ni_{74.3}$, ap-$Ni_{74.8}$ and ap-$Ni_{76.1}$, respectively. The continuous lines through the M(T, H) data (open circles) and M(T, H = 0) data (crosses) are the least-squares fits based on the equation (4). The lower panels (a) – (c) demonstrate that the coefficient A_n of the T^n term in equation (4.4) varies linearly with $H^{0.5}$ and thereby testify to the validity of equation (4.5).

The suppression of spin waves or overdamped spin waves by the external magnetic field can be quantified by monitoring the field dependence of either the coefficient, $A_{3/2}$, of the $T^{3/2}$ term when Eq.(4.3b) is cast in the form of Eq.(4.4) or the coefficient A_n in Eq.(4.4). The coefficients A_n with $n = 1.2$, 1.25, 1.5 are nothing but the slopes of the *linear* $M - T^n$ plots at fixed values of *H*, shown in the top panels of figure 4.5(a), 4.5(b) and 4.5(c) for the samples *ap-*$Ni_{74.3}$, *ap-*$Ni_{74.8}$ and *ap-*$Ni_{76.1}$. That the exponent *n* does not depend on *H*

but the coefficient A_n of the T^n term decreases with increasing H in accordance with the relation [19]

$$A_n(H) = A_n(0)\left(1 - \nu\, H^{1/2}\right), \tag{4.5}$$

is evident from the data presented in the bottom panels of Fig. 4.5. The spin fluctuation theory [19] thus correctly predicts a *field-independent* exponent *n* and the $\sqrt{H}$ suppression of spin waves with magnetic field. For a given composition, the value of $A_n(0) \equiv A_n(H=0)$, obtained by extrapolating the

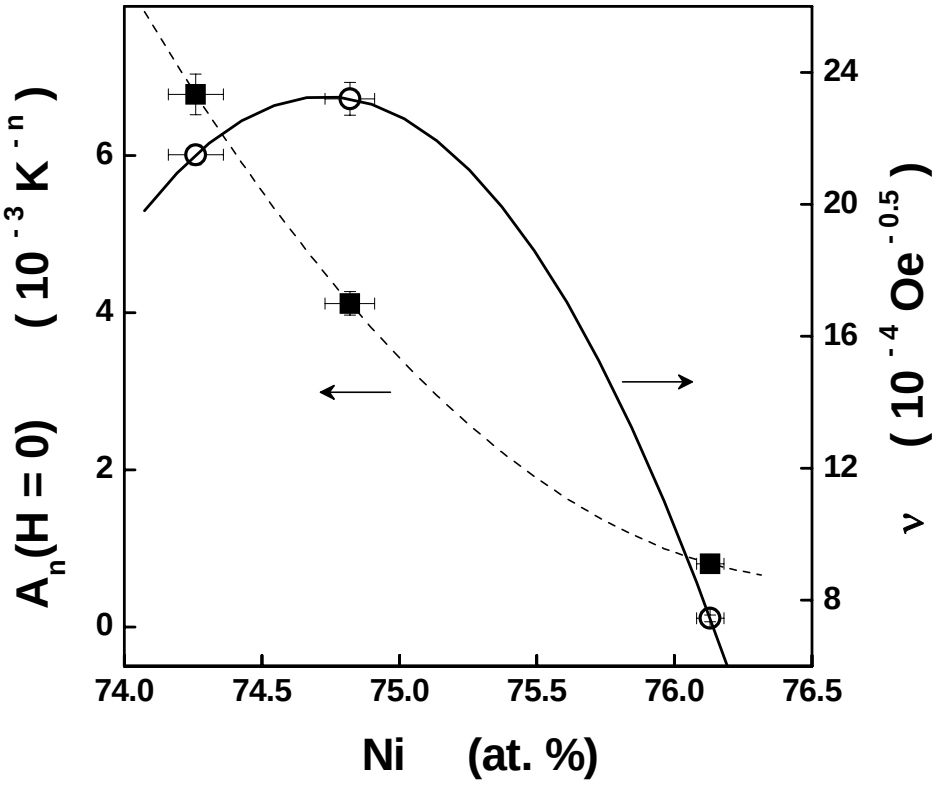

Figure 4.6: Variations of the prefactor $A_n(0) \equiv A_n(H=0)$ and the coefficient ν (appearing in equation (5)) with Ni concentration. Smooth curves through the data serve only as a guide to the eye.

linear $A_n(H) - \sqrt{H}$ plot (the least-squares fit straight lines shown in the bottom panels of Fig.4.5) to $H = 0$, exactly coincides with that (solid circle) determined directly from the slope of the linear spontaneous magnetization,

$M(T, H = 0)$, versus T^n plot (the straight lines through the data points denoted in Fig. 4.5 by crosses). Figure 4.6 displays the variations of $A_n(H = 0)$ and ν with the Ni concentration, *x*. While $[A_n(H = 0)]^{-1}$ is a measure of spin-wave stiffness (cf. Eqs.(4.3a) and (4.4)), the coefficient ν of the $\sqrt{H}$ term quantifies the suppression of spin waves by *H*. Thus, the observed increase in $A_n(H = 0)$ as $x \to x_c$ implies that the compositional disorder lowers the thermal energy required to excite long-wavelength spin waves. Similarly, the observed variation of ν with *x* conveys that the compositional disorder promotes the field-induced suppression of spin waves by reducing their stiffness.

4.3.2 Intermediate temperatures ($T < T_C$)

In the intermediate range of temperatures, the spin-wave contribution to $M(T,0)$ and $M(T,H)$ is completely masked by that arising from non-propagating spin fluctuations (SF). The self-consistent spin-fluctuation calculations [14] yield the following expression for the spin-fluctuation contribution to magnetization at intermediate temperatures

$$[M(T,H)]_{SF} = M(0,H)\,[1 - A_2(H)\,T^2 - A_{4/3}\,T^{4/3}]^{1/2}, \qquad (4.6)$$

which is valid for both $H = 0$ and $H \neq 0$. In equation (4.6), the T^2 term is solely due to the thermally-excited (TE) spin fluctuations while the $T^{4/3}$ term is the net result of the competing claims [14] made by TE and zero-point (ZP) components of spin fluctuations with ZP contribution dominating over the TE one. The TE contribution gets progressively suppressed by *H* whereas the ZP contribution is nearly independent of *H*. The 'range-of-fit' analysis of the $M(T, H = 1kOe)$ data based on Eq.(4.6) yielded different results for different

compositions (figure 4.7). Since the contribution of spin waves to magnetization persists to temperatures well above $0.5T_C$ in *ap-$Ni_{74.3}$*, an extremely narrow intermediate temperature range precluded a meaningful

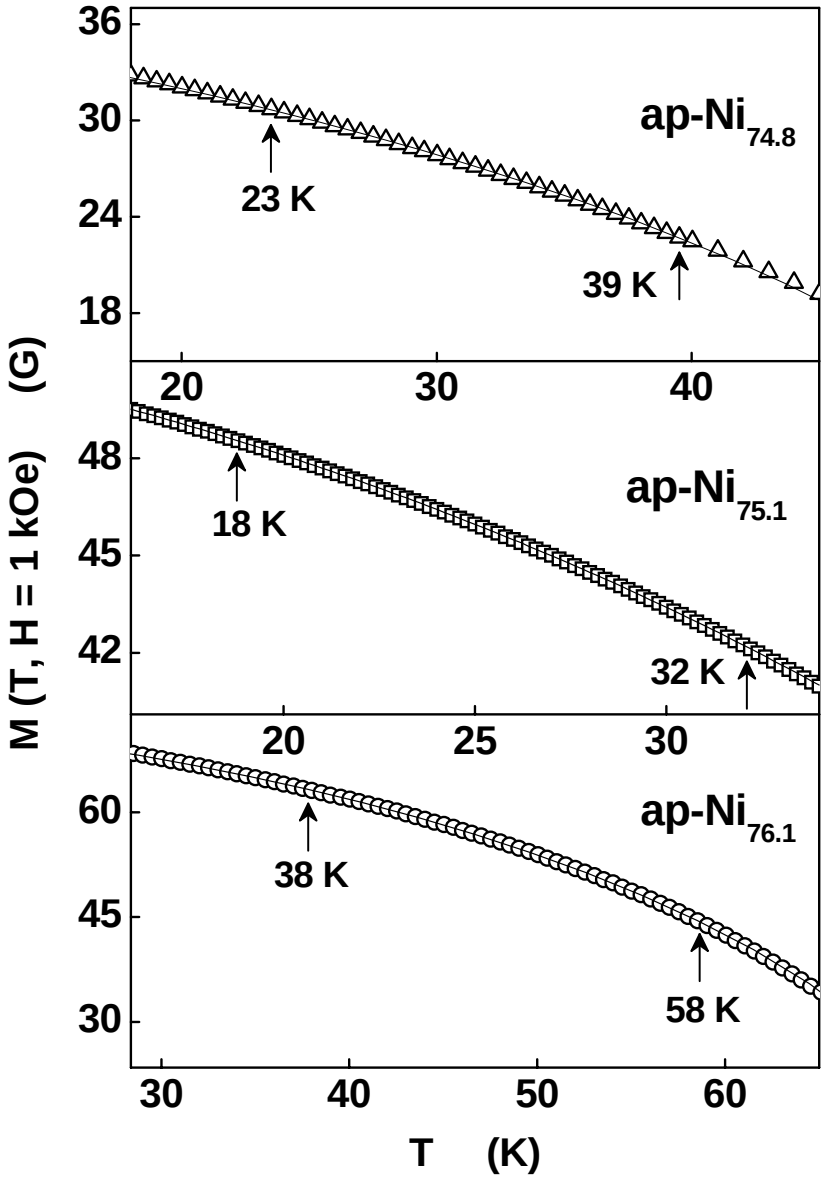

Figure 4.7: Temperature variations of M(T, H =1 kOe) at intermediate temperatures for the samples ap-$Ni_{74.8}$, ap-$Ni_{75.1}$ and ap-$Ni_{76.1}$. The continuous curves through the data points (open symbols) represent the theoretical fits based on equation (4.6) of the text.

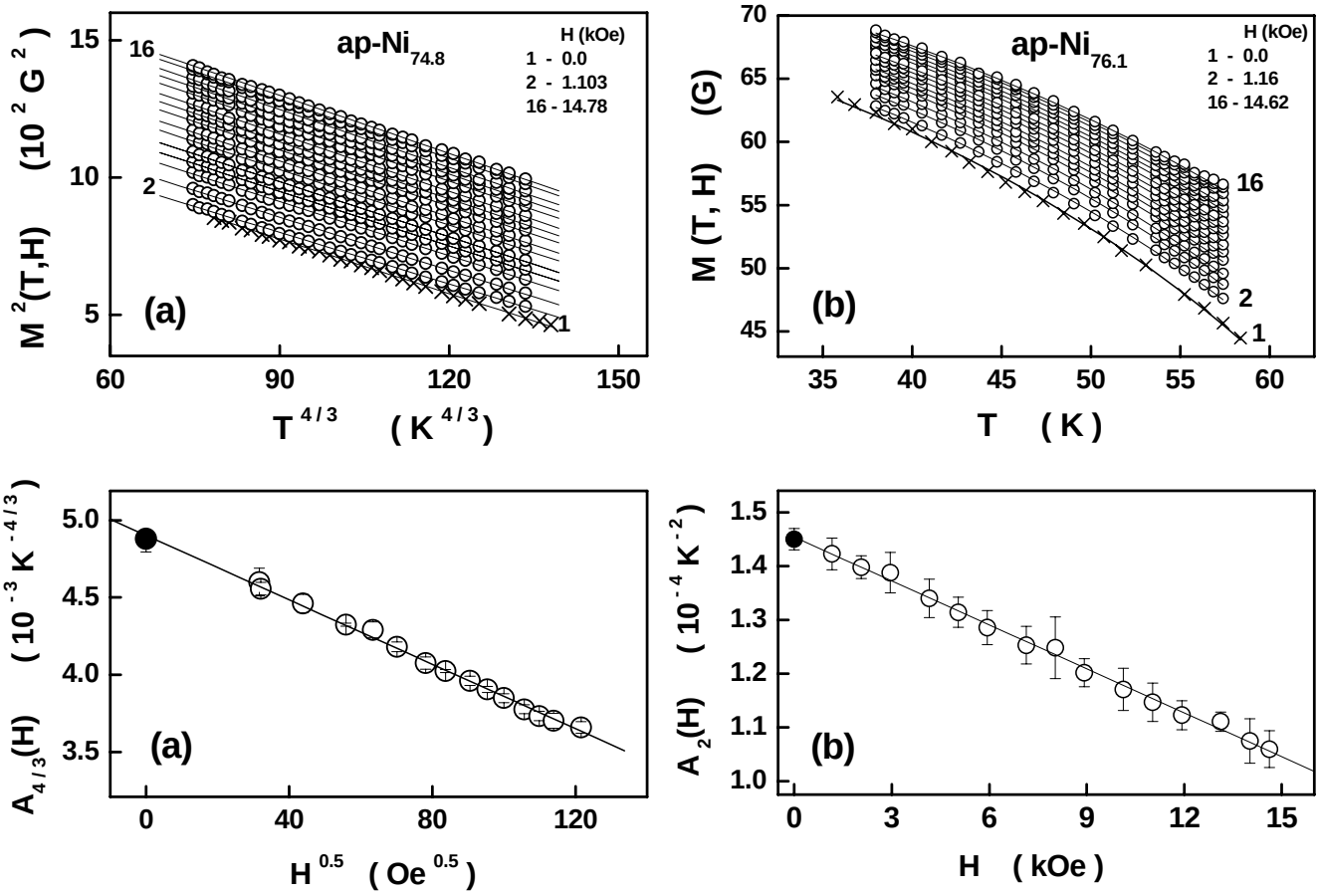

Figure 4.8: The upper panels (a) and (b) display the $M^2 - T^{4/3}$ and M - T plots at intermediate temperatures for a few representative but fixed values of H for the samples ap-$Ni_{74.8}$ and ap-$Ni_{76.1}$, respectively. The continuous lines through the M(T,H) data (open circles) and M(T,H = 0) data (crosses) are the least-squares fits based on equation (6). The lower panel (a) [(b)] demonstrates that the coefficient $A_{4/3}(H)$ [$A_2(H)$] of the $T^{4/3}$ [T^2] term in equation (4.6) varies linearly with $H^{0.5}$ [H].

comparison with theory [14], i.e., with Eq.(4.6). In the sample *ap-$Ni_{74.8}$*, the T^2 term is so small that $[M(T,H)]^2$ varies as $T^{4/3}$ (the upper panel in figure 4.8(a)) and contrary to the theoretical expectation [14] that the coefficient $A_{4/3}$ *is independent of H,* $A_{4/3}(H) \sim \sqrt{H}$ (see the lower panel of Fig.4.8(a)). As we shall show in the subsection 4.3.3, a total absence of the T^2 term and hence a complete dominance of the $T^{4/3}$ term, and the $\sqrt{H}$ variation of $A_{4/3}(H)$, mark the characteristic attributes of the spin-fluctuation contribution to $M(T,H)$ at

temperatures close to T_C. In this context, at intermediate temperatures, *ap-Ni*$_{74.8}$ behaves as if it were near a quantum critical point. Thus, in concurrence with the conclusions drawn from the resistivity data [18], the non-Fermi liquid behaviour is observed over an unusually wide temperature range $T \leq 0.55T_C$ in *ap-Ni*$_{74.3}$ and *ap-Ni*$_{74.8}$. Contrasted with this behaviour, Eq.(4.6) completely accounts for (continuous curves through the data points) the observed temperature dependence of $M(T,H)$ (open squares or circles) and $M(T,H=0)$ (crosses) in *ap-Ni*$_{75.1}$ and *ap-Ni*$_{76.1}$ over the temperature ranges $0.3T_C \leq T \leq 0.6T_C$ and $0.5T_C \leq T \leq 0.75T_C$, apparent in figure 4.7 and in the upper panel of figure 4.8(b). In conformity with the predictions of the self-consistent spin fluctuation model [14], the coefficient $A_{4/3}$ of the $T^{4/3}$ term is *independent* of H whereas that of the T^2 term, A_2, depends *linearly* on H (the lower panel of figure 4.8(b)) and follows the relation $A_2(H) = A_2(0)\left(1 - \varphi H\right)$ with $A_2(0) = 1.45(2) \times 10^{-4}\ K^{-2}$ and $\varphi = 1.87(5) \times 10^{-5}\ Oe^{-1}$. These values are *lower* than those $A_2(0) = 3.12(2) \times 10^{-4}\ K^{-2}$ and $\varphi = 2.12(13) \times 10^{-5}\ Oe^{-1}$ reported [10, 11] for the ordered Ni_3Al compound. Recognizing that [14] $[A_2(0)]^{-1}$ is a measure of the spin-fluctuation stiffness while the slope φ of the A_2 versus H straight line quantifies the suppression of thermally-excited (TE) spin fluctuations by magnetic field, reduced values of $A_2(0)$ and φ in the sample *ap-Ni*$_{76.1}$ indicate that, with increasing Ni concentration, the TE spin fluctuations become more 'stiff' and hence the rate of their suppression with H also slows down.

4.3.3 Temperatures close to T_C

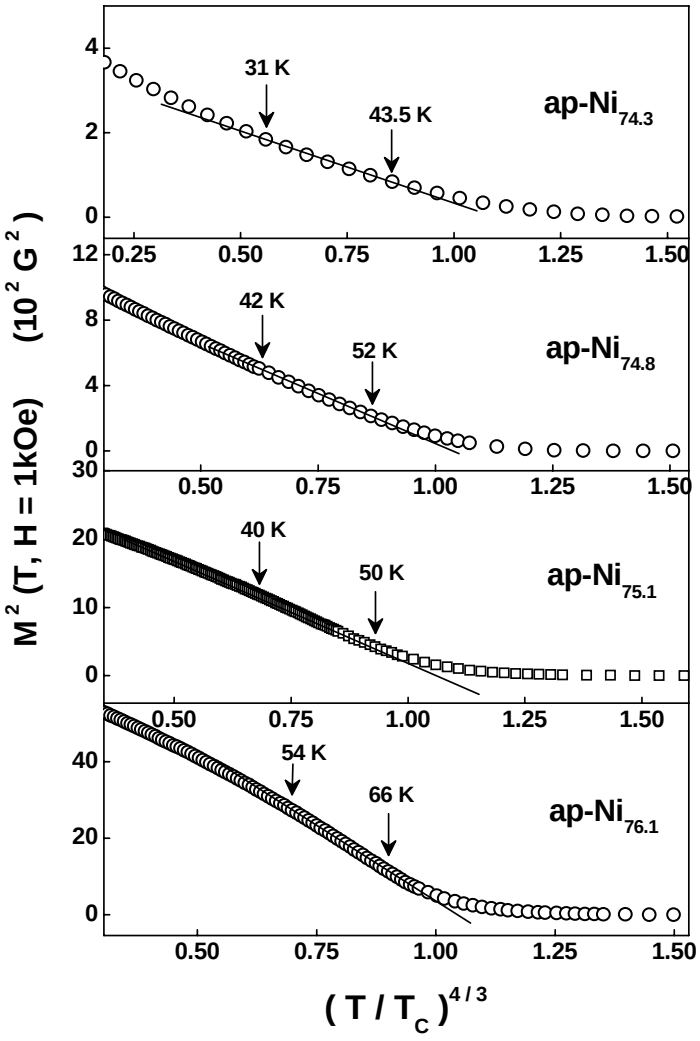

Figure 4.9: $M^2(T, H=1\ kOe)$ as a function of $(T/T_C)^{4/3}$ at temperatures close to the Curie point, T_C, for the samples ap-$Ni_{74.3}$, ap-$Ni_{74.8}$, ap-$Ni_{75.1}$ and ap-$Ni_{76.1}$. The best least-squares fits (continuous curves) through the data (open symbols) are based on the equations (4.7) of the text.

For temperatures close to T_C but outside the critical region, the self-consistent calculations [14] of the thermally-excited (TE) and/or zero-point (ZP) spin-fluctuation contributions to magnetization, in the presence ($H \neq 0$) and absence ($H = 0$) of magnetic field, yield the expression

$$[M(T,H)]_{SF} = M(0,H)\,[1 - A_{4/3}(H)\ T^{4/3}]^{1/2} \qquad (4.7)$$

and make the specific prediction [14]

$$A_{4/3}(H) = A_{4/3}(H=0)\ [1-\eta\ H^{1/2}] \tag{4.8}$$

about the functional form of the coefficient $A_{4/3}(H)$ of the $T^{4/3}$ term in equation (4.7). In Eq.(4.7), the $T^{4/3}$ term for $H=0$ (or equivalently, $A_{4/3}(H=0)$) originates from both ZP and TE spin fluctuations whereas the same term in finite fields, i.e., $A_{4/3}(H\neq 0)$, arises from the TE spin fluctuations alone. An elaborate analysis of the $M(T,H)$ and $M(T,H=0)$ data taken at temperatures close to T_C (typically in the temperature range, $0.75T_C \le T \le 0.93T_C$) based on Eq.(4.7), along

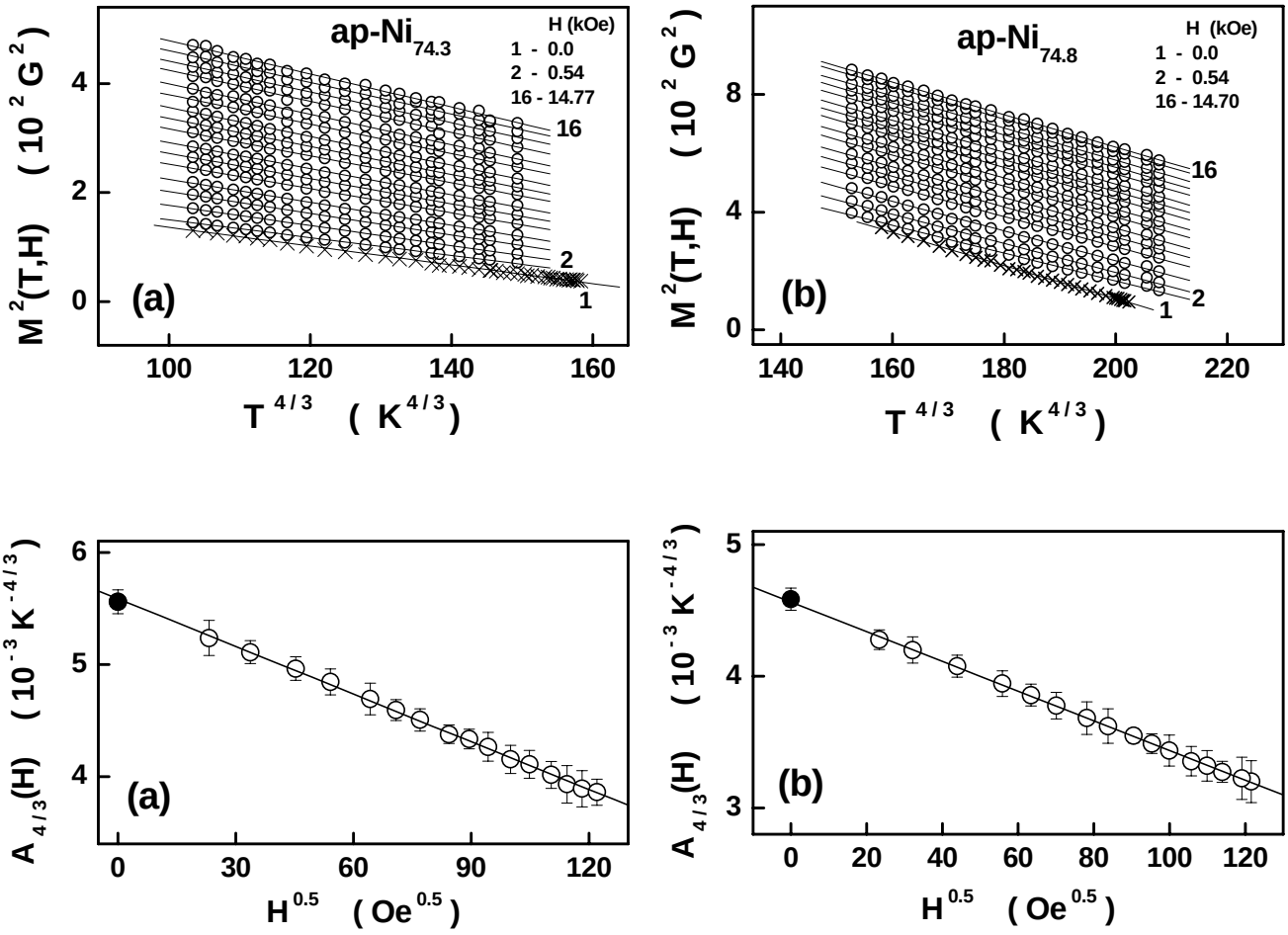

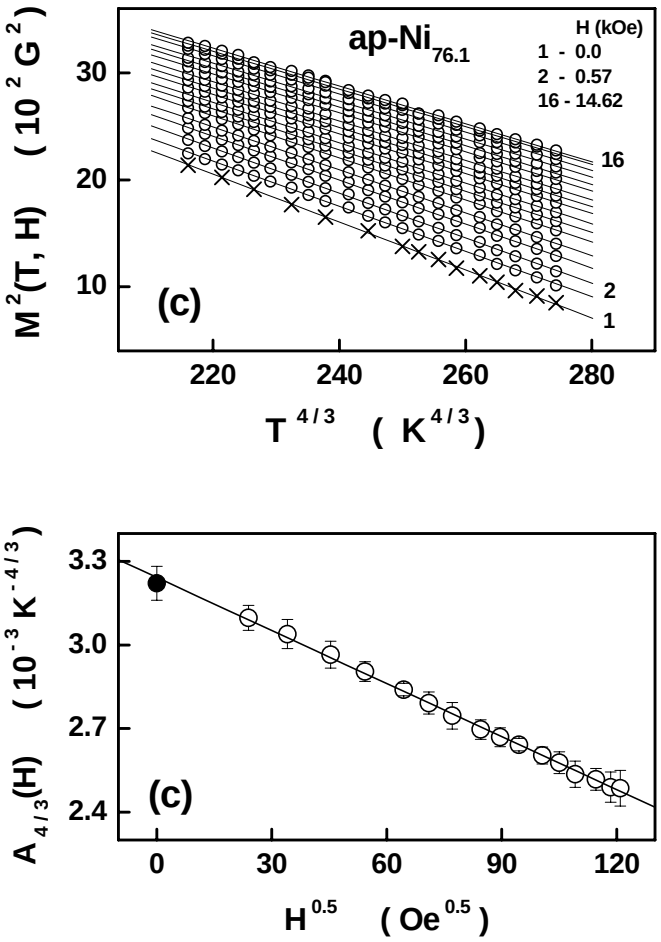

Figure 4.10: The upper panels (a), (b) and (c) display the $M^2 - T^{4/3}$ plots at temperatures close to T_C for a few representative but fixed values of H for the samples ap-$Ni_{74.3}$, ap-$Ni_{74.8}$ and ap-$Ni_{76.1}$, respectively. The continuous lines through the $M^2(T, H)$ data (open circles) and $M^2(T, H = 0)$ data (crosses) are the least-squares fits based on equation (4.7). The lower panels (a) – (c) demonstrate that the coefficient $A_{4/3}(H)$ of the $T^{4/3}$ term in equation (4.7) varies linearly with $H^{0.5}$ and thereby testify to the validity of equation (4.8).

the lines already described in sub-sections 4.3.1 and 4.3.2, allows us to make the following important observations. (i) That the observed functional forms of the 'in-field' magnetization, $M(T,H)$, and spontaneous magnetization, $M(T,H=0)$, at such temperatures, are best described by Eq.(4.7), is evident from the linear $M^2(T,H) - T^{4/3}$ (open circles) and $M^2(T,H=0) - T^{4/3}$ (crosses) plots, shown in figure 4.9 and the upper panels of figure 4.10. (ii) Similarly, the linear variation of the coefficient $A_{4/3}(H)$ with $\sqrt{H}$ (the lower

panels of figure 4.10) conforms very well with the theoretical prediction [14], Eq.(4.8). Furthermore, a linear extrapolation of the $A_{4/3}(H) - \sqrt{H}$ plots to $H = 0$ always yields the same value (within the uncertainty limits) for $A_{4/3}(H = 0)$ as that directly determined (solid circle) from the slope of the linear $M^2(T, H = 0) - T^{4/3}$ plot. (iii) Both $A_{4/3}(H = 0)$ and η decrease with increasing Ni concentration, as shown in figure 4.11. The values $A_{4/3}(H = 0) = 4.65(3) \times 10^{-3}\ K^{-4/3}$ and $\eta = 2.63(2) \times 10^{-3}\ Oe^{-1/2}$, reported [10,11] for the *ordered* Ni_3Al, included in Fig. 4.11 for comparison, are much higher than the 'as-prepared' site-disordered counterpart.

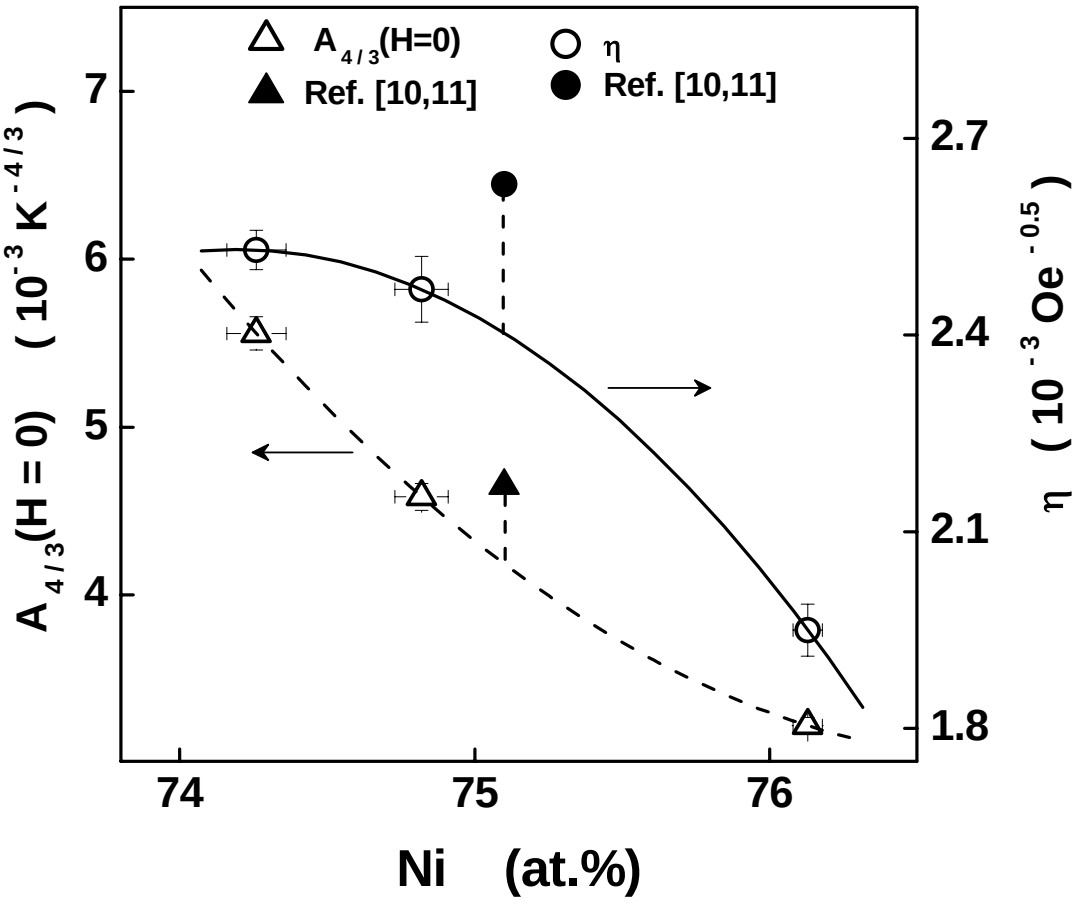

Figure 4.11: Variations of the prefactor $A_{4/3}(H = 0)$ and the coefficient η (appearing in equation (8)) with Ni concentration. The values for $A_{4/3}(H = 0)$ and η reported in references [10,11] for the stoichiometric composition are included for comparison. Smooth curves through the data serve only as a guide to the eye.

Considering that both ZP and TE (only TE) spin fluctuations give rise to $A_{4/3}(H=0)$ ($A_{4/3}(H\neq 0)$), $[A_{4/3}(H=0)]^{-1}$ is a direct measure of the 'stiffness' of the ZP and TE spin fluctuations while the coefficient η in the expression, Eq.(4.8), for $A_{4/3}(H)$ *quantifies* the suppression of TE spin fluctuations by magnetic field. In view of this assignment, the above observation (iii) implies that increasing compositional disorder ($x \rightarrow x_c$) progressively lowers the 'stiffness' of the ZP and TE spin fluctuations so thatthe suppression of TE fluctuations, in particular, by field becomes correspondingly large (the ZP contribution is essentially independent of H [14]); site disorder also plays the same role so far as the stoichiometric composition is concerned. This inference becomes all the more evident when Eq.(4.8) is cast into the following scaling form.

$$[A_{4/3}(H)/A_{4/3}(H=0)] = 1 - (H/H_0)^{1/2} \qquad (4.9)$$

where $H_0 = \eta^{-2}$ denotes the critical field at which the contribution to magnetization arising from the thermally-excited spin fluctuations gets completely quenched. While figure 4.12 serves to demonstrate the validity of this scaling for the samples *ap-Ni*$_{74.3}$, *ap-Ni*$_{74.8}$ and *ap-Ni*$_{76.1}$, its inset shows that lower and lower fields are required to quench the TE spin-fluctuation contribution as the compositional disorder increases, i.e., as $x \rightarrow x_c$. The same decreasing trend in the fields required to quench the TE spin-fluctuation contribution to resistivity with the increasing degree of compositional disorder was observed in chapter 3 but the values of H_0 were an order of magnitude higher. Another important aspect of the presently determined values of $A_{4/3}(H=0)$ is that they yield the values for the Curie temperature

$T_C^{SF} \cong 49.1K$, 56.8 K and 72.3 K for the samples *ap-Ni*$_{74.3}$, *ap-Ni*$_{74.8}$ and *ap-Ni*$_{76.1}$, respectively, when the relation [14] $T_C^{SF} = [A_{4/3}(H=0)]^{-3/4}$ is used. These values are fairly close to the actual values of T_C determined from the Arrott plots (figure 4.13).

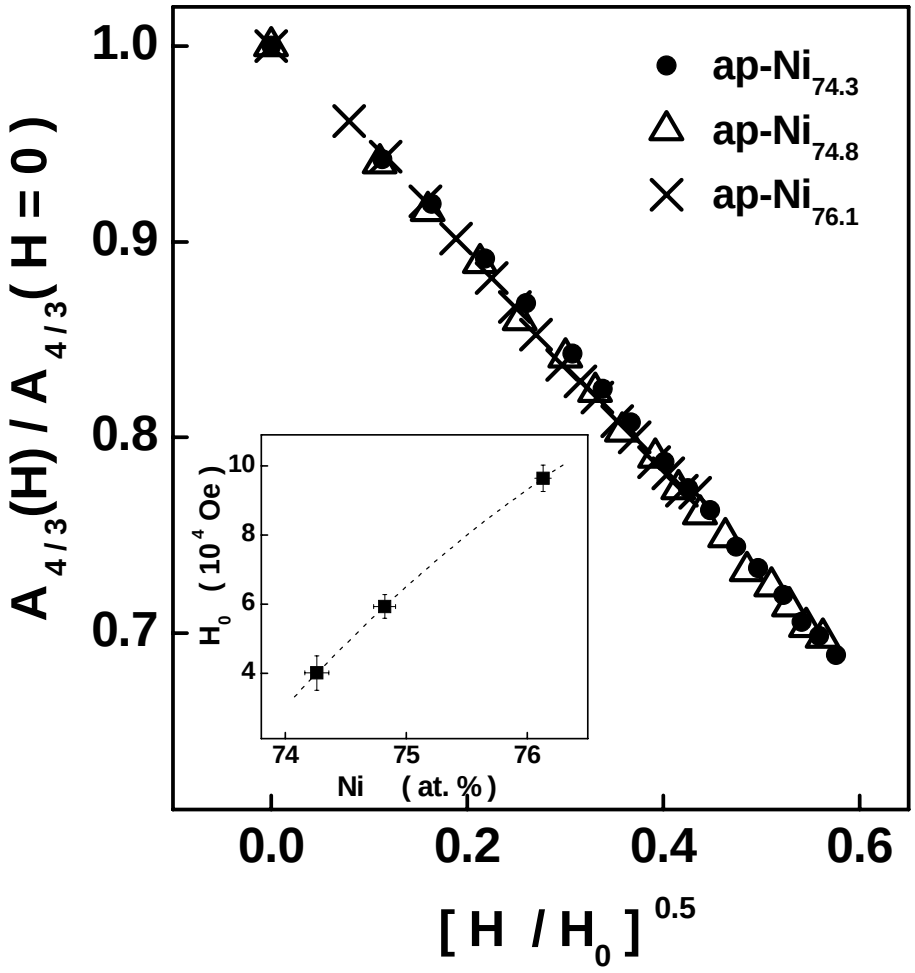

Figure 4.12: $A_{4/3}(H)/A_{4/3}(H=0)$ versus $(H/H_0)^{0.5}$ scaling plot for the samples ap-Ni$_{74.3}$, ap-Ni$_{74.8}$ and ap-Ni$_{76.1}$. The inset depicts the variation of the critical field H_0 (required to quench the spin-fluctuation contribution to magnetization at temperatures close to T_C) with the Ni concentration.

At this stage, we return to the basic question as to why, in a previous report [1], the temperature dependence of magnetization at $H = 1kOe$ in the samples *ap-Ni*$_{74.31}$, *ap-Ni*$_{74.73}$ and *ap-Ni*$_{75.98}$ with composition similar to those

used in this work, could be closely reproduced, over an unusually wide temperature range, $T \leq T_C$, by only the crossover percolation (*localized-spin*) theories but not by the spin-fluctuation (*itinerant-electron*) models. In the present case, the $M(T, H = 1kOe)$ data for the samples *ap-Ni*$_{74.3}$, *ap-Ni*$_{74.8}$, *ap-Ni*$_{75.1}$ and *ap-Ni*$_{76.1}$ could also be described very well by the crossover percolation theories with the values $T_{co}^{*} \cong 0.5\,K$, 5 *K*, 20 *K* and 40 *K* for the temperature T_{co}^{*} at which a crossover from the low-temperature magnon regime to high-temperature fracton regime occurs in a three-dimensional ferromagnetic percolating network. Note that these values of T_{co}^{*} agree quite well with those (Table 2 in [1]) reported [1] previously for the similar alloy compositions. In view of this result, a spin-wave (*propagating transverse spin-fluctuation*) description of the temperature variations of the 'zero-field' (spontaneous) and 'in-field' magnetizations, within the framework of the localized-spin (spin-fluctuation) theories, is possible only for $T \leq T_{co}^{*}$. This inference is borne out by our finding that Eqs.(4.3a) and (4.3b) correctly account for the decline in $M(T,0)$ and $M(T, H)$ with increasing temperature observed in *ap-Ni*$_{75.1}$ and *ap-Ni*$_{76.1}$ for $T \leq 20\,K$ but fail to do so in *ap-Ni*$_{74.3}$ and *ap-Ni*$_{74.8}$ for $5\,K \leq T << T_C$ (Figs. 4.4 and 4.5), where these alloys with $x \approx x_c$ exhibit non-Fermi liquid behaviour. In the hindsight, it now becomes apparent that the ferromagnetic fractons mimic the behaviour of over-damped spin waves and/or exchange-enhanced spin-density fluctuations at temperatures $T \geq T_{co}^{*}$.

4.3.4 Critical region

Figure 4.13(a) - (c) displays the Arrott ($M^2(T,H)$ versus $H/M(T,H)$) plots for the samples *ap-Ni*$_{74.3}$, *ap-Ni*$_{74.8}$ and *ap-Ni*$_{76.1}$ over a wide temperature range which embraces the critical region near the ferromagnetic (FM) – paramagnetic (PM) phase transition. It is customary [24] to compute spontaneous magnetization, $M(T,0) \equiv M(T,H=0)$, and inverse initial susceptibility, $\chi^{-1}(T)$, from the intercept values at different temperatures on the ordinate ($T \le T_C$) and abscissa ($T \ge T_C$) obtained when the *linear high-field* portions of the Arrott plot (AP) isotherms are extrapolated to $H = 0$ and $M^2 = 0$, respectively, as shown in figure 4.13. However in the present case, the AP isotherms for temperatures in the close vicinity of the Curie point, T_C, acquire concave-upward curvature as $x \to x_c$.

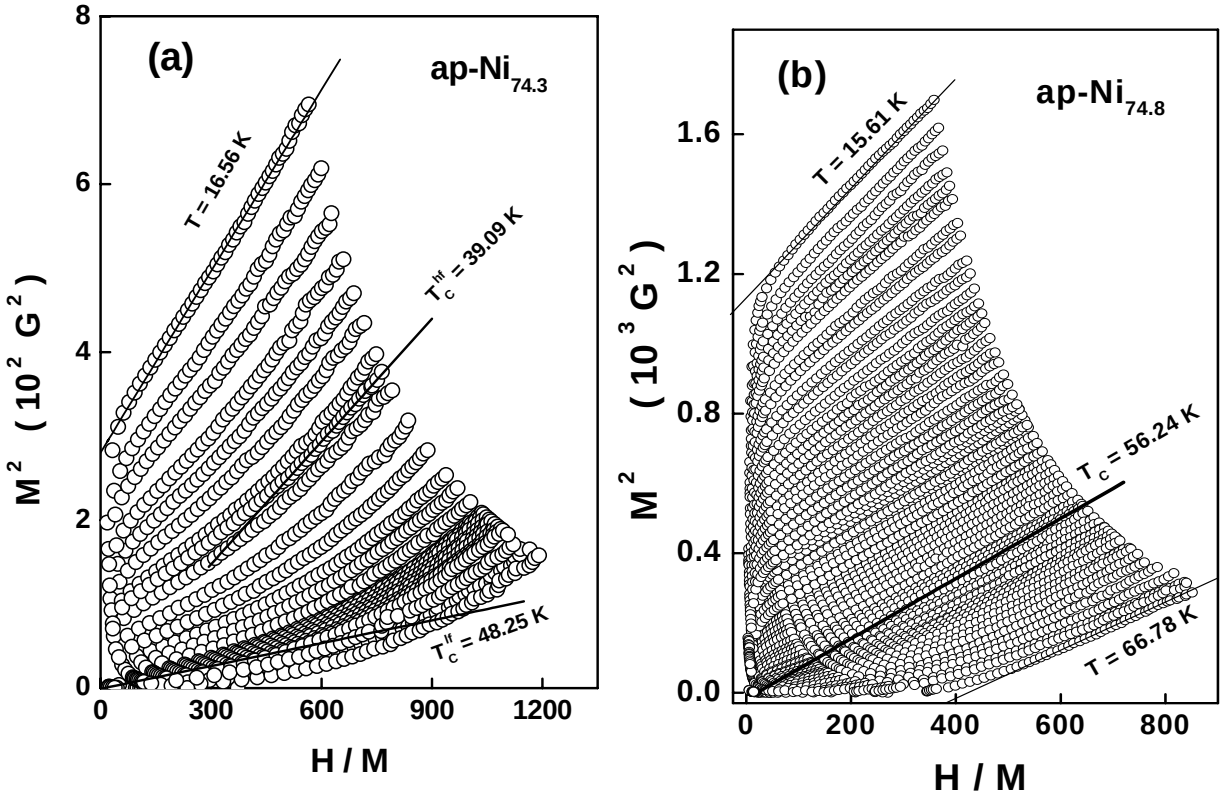

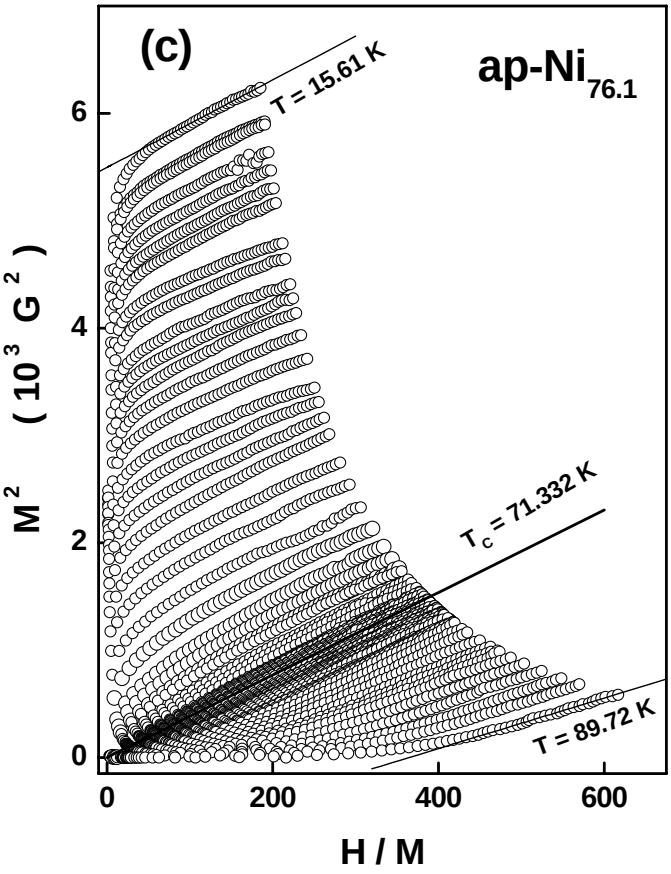

Figure 4.13: $M^2(T,H)$ versus H/M(T,H) (Arrott) plots for the samples (a) ap-$Ni_{74.3}$, (b) ap-$Ni_{74.8}$ and (c) ap-$Ni_{76.1}$ over a wide temperature range that embraces the critical region near the ferromagnetic-to-paramagnetic phase transition. These Arrott plots also indicate the values of T_C for the samples in question.

To elucidate this point further, the concave-upward curvature is completely absent in *ap-$Ni_{76.1}$*, starts showing up in *ap-$Ni_{74.8}$* but the AP isotherms are linear above $(H/M) \cong 200$, and becomes pronounced in *ap-$Ni_{74.3}$*. In view of the finding, based on the electrical resistivity and EDAX data on *ap-$Ni_{74.3}$* [18], that a trace second iso-structural crystallographic phase of lower Ni concentration and hence lower T_C is present in this sample, such a departure from linearity basically reflects the presence of this additional magnetic phase. Taking cognizance of this result, extrapolations to $H = 0$ and $M^2 = 0$ of the *two linear regions* in the AP isotherms for *ap-$Ni_{74.3}$*, $(H/M) < 300$ (low-field (lf) region) and $(H/M) > 500$ (high-field (hf) region), have been carried out to

obtain $M(T,0) \equiv M(T, H=0)$ and $\chi^{-1}(T)$ whereas the customary approach has been used for the remaining compositions. T_C marks the temperature at which the AP isotherm is *linear* over the entire (H/M) range and upon extrapolation

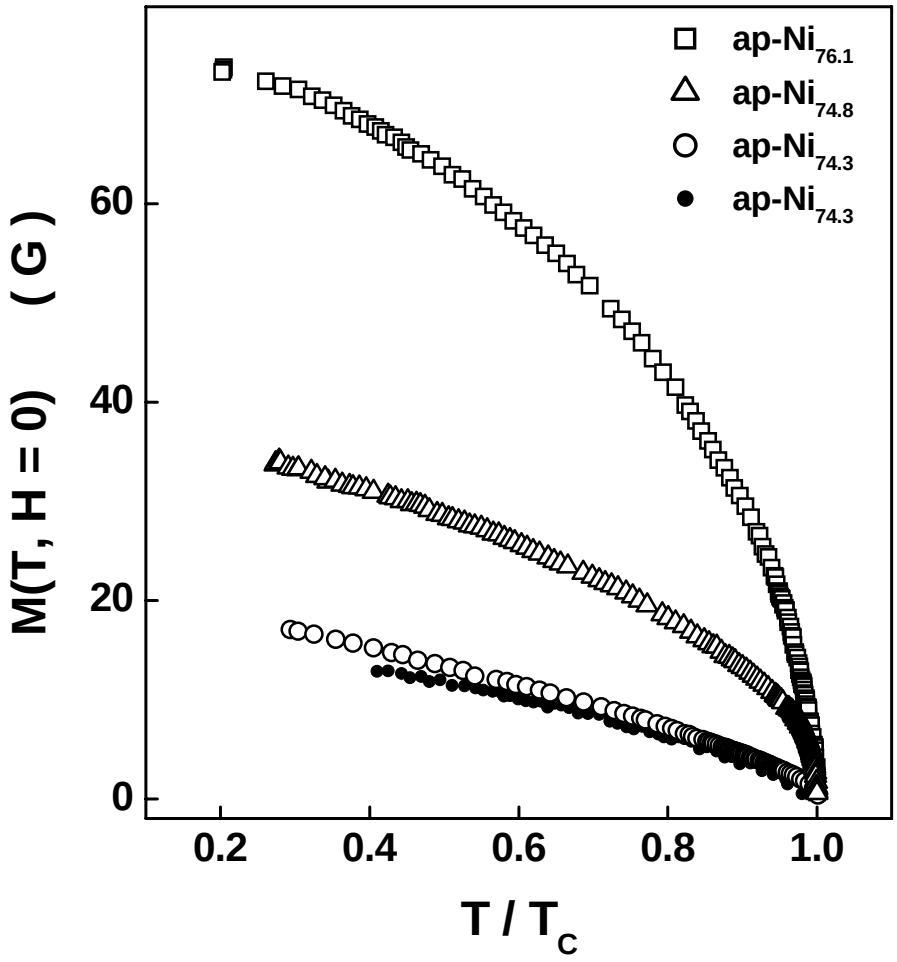

Figure 4.14: Spontaneous magnetization, M(T,H=0), as a function of reduced temperature, T/T_C, over a wide temperature range for the samples ap-$Ni_{74.3}$, ap-$Ni_{74.8}$ and ap-$Ni_{76.1}$. M(T,H=0) data denoted by the open symbols (closed circles) are obtained by the linear extrapolation of the high-field (low-field) portions of the Arrott plot isotherms to H = 0, see the text for details.

passes through the origin, where both $M(T,0)$ and $\chi^{-1}(T)$ go to zero. $M(T,0)$ data, so obtained, over the entire temperature range ($0.25T_C \le T \le T_C$) covered in VSM experiments, are plotted against reduced temperature, T/T_C, in figure 4.14. The $M(T,0)$ data for *ap-$Ni_{74.3}$*, obtained by low-field (high-field)

extrapolation, are denoted by solid circles (open circles) in this figure whereas the corresponding T_C value $T_C^{lf} = 48.25(5)\,K$ ($T_C^{hf} = 39.10(1)\,K$) is indicated in Fig. 4.13(a). Note that these $M(T,0)$ data (represented by crosses) have been used in figures 4.5, 4.8 and 4.10. The critical exponents β, γ and δ, defined as [24]

$$M(T,0) = B\ (-\varepsilon)^{\beta}, \qquad \varepsilon < 0 \tag{4.10}$$

$$\chi^{-1}(T) = \Gamma\ \varepsilon^{\gamma}, \qquad \varepsilon > 0 \tag{4.11}$$

$$M(T = T_C, H) = A\,H^{1/\delta}, \qquad \varepsilon = 0 \tag{4.12}$$

with $\varepsilon = (T - T_C)/T_C$, that characterize the asymptotic critical behaviour of spontaneous magnetization and initial susceptibility near the FM-PM phase transition, have been determined from the $M(T,0)$, $\chi^{-1}(T)$ and $M(T = T_C, H)$ data using the method of analysis whose details are given elsewhere [24-26]. That the plots of $M^2(T,0)$ against ε and $\chi^{-1}(T)$ against ε, based on Eqs.(4.10) and (4.11), and shown in figure 4.15, are *linear* within the asymptotic critical region $-0.03 \le \varepsilon \le 0.03$, imply that the presently determined (mean-field) values for the critical exponents $\beta = 0.50(5)$ and $\gamma = 1.00(5)$ correctly describe the asymptotic critical behaviour of $M(T,0)$ and $\chi^{-1}(T)$. However, larger than usual scatter in the $M(T,0)$ and $\chi^{-1}(T)$ data precluded an unambiguous determination of the multiplicative logarithmiccorrections to the mean-field power laws in the asymptotic critical region. Such corrections were previously reported [25,26] for

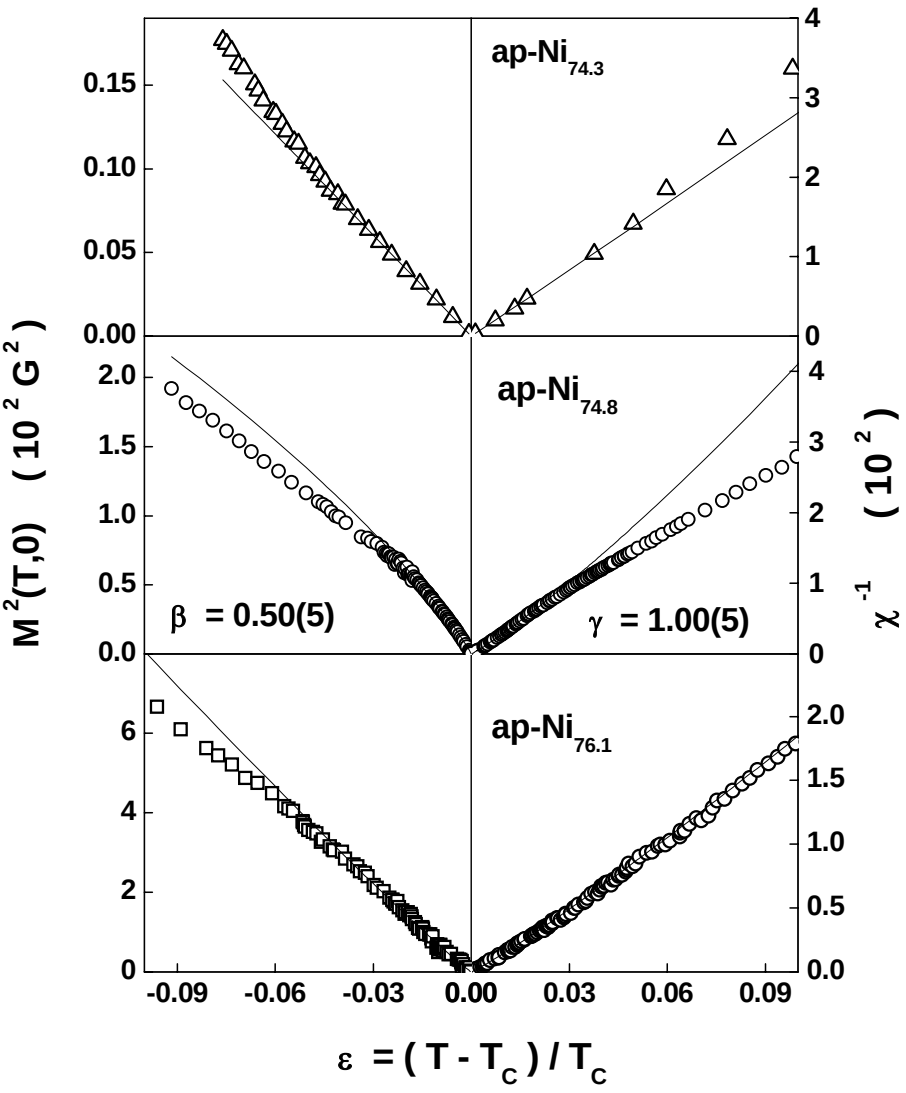

Figure 4.15: Spontaneous magnetization squared, $M^2(T, H = 0)$, and inverse initial susceptibility, $\chi^{-1}(T)$, as functions of the reduced temperature $\varepsilon = (T-T_C)/T$ within the range $-0.1 \leq \varepsilon \leq 0.1$. The continuous straight lines through the data (open symbols) represent the temperature variations of $M^2(T, H = 0)$ and $\chi^{-1}(T)$ predicted by the equations (4.10) and (4.11) of the text in the asymptotic critical region when $\beta = 0.5$ and $\gamma = 1.0$

the $Ni_{75}Al_{25}$ alloys of stoichiometric composition prepared in different states of site disorder. Consistent with the mean-field values of the critical exponents β and γ, the $\log M - \log H$ plots at $T = T_C$, based on Eq.(4.12) and shown in figure 4.16, yield the mean-field value $\delta = 3$ (inverse slope of the straight lines) for the critical exponent of the critical $M - H$ isotherm in the *same magnetic field regimes* as those used for the extrapolation of the Arrott plot isotherms to

$H = 0$ and $M^2 = 0$ in order to obtain $M(T,0)$ and $\chi^{-1}(T)$. A comparison of the presently determined values for the critical exponent in samples with both compositional disorder and site disorder with those [25,26] in the samples of stoichiometric composition but having different degree of site disorder, permits us to conclude that both compositional disorder and site disorder have no effect on the critical behaviour of the weak itinerant-electron ferromagnets in question.

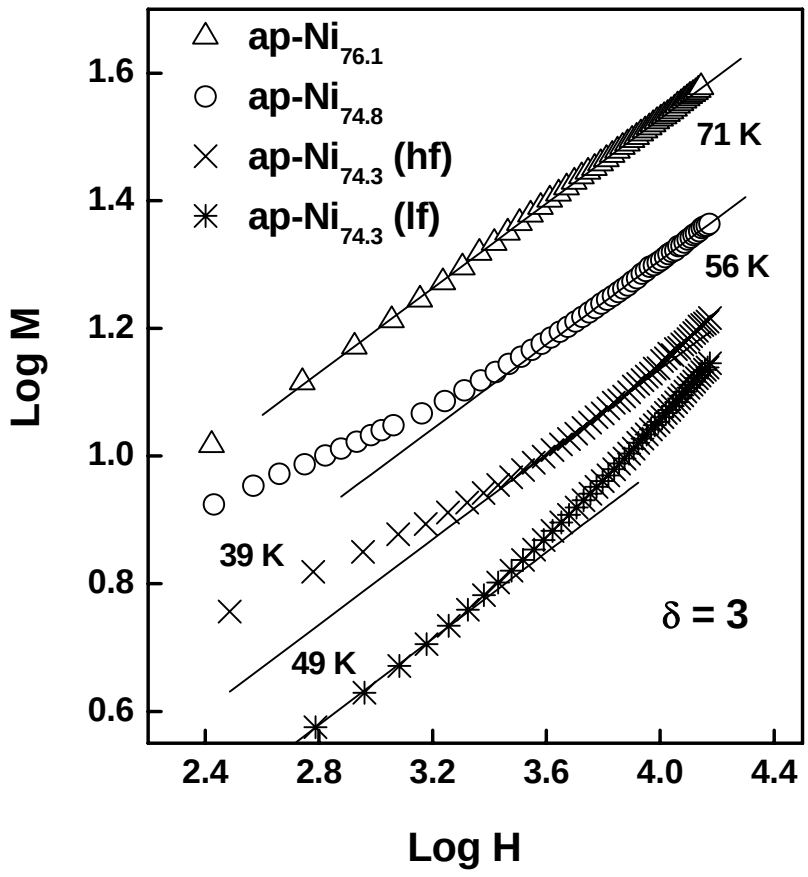

Figure 4.16: log M versus log H plots at $T = T_C$ for the samples ap-$Ni_{74.3}$, ap-$Ni_{74.8}$ and ap-$Ni_{76.1}$. The continuous straight lines through the data (symbols) represent the variations of log M with log H at $T = T_C$ predicted by equation (12) for the mean-field value $\delta = 3$.

4.4 Summary and Conclusions

Magnetic behaviour of the binary Ni_xAl_{100-x} alloys with $x = 74.3$, 74.8, 75.1 and 76.1 at. % Ni, which possess both compositional disorder and site disorder, has been extensively studied over a wide temperature range that embraces the critical region near the ferromagnetic-to-paramagnetic phase transition. The results, so obtained, are compared with those reported in the literature on the ordered counterparts (which have only compositional disorder) and with the theoretical predictions, based on the spin-fluctuation models. Such a comparison reveals the following. (i) With increasing compositional disorder, i.e., as $x \to x_c$, Curie temperature, T_C, and spontaneous magnetization at 0 K, M_0, in the alloys with compositional disorder alone, decrease in accordance with the power laws $T_C(x) = t_x\ (x - x_c)^{\tau}$ and $M_0(x) = m_x\ (x - x_c)^{\psi}$. In the presence of site disorder, in addition to compositional disorder, these power laws still hold but with distinctly different values for the exponents τ and ψ, and a lower value (by nearly $1 at.\% Ni$) for the threshold Ni concentration, x_c. Compared to the values of T_C for the Ni_xAl_{100-x} alloys with compositional disorder alone, site disorder enhances T_C for a given composition (leaves T_C essentially unaltered) and this enhancement grows rapidly as $x \to x_c$ (for $x \geq 76 at.\%$). Contrast with this behaviour, except for $x \approx x_c$, M_0 is relatively *insensitive* to site disorder. Insensitivity of M_0 to site disorder basically reflects that site disorder has essentially no effect on the density of states, $N(E_F)$, at the Fermi level, E_F, and the shape of density of states curve near E_F (except for $x \approx x_c$, where site disorder tends to primarily enhance $N(E_F)$ and thereby stabilize long-range ferromagnetic order for *Ni* concentrations below the threshold concentration, $x_c \cong 74.6 at.\%$, dictated by compositional disorder). As $x \to x_c$, site disorder increases the concentration of Ni atoms on the Al sub-

lattice beyond that allowed by the compositional disorder and thereby enhances the number of Ni nearest neighbours for a given Ni atom and hence the T_C. (ii) At low and intermediate temperatures, spontaneous magnetization, $M(T, H = 0)$, as well as the 'in-field' magnetization, $M(T, H)$, exhibit *non-Fermi liquid* behavior in the samples *ap-*$Ni_{74.3}$ and *ap-*$Ni_{74.8}$. As the critical concentration, x_c, is approached from above, i.e., as the *compositional disorder* increases, *stronger deviations* from the Fermi liquid behavior occur and the temperature range over which the *non-Fermi liquid behavior* persists *widens*. The non-Fermi liquid behavior is taken to basically reflect that the increased compositional disorder *alters the spin-wave dispersion* at *finite q* such that as *q* increases from $q = 0$, the spin-wave dispersion becomes increasingly similar to the non-propagating spin-fluctuation dispersion prevalent at temperatures close to T_C. By contrast, the *ap-*$Ni_{75.1}$ and *ap-*$Ni_{76.1}$ alloys follow the behaviour that the self-consistent spin-fluctuation theory [14] predicts for weak itinerant-electron ferromagnets without any disorder, i.e., (a) spin waves, at low temperatures ($T \leq 18K$) and thermally-excited (TE) plus zero-point (ZP) exchange-enhanced spin-density fluctuations, at intermediate temperatures and for temperatures close to T_C ($0.5T_C \leq T \leq 0.95T_C$), completely account for the observed temperature variations of $M(T, H = 0)$ and $M(T, H)$, (b) in accordance with the theoretical predictions [14,19], the functional form for the suppression of spin waves and TE spin fluctuations by the magnetic field, *H*, is $\sqrt{H}$ for spin waves at low temperatures and $\sim$ H ($\sqrt{H}$) for TE spin fluctuations at intermediate temperatures (temperatures close to T_C), and (c) compositional disorder and site disorder both leave these functional forms unaltered but reduce the spin-wave and (ZP + TE) spin-fluctuation 'stiffness' so that the suppression of these low-lying magnetic excitations by *H* becomes

correspondingly large. (iii) For temperatures in the vicinity of T_C, $M^2(T, H=0) \sim T^{4/3}$ and $M^2(T, H) \sim T^{4/3}$ for all the samples irrespective of the type of disorder present and regardless of the magnitude of field provided $H < H_0$, the field required to quench the spin-fluctuation contribution to spontaneous magnetization. That these power-law temperature variations are independent of H conforms well with the results of the self-consistent spin-fluctuation calculations [14]. (iv) Both compositional disorder and site disorder have no effect on the critical behaviour of the alloys near the ferromagnetic-to-paramagnetic phase transition.

The observations similar to (ii) – (iv) stated above have also been made in chapter 3, based on the resistivity and magnetoresistance data taken on the same alloy compositions.

References

[1] S. N. Kaul and A. Semwal, J. Phys.: Condens. Matter **16**, 8695 (2004).

[2] P. F. de Chatel and F. R. de Boer, Physica **48**, 331 (1970).

[3] F.R. de Boer, C.J. Schinkel, J. Biesterbos and S. Proost, J. Appl. Phys. **40**, 1049 (1969).

[4] P. D. Hambourger, R. J. Olwert and C. W. Chu, Phys. Rev. B **11**, 3501 (1975).

[5] N. Buis, J. J. M. Franse and P.E. Broumer, Physica **106B**, 1 (1981).

[6] H. Sasakura, K. Suzuki and Y. Masuda, J. Phys. Soc. Jpn. **53**, 352 (1984); J. Phys. Soc. Jpn. **53**, 754 (1984).

[7] K. Masuda and Y. Masuda, J. Phys. Soc. Jpn. **54** 630 (1985).

[8] S. K. Dhar and K. A. Gschneidner, Jr., L. L. Miller and D. C. Johnston, Phys. Rev. B **40**, 11488 (1989).

[9] M. Yoshizawa, H. Seki, K. Ikeda, K. Okuno, M. Saito and K. Shigematsu, J. Phys. Soc. Jpn. **61**, 3313 (1992).

[10] A. Semwal and S. N. Kaul, J. Phys.: Condens. Matter **16**, 8675 (2004).

[11] Anita Semwal and S. N. Kaul, Phys. Rev. B **60**, 12799 (1999).

[12] T. Moriya, A. Kawabata, J. Phys. Soc. Jpn. **34**, 639 (1973); **35**, 669 (1973); T. Moriya. *Spin Fluctuations in Itinerant Electron Magnetism* (Springer Verlag, Berlin, 1985) and references cited therein.

[13] G.G. Lonzarich and L. Taillefer, J. Phys. C: Solid State **18**, 4339 (1985).

[14] S.N. Kaul, J. Phys.: Condens. Matter **11**, 7597 (1999).

[15] A. Aharony, S. Alexander, O. Entin-Wohlman, and R. Orbach, Phys. Rev. B **31**, 2565 (1985); A. Aharony, O. Entin-Wohlman, S. Alexander, and R. Orbach, Phil. Mag. B **56**, 949 (1987).

[16] T. Nakayama, K. Yakubo, and R. Orbach, Rev. Mod. Phys. **66**, 381 (1994) and references cited therein.

[17] S. N. Kaul and S. Srinath, Phys. Rev. B **63**, 094410 (2001).

[18] A. C. Abhyankar and S. N. Kaul, Accepted for publication in J. Phys.: Condens. Matter.

[19] S.N. Kaul, J. Phys.: Condens. Matter, **17**, 5595 (2005).

[20] N. R. Bernhoeft, G. G. Lonzarich, P. W. Mitchell and D. McK Paul, Phys. Rev. **28**, 422 (1983).

[21] F. Sedameni, B. Roessli, P Böni, P. Vorderwish, and T. Chaterji, Phys. Rev. B **62**, 1083 (2000).

[22] G. G. Lonzarich *The Electron* ed. M. Springford (New York: Cambridge University Press) Chap. 6, (1997).

[23] G. R. Stewart Rev. Mod. Phys. **73**, 797 (2001).

[24] S. N. Kaul, J. Magn. Magn. Mater. **53**, 5 (1985).

[25] Anita Semwal and S. N. Kaul, Phys. Rev. B. **64**, 014417 (2001).

[26] Anita Semwal and S. N. Kaul, J. Phys.: Condens. Matter **14**, 5829 (2002).

Chapter 5

Non Fermi liquid behaviour and magnetically-mediated superconductivity in nanocrystalline Ni_3Al

5.1 Introduction

Nanostructured materials have properties that are different from their bulk counterparts. As the size of the particles becomes smaller, the number of atoms near the surface of the particle becomes comparable to that in the bulk volume. The competition between the surface and volume energy due to the size reduction affects the mechanical, electrical, optical and magnetic properties [1]. Nanostructured magnetic materials have generated enormous interest because of their novel magnetic attributes that are neither bulk like nor atomic like [2]. At the nanometer length scale, a rich variety of magnetic properties in systems with localised spins result from a interplay between the range of interatomic magnetic interactions (magnetic exchange and spin diffusion lengths) and the structural length scale (determined basically by the nanocrystalline grain size). In itinerant-electron system, however, alterations in the density of states at the Fermi level, $N(E_F)$, due to reduced crystallite size, play a decisive role in determining the nature of magnetism.

The saturation magnetization (M_S) and Curie temperature (T_C) of the strong itinerant-electron ferromagnet, nickel, decrease [3, 4] by 15% and 4%, respectively, compared to their polycrystalline values, when Ni is in the nanocrystalline form. Substantial decrease in M_s reflects a significant decrease in the density of the states (DOS) at Fermi level, $N(E_F)$. According to the Stoner criterion for ferromagnetism, long range ferromagnetic order in itinerant-electron spin system can be sustained only when the product of Stoner parameter I and $N(E_F)$ is larger than unity. Now that this product barely exceeds unity in case of weak itinerant-electron ferromagnets, even a slight

change (particularly reduction) in $N(E_F)$ is expected to have profound effect on the magnetic properties of such systems.

Earlier studies on nanocrystalline Ni_3Al concentrated mainly on structural aspects and on understanding mechanisms and nature of crystalline-to-amorphous phase transition. Ball milling of intermetallic compound Ni_3Al was extensively studied because of the potential high temperature applications [4,5]. The long-range atomic order parameter reduced to zero within the first few hours of milling whereas the *appearance* of a small fraction of amorphous phase was detected well after the *disappearance* of the long-range atomic order [5]. It was argued that the energy stored in the nano-grain boundaries provides the driving force for the amorphization of Ni_3Al [4]. However, this conclusion was in contradiction with the observation that crystallite size decreases to about 25 nm - 50 nm in the early stage (within 5 hours) of the milling and stays constant for longer milling periods. Zhou and Bakker [5] proposed that short-range disorder could be an alternate mechanism for the amorphization phenomenon. While 5 hours of ball milling reduced the crystallite size of Ni_3Al to 30 nm, the long-range order parameter, inferred from the ratio of superlattice Bragg reflection intensities to fundamental Bragg reflection intensity, dropped to zero. Ferromagnetic order (inferred from M^2 vs. H/M, Arrott plots) was lost at the same crystallite size. Precipitates of Ni_3Al powder with average crystallite size of 90 nm and 450 nm were extracted from single crystalline Ni-based superalloy [6]. Ferromagnetic hysteresis loops were observed at 5 K for both the sizes. Moreover, the specific magnetization had higher value in the 90 nm sample than in the 450 nm sample. This discrepancy was attributed to the change in composition during the preparation method. Recently, a detailed comparative bulk magnetization study [7] of the nanocrystalline (prepared by

inert-gas condensation method) and polycrystalline forms of the well-known [8] weak itinerant-electron system, Ni_3Al, has revealed that the long-range ferromagnetic order prevalent in the crystalline Ni_3Al is completely absent in the nanocrystalline counterpart, which exhibits exchange-enhanced Pauli spin paramagnetism instead. Another intriguing feature is that this Pauli spin contribution to magnetic susceptibility is concomitant with the Curie-Weiss contribution (which arises from the antiferromagnetic-spin fluctuations). Recognizing that electrical resistivity (ρ) and magnetoresistance (MR) measurements provide a means of probing the spin system on a length scale of the order of mean free path (which in nanocrystalline materials can be less than 1 nm), an extensive investigation of $\rho(T)$ and MR in both polycrystalline and nanocrystalline Ni_3Al was undertaken a view to gain insight into the physical phenomena that occur when a magnetic system is at the verge of a magnetic instability, where long-range magnetic order collapses.

5.2 Non-Fermi liquid behaviour

In this section, a brief introduction to non-Fermi liquid (NFL) behaviour and quantum phase transitions is provided. In ordinary metals, average distance between the free electrons is of the order of a few *Å* or of the order of the lattice parameter. So at such small distances, repulsive Coulomb interactions are expected to be strong and hence free electron theory should break down. However, still in the case of metals, free-electron theory works fairly well. This is so for two fold reasons.

First, the strong electron-electron interactions are greatly reduced because of Pauli's exclusion principle as electrons with the same orientation of spins try to avoid one another. Second, short-range electron-electron

interactions result in a distorted electron cloud. A given electron screened by this distorted-electron cloud does not experience the short-range Coulomb force due to all other free electrons. This theoretical formalism was first proposed by Landau and come to be known as the Fermi liquid theory as electrons are no longer completely free but short-lived short-range Coulomb interactions do operate between them. As a consequence, the rest mass of the electron changes, which, in turn, affects the dispersion relation, i.e., ε vs. k curve. Hence, these electrons are called the quasi-particles. This theory was quite successful in explaining thermodynamic properties like resistivity, susceptibility, specific heat of metals and alloys at low temperatures. The Fermi-liquid model of Landau predicts certain temperature dependences at sufficiently low temperatures (often < 1 K) for physically observable quantities. For example, as the temperature nears absolute zero, the specific heat C, divided by temperature T, $C/T \sim$ const, the magnetic susceptibility χ also becomes independent of temperature, and the electrical resistivity, ρ, behaves as $\rho_0 + AT^2$. The Fermi-liquid model forms a correct description of the low-temperature measurable parameters of a metal provided that the electron-electron interactions as $T \to 0$ become temperature-independent and are short-ranged in both space and time. In 1990-91, Seaman [9] *et al.* discovered that in $Y_{1-x}U_xPd_3$ electron-electron interactions are very strong and that the ground state properties of the system can not be described by the Fermi-liquid theory. Possible theoretical explanations for this behaviour of $Y_{1-x}U_xPd_3$ include: nearness to a magnetic instability in the phase diagram, disorder causing incomplete screening of local moments, or overcompensation of local moments. The discovery by Seaman was preceded by a number of experimental results that had shown clear violation of Fermi-liquid behaviour at low temperatures in bulk d- and f-electrons, e.g., the work of Mydosh and

Ford [10], who showed $\rho = \rho_0 + AT^{3/2}$ behaviour in the spin glass AuFe, and Rivier and Adkins [11], who offered the theoretical explanation. In the weak itinerant-electron ferromagnet, Ni_3Al, deviations from Fermi-liquid behaviour were first observed by Fluitmann et al. [12] near the critical concentration $x_c \sim$ 74.6 at.% of Ni at which (Curie Temperature) $T_C \rightarrow 0$. In addition, the current theory of non-Fermi-liquid behaviour, in general, has important early predecessors, including, e.g., the work by Hertz [13] and Nozières and Blandin [14].

The current theories to explain non-Fermi-liquid behaviour can be divided into three general categories: (i) the multichannel Kondo models, (ii) the models based on the nearness to a magnetic transition with an ordering temperature near 0 K (the quantum critical point), and (iii) the models based on the type of disorder that can, for example, induce a spread of Kondo temperatures, T_K, with a finite weight in the distribution for $T_K = 0$.

Non-Fermi-liquid behaviour is often experimentally observed at very low temperatures when a magnetic system is driven close to a magnetic instability by destroying long-range magnetic order at a critical value of external pressure or applied magnetic field or concentration of magnetic atoms. Thus, the non-Fermi liquid state in those system may be connected with a magnetic instability that occurs at $T = 0$. A number of investigators, Continentino [15], Millis *et al.* [16], Tsvelik *et al.* [17], Moriya and Takomoto [18], Lonzarich [19], Sondhi [20], Coleman [21], have treated the thermodynamic and transport properties within in the framework of theoretical models that are specific to a quantum phase transition. The classical phase transitions (Fig. 5.1a) occur at $T \neq 0$ and are driven by thermal fluctuations with temperature as a control parameter. In contrast to this, a quantum phase transition is driven by zero-

point or quantum spin fluctuations, with a control parameter other than temperature, e.g., external pressure or doping or magnetic field, at absolute zero. Such a control parameter causes a phase transition, along the zero-temperature boundary, from an ordered ground state to a disordered state at the quantum critical point. Although this definition of a quantum phase transition is strictly valid only for $T = 0$, the behaviour of the system sufficiently close in temperature to this critical point is still determined by the quantum critical fluctuations (Fig 5.1b). The nature of a classical transition at some finite temperature T_C is characterized by the divergence in both correlation length and correlation time as T_C is approached closely enough. Such fluctuations of the order parameter are associated with a frequency ω^* that vanishes at the transition. At finite temperatures, a quantum system behaves in a classical way,

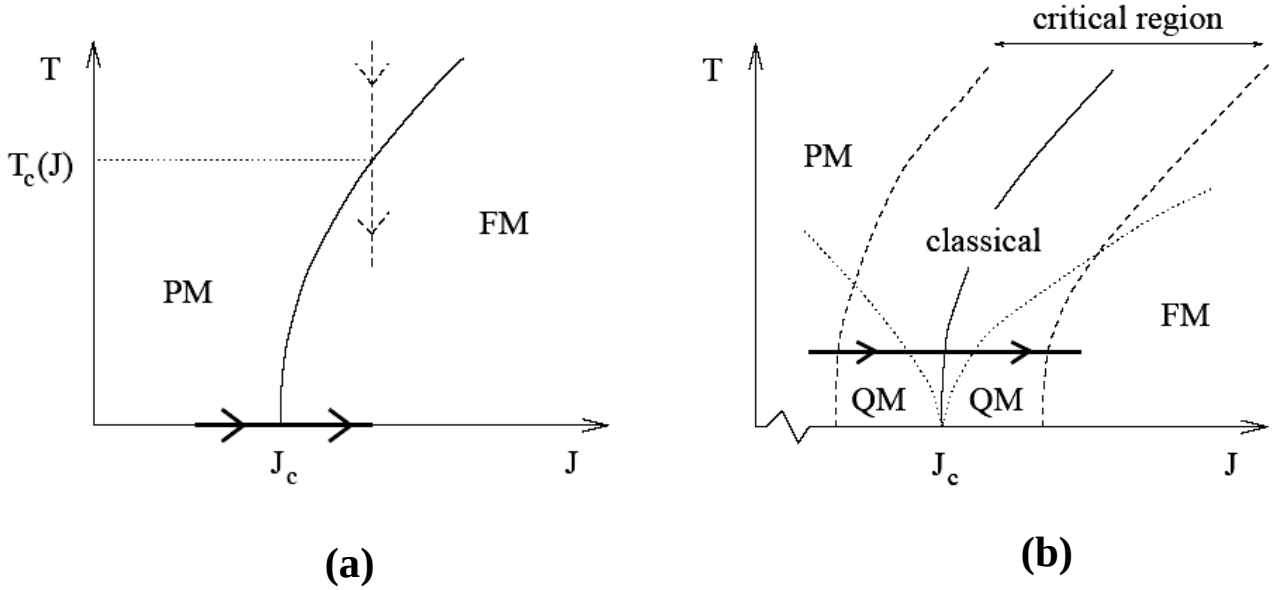

Fig. 5.1 :(a) Schematic phase diagram showing paramagnetic (PM) and ferromagnetic (FM) phases. Dashed line path represents classical phase transition (at a finite temperature) whereas solid line represents quantum phase transition (at zero temperature). (b) The vicinity of the quantum critical point ($J = J_C$, $T = 0$). Dotted lines indicate the regions dominated by classical and quantum mechanical critical behaviour. A measurement along the path shown will observe the crossover from quantum critical behaviour away from the transition to classical critical behaviour asymptotically close to it [23].

if the thermal energy exceeds the energy associated with quantum fluctuations. Detailed overview and description of non-Fermi liquid behaviour in transition and rare earth metals and alloys is given in reference [22] and the references cited therein.

5.3 Experimental Details

The rectangular samples of dimensions 25×3×0.5 mm^3 and spheres of diameter 3mm were spark-cut from the 'as prepared' polycrystalline rod (10 mm in diameter and 100 mm in length) of composition $Ni_{75.08}Al_{24.92}$. These samples are henceforth referred to as p-Ni_3Al. From a portion of the same rod, nanocrystallites size grains were prepared by inert gas (helium) condensation method. These crystallites were compacted *in situ* under a pressure > 1 GPa to form metallic discs of diameter = 8 mm and thickness = 0.2 mm. From the 'as-prepared' discs, discs of 3mm diameter and 0.2 mm thickness as well as rectangular strips of dimensions 7 × 2 × 0.1 mm^3 were spark-cut. These samples are henceforth referred to as n-Ni_3Al.

X-ray diffraction patterns were taken on p-Ni_3Al and n-Ni_3Al samples at room temperature. Atomic Force micrographs of n-Ni_3Al samples in dynamic force mode were taken at room temperature. Electrical resistivity at 'zero-field', $\rho(T, H = 0)$ and longitudinal magnetoresistance (MR), $\Delta\rho_{||} / \rho = [\rho(T,H) - \rho(T,H=0)] / \rho(T,H=0)$, in external magnetic fields, H, up to 80 kOe were measured, by the standard four probe dc method, in the temperature range 1.7 K to 300 K. Magnetization (M) of the spherical samples of p-Ni_3Al and the disc shaped samples of n-Ni_3Al was measured as a function of H at 5 K in fields up to 70 kOe (at a few specific temperatures ranging from 1.8 K to 300 K in n-Ni_3Al samples). AC susceptibility measurements were

performed on n-Ni_3Al samples in the 'field-cooled' (FC) and 'zero-field-cooled' (ZFC) modes, at an ac driving field of rms amplitude, H_{rms} = 1 Oe, and frequencies 87 Hz, 111 Hz and 1.11 kHz, without and with superposed dc fields of 25, 50, 75, and 100 Oe, over a wide temperature range from 1.8 K to 200 K, using a SQUID magnetometer with the ac option as well as Physical Property Measurement System (PPMS), of Quantum Design make.

5.4 Surface morphology, crystallographic structure, transport and magnetic properties

5.4.1 AFM and x-ray diffraction

The atomic force microscopic (AFM) images were obtained, using SPA 400 of Seiko make, in the dynamic force mode. Figure 5.2 shows a three-dimensional view of the AFM images of n-Ni_3Al samples at different magnifications. These pictures were taken from different regions of the sample surface. The AFM picture in Fig. 5.2 shows the agglomeration and consolidation of nanocrystallites under applied pressures in excess of 1 GPa. The crystallite sizes over the entire area of the several images were calculated using the line profile analysis, as shown in Fig. 5.3. This analysis yields an average crystallite size of 50 nm with lognormal size distribution, as shown in Fig. 5.4.

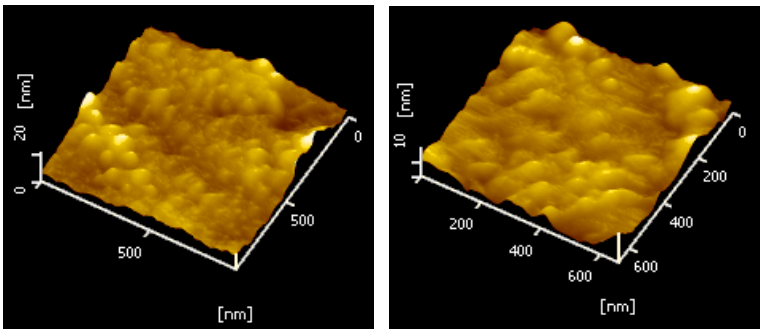

Fig. 5.2: Atomic force micrographs taken in Dynamic force Mode at different magnifications

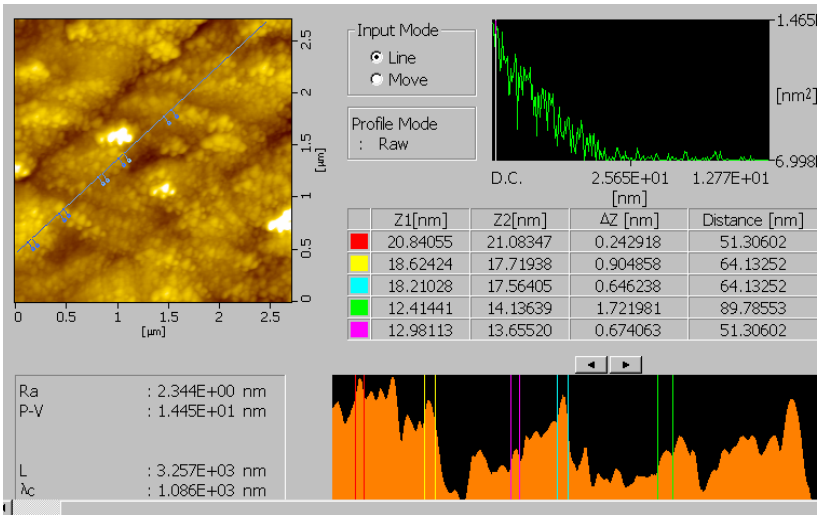

Fig. 5.3: Grain size determination using the line profile analysis option. Average crystallite size of 55(5) nm is obtained from the line profile analysis of different parts of the images and also from the images taken from different regions of the sample.

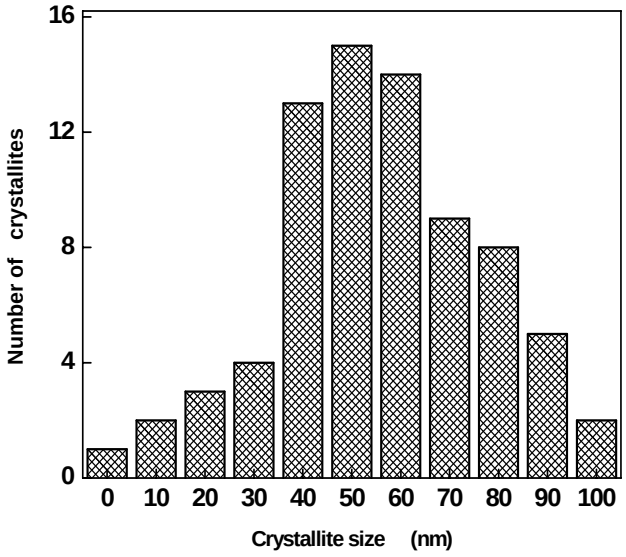

Fig. 5.4: Typical crystallite size distribution obtained from the line profile analysis

Figure 5.5 displays the x-ray diffraction pattern taken on the p-Ni_3Al and n-Ni_3Al samples at room temperature. All the peaks in both the samples have been indexed based on $L1_2$ structure with lattice parameters of a_n = 3.570(2) Å and a_p = 3.564(2) Å. In the ordered Ni_3Al, Ni atoms occupy the face centres while Al atoms occupy the corner sites of the *fcc* lattice. Presence of superstructure peaks, such as (100), (110), along with the fundamental peaks of

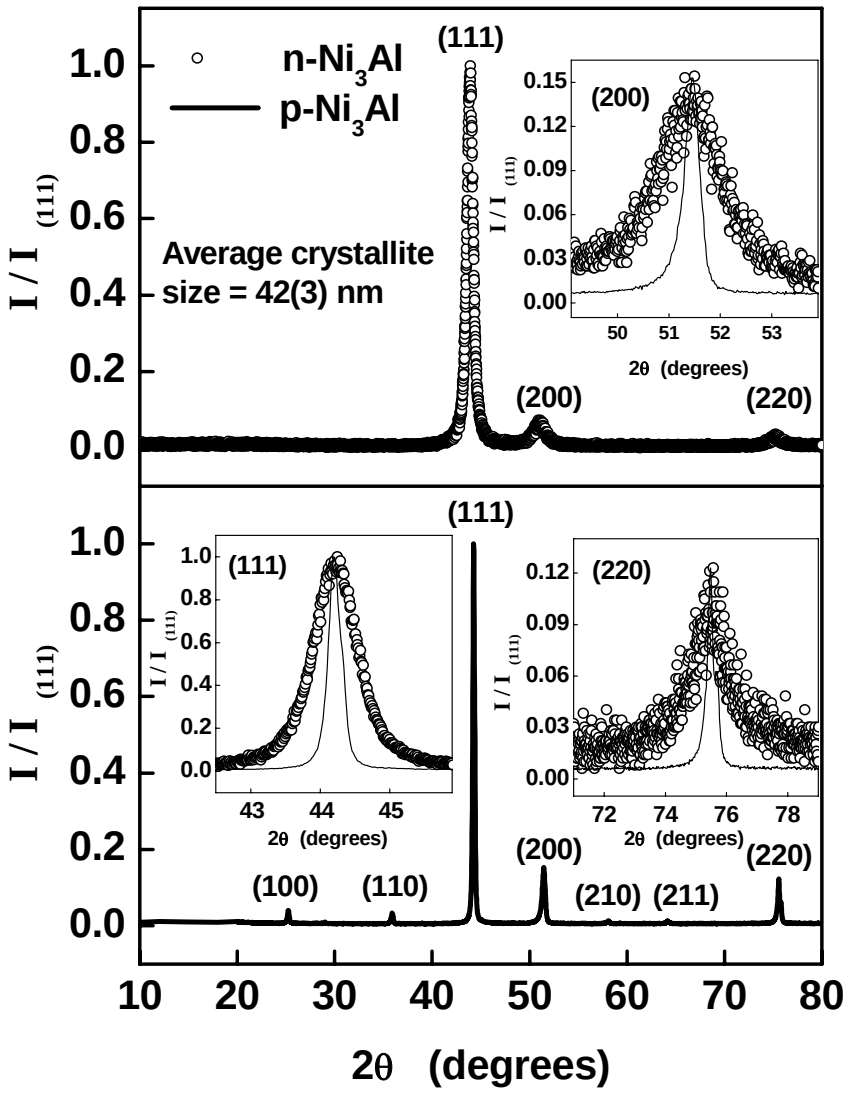

Fig. 5.5: X-ray diffraction patterns of nanocrystalline and polycrystalline Ni_3Al samples at room temperature. Insets show peak broadening in n-Ni_3Al as compared to p-Ni_3Al.

fcc lattice, e.g., (111), (200) and (220) in p-Ni_3Al, is a characteristic feature of the ordered $L1_2$ (Cu_3Au) structure. Occurrence of only the fundamental peaks (111), (200) and (220) in n-Ni_3Al, implies that Ni and Al atoms are *randomly* distributed on the *fcc* lattice; this atomic arrangement corresponds to the highest degree of site-disorder. Insets in the Fig. 5.5 compare the fundamental peaks of p-Ni_3Al and n-Ni_3Al normalised to the highest intensity Bragg peaks corresponding to the (111) reflection. The fundamental peaks of n-Ni_3Al are much broader than p-Ni_3Al due to size and strain broadening. After correcting for the instrumental and strain broadening, the mean crystallite size 't' was

estimated from the Scherrer formula, $t = 0.94\lambda/B\cos\theta$ (where λ = wavelength of x-rays, B = corrected linewidth in radians and θ = Bragg angle), to be 45(3) nm, which is comparable to the value obtained by the AFM line profile analysis.

5.4.2 Electrical resistivity and magnetoresistance

Figure 5.6 compares the temperature variations of the electrical resistivity (ρ) observed in nanocrystalline and polycrystalline Ni_3Al samples. The residual resistivity, RR = $\rho(T = 1.7\ K)$, is nearly six times larger while the temperature coefficient of resistivity over the entire temperature range 1.7 K to 300 K ($TCR = [\rho(300\,K) - \rho(1.7\,K)]/(300 - 1.7)K$) is roughly three times smaller in n-Ni_3Al. Obviously, enhanced RR and reduced TCR are the manifestations of the intense scattering, of both non-magnetic (scattering of conduction electrons from structural defects/imperfections) and magnetic (spin-spin exchange interaction) nature, from increased grain boundaries as well as from the interfacial regions between nanocrystallites. Insets (a) and (b) in Fig. 5.6 highlight an abrupt fall in the resistivity of n-Ni_3Al as the temperature is lowered below 4 K and the $T^{5/3}$ ($T^{1.64}$) temperature variation of resistivity in n-Ni_3Al (p-Ni_3Al) over the range 4.2 K < T < 22 K (1.7 K < T < 21 K). These temperature variations clearly deviate from T^2-law, which is expected from the conventional Fermi-Liquid theory at low temperatures. Note that $\rho(T)$ does not exhibit any thermal hysteresis when the n-Ni_3Al sample is warmed or cooled through 4 K. The resistivity was measured in magnetic fields up to 80 kOe at different fixed temperatures (isotherms) in the range from 1.7 K to 300 K. Figure 5.7 displays the 'in-field' resistivity, $\rho(T, H)$, at a few fixed values of magnetic field ranging from 0 to 80 kOe, obtained from the $\rho(H)$ isotherms, only in the temperature range from 1.7 K to 100 K for clarity. It is evident from

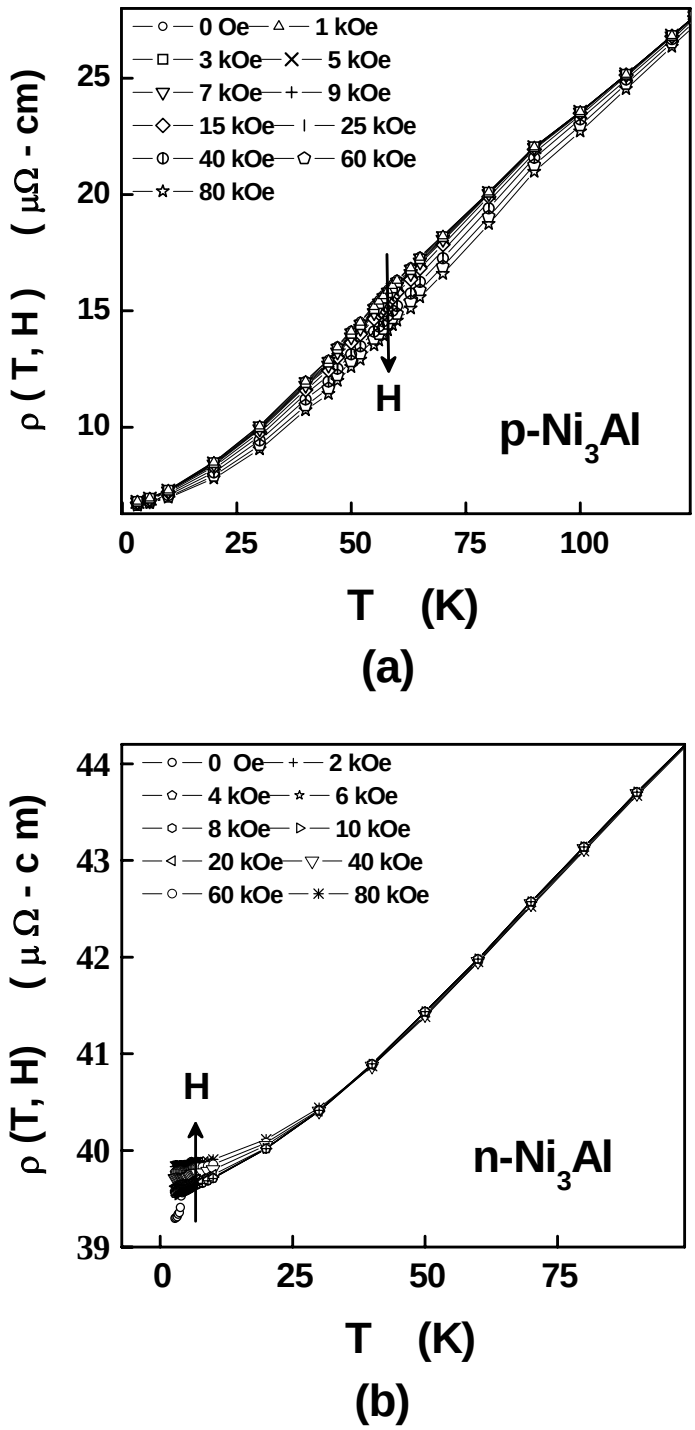

Fig. 5.7: Resistivity as a function of temperature at different fixed magnetic fields from 0 to 80 kOe, (a) for polycrystalline Ni_3Al and (b) for nanocrystalline Ni_3Al with an average crystallite size of 50 nm. The arrows indicate the increase in the magnetic field.

Fig. 5.7(a) that the p-Ni_3Al exhibits a negative magnetoresistance, MR, (resistivity decreases with increasing magnetic field, H) in the entire temperature range whereas n-Ni_3Al (Fig. 5.7(b)) exhibits a positive MR (resistivity increases as *H* increases) at very low temperatures. The reduction

(enhancement) in the resistivity of p-Ni_3Al (n-Ni_3Al) in the presence of magnetic field is the highest near the Curie temperature, $T_C \cong 55$ K (lowest temperature ~ 1.7 K) and at $H = 80$ kOe.

The longitudinal magnetoresistance, $\Delta\rho_{\|}/\rho$, measured with the directions of electric current and magnetic field along the length within the plane of the strip, is plotted against magnetic field, H, (temperature, T) at a few selected values of temperature (field) in figure 5.8 (figure 5.9). The main salient features of the $\Delta\rho_{\|}/\rho$ data displayed in figures 5.8 and 5.9 are as follows. (i)

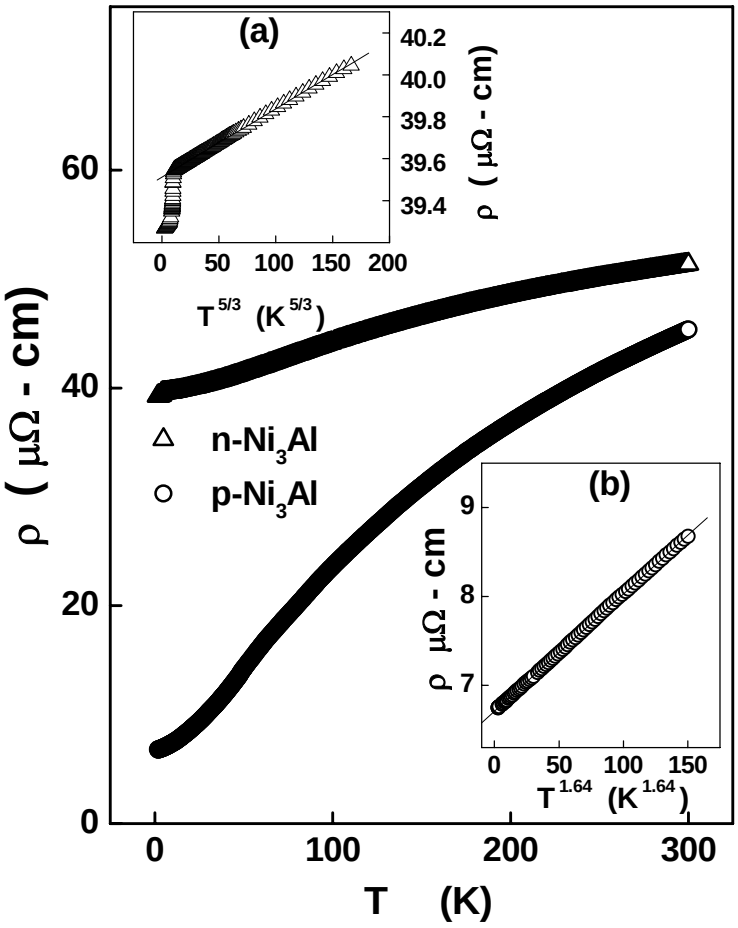

Fig. 5.6: 'Zero field' resistivity as a function of temperature for nanocrystalline (n) and polycrystalline (p) samples of Ni_3Al. Insets (a) and (b) highlight the $T^{5/3}$ and $T^{1.64}$ power law variations in the temperature intervals 4 K $\leq T \leq$ 22 K and 1.7 K $\leq T \leq$ 21 K in n-Ni_3Al and p-Ni_3Al samples respectively. Insert (a) also displays a sudden drop in resistivity of n-Ni_3Al at $T \cong 4$ K.

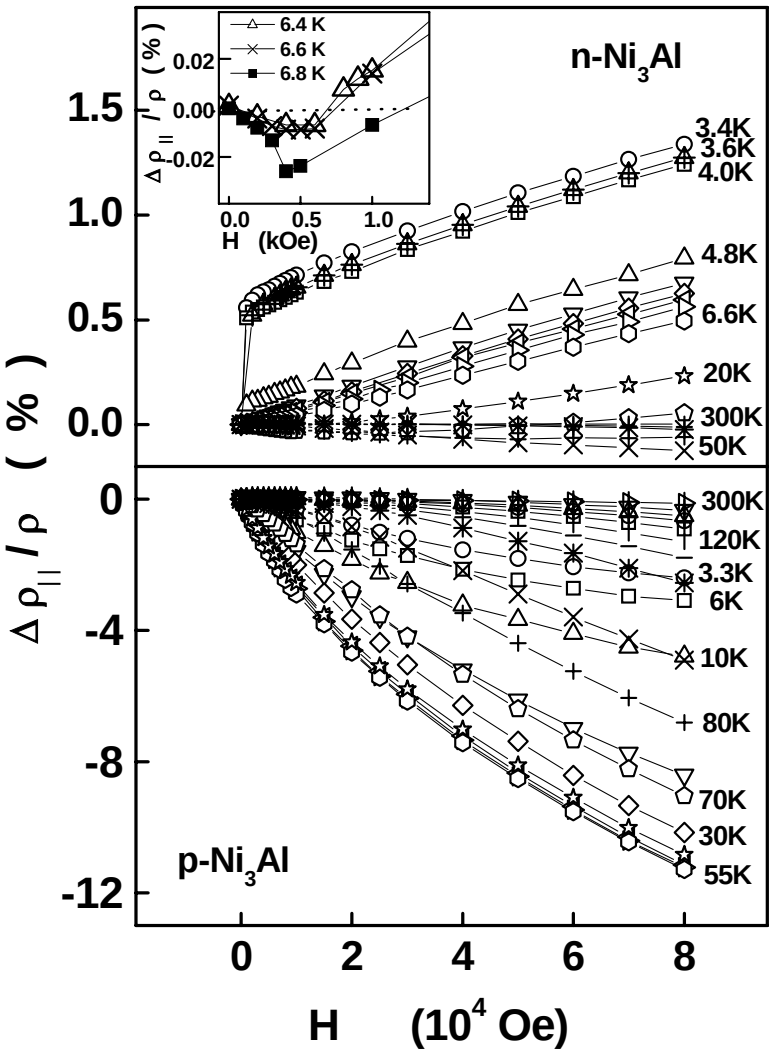

Fig. 5.8: Longitudinal magnetoresistance, $\Delta\rho_{||}/\rho$ vs. magnetic field, H isotherms at a few selected temperatures for n-Ni_3Al and p-Ni_3Al. The inset shows enlarged view of some the isotherms of n-Ni_3Al at low fields.

MR is positive for temperatures up to 20 K (except for fields $H \leq 1000$ Oe at T $\geq$ 6.4 K, where MR is negative, inset of Fig. 5.8) and reaches a maximum value of 1.4% at T = 2.5 K and H = 80 kOe in n-Ni_3Al. By contrast, MR is negative over the entire temperature range 3 K $\leq T \leq$ 300 K and assumes a maximum value of 12% at the Curie temperature T_C = 55 K and H = 80 kOe in p-Ni_3Al. (ii) With increasing temperature, MR changes sign at a crossover temperature T^*, and goes through a negative peak at $T = T^p$ with the peak value reaching its maximum value of - 0.14% at H = 80 kOe in n-Ni_3Al; T^* (T^p) increases from 20 K (30 K) at H = 2 kOe to 38 K (54 K) at H = 80 kOe (inset

(b) in Fig. 5.9). In p-Ni_3Al, however, magnetic field substantially increases the negative peak value but has essentially no effect on the temperature T^p at which the negative peak value occurs in MR. (iii) Irrespective of the magnitude of field, positive MR in n-Ni_3Al drops rapidly from its maximum value at 3 K (which is field-dependent) as the temperature approaches 4 K from below and then varies slowly with temperature for $T > 4$ K (Fig 5.8 and inset (a) in Fig. 5.9).

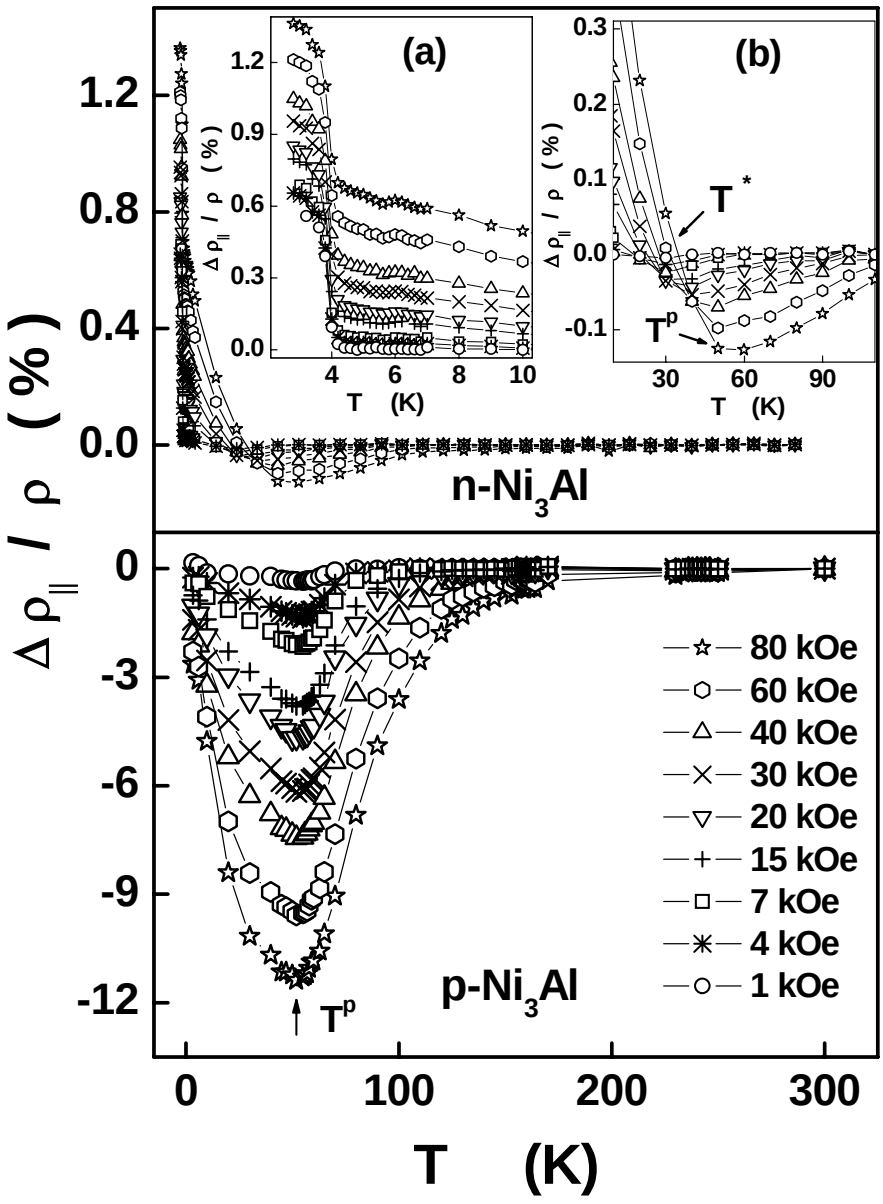

Fig. 5.9: Temperature variations of $\Delta\rho_{||}/\rho$ at a few selected fields for n-Ni_3Al and p-Ni_3Al. The insets (a) and (b) show an enlarged view of $\Delta\rho_{||}(T)/\rho(T)$ of n-Ni_3Al within the temperature intervals of 2.6 K $\leq T \leq$ 10 K and 20 K $\leq T \leq$ 110 K, respectively.

It is well-known [24] that in weak itinerant-electron ferromagnet such as p-Ni_3Al, the negative MR is a consequence of the suppression of thermally-excited ferromagnetic spin fluctuations by magnetic field. The negative peak in MR at $T = T_C$ thus reflects the fact that critical spin fluctuations have maximum amplitude at (in the vicinity of) T_C and the suppression by magnetic field is also correspondingly large only at such temperatures. Usually, positive MR is understood in terms of the Lorentz contribution to resistivity in the presence of a magnetic field. Lorentz contribution gives rise to a large positive MR only when the condition $\omega_c\tau >> 1$ (where ω_c and τ are the cyclotron frequency and conduction electron relaxation time, respectively) is satisfied. This contribution holds good for extremely pure metallic single crystals at very low temperatures (where τ is very large, which, in turn, implies that the ρ is at least less than two orders of magnitude than μΩ-cm (~10^{-8} Ω-cm or less)) and in high magnetic fields (where ω_c is large). In n-Ni_3Al with a residual resistivity of ≅ 40 μΩ- cm at 1.7 K, τ is so small that even at fields as high as H = 80 kOe the above condition is violated. This mechanism for positive MR in n-Ni_3Al is completely ruled out because positive MR is not observed in the crystalline counterpart, which has six times lower residual resistivity. According to the theoretical predictions, due to Yamada and Takeda [25], a small positive MR can occur in an antiferromagnetic system with localized magnetic moments due to the enhancement of spin fluctuations in one of the magnetic sublattices. This model is not applicable to a system like n-Ni_3Al in which magnetic moments are itinerant and long-range antiferromagnetic order does not set in even at temperatures as low as 1.7 K. The observation of an anomalous positive MR in n-Ni_3Al at low temperatures is, therefore, quite intriguing and one needs to explore other mechanisms to explain this finding.

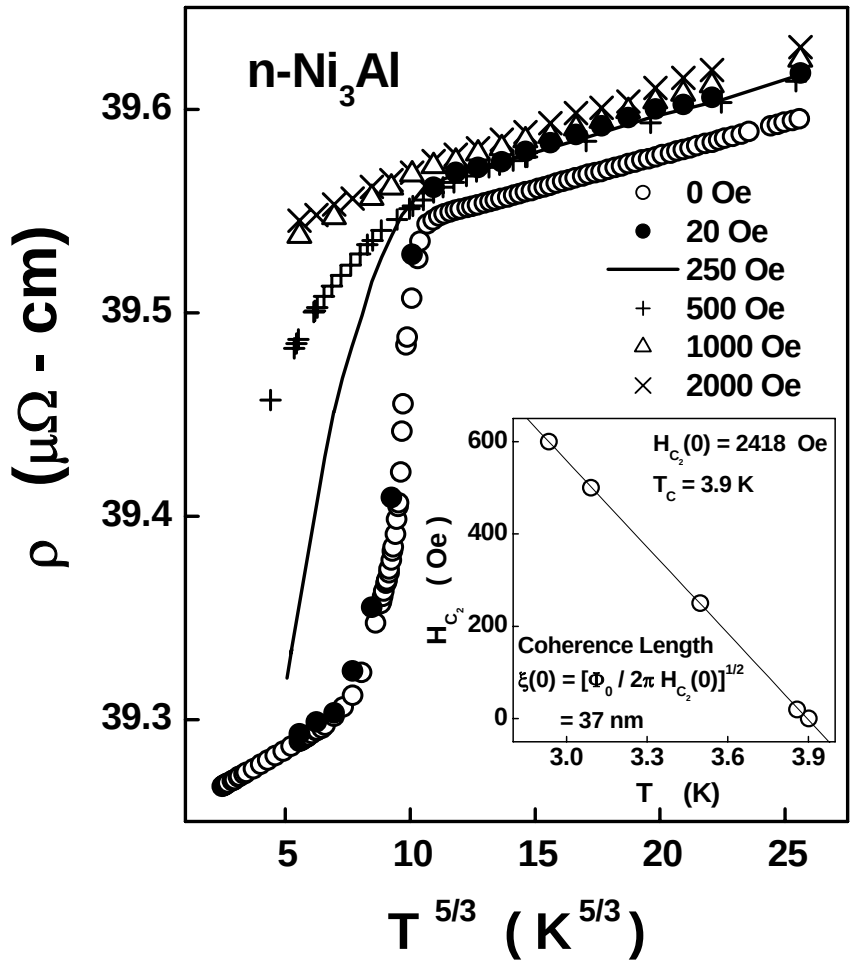

Fig. 5.10: Temperature variations 'zero-field' and 'in-field resistivities of 50nm-Ni_3Al in the temperature range from 1.7 K to ≅ 7 K at a few fixed field values in the low-field region. Inset shows that the upper critical field, H_{C2}, varies linearly with the temperature, as is normally observed in a type-II superconductor.

A close scrutiny of the data presented in the figures 5.6 - 5.10 reveals that a step rise in positive MR, (inset (a) of Fig. 5.9) has more to do with a rapid fall in the 'zero-field' resistivity, as the temperature drops below 4 K (Fig. 5.10), than that with the change in resistivity with field. A sudden drop in $\rho(T, H = 0)$ at $T \leq 4$ K and its progressive suppression by magnetic field (Fig. 5.10) is a behaviour reminiscent of superconductivity. In n-Ni_3Al, however, $\rho(T, H = 0)$ does not drop to zero for $T \leq 4$ K. A drop of nearly 1% observed in $\rho(T, H =$) at $T \leq 4$ K could reflect that only a small portion of the sample is superconducting.

Recently, unconventional superconductivity, arising from electron pairing mediated by antiferromagnetic (ferromagnetic) spin fluctuations, has been observed in heavy fermion compounds [26] (itinerant-electron ferromagnets [27, 28]) at a system-specific critical value of the external hydrostatic pressure where the long-range antiferromagnetic (ferromagnetic) order collapses and the resistivity exhibits a non-Fermi-liquid behaviour in that it does not follow the T^2-law predicted by the Fermi-liquid theory. The present scenario is analogous in that the reduction of crystallite size to nanometer range drives the weak itinerant-electron ferromagnet Ni_3Al to magnetic instability (where the long-range ferromagnetic order collapses) much the same way as the external pressure does. Thus, it is quite possible that most of the nanocrystallites in our sample have size that lies well below the critical size at which the magnetic instability and concomitant magnetically-mediated superconductivity set in. This would explain the weak superconducting drop in $\rho(T, H = 0)$ at $T \leq 4$ K and the non-Fermi liquid [29] behaviour of resistivity for $T > 4$ K (inset (a) of Fig. 5.6). In this connection, it is interesting to note that $T^{1.65}$ power law temperature variation of resistivity in the temperature range 50 mK to 7 K up to the critical pressure has been observed [30] in Ni_3Al. Pursuing the above line of argument, we have determined [31] the temperature variation of the upper critical field, $H_{C2}(T)$, from the field dependence of the peak in the temperature derivative of 'zero-field' and 'in-field' resistivity. $H_{C2}(T)$, so determined, varies linearly with temperature, as shown in the inset of Fig. 5.10, and yields the value $H_{C2}(0) = 2418$ Oe for the upper critical at zero Kelvin and $T_C = 3.9$ K for the superconducting transition temperature. A linear temperature dependence of the upper critical field is symptomatic of a type-II superconductor. Using the well-known relation $\xi(0) = [\Phi_0 / 2\pi H_{C2}(0)]^{1/2}$ between the coherence length at 0 K, $\xi(0)$, $H_{C2}(0)$ and the flux quantum Φ_0, gives $\xi(0) = 37$ nm, which is

smaller than the mean crystallite size (~50 nm [32]); as it should be for the superconductivity to survive. Those crystallites that have a size less than 37 nm cannot sustain superconductivity. The electronic mean free path, calculated from the residual resistivity, has a value which is greater than the coherence length. While the positive MR observed at $T \leq 4$K (Fig. 5.10) can be understood in terms of the suppression of antiferromagnetic-spin-fluctuation mediated superconductivity by field, the positive MR at $H > H_{C2}(T)$ for $T \leq 4$ K and in the temperature interval 4 K ≤ T ≤ 30 K for $H > H^*(T)$ (the threshold field below which MR is negative; inset (b) in Fig. 5.9) presumably originates from the antiferromagnetic (AF) spin fluctuations which, according to the Curie-Weiss law behaviour of susceptibility observed previously [7] in n-Ni_3Al, dominate in that temperature region. On the other hand, negative MR for $H < H^*(T)$ in the temperature range 4 K ≤ $T \leq 30$ K and at all fields above 30 K arises from the suppression of the ferromagnetic (FM) spin fluctuations [8] by field. Thus the main role of the field is to at first stabilize FM spin fluctuations at the cost of their AF counterpart, particularly for $T \leq 30$ K, and then suppress them. This field-induced crossover from AF to FM spin fluctuations offers a simple explanation for the field dependence of the crossover temperature T^* and the peak (negative MR) temperature T^p (aforementioned observation (ii)).

5.4.3 Magnetic properties

a) ac Susceptibility

Magnetic susceptibility as a function of temperature and field gives important information about the magnetic behaviour of, and interactions in, a material. In order to gain more physical insight into the drop in resistivity as the temperature falls below ≅ 4 K, ac susceptibility (χ_{ac}) measurements were

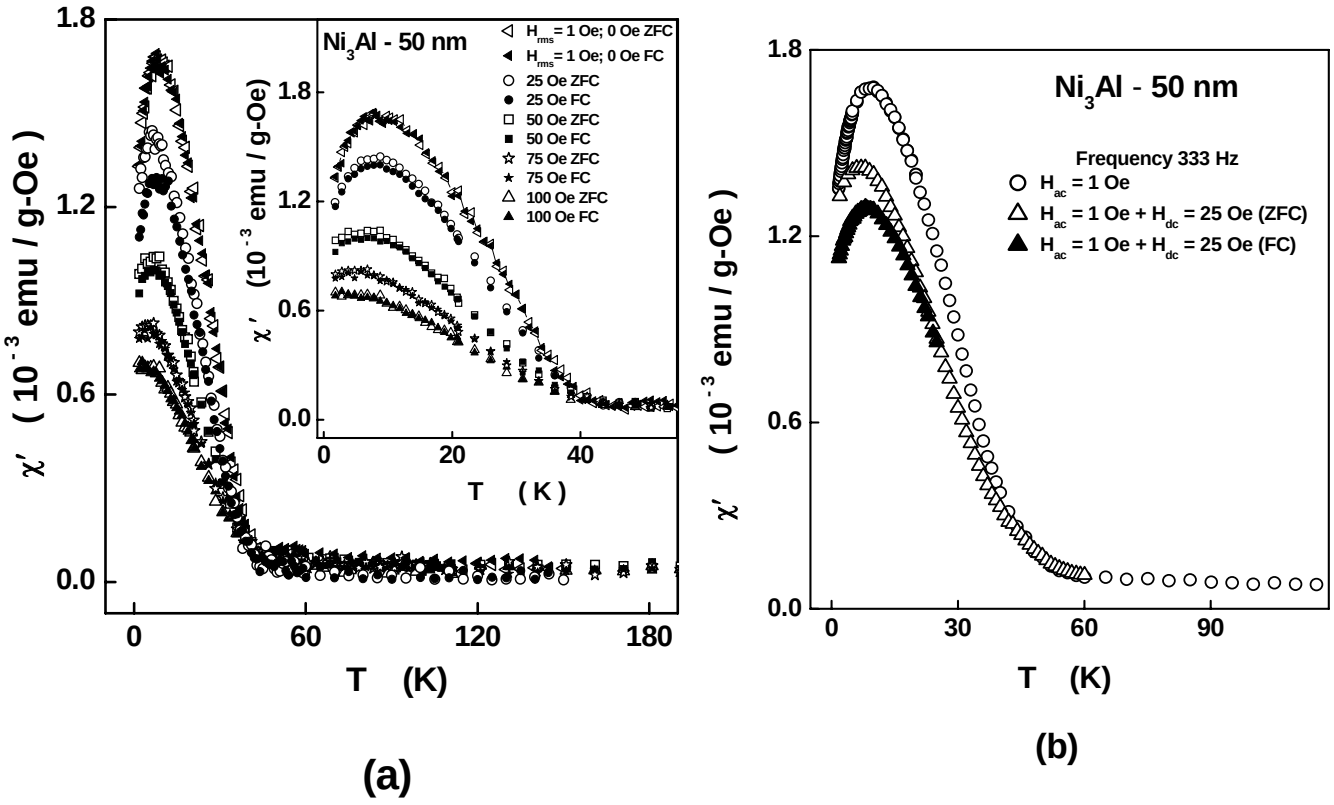

Fig.5.11: ac susceptibility of n-Ni_3Al as a function of temperature at different fixed dc magnetic fields in the ZFC-FC modes measured on (a) SQUID magnetometer with ac option and (b) PPMS. The inset in (a) shows enlarged view of the low temperature data.

performed in the zero-field-cooled (ZFC) and field-cooled (FC) modes, on n-Ni_3Al at a driving field of rms amplitude 1 Oe and frequency 111 Hz with and without superposed dc fields, H. Figure 5.11 shows the 'in-phase' component of χ_{ac}, χ', plotted against temperature at H = 0, 25, 50, 75 and 100 Oe. It is evident from figure 5.11 that the value of the rest field in the SQUID coils is less that 25 Oe. χ' is very small above 60 K. Inset in Fig 5.11 shows an enlarged view of $\chi'(T)$ for $T \leq 60$ K. χ' rises rapidly as temperature falls below 40 K at H = 0 Oe, attains a maximum value at around 9 K and then decreases till the temperature reaches 1.8 K. The bifurcation in the FC and ZFC $\chi'(T)$ curves (which *marks the* onset of weak irreversibility) taken at H = 0 Oe starts at ~ 36 K and increases as the temperature decreases to 1.8 K. With dc

magnetic field increasing from 25 Oe to 100 Oe , the temperature, T_p, corresponding to the peak in $\chi'(T)$ and the value of χ' at T_p, χ_m, decrease with the static magnetic filed, H, in accordance with the empirical relations $T_p(H) = T_p(0)\,[1 - a\,H^n]$ and $\chi_m(H) = \chi_p + \chi_{max}(H = 0)\exp(-H/H_0)$, respectively, as is clearly noticed from figures 5.12(a) and 5.12(b). The bifurcation temperature, T_{irr}, where the irreversibility in susceptibility sets in, decreases exponentially with H as $T_{irr}(H) = T_{irr}(0)\exp(-H/H_0)$, as shown in Fig. 5.12(c). The exponential field dependence of T_{irr} at low fields, when compared with the field variation of T_{irr}, i.e., $T_{GT}(H) = T_{GT}(0)\,[1 - C\,H^2]$, predicted for an *isotropic* Heisenberg spin glass at low fields along the Gabay-Toulouse (GT) weak irreversibility line [33] in the H-T phase diagram, asserts that the irreversibility observed in 50 nm n-Ni_3Al does not have the same origin as that in a spin glass or a cluster spin glass. It is important to note that no discernable shift in the peak of $\chi'(T)$ or T_P with the frequency of the ac driving field in the range 87

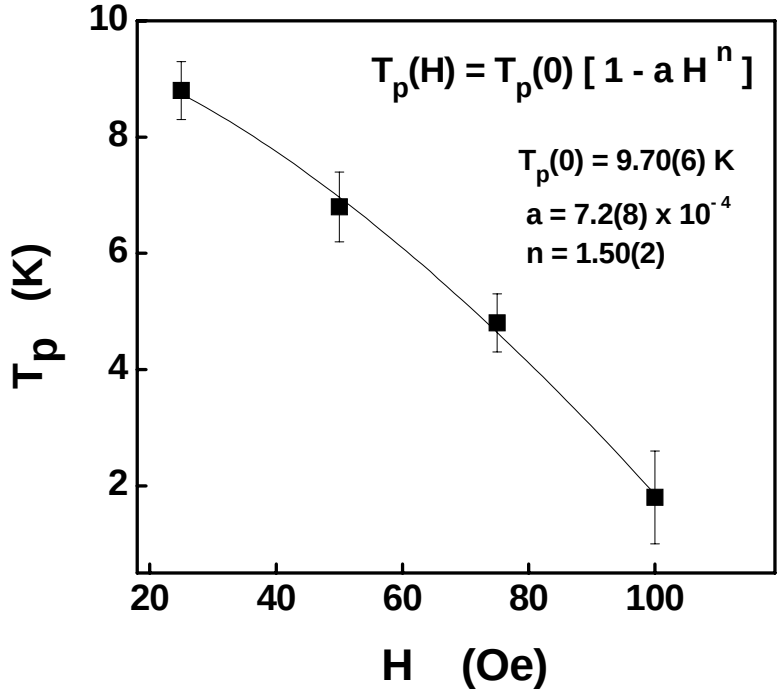

Fig. 5.12(a): Temperature corresponding to the peak in $\chi'(T)$, T_p, as a function of static magnetic field.

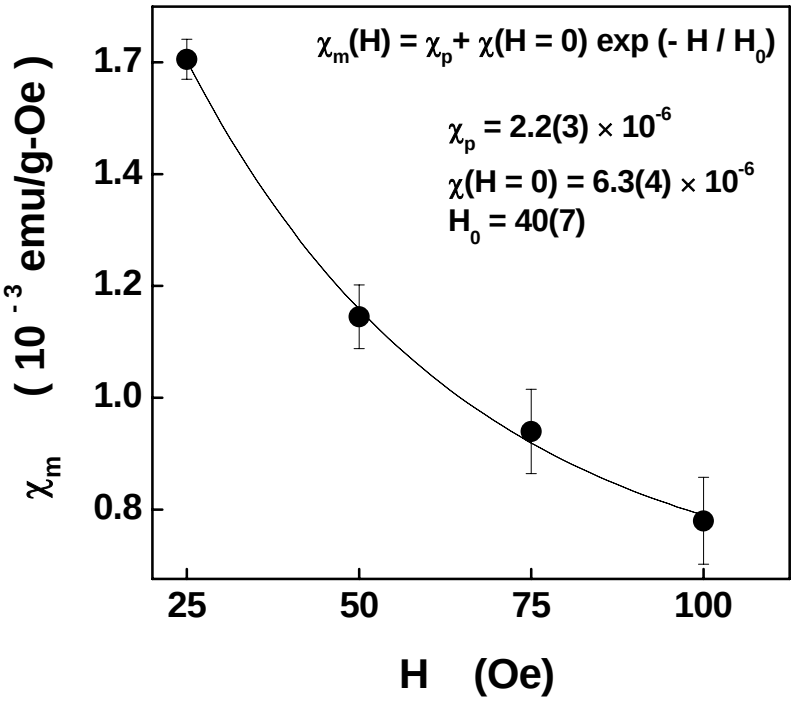

Fig. 5.12(b): χ_m as a function of magnetic field.

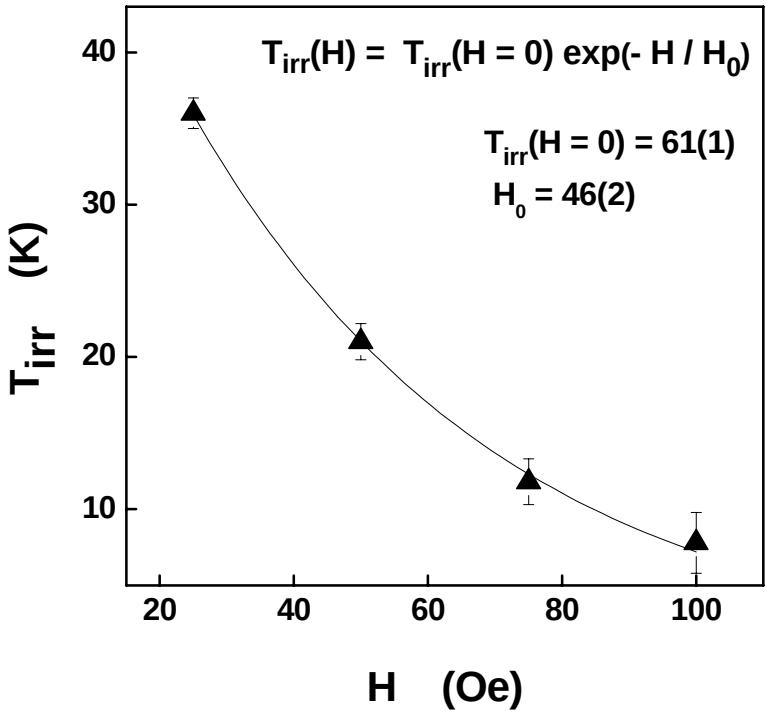

Fig. 5.12(c): Temperature at which irreversibility sets in the field cooled and zero-field cooled curves of χ' as a function of magnetic field.

$\leq \nu \leq$ 1 kHz was detected (figure 5.13). This observation goes against the possibility of attributing the peak in $\chi'(T)$ to either spin glass or interacting

superparamagnetic particle system. Another observation that merits attention is that, for fields $H \leq 75$ Oe where a clear bifurcation between ZFC and FC $\chi'(T)$ curves could be observed, FC curves *lie consistently below* the ZFC thermomagnetic curves. This was the case irrespective of whether the $\chi'(T)$ data were taken on the ac option of the SQUID magnetometer (Fig.5.11(a)) or on the PPMS set up (Fig.5.11(b)). Usually, FC curves lie above the ZFC ones since the spin system has a memory of the field during the cooling cycle. The observation that the FC susceptibility has nearly the same temperature dependence as the ZFC susceptibility and decreases continuously as the temperature falls below T_p is probably an indication of the onset of superconductivity at $T \cong 4$ K.

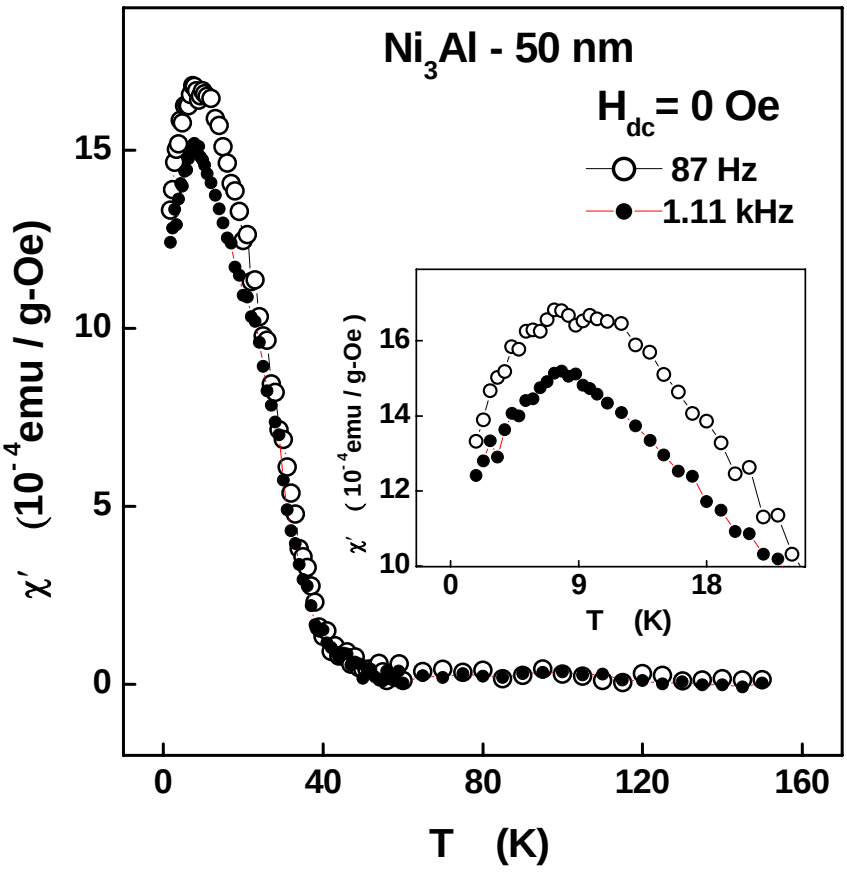

Fig. 5.13: $\chi'(T)$ of n-Ni_3Al (50 nm average crystallite size) in the temperature range, from 1.8 K to 150 K at H_{ac} = 1 Oe and frequencies 87 Hz and 1.11 kHz in the absence of superposed dc magnetic field.

A steep rise in χ' below 40 K is taken to reflect the contribution to susceptibility arsing from the non-superconducting (normal) part of the sample. To remove this contribution from the measured $\chi'(T)$, $\chi'(T)$ data are fitted to the expression, $\chi'(T) = \chi_0(T) + b\ T^{-n}$, since the Curie-Weiss law failed to describe $\chi'(T)$ irrespective of the value of H, including $H = 0$. The inset of Fig 5.14 shows such a fit to the $\chi'(T)$ data taken at $H = 50$ Oe over the temperature range of 15 K $\leq T \leq$ 200 K. In spin glasses or cluster spin glasses (interacting superparamagnetic particles/grains), $\chi'(T)$ follows the Curie-Weiss behaviour for temperatures above the freezing (blocking) temperature, T_f (T_b) $\rightarrow T_p$ [34-36]. Thus, in 50 nm n-Ni_3Al, we are not dealing with a spin glass or a cluster spin glass or system of interacting superparamagnetic particles. This non-Curie

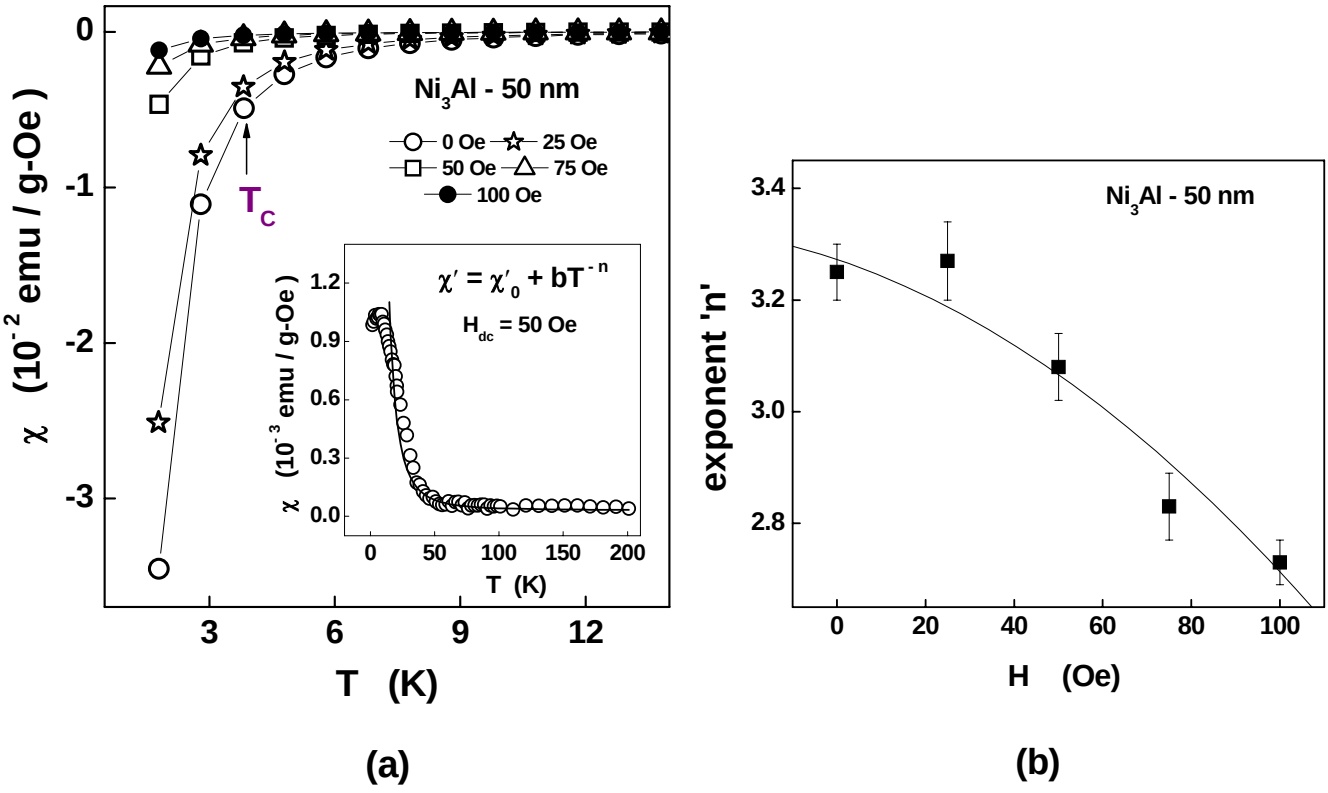

Fig. 5.14: (a) Residual diamagnetic contribution to ac susceptibility, symptomatic of Meissner effect, after removing the power-law normal contribution, which is shown in the inset. (b) Field dependence of the exponent 'n'.

-Weiss contribution instead characterizes the non-Fermi liquid (NFL) behaviour in the normal state. When NFL contribution is subtracted from the total (measured) χ', we obtain the contribution due to Meissner effect, as shown in figure 5.14. With increasing magnetic field, (i) the transition temperature, T_C, shifts to lower temperatures, and (ii) at any temperatures below T_C, the diamagnetic contribution to susceptibility is progressively reduced. However, the scanty data in the lower temperature range makes it difficult to determine the critical field, H_{C2}, as a function of temperature explicitly.

b) dc Magnetization

Figure 5.15(a) depicts the magnetization versus magnetic field isotherms at a few temperatures in the temperature range 1.8 K to 300 K. After correcting

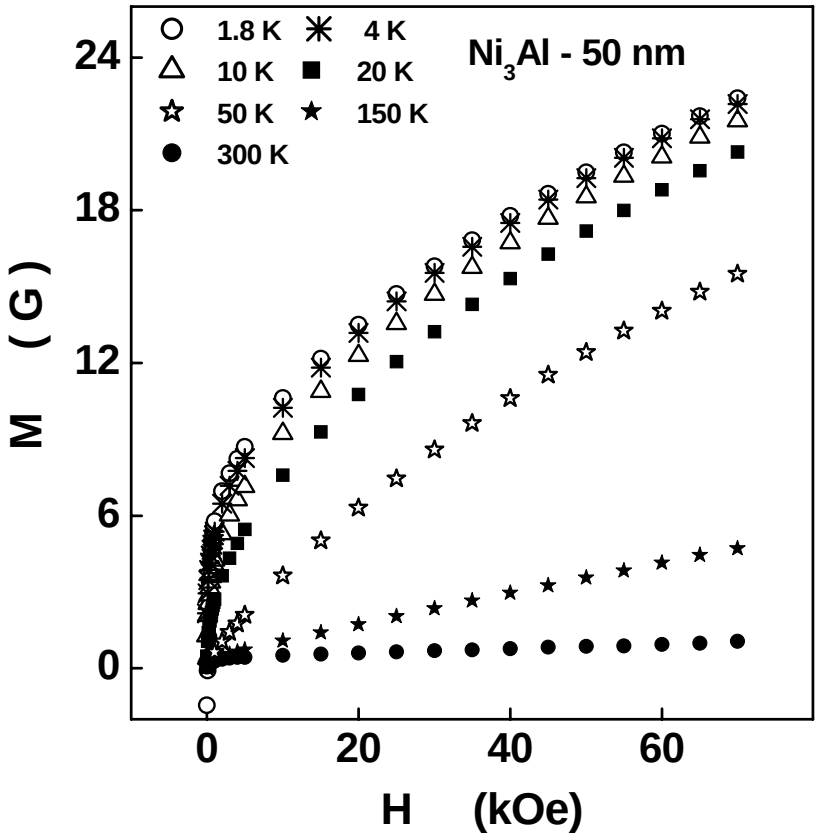

Fig. 5.15(a): M versus H isotherms at temperatures ranging from 1.8 K to 300 K.

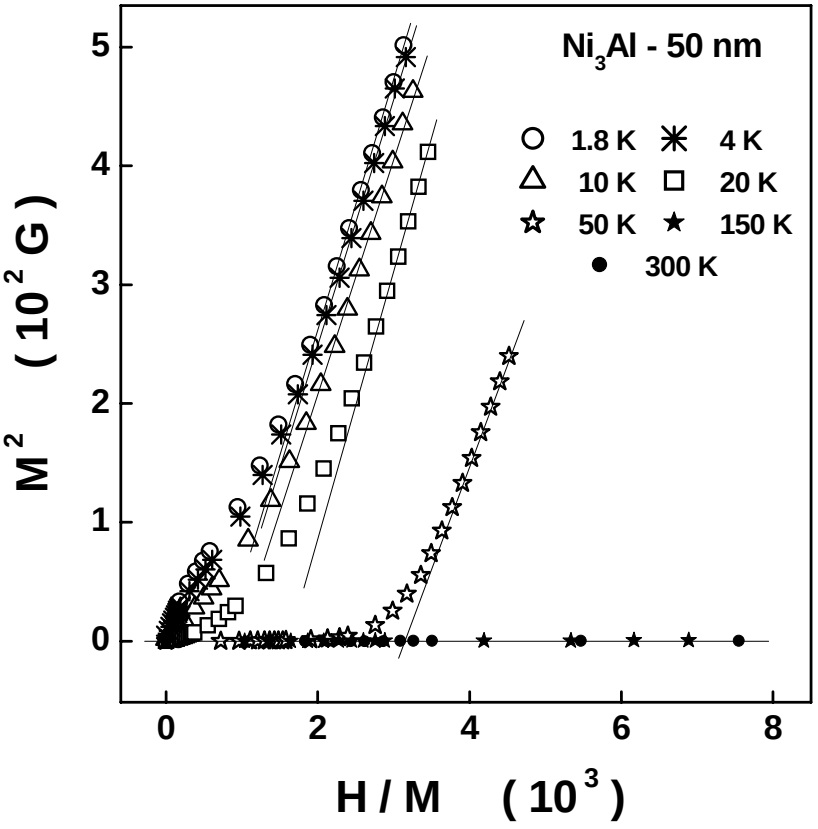

Fig. 5.15(b): M^2 vs. H/M isotherms (Arrott plots) demonstrating the absence of long-range ferromagnetic order down to 1.8 K.

the external magnetic field for demagnetization, these isotherms are converted into the Arrott (M^2 vs. H/M) plots, which are based on the magnetic equation of state, $H/M = a + b\ M^2$. A linear extrapolation of the high-field portions of the Arrott plot isotherms to $H = 0$ does not yield any intercept on the M^2- axis even at the lowest temperature of $T = 1.8$ K, as shown in the figure 5.15(b). Since no spontaneous magnetization exists at any temperature within the temperature range covered in the present experiments, no long-range ferromagnetic order exists down to 1.8 K. However, the deviations from the linear Arrott plot isotherms at low fields and low temperatures, can be attributed to the presence of spin fluctuations, which is consistent with the low-field magnetoresistance data at low temperatures. $M(T)$ data at low magnetic fields ranging from 0 to 1 kOe, obtained from the M - H isotherms,

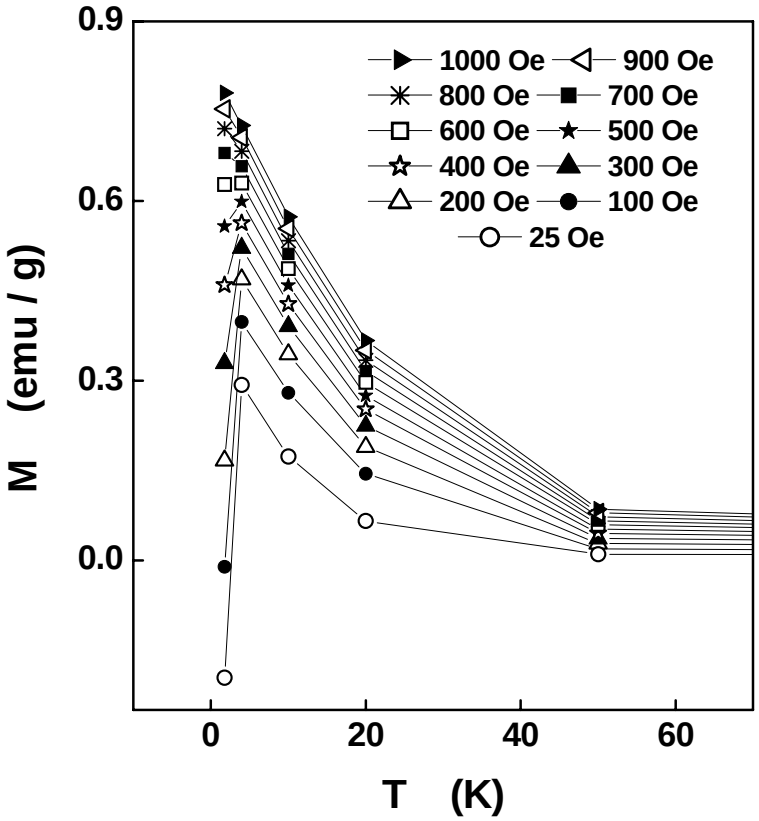

Fig. 5.16: Low-field dc magnetization as a function of temperature obtained from the M vs. H isotherms. Note the negative magnetization at fields of 100 Oe and below at the lowest temperature of 1.8 K. The fall in magnetization below 4 K gets arrested at H = 600 Oe. Note that at the same field value the analogous drop in resistivity also ceases (see, Fig 5.10).

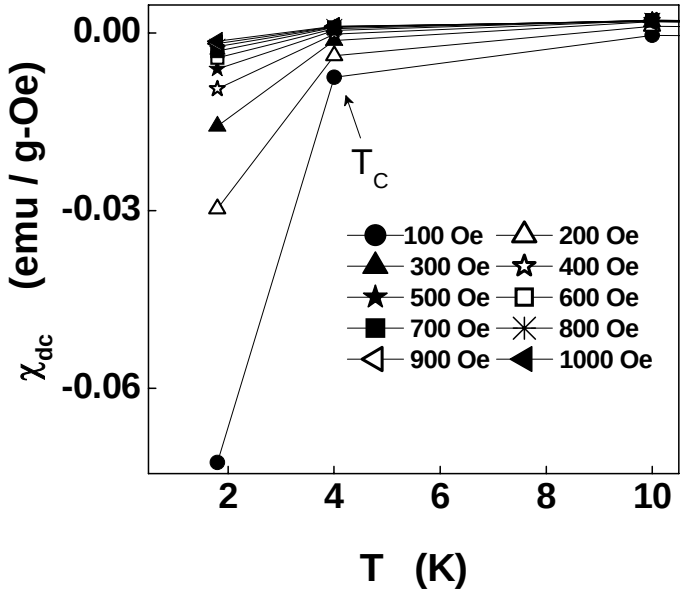

Fig. 5.17: Diamagnetic contribution, characteristic of Meissner effect, obtained after removing the power-law normal contribution from the total measured dc susceptibility, χ_{dc} = M/H, (c.f. Fig.5.14 and Fig. 5.17).

are shown in figure 5.16. The dc magnetization increases rapidly as the temperature falls below 50 K (as was the case for $\chi'(T)$, see figures 5.11, 5.13 and inset of Fig. 5.14) and for temperatures below 4 K, M decreases at low fields (< 600 Oe) but continues to increase at H > 600 Oe. The drop in dc magnetization and 'in-field' resistivity (see, Fig. 5.10) for T < 4 K ceases to exist when $H \geq 600$ Oe. Such a drop in magnetization for T < 4 K and H < 600 Oe is indicative of the superconducting behaviour of the sample. As evidenced earlier based on the ac susceptibility data in Fig. 5.14, the Meissner diamagnetic signal, characteristic of superconductivity, is estimated from the dc susceptibility, $\chi_{dc} = M/H$, data by subtracting out the (non-Curie-Weiss) power-law, or equivalently the non-Fermi liquid, contribution to $\chi_{dc}(T)$ for $T \geq$ 4 K, from the total measured $\chi_{dc}(T)$ at T ≥ 1.8 K. The diamagnetic contribution to $\chi_{dc}(T)$, so estimated, is shown in the figure 5.17.

5.5 Studies on 3 nm crystallite size n-Ni_3Al

The novel physical phenomena such as the absence of long-range ferromagnetic order, non-Fermi liquid behaviour, anomalous positive magnetoresistance and magnetically-mediated superconductivity observed in nanocrystalline Ni_3Al, with an average grain size of 50 nm [31], served as the main motivation to investigate the effect of crystallite size on these properties near the quantum critical point (magnetic instability) in Ni_3Al. To this end, nanocrystalline samples of Ni_3Al with an average crystallite size of 3 nm have been prepared by the inert gas condensation method. The partial pressure of inert gas (Helium) and angular speed of the liquid-nitrogen-cooled steel drum, on which the condensation of nanocrystallites takes place, were the main process parameters to achieve such a small nanocrystallites size.

5.5.1 X-ray diffraction

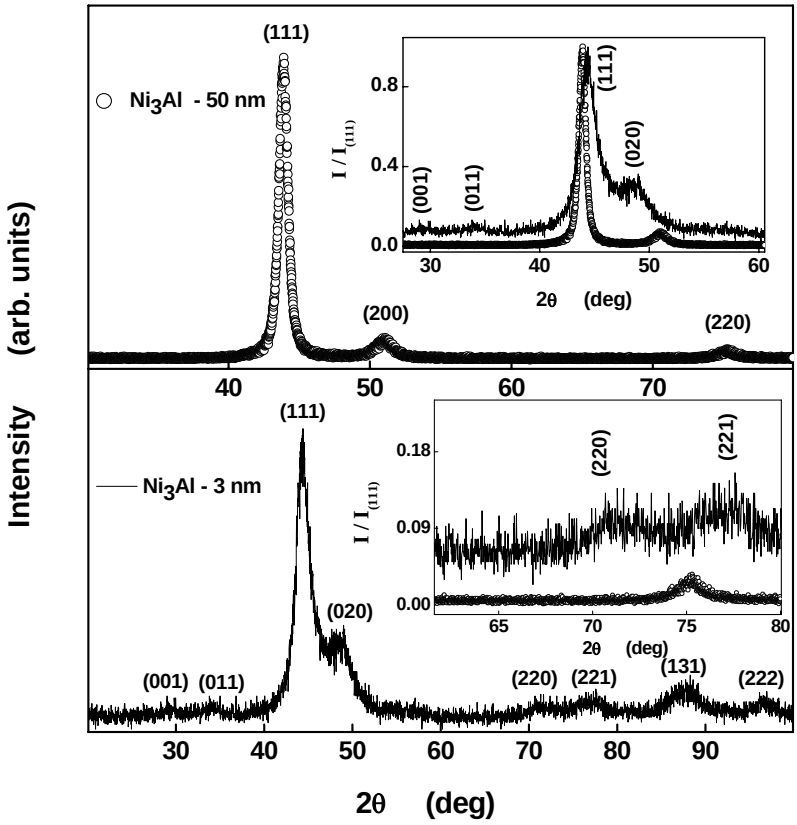

Fig. 5.18: X-ray diffraction patterns (XRD) of the 50 nm and 3 nm nanocrystalline Ni_3Al samples at room temperature. The insets compare the Bragg peak positions and linewidths in the two samples. In the insets the Bragg peaks corresponding to only the tetragonal structure are labelled.

The x-ray diffraction (XRD) patterns were recorded at room temperature on the 3 nm n-Ni_3Al samples using the Phillips x-ray diffractometer with Cu target, in the step-scan mode. Figure 5.18 compares the XRD patterns of the Ni_3Al samples with the average crystallite sizes of 50 nm and 3 nm. Note the difference in the abscissa (2θ) scales. All the Bragg peaks of 50 nm (3 nm) sample can be indexed based on the cubic $L1_2$ (tetragonal $L1_0$) structure, as shown in the top (bottom) panel of figure 5.18. The intensity of the Bragg peaks of the two samples, normalised to the corresponding peak intensity of the (111) Bragg peak, in two different ranges of the Bragg angles (2θ), are depicted in the insets of the figure 5.18. These insets highlight the difference in

the peak positions and larger full width-at-half maxima (FWHM) in the case of the 3 nm Ni_3Al sample as compared to the 50 nm counterpart. Figure 5.19

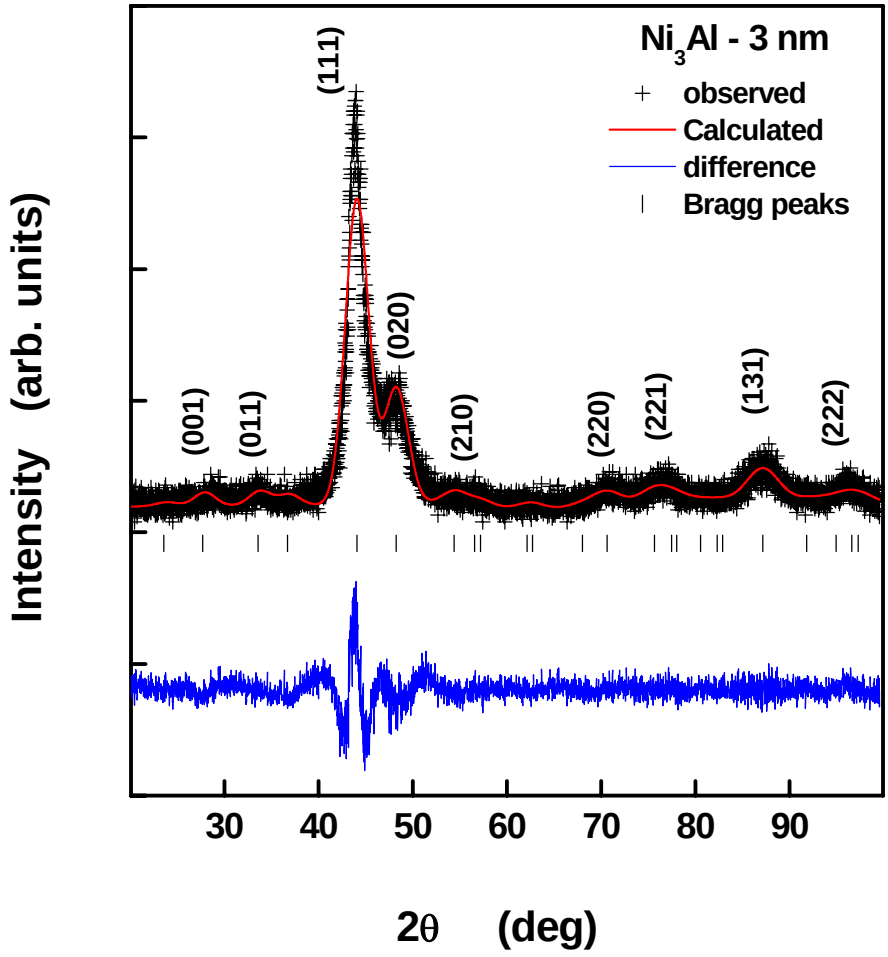

Fig. 5.19: The observed and calculated x-ray diffraction patterns of 3 nm Ni_3Al sample at room temperature, together with the difference plot.

Table 5.1: Structural parameters of the tetragonal Ni_3Al phase in the 3 nm nanocrystalline Ni_3Al sample.

Space group (number)	P4/mmm (123)
Lattice parameters *a* *c*	3.792(3) Å 3.236(4) Å
Atom Wykoff position Al 2g Ni 2h	(x,y,z) (0.0, 0.0, 0.08(2)) (0.5, 0.5, 0.0)
Preferred orientation	(101)
R_P	22.05
R_{WP}	27.8
Goodness of fit (χ^2)	3.0

Table 5.2: Lattice strain and crystallite size obtained using Scherrer formula.

hkl	2θ	FWHM	STD-FWHM	Crystallite size (nm)	Lattice strain (%)
(001)	28.366	2.875	0.15	3.0	4.97
(110)	34.207	2.909	0.15	3.0	4.12
(111)	44.632	2.971	0.15	3.0	3.15
(020)	48.757	2.996	0.15	3.1	2.88
(220)	70.95	3.146	0.15	3.3	1.92
(221)	77.727	3.198	0.15	3.3	1.73
(131)	87.294	3.279	0.15	3.5	1.50
(222)	96.717	3.370	0.15	3.7	1.31

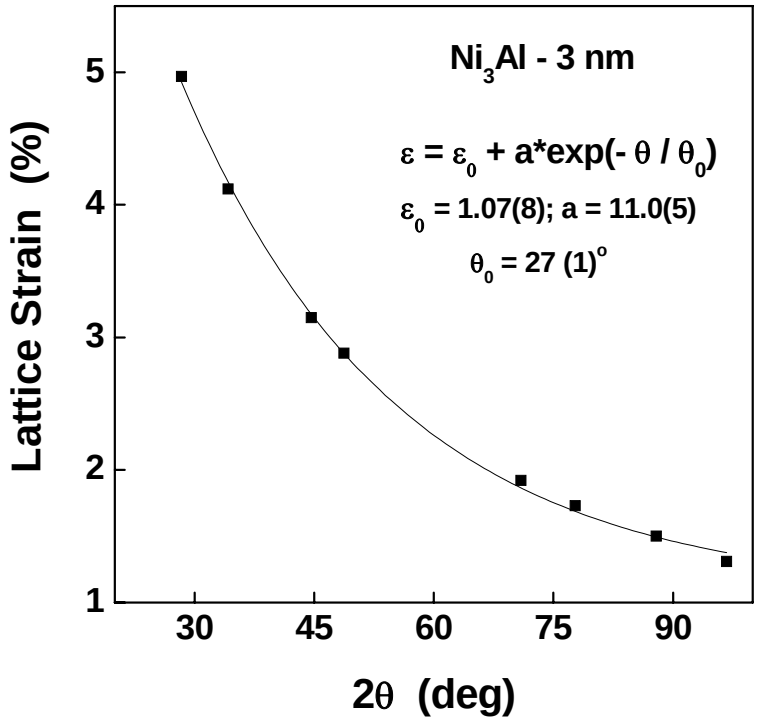

Fig. 5.20: Variation of Lattice strain as a function of 2θ of 3 nm n-Ni_3Al sample.

depicts the observed, calculated and difference x-ray diffraction patterns for the 3 nm Ni_3Al sample, using Philips X-pert software, which yields the lattice

parameter values of the tetragonal structure (P4/mmm) as a = 3.792(3) Å and c = 3.236(4) Å. The preferred orientation, half width parameters and peak shape parameters are varied by the least-squares fitting method in the Rietveld procedure. The values of other refined parameters and relevant details are given in table 5.1. The XRD data shown in figure 5.18 thus confirm the occurrence of a size-dependent structural phase transformation in nanocrystalline Ni_3Al. Occurrence of tetragonal phases of Ni_3Al was earlier reported in the pulsed laser deposited thin films [37-39]. To separate out the lattice strain and size broadening contributions, the Scherrer Calculator is used in the X-pert software and the results are displayed in table 5.2. The instrumental broadening was kept constant at 0.15 degrees over the whole angular range in these calculations. Even if this value of instrumental broadening is changed by 50%, the results shown in the table 5.2 are insensitive to this change since the instrumental broadening is negligible compared to the FWHM of 3 nm sample. This analysis yields average crystallite size of 3.3(3) nm with the lattice strain decreasing exponentially (Fig.5.20) with increasing Bragg angle, 2θ. Since the penetration depth of x-rays into the sample increases with 2θ, exponentially decreasing lattice strain implies that the lattice strain reaches its residual value within atomic layers at the surface. The AFM studies carried out on this sample failed to produce good quality images presumably because the crystallite size of 3 nm falls below the resolution limit of the AFM set up used.

5.5.2 Arrott plots

After correcting the external magnetic field for demagnetization (i.e. $H = H_{ext} - 4\pi N\, M(T,H_{ext})$), the raw $M(H)$ isotherms taken at various temperatures on the 3 nm Ni_3Al sample, shown in figure 5.21(a), are converted into the Arrott

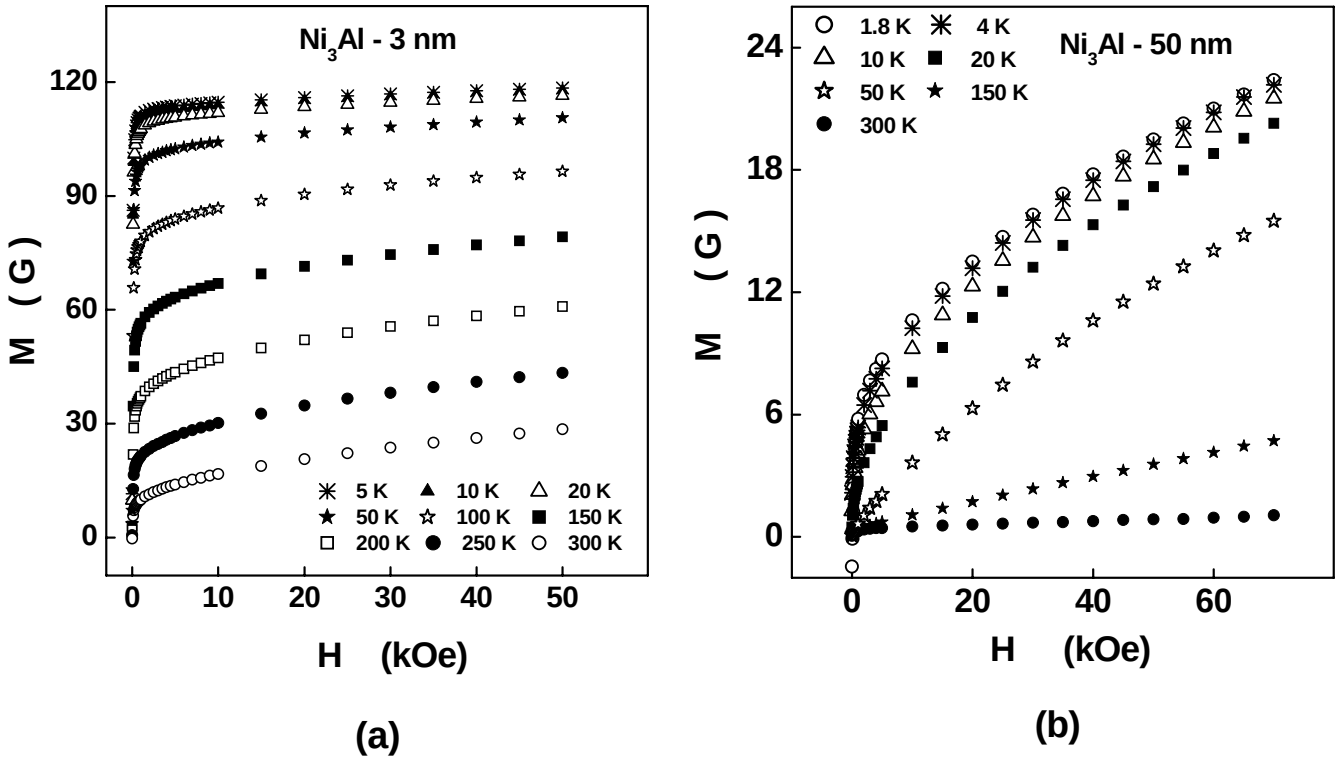

Fig. 5.21: M versus H isotherms taken at a few temperatures ranging from 5 K to 300 K on (a) 3 nm (b) 50 nm nanocrystalline Ni_3Al samples.

(M^2 vs. H/M) plots, which are based on the magnetic equation of state, M^2 = a + b (H/M). For the sake of comparison, M(H) isotherms and Arrott plots of 50 nm samples are given in Fig.5.21(b) and Fig. 5.22(b), respectively. $M(H)$ value is an order of magnitude higher in 3 nm compared to 50 nm sample. From Fig.5.21, it is observed that in case of 3 nm (50 nm) sample, magnetization increases very steeply (slowly) in small applied fields and saturates in fields as low as 1 kOe (does not saturate even in the fields as high as 70 kOe). In sharp contrast to 50 nm sample (see, Fig 5.22(b)), 3 nm Ni_3Al sample seems to exhibit long-range ferromagnetic order. Since, a linear extrapolation of the high-field portions of the Arrott plot isotherms yields finite intercepts on the M^2-axis for T ≤ 300 K, as noticed from Fig.5.22(a). This result is all the more intriguing because the saturation magnetic moment per Ni atom at 5 K ≅ 0.19 μ_B in 3 nm Ni_3Al is very large compared to the magnetic moment of 0.075 μ_B/Ni atom in the bulk polycrystalline counterpart [8].

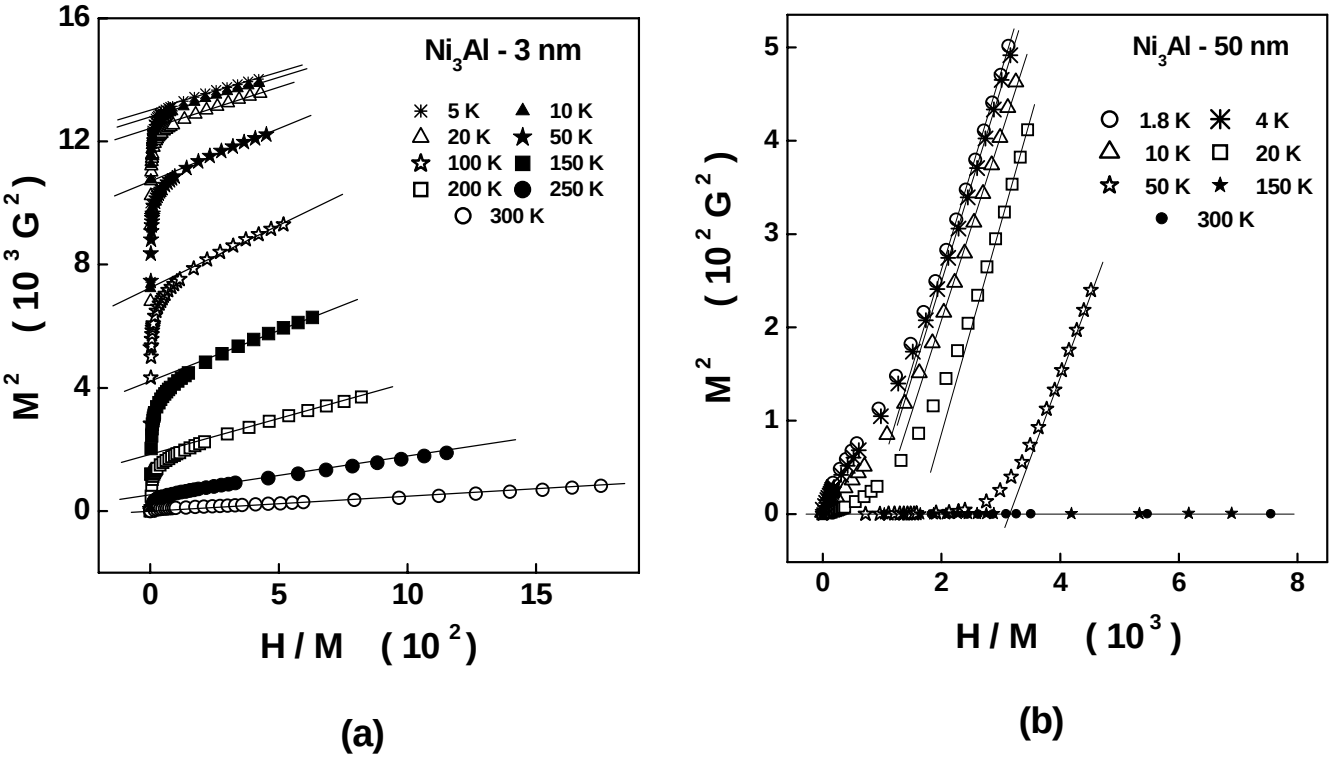

Fig. 5.22:Arrott plots for the (a) 3 nm and (b) 50 nm samples at a few temperatures ranging from 1.8 K to 300 K.

A close scrutiny of the $M(H)$ isotherms revealed that a steep rise in magnetization at low-fields followed by near saturation at high-fields is at variance with the theoretical expectation that a weak itinerant-electron ferromagnet, such as Ni_3Al, should possess a small magnetic moment and a large high-field susceptibility [8]. The spontaneous magnetization a function of temperature (displayed in figure 5.26(a)), computed from the intercepts on the M^2-axis in Fig.5.22(a), indicates the value of the Curie temperature $T_C \approx 300$ K, which is again an order of magnitude higher than the value $T_C = 56.4$ K [8] for polycrystalline (bulk) Ni_3Al.

5.5.3 ac susceptibility

In order to clarify the nature of magnetic order, ac susceptibility (χ_{ac}) measurements were performed, on 3 nm and 50 nm samples, at a driving field of rms amplitude 1 Oe and frequency 87 Hz and 1.11 kHz without any super-

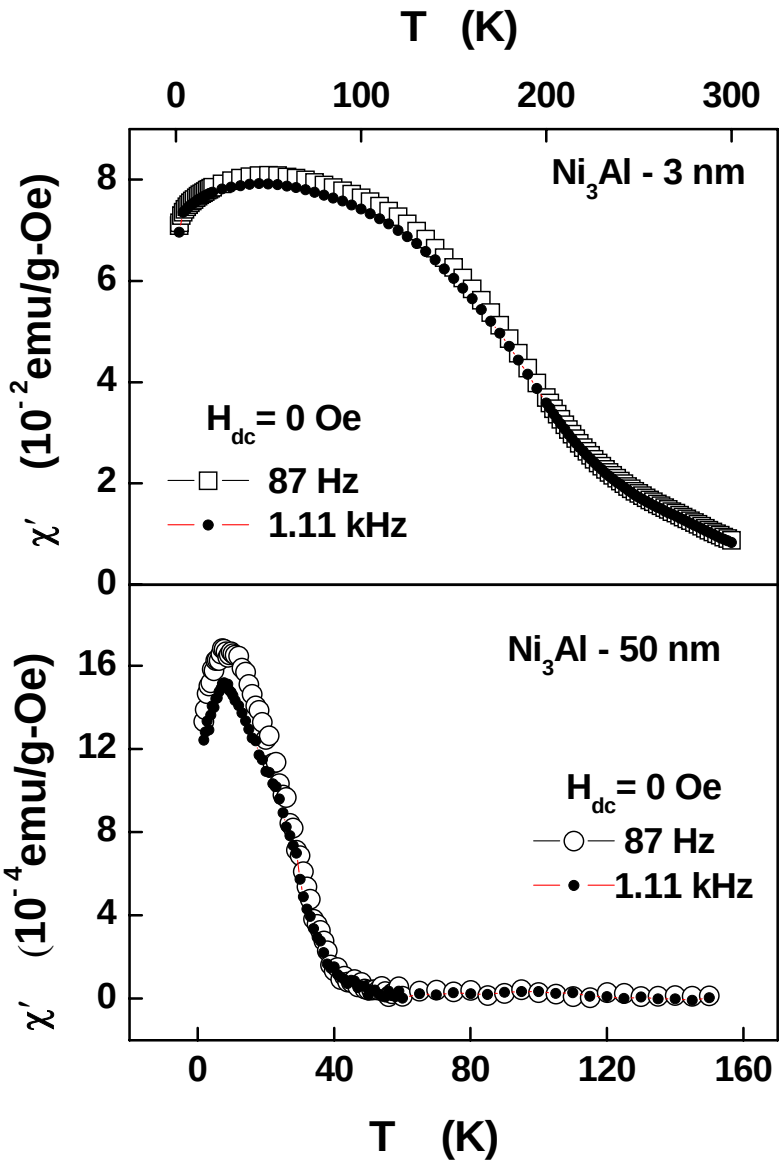

Fig. 5.23: $\chi'(T)$ for 3 nm and 50 nm Ni_3Al samples in the temperature ranges from 1.8 K to 300 K and 1.8 K to 150K at H_{ac} = 1 Oe and frequencies 87 Hz and 1.11 kHz.

posed dc fields, H (see, Fig. 5.23). $\chi'(T)$ is two orders of magnitude higher in 3 nm than 50 nm sample. While a broad hump in $\chi'(T)$ and no discernible shift in the peak of $\chi'(T)$ with the frequency of the ac driving field rule out the possibility of a spin glass or cluster spin-glass like transition in both the 3 nm and 50 nm samples, a complete absence of a steep rise in $\chi'(T)$ as $T_C \approx 300$ K is approached from above in 3 nm sample strongly indicates that no long-range ferromagnetic order exists at temperatures down to 1.8 K. An extremely broad peak in $\chi'(T)$ in nanocrystalline 3 nm Ni_3Al could be a manifestation of the

blocking of nanocrystalline grains with a very broad size distribution over a very wide temperature range since a broad size distribution leads to a wide spectrum of relaxation times for the nano-grains.

5.5.4 Hysteresis loops and dc magnetization

Magnetic hysteresis loops of the 3 nm and 50 nm samples were measured on MPMS SQUID magnetometer at a few temperatures ranging from 1.7 K to 300 K in magnetic fields up to 70 kOe. During the measurement the magnetic field was increased using 'no overshoot mode' of SQUID magnetometer. Figure 5.24 compares the hysteresis loops taken at various temperatures on the nanocrystalline Ni_3Al samples of average crystallite sizes 3 nm and 50 nm. It is evident that in 50 nm sample, magnetization does not saturate even at fields that are an order of magnitude larger compared to the 3 nm sample; comparatively, saturation in magnetization can be achieved at fields as low as

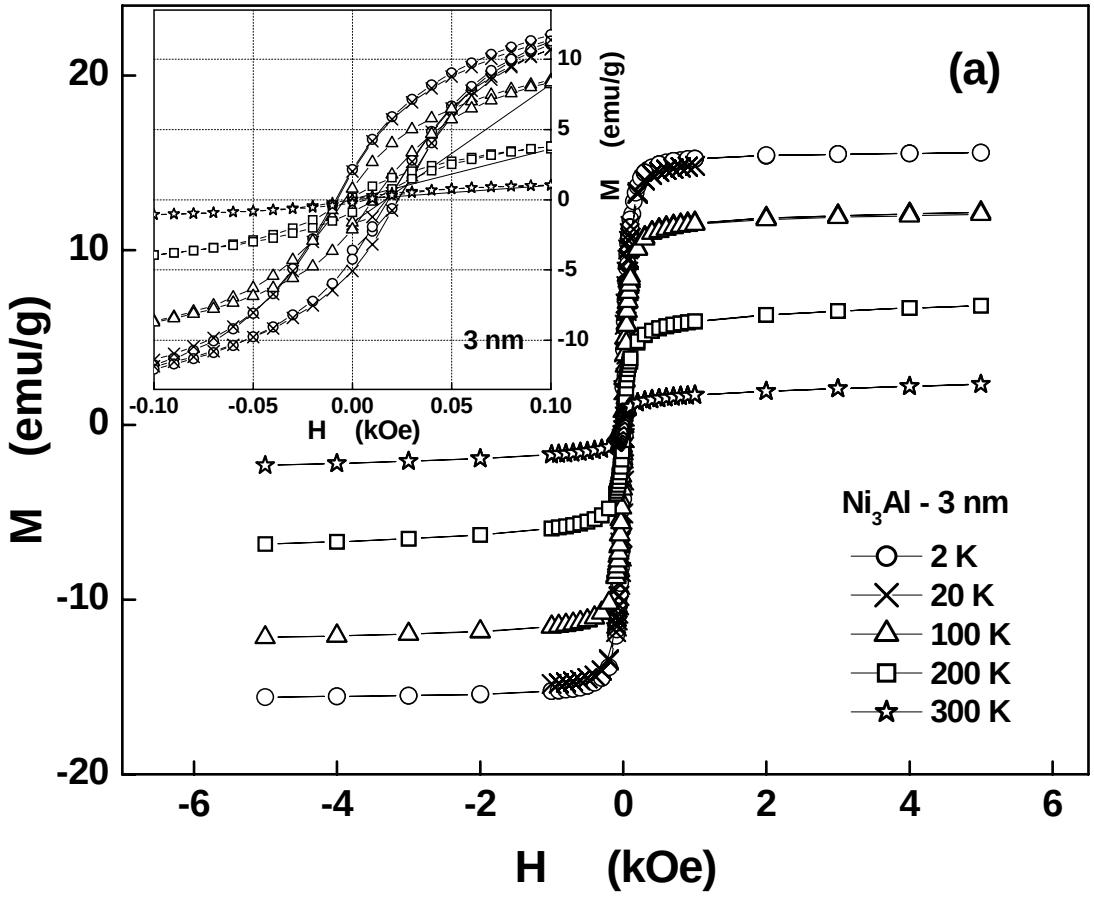

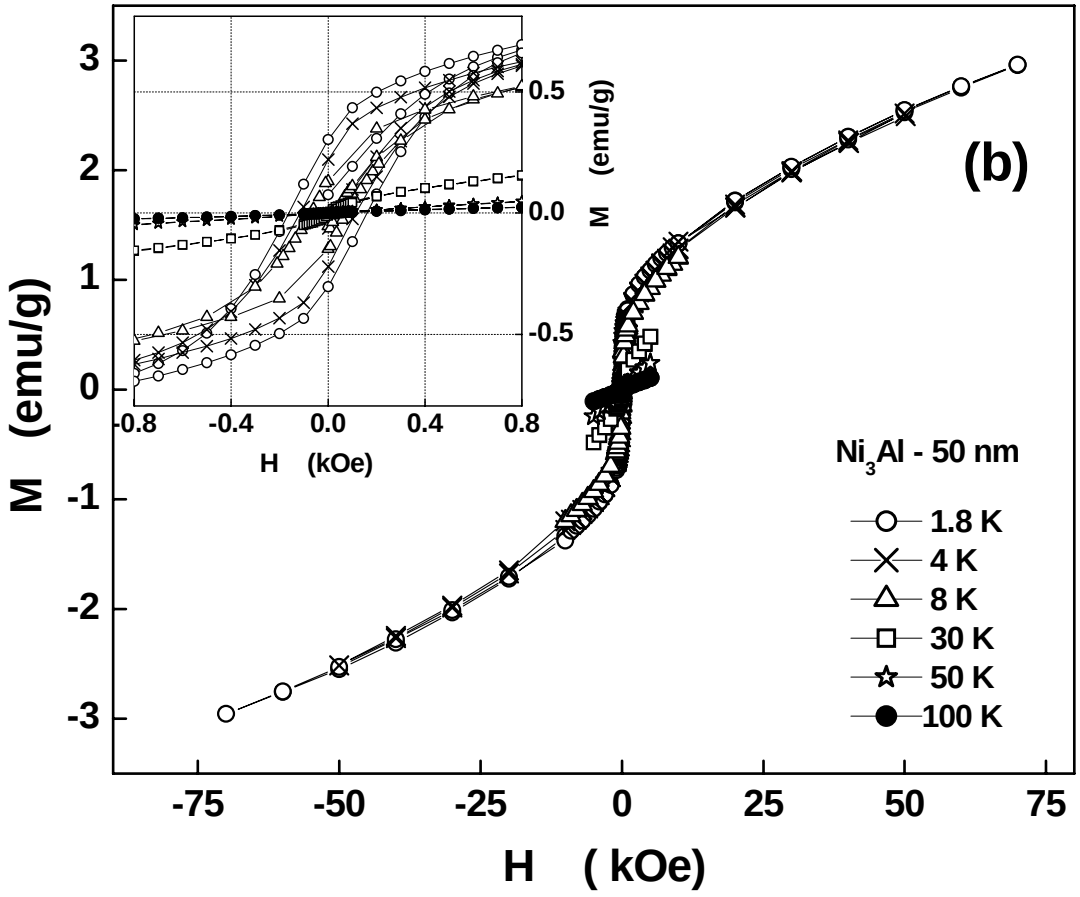

Fig. 5.24: Hysteresis loops of (a) 3 nm sample and (b) 50 nm sample at a few temperatures ranging from 1.8 K to 300 K. Insets of the figure show an enlarged view of the magnetic hysteresis at low fields.

100 Oe in 3 nm sample. The enlarged views of hysteresis loops, in the low field region, are shown in insets of Fig.5.24 for 3 nm and 50 nm samples. Evidently, coercivity, H_c, (remanence, M_r) has an order of magnitude higher (lower) value in the 50 nm sample than in the 3 nm one.

The following arguments based on the observed $H_c(T)$ and $M_r(T)$ curves, displayed in the figure 5.25, permit us to conclude that the apparent long-range ferromagnetic order in the 3 nm sample is *field-induced*. (i) In sharp contrast with the characteristic feature of a system with true long-range ferromagnetic order that M_r follows roughly the same temperature dependence as that of the spontaneous magnetization, M_s, $M_r(T) \neq M_s(T)$ in both the nanocrystalline samples in that the $M_r(T)$ curve has a concave upward curvature as against the

concave downward curvature of $M_s(T)$. The large (small) H_c values could result from strong (weak) interactions between nanocrystallites mediated by the spins

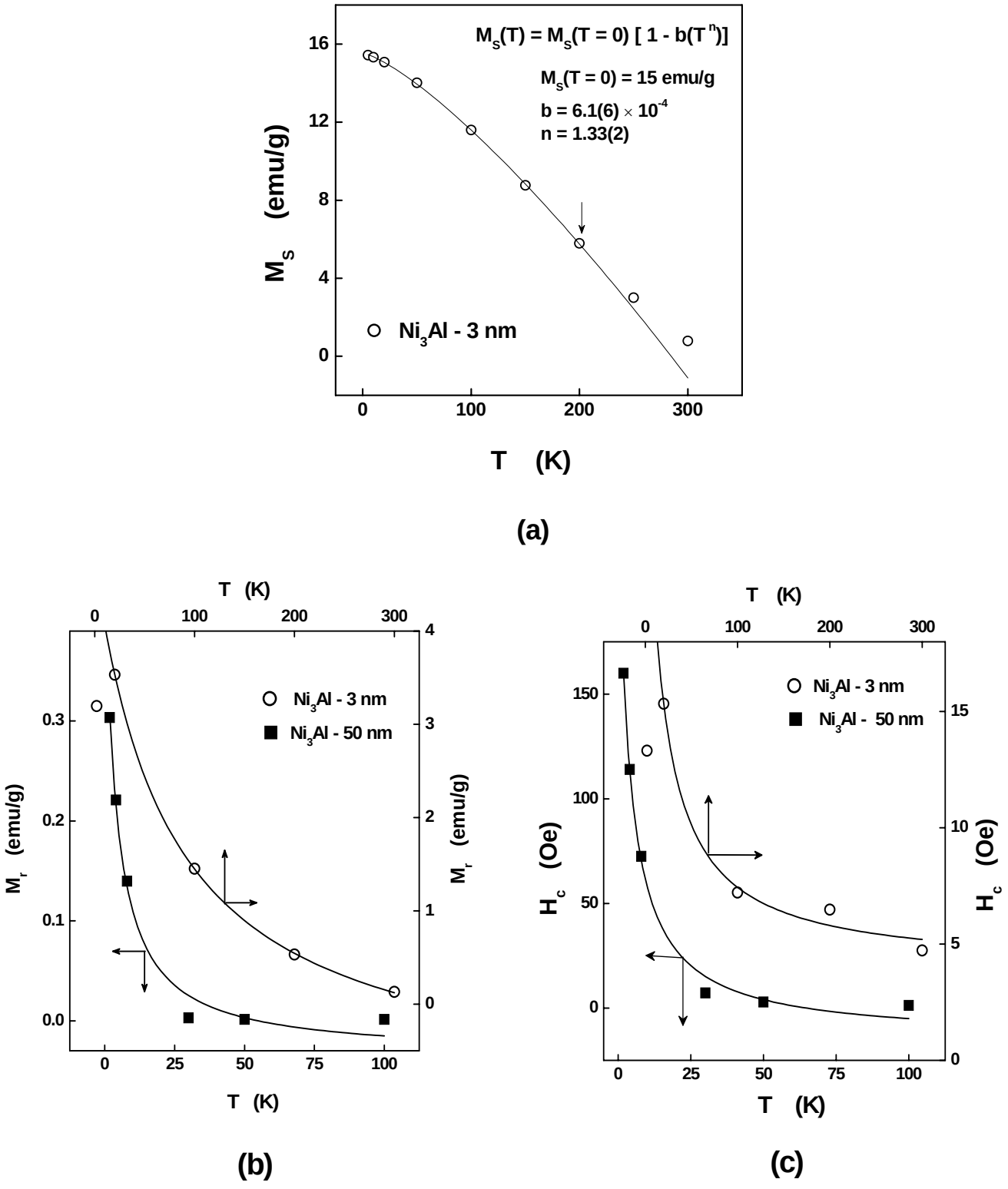

Fig. 5.25: Temperature dependence of (a) M_s for the 3 nm, while (b) H_c and (c) M_r for both the 3 nm and 50 nm nanocrystalline Ni_3Al samples.

at the surfaces of the neighbouring crystallites in 50 nm (3 nm) nanocrystalline sample and intragrain magneto-crystalline anisotropy being small, the spins of the grains as well as the surface spins particularly in the case of the 3 nm sample, can be rotated easily by the application of a small magnetic field.

Figure 5.26(a) [5.26(b)] shows the enlarged view of the thermomagnetic, $M(T)$ curves taken at different magnetic fields in the range 25 Oe $\leq H \leq$ 10 kOe (25 Oe $\leq H \leq$ 150 Oe) and temperatures 5 K $\leq T \leq$ 300 K (1.8 K $\leq T \leq$

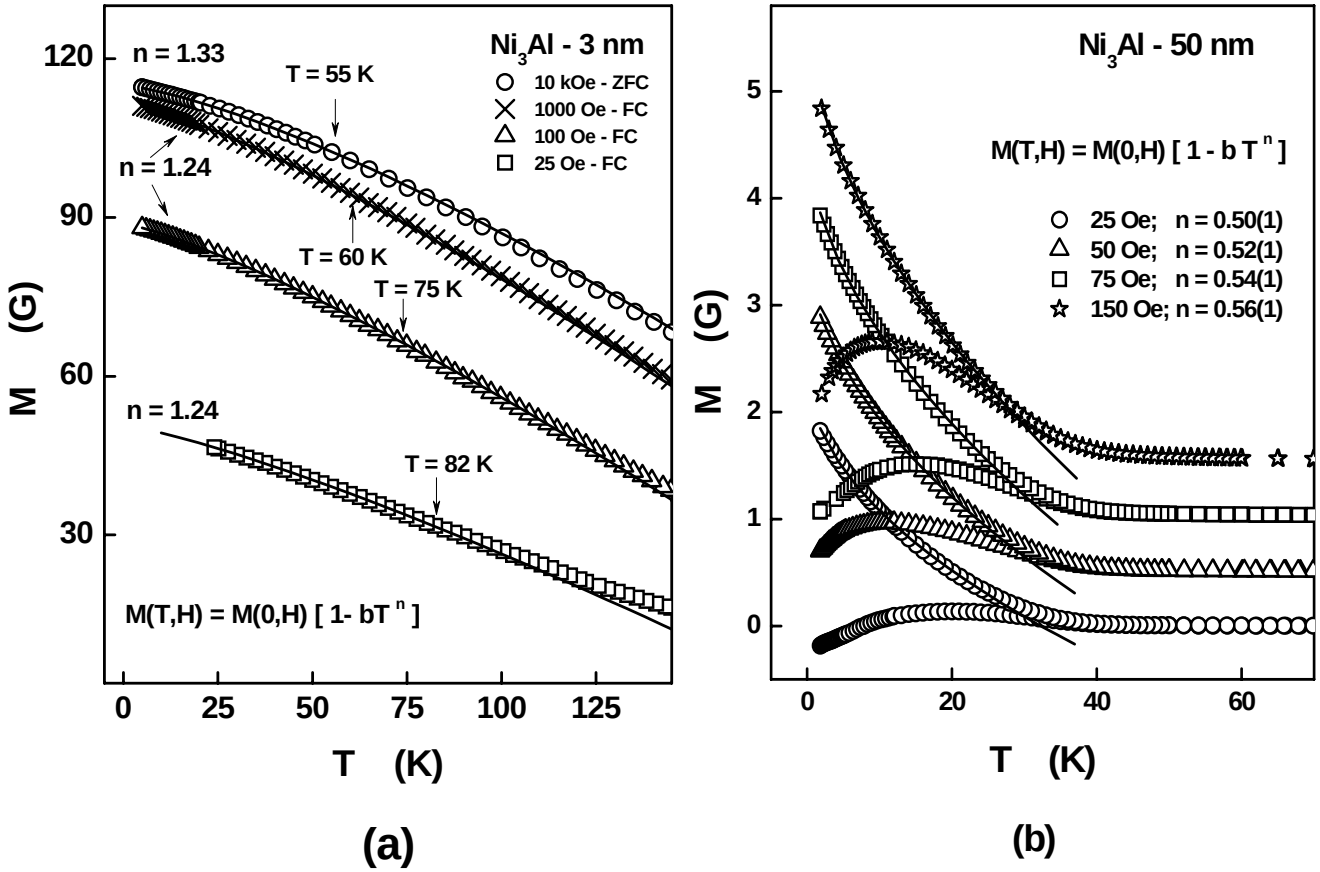

Fig. 5.26: (a) FC or ZFC M(T) curves for the 3 nm sample at temperatures ranging from 5K to 130 K and magnetic fields, H, in the range 25 Oe $\leq H \leq$ 10 kOe. (b) ZFC-FC M(T) curves of 50 nm sample at different fields. For clarity, a upward shift of 0.5 G is given to M(T,H) data starting from that taken at H = 25 Oe Continuous curves through the M(T) data in both Fig.5.26(a) and Fig.5.26(b) denote the best least-square fits based on equation fit based on equation (5.2) of the text.

150 K) on 3 nm (50 nm) Ni_3Al. As a further verification of the presence or absence of the true long-range ferromagnetic order, an attempt was made to determine the 'zero-field' spin wave stiffness at 0 K, $D(0,0)$, from the $M(T,H)$ data using the well-known spin-wave stiffness expression for $M(T,H)$ ([8,40]

$$M(T,H) = M(0,H) - g\mu_B Z(3/2,t_H)[k_B T / 4\pi D(T,H)]^{3/2} \qquad H \neq 0 \qquad (5.1)$$

where the spin-wave stiffness, *D(T,H)* renormalizes with temperature for weak itinerant-electron ferromagnets as $D(T,H) = D(0,H)\,[1 - D_2\,T^2]$, where $D(0,H)$ is related to the magnetization M (0, H) as $D(0,H) = g\mu_B c_\perp M(0,H)$. The details about various physical parameters appearing in Eq.(5.1) are given elsewhere [37]. A concave *upward* curvature in the M - $T^{3/2}$ plots (Figure 5.27)

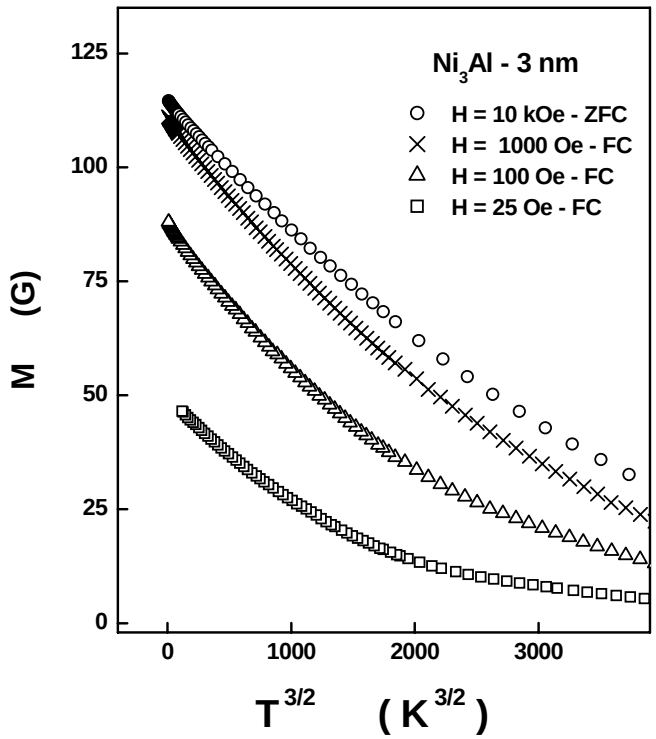

Fig. 5.27: Magnetization of the 3 nm sample at fixed magnetic fields in the range 25 Oe ≤ H ≤ 10 kOe plotted against $T^{3/2}$. Note that the concave upward curvature in M(T) at all field values.

observed at all the magnetic field values precludes any description in terms of the spin-wave expression, Eq.(5.1), since Eq.(5.1) predicts a concave *downward* curvature in $M(T^{3/2})$. Instead the expression

$$M(T,H) = M(0,H)\ [1 - A_n(H)\,T^n] \tag{5.2}$$

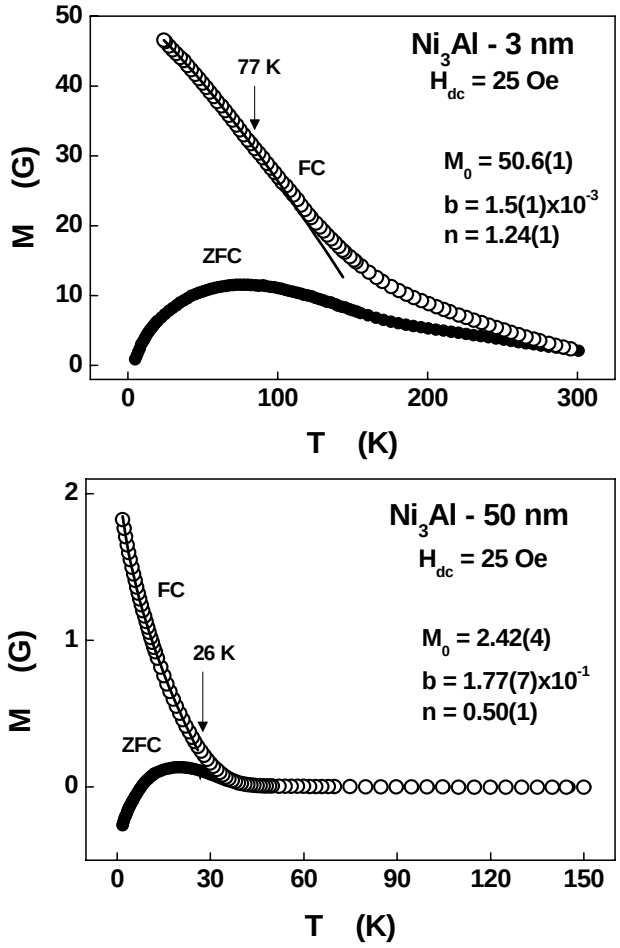

Fig. 5.28: A comparison between the ZFC-FC M(T) curves taken at 25 Oe on the 3 nm and 50 nm nanocrystalline Ni_3Al samples. The continuous curves through the FC M(T) data denote the best least-squares fits based on equation (5.2) of the text.

closely reproduces (Figure 5.26) the observed $M(T)$ at all the fields in both 3 nm and 50 nm n-Ni_3Al samples with the values of the exponent 'n' that depend on H as shown in figure 5.26 (a) and 5.26 (b). Such values of the exponent 'n' are typical of the non-Fermi liquid behaviour near the magnetic instability [22].

An increase in the magnetic field strength reduces the temperature range over which the non-Fermi liquid behaviour is observed.

Figure 5.28 compares 'zero-field-cooled' (ZFC) and 'field-cooled' (FC) thermomagnetic curves for the 3 nm and 50 nm nanocrystalline Ni_3Al samples. While the ZFC and FC $M(T)$ curves in the two cases present some similarities, the irreversibility in magnetization marked by the bifurcation in the ZFC-FC $M(T)$ curves, sets in much higher temperature, $T > 300$ K, in the 3 nm sample compared to that $T \cong 40$ K in the 50 nm counterpart. Recognizing that the ZFC $M(T)$ curves have a striking resemblance with $\chi'(T)$ curves shown in Fig.5.23 and in view of the explanation already provided for the extremely broad peak in $\chi'(T)$ for the 3 nm sample, the blocking of nano-grain spins starts at temperatures above 300 K in 3 nm n-Ni_3Al as compared to 45 K in the 50 nm sample.

Cubic-to-tetragonal structural transformation can change the density of states at the Fermi level, $N(E_F)$, in the 3 nm n-Ni_3Al as compared to that in the 50 nm n-Ni_3Al. Drastic change in $N(E_F)$ could be responsible for the enhanced (*field-induced*) magnetic moment in the 3 nm n-Ni_3Al. The non-Fermi liquid behaviour of magnetization over a wide temperature range at different applied magnetic fields suggests that both the systems (3 nm and 50 nm samples) are near the magnetic instability.

5.6 Summary and conclusions

The present investigation of electrical resistivity (ρ) and longitudinal magnetoresistance (MR) in nanocrystalline (mean crystallite size ~ 50 nm) and polycrystalline samples of Ni_3Al has revealed a number of interesting physical

phenomena that include the following. The ‘zero-field’ resistivity abruptly drops in magnitude as the temperature falls below 4 K and exhibits a non-Fermi-liquid behaviour at temperatures in the range 4 K to 22 K in the nanocrystalline (n-) Ni_3Al. The drop in resistivity gets completely suppressed by a field of ~ 1 kOe. Positive MR increases rapidly for temperatures below 4 K and reaches its highest value of 1.4% at T = 2.5 K and an external magnetic field (H) of 80 kOe in 50 nm n-Ni_3Al. The polycrystalline counterpart neither shows a sudden drop in resistivity nor a positive MR at any temperature, including low temperatures. Magnetic field induces a crossover from positive to negative MR in 50 nm n-Ni_3Al particularly for T > 30 K. The usual Lorentz mechanism cannot account for the magnitude of the positive MR for temperatures up to 20 K in this sample. Antiferromagnetic spin fluctuation mediated superconductivity (thought to be responsible for the drop in resistivity at T < 4 K) and non-Fermi-liquid behaviour are physical phenomena that occur when the system is near the magnetic instability. The reduction of crystallite size to ~ 45 nm drives the weak itinerant-electron ferromagnet Ni_3Al to magnetic instability (where the long-range ferromagnetic order breaks down, as is evident from our previous [8] and present magnetization results). Now that the magnetically-mediated superconductivity and non-Fermi-liquid behaviour are symptomatic of the behaviour near a magnetic quantum critical point, the results of the present investigation open up an interesting possibility of using nanocrystallite size as a control parameter (instead of external pressure or magnetic field hitherto used in the literature) to study quantum critical phenomena (which may be occurring over wider temperature and crystallite size (control parameter) domain than theoretically predicted), non-Fermi liquid behaviour and magnetically-mediated superconductivity.

When the average crystallite size drops to ≅ 3 nm, n-Ni_3Al system undergoes a cubic-to-tetragonal structural phase transformation that leads to a drastic change in the density of states at the Fermi level, $N(E_F)$. The large magnetic moment observed in the 3 nm n-Ni_3Al could originate from the increased $N(E_F)$. The non-Fermi liquid behaviour of magnetization is observed over a much wider temperature range, 5 K ≤ T ≤ 80 K, in 3 nm sample than in the 50 nm counterpart. The magnetic field does not change the functional form of $M(T)$ but reduces the temperature range over which non-Fermi liquid behaviour is observed. At first sight, the magnetization versus magnetic field, $M(H)$, isotherms, taken on 3 nm n-Ni_3Al, give the impression that this sample exhibits long-range ferromagnetic order for T ≤ 300 K. However, based on the results of a detailed investigation of ac susceptibility, magnetic hysteresis loops and 'zero-field-cooled' and 'field-cooled' thermomagnetic curves, ample experimental evidence is provided in favour of the field-induced long-range ferromagnetic order in 3 nm n-Ni_3Al.

References

[1] H. Gleiter, Prog. Mater. Sci. **33**, 223-315 (1989).

[2] R. Skomsky, J. Phys.: Condens. Matter **15**, R814 (2003).

[3] H. Kisker, T. Gessmann, R. Wirschum, H. Kronmüller, and H.-E. Schaefer Nanostruct. Mater. **6**, 925(1995) and references sited therein.

[4] J. S. C. Jang and C. C. Koch, J. Mater. Res. **5**, 498 (1990).

[5] G. F. Zhou, M. J. Zwanenberg, and H. Bekker, J. Appl. Phys. **78** 3438 (1995).

[6] D. Mukherji, R. Müller, R. Gilles, P. Strunz, J. Rössler, and G. Kostorz, Nanotechnology, **15**, 648 (2004).

[7] S. N. Kaul, Anita Semwal and H.-E. Schaefer, Phys. Rev. B **62**, 13892 (2000).

[8] Anita Semwal and S. N. Kaul, Phys. Rev. B **60**, 12799 (1999) and references cited therein.

[9] C. L. Seaman, M. B. Maple, B. W. Lee, S. Ghamaty, M. S. Torikachvili, J. -S. Kang, L. Z. Liu, J. W. Allen, and D. L. Cox, Phys. Rev. Lett. **67**, 2882 (1991).

[10] A. P. Mydosh and P. J. Ford, *Amorphous Magnetism* (edited by H. O. Hooper and A. M. de Graaf, Plenum, New York) 1973.

[11] N. Rivier and K. Adkins, J. Phys. F: Met. Phys. **5**, 1745 (1975).

[12] J. H. J. Fluitmann, R. Boom, P. F. De Chatel, C. J. Schinkel, J. L. L. Tilanus and B. R. De Vries, J. Phys. F: Metal Phys. **3**, 109 (1973).

[13] J. A. Hertz, Phys. Rev. B 14, 1165 (1976).

[14] P. Nozières and A. Blandin, J. Phys. (France) **41**, 193 (1980).

[15] M. A. Continentino, Phys. Rev. B **47**, 11587 (1993).

[16] A. J. Mills, Phys. Rev. B **48**, 7183 (1993).

[17] A. Tsvelik and M. Reizer, Phys. Rev. B **48**, 9887 (1993).

[18] T. Moriya and T. Takimoto, J. Phys. Soc. Jpn. **64**, 960 (1995).

[19] G. G. Lonzarich, *The electron* (edited by M. Springford, Cambridge University press, Chap. 6).

[20] S. L. Sondhi, S. M. Girvin, J. P. Carini, and D. Shahar, Rev. Mod. Phys. **69**, 315 (1997).

[21] P. Coleman, Physica B **259-261**, 353 (1999).

[22] G. R. Stewart, Rev. Mod. Phys. **73**, 797 (2001).

[23] D. Belitz and T. R. Kirkpatric, *Dynamics: Models and Kinetic Methods for Non-Equilibrium Many Body Systems* (edited by J. Karkheck, Kluwer, Dordrecht) 399 (2000).

[24] S. N. Kaul, J. Phys.: Condens. Matter **17**, 5595 (2005) and the reference cited therein.

[25] H. Yamada and S.Tanaka, Prog. Theor, Phys. 48, 1828 (1972); J. Phys. Soc. Jpn. **34**, 51 (1973).

[26] N. D. Mathur, F. M. Grosche, S. R. Julian, I. R. Walker, D. M. Freye, R. K. W. Haselwimmer and G. G. Lonzarich, Nature **394**, 39 (1998).

[27] S. S. Saxena, P. Agarwal, K. Ahilan, F. M. Grosche, R. K. W. Haselwimmer, M. J. Steiner, E. Pugh, I. R. Walker, S. R. Julian, P. Monthoux, G. G. Lonzarich, A. Huxley, I. Sheikin, D. Braithwaite and J. Floquet, Nature **406**, 587 (2000).

[28] C. Pflieder, M. Uhlarz, S. M. Hayden, R. Vollmer, H. Von Löhneysen, N. R. Bernhoft, and G. G. Lonzarich Nature **412**, 58 (2001).

[29] M. J. Steiner et. al., Physica B **329**, 1079 (2003).

[30] P. Niklowitz, F. Beckers and G.G. Lonzarich, G. Kneble, B. Salce, J. Thomsson, N. Bernhoeft, D. Braithwaite, and J. Flouquet, Phys. Rev. B **72**, 024424 (2005).

[31] A. C. Abhyankar and S. N. Kaul, Appl. Phys. Lett. **89**, 193125 (2006).

[32] Note that correct estimate for the size is d = 45(3) nm instead of t = 25(3) nm mentioned in the reference 2.

[33] S. N. Kaul and S. Srinath, JPCM **10**, 11067 (1998).

[34] S. N. Kaul and S. Methfessel, Solid State Commun. **47**, 147 (1983).

[35] K. Binder and A. P. Young, Rev. Mod. Phys. **58**, 801 (1986).

[36] J. A. Mydosh, *Spin glasses: an experimental introduction* (Taylor & Francis, 1993).

[37] S. Bysakh, P. K. Das, and K. Chattopadhyay, Scripta mater. **44**, 1847 (2001).

[38] R. Banerjee, G. B. Thomson, G. B. Viswanathan, and H. L. Fraser, Philos. Mag. Lett. **82**, 623 (2002).

[39] R. Banerjee, P. Ayyub, G. B. Thomson, R, Chandra, P. Taneja, and H. L. Fraser, Thin Solid films **441**, 225 (2003).

[40] S. N. Kaul, J. Phys.: Condens. Matter **11**, 7597 (1999).

Chapter 6

Martensitic phase transformation in $Ni_{55}Fe_{20}Al_{25}$ alloys: Effect of quenched disorder

6.1 Introduction

In the previous three chapters, we discussed the effect of off-stoichiometry, site-disorder and crystallite size on the magnetic, transport and galvanomagnetic properties of binary Ni_3Al compound in polycrystalline as well as nanocrystalline forms. The defects and different types of disorder in this system strongly influence the magnetic excitations and hence the functional dependences of thermodynamic properties, such as magnetization, susceptibility and resistivity, on temperature are modified so as to give rise to many interesting physical phenomena that include the non-Fermi liquid behaviour of resistivity and magnetization over extended temperature range and magnetically-mediated superconductivity. Consequently, the nano-crystallite size emerges as a new control parameter to study quantum phase transitions. This scenario may change completely when Ni in Ni_3Al compound is partially substituted by another 3d transition metal atom such as Fe, Co, Mn, etc. The crystal structure and interactions among the constituent atoms can get modified depending on the type and amount of substitution by the third element. For example, a substitution of a very small fraction of Ni atoms on the Ni sublattice in Ni_3Al by Fe can lead to the nucleation of body-centred-cubic NiAl phase. Substitution by Mn may lead to antiferromagnetic interactions between Ni and Mn atoms. Moreover, site occupancy of the third element is an important issue in that it has profound effect on the mechanical, magnetic and transport properties of ternary alloys, Ni-M-Al with M = Fe, Mn or Co.

Ni-Fe-Al is an example of a ternary alloy that is derived from the ordered (β or B2) Ni-Al compound. Intermetallic alloys based on Ni-Al binary system have attractive properties such as the high melting point (~1680 °C), low

density, excellent oxidation resistance [1] and shape memory effect [2]. But brittleness of B2 Ni-Al alloys makes them unsuitable for industrial applications. Inoue et al. [3, 4] have shown that Ni_3Al (γ') and ($\gamma' + \beta$) alloys in Ni-Fe-Al system, with good ductility and high strength, can be obtained by rapid solidification; these alloys also exhibit shape memory effect. Furukawa et al. [5] reported that 170 ppm addition of boron to Ni-Fe-Al alloys increases its fracture strength from 394 to 1130 MPa and elongation-to-fracture ratio increases from 2.8% to 18.1%. Wallin and Savage [6, 7] were first to report shape memory effect in Ni-Fe-Al-B rapidly solidified ribbons. X-ray diffraction studies of their samples revealed the presence various phases like, NiAl (β and β'), Ni_3Al (γ and γ'), Fe_3Al, FeAl, FeNi, and Al_5Fe_2 etc. Liu et al. [8,9] confirmed the shape memory effect and did systematic study with different Fe concentrations ranging from 4 at.% to 20 at.% in Ni rich (60 at.%, rest Al + Fe) melt-spin ribbons. From the TEM and x-ray diffraction studies, they found that the martensite phase has a body-centered orthorhombic structure. Effect of annealing at ~ 400 °C was to reduce the martensite transformation temperature. Kainuma et al. [10] studied the phase transformation and microstructural evolution in bulk Ni-Fe-Al alloys with the help of TEM and DSC techniques. On annealing at 1300 °C at 1 hr and then re-annealing at 800 °C for 24 hrs, different kinds of microstructures were observed in different compositions of the alloys; namely, lameller, blocky and widemanstätten microstructures were found in Ni-25Al-13Fe, -15Fe and -18Fe alloys, respectively. Highest shape recovery of about 71 % was found in the Ni-25Al-15Fe alloy with the martensite start, M_S, temperature at 416 K.

Compared to many mechanical and structural investigations on Ni-Al-Fe alloys, only a few reports are available on electronic structures, atomic

arrangements and magnetic properties. Goldberg and Shevakin [11] measured magnetic susceptibilities and NMR^{27}Al spectra for $Ni_{50-x}Al_{50}Fe_x$ and $Ni_{50}Al_{50-x}Fe_x$ with x = 0, 1, 2 - 10 alloys and calculated density of states (DOS) and electronic structure of 15 atomic clusters using tight-binding approximation and LCAO (Linear Combination of Atomic Orbitals) Hamiltonian. They observed Pauli type paramagnetism with no or negligible dependence of susceptibility, χ, on temperature for ternary compounds with deficiency of Ni-atoms while rest of alloys showed Curie-Weiss susceptibility. New peaks in ^{27}Al NMR spectra and increase in paramagnetic susceptibility suggested new type of atomic arrangements consisting of Fe-atoms in the first or second shell of Al-atoms. This observation was consistent with the atom-probe field-ion microscopic studies of Duncan et al. [12], where more than 90% of Fe atoms were found to occupy Al sites. Experimental and electronic structure calculations indicated an increase in the density of states at the Fermi level by the substitution of Fe for both the Ni- and Al-atoms. Fu et al [13], in their study of the solid solution effects on $[Ni_{50}][Al_{40}Ni_{10-x}Fe_x]$ alloys, concluded that: 1) Addition of Fe softens the Ni-rich Ni-Al alloys; this unusual softening behaviour is concomitant with large increase in lattice parameter. 2) The presence of Fe atom at Al sites results in a large magnetic moment of 2.55 μ_B on Fe atoms, which, in turn, induces a magnetic moment of 0.1 μ_B on Ni atoms. 3) The enhancement of magnetic moment at the Fe atoms originates from both the magnetic coupling between the Ni and Fe and the electronic localization (and hence the local magnetic moment) of Fe atoms. 4) The other solute atoms such as Mn and Cr have a behaviour similar to that of Fe but the addition of cobalt has a contrasting behaviour because Co atoms preferentially occupy Ni sites. Thus, magnetism plays a major role in modifying the mechanical properties, e.g., the hardness in Ni-Al alloys. Lechermann and

Fähnle [14] performed theoretical calculations using the cluster expansion method and constructed global phase diagram of Ni-Fe-Al system. They showed that a face-centred cubic structure is more favourable than body-centred cubic structure in a wide compositional range with the exception of the equi-atomic B2 Ni-Al phase. Magnetic energy gain is 50 meV/atom in the ternary B2 phase that has negligible fraction of Fe-atoms thus the magnetism influences the atomic ordering in this phase.

In order to ascertain the effect of Fe substitution on the magnetic properties of $Ni_{75}Al_{25}$ and to determine the role of site-disorder in the ternary alloys, the samples of $Ni_{75-x}Fe_xAl_{25}$ alloys with x = 0, 5, 10, 20, have been prepared in different states of site disorder by suitable heat treatments. The detailed room temperature x-ray investigations [15] performed on these samples revealed the following: (I) Regardless of the sample thermal history, the nucleation of the Fe_3Al phase occurs at a Fe concentration as low as 3 at.%. With further increase in Fe concentration, the volume fraction of the Fe_3Al phase increases at the expense of the Ni_3Al phase so much so that at 20 at.% in melt quench ribbon, Fe_3Al phase becomes the majority phase (> 95 %) and Ni_3Al (< 5%) is reduced to a minority phase. The long-range order parameter decreases with Fe substitution and at Fe = 20 at.% it has the lowest value. (II) Ductility increases with Fe substitution, more so in the melt-quenched ribbons. (III) For a given sample thermal history, the composition essentially determines the site preference of Fe solute atoms. Thus in Ni-deficient alloys Fe atoms occupy Ni-sites whereas in Al-deficient alloys Fe atoms prefer Al-sites. These observations were made considering Ni_3Al as a reference alloy system.

The temperature dependence of magnetization at different but fixed magnetic fields was analysed and contributions of spin waves (SW) and spin fluctuations (SF) to thermal demagnetization were estimated [16]. An elaborate analysis of the magnetization (M) versus magnetic field (H) isotherms, taken at 5 K, in magnetic fields up to 70 kOe, yielded the physical parameters such as the high-field susceptibility, χ_{hf}, density of states (DOS), at Fermi level, $N(E_F)$, spin-wave stiffness at T = 0 K, D_0, Curie temperature, T_C, and spontaneous magnetization at T = 0, M_0. Irrespective of the state of disorder (i.e., 'as prepared', 'annealed' and 'melt-quenched'), strong deviations from the compositional dependence of M_0, D_0, T_C and χ_{hf}, for the alloys with $0 < x < 10$ were observed in the case of 20 at.% Fe alloy. For example, M_0 and D_0 varied *linearly* with increasing Fe concentration up to x = 10 at.%, but the samples of composition x = 20, did not follow the same trend. DOS were considerable higher while χ_{hf} was very low for 20 at.% Fe samples as compared to other compositions. The dc electrical resistivity of the $Ni_{75-x}Fe_xAl_{25}$ alloys was measured in the temperature range from 1.7 K to 300 K. The thermal hysteresis in resistivity was observed [17] only in the samples containing 20 at.% Fe. The thermal hysteresis normally reflects the presence of supercooled and superheated states, which form the main characteristics of first-order phase transformation. The martensitic transformation is a first-order solid-solid phase transformation, which takes place by the diffusionless shearing of the parent austenite phase, which, in turn, causes the shape memory effect in alloys. This possibility prompted an extensive structural investigation aimed at determining the nature of phase transition in the $Ni_{55}Fe_{20}Al_{25}$ alloy using neutron diffraction and transmission electron microscopy (TEM) techniques. The effect of site-disorder on the martensitic phase transition in $Ni_{55}Fe_{20}Al_{25}$, as reflected in the

electrical transport, magnetoresistance and magnetic properties, is described in this chapter.

6.2 Synthesis, and structural, magneto-transport and magnetic characterization

Polycrystalline rods (10 mm in diameter and 100 mm in length) with nominal composition $Ni_{55}Fe_{20}Al_{25}$ were prepared by radio frequency induction-melting technique. Rectangular strips of dimensions 40 x 2.5 x 0.5 mm^3 and spheres of 3 mm diameter were spark-cut from the rods. The spark-cut samples were *annealed* at 520 °C for 16 days in a sealed quartz tube filled with 99.999% purity argon and subsequently quenched in ice water. The remaining portions of these rods were *melt-quenched* to form ribbons of width of 2 mm and thickness of ~ 30 μm. The "annealed" and "quenched" samples of $Ni_{55}Fe_{20}Al_{25}$ alloy are henceforth referred to as a-Fe_{20} and q-Fe_{20}, respectively. Neutron diffraction (ND) measurements were performed on the strips (a-Fe_{20}) and several ribbons (q-Fe_{20}), on the high-flux two-axis D20 diffractometer at Institut Laue-Langevin (ILL), Grenoble, using thermal-neutron wavelength of 1.297 Å. The diffracted intensity was measured in the steps of 0.1° over the scattering angle range of 10° - 150°. In the case of the a-Fe_{20} samples, diffraction intensities were collected for 2 minutes in the steps of 5 K over the temperature range of 300 K to 48 K while cooling, using position sensitive microstrip gas-detector. By contrast, the diffraction data were collected on the q-Fe_{20} sample while heating at temperatures 90 K, 200 K, 240 K and 280 K keeping all other experimental parameters same. TEM studies were performed using Tecnai 20 UT high-resolution TEM (200 kV) and Tecnai 20 G2 analytical TEM (200 kV). For investigations at room temperature and for compositional studies, the samples were loaded in a low-background double tilt TEM holder. For microstructural studies at low temperatures (103 K),

cryogenic double-tilt TEM holder (Model 636, M/s Gatan) was used. The compositional studies were performed with EDS (sapphire) detector attached to the Tecnai 20 G2 analytical TEM. Longitudinal magnetoresistance, $\Delta\rho_{||}/\rho = [\rho_{||}(T,H) - \rho(T,H=0)]/\rho(T,H=0)$ versus magnetic field, H, isotherms were measured in the fields up to 80 kOe during the heating cycle. The electrical resistivity, $\rho(T)$, was measured by standard four-probe dc method in the range of 3 K - 300 K on rectangular strips and ribbons of length 40 mm in both the heating and cooling cycles. 'Field-cooled' (FC) and 'zero-field-cooled' (ZFC) magnetization measurements were performed on spherical samples of a-Fe_{20} and on several ribbon-pieces of q-Fe_{20}, stacked one above the other, with magnetic field, H, applied along the length within the ribbon plane, using a SQUID magnetometer, in external magnetic fields, H, ranging from 20 Oe to 10 kOe at temperatures in the range 5 K $\leq T \leq$ 300 K. The $M(H)$ isotherms were measured in magnetic fields up to 20 kOe at several fixed temperature values in the range 5 K $\leq T \leq$ 300 K in the heating cycle only.

6.3 Structural and physical property changes associated with martensitic phase transformation

6.3.1 Neutron diffraction

Shape memory alloys scatter neutrons very effectively and as such, neutrons are an almost ideal probe to study these alloys at a microstructural level. The similarity in the atomic scattering factors of the neighbouring elements in the periodic table (as is the case in transition metals, in particular) makes it extremely difficult to obtain much information about the chemical ordering from x-ray diffraction. However, neutron scattering cross-sections vary erratically with the atomic number and hence the neutron scattering lengths can be radically different for neighbouring elements in the periodic

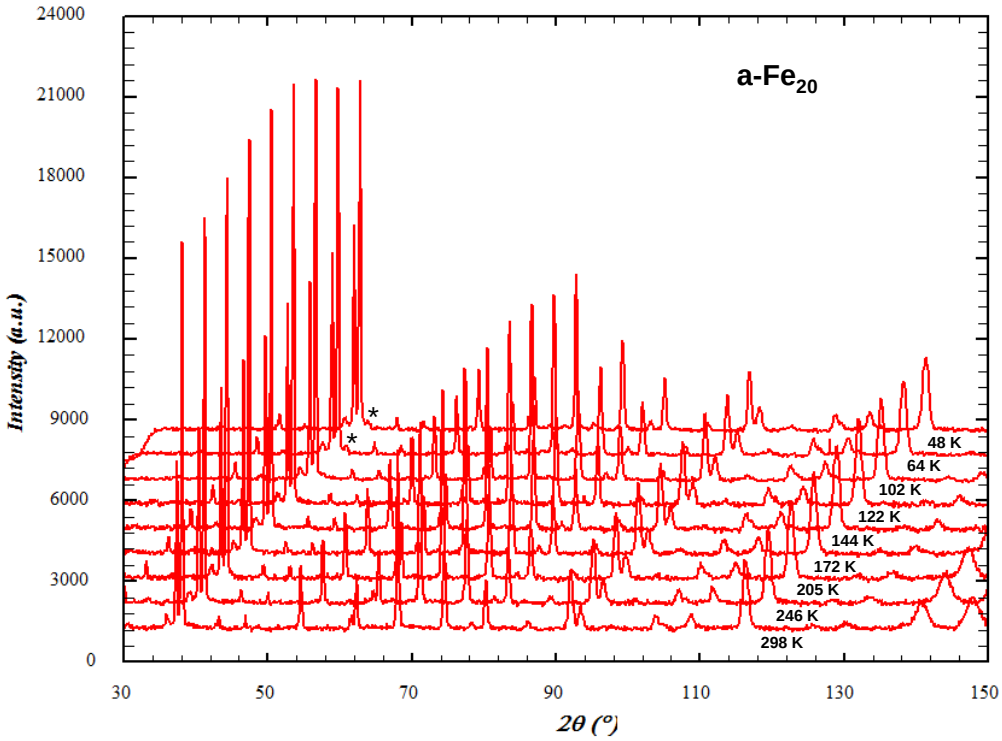

*Fig. 6.1: Neutron diffraction patterns of a-Fe_{20} at a few representative temperatures taken while cooling. No peaks corresponding to martensite phase are observed except near mark * at the lower temperatures.*

table. Moreover, the neutron scattering power is not a function of diffraction angle [18]. Due to appreciable difference in neutron scattering lengths, neutron diffraction is well-suited for determining the site preference for, or occupancy of, solute atoms. Neutron diffraction techniques have the advantage that the entire bulk of the sample, together with its inherent defects, is probed. Figures 6.1 and 6.2 show the neutron diffraction (ND) patterns of a-Fe_{20} and q-Fe_{20} samples taken at different temperatures in the ranges 50 K ≤ T ≤ 300 K and 90 K ≤ T ≤ 280 K, respectively. ND spectra on the annealed sample (a-Fe_{20}) were taken at every 5 K intervals while cooling whereas in the case of melt-quenched sample (q-Fe_{20}) ND spectra were taken at 90 K, 200 K, 240 K and 280 K while heating. The phase transformation is evident (Fig. 6.2) in q-Fe_{20} but not in a-Fe_{20} (Fig. 6.1). Figure 6.3 shows a comparison between the neutron diffraction patterns taken at 298 K and 48 K in different scattering angle ranges

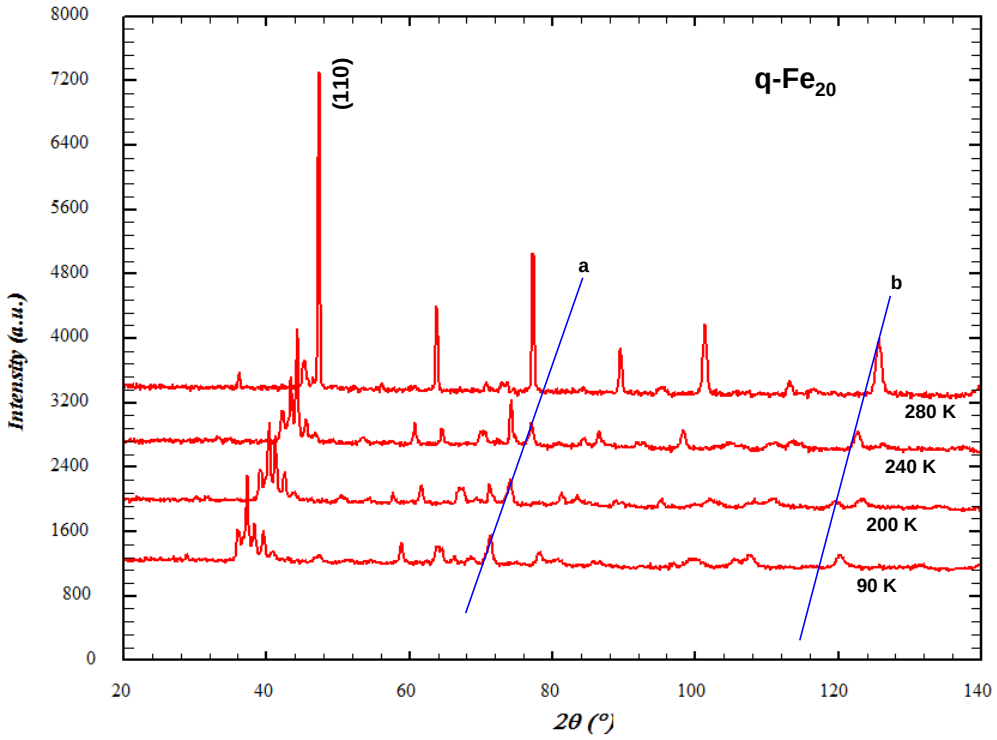

Fig. 6.2: Neutron diffraction patterns of q-Fe_{20} taken while heating. MT occurs at ~ 240 K. The line (a) serves to highlight the disappearance of the martensite peak whereas the line (b) follows the evolution of the austenite peak. Splitting of austenite peak (110) into four peaks suggests 14 M modulated structure.

for the sample a-Fe_{20}. This comparison clearly demonstrates that a very weak phase transformation occurs in a-Fe_{20}. The neutron diffraction patterns shown in figures 6.1- 6.3, thus reveal that a-Fe_{20} and q-Fe_{20} samples both undergo martensitic transformation (MT), but the MT is complete (partial and sluggish) in q-Fe_{20} (a-Fe_{20}). To know the crystal structure and identify the phases present in the samples q-Fe_{20} and a-Fe_{20}, LeBail profile fitting procedure was followed using the FULLPROOF package. In the LeBail fitting, all possible diffraction peaks are generated for a given space group as per the symmetry conditions; it is just a mathematical way of fitting a powder diffraction profile with peak positions constrained by cell parameters. Thus, only approximate unit cell parameters and space group are required for LeBail profile fitting. In the case of full-pattern Rietveld refinement method, initial structural model is required, i.e., approximate atomic (Wykoff) positions, number of atoms, occupancies,

and the details of experimental conditions are required. The advantage is that the actual atomic positions can be refined, individual isotropic/anisotropic thermal parameters, site occupancies and magnetic structure can be obtained by the method of least-squares refinement. However, LeBail fitting is considered to be an easy and efficient way to check the plausibility of the space groups [19]. The parameters used to measure the progress of a Rietveld refinement (and also LeBail method) [20] with a good agreement between the crystal structure model and observed diffraction pattern are tabulated in table 6.1. The R_{wp} and χ^2 are the most important parameters, as the numerator of these

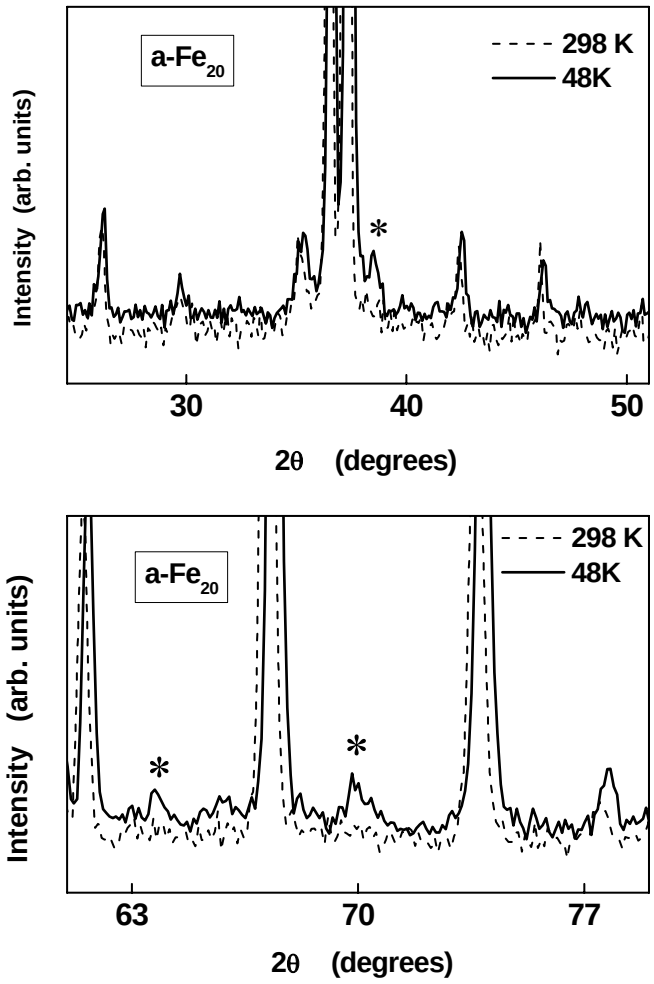

Fig. 6.3: Comparison of neutron diffraction patterns of a-Fe_{20} taken at 298 K and 48 K. Small peaks (marked by asterisk) belongs to martensite phase at 48 K.

parameters contains the quantity minimized during the least-squares fitting. The R_{exp} is a measure of statistics of the experimental data and is the minimum possible value for R_{wp} for a given pattern. Thus χ^2 will have a value of 1 when $R_{exp} = R_{wp}$.

Table 6.1: Rietveld refinement agreement parameters.

$R_p = 100 \frac{\sum_{i=1,n} \lvert y_i - y_{c,i} \rvert}{\sum_{i=1,n} y_i \sum Y_i}$	- - - - - - - - - - - - - - - - - Profile R-factor
$R_{wp} = 100 \sqrt{\left[\frac{\sum w_i \lvert y_i - y_{c,i} \rvert^2}{\sum w_i y_i^2} \right]}$	- - - - - - - - - - - - - - Weighted profile R-factor
$R_{exp} = 100 \sqrt{\left[\frac{(n-p)}{\sum_i w_i y_i^2} \right]}$	- - - - - - - - - - - - - - - - - - Expected R-factor
$\chi^2 = \left(\frac{R_{wp}}{R_{ep}} \right)^2$	- - - - - - - - - - - - - - - - - - Reduced chi-square

where n = total number of data points and p = number of parameters refined

In ternary shape memory alloys, with the general formula X_2YZ (X = Ni, Y = Fe or Mn, Z = Al or Ga), Heusler type cubic $L2_1$ structure is expected [21] at room temperature, whereas binary Ni_xAl_{100-x} alloys with x = 50 to 69 at.% have an ordered *bcc* (B2) structure. $L2_1$ type structure can be represented by a *bcc* lattice in which Ni (X) atoms occupy the centre of the cube, while the Mn (Y) and Ga (Z) atoms alternatively occupy the positions at the apexes. We have found that the LeBail fitting procedure cannot unambiguously distinguish between the $L2_1$ (space group Fm3m) and B2 (space group Pm3m) structures

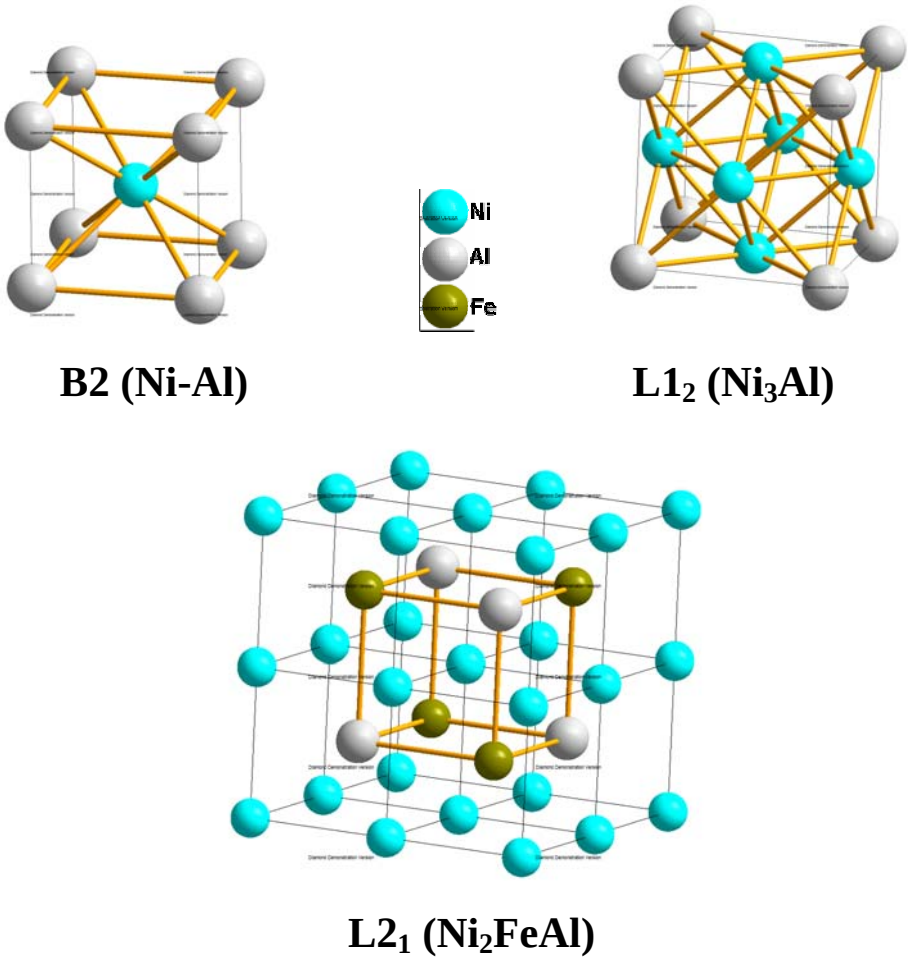

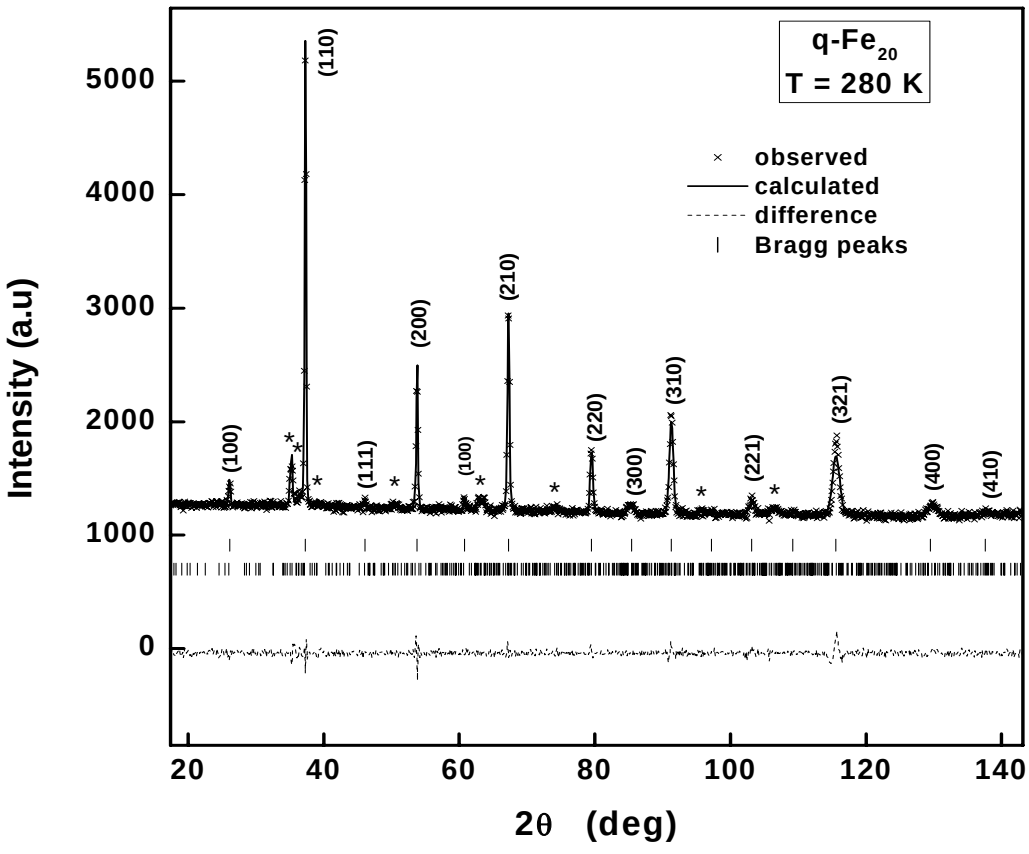

Fig. 6.5: The observed and calculated (Lebail) neutron diffraction pattern of q-Fe$_{20}$ at 280 K. The '' marked peaks are from the minor martensite phase.*

in the diffraction patterns of the presently studied quenched and annealed samples. To resolve this issue and to study the microstructure of the austenite and martensite phases in the samples q-Fe_{20} and a-Fe_{20}, transmission electron microscopy (TEM) studies were undertaken at 300 K and 103 K. At room temperature, TEM investigations revealed that the austenite phase in q-Fe_{20} has a B2 structure. A detailed discussion about the TEM results and analysis is given in the next section. After confirming the crystal structure of the majority phase as B2, the LeBail method was used to account for the unidentified peaks of the minority phase in the neutron diffraction pattern of q-Fe_{20} at 280 K (see Fig. 6.2). Fits with the space groups of various phases in Ni-Al and Ni-Fe-Al phase diagrams [22] from the literature such as face-centred tetragonal, $L1_0$, NiAl (P4/mmm) [2,9,10], tetragonal Ni_3Al (I4/mmm) [23], orthorhombic Ni_5Al_3 (Cmmm) [9,24], hexagonal Ni_2Al or Ni_2Al_3 ($P\bar{3}m1$) [25] and monoclinic Ni_2Al (P2/m) [26] were attempted. All the extra peaks were accounted for only by the space group P2/m of the monoclinic structure and the corresponding LeBail fit (B2 + monoclinic) at 280 K is shown in figure 6.5 and the lattice parameters are given in table 6.2.

Table 6.2: LeBail profile fitting parameters for the neutron diffraction (ND) pattern of q-Fe_{20} taken at T = 280 K.

q-Fe_{20} at 280 K	**Pm3m B2**	***P2/m monoclinic***
a (Å)	2.8676(1)	*4.161(1)*
b (Å)	-	*2.627(1)*
c (Å)	-	*14.781(2)*
β°		*94.94(1)*
R_p	*1.45*	
R_{wp}	*2.03*	
χ	*1.97*	

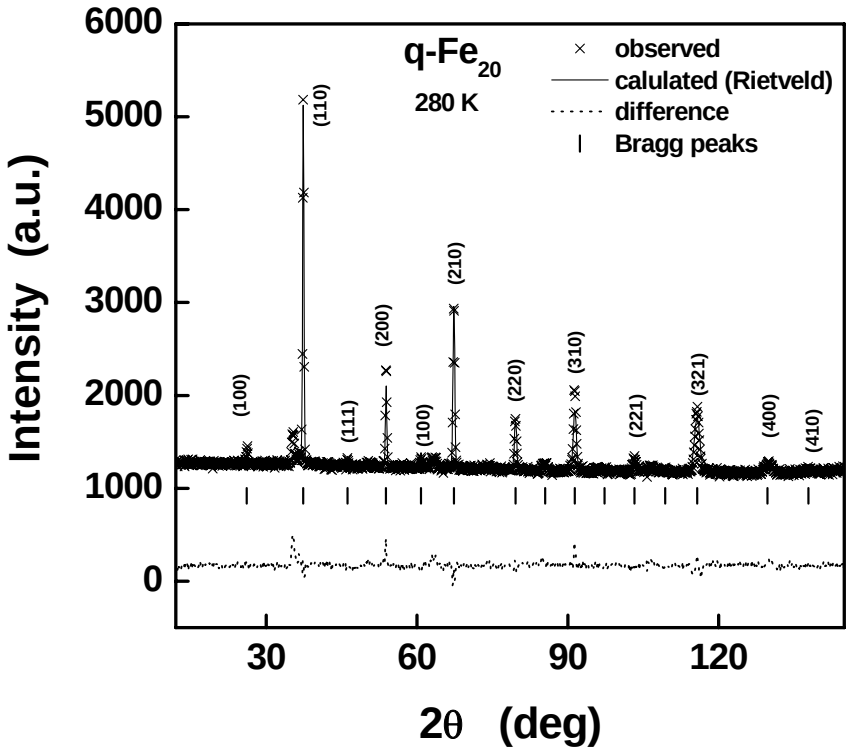

Fig. 6.6: The observed and calculated (Rietveld) neutron diffraction pattern of q-Fe_{20} at 280 K. Only the B2 phase is refined.

Table 6.3: Rietveld refinement parameters for the ND pattern of q-Fe_{20} at T = 280 K.

Atoms	**q-Fe_{20} at T = 280 K/ Pm3m (B2)**		
	Site	Occupancy (%)	Biso ($Å^2$)
Ni	(0.0,0.0,0.0)	1.0(1)	0.45(5)
Al	(0.5,0.5,0.5)	0.44(3)	1.03(9)
Fe	(0.5,0.5,0.5)	0.54(3)	1.03(9)
a (Å)	2.8658(2)		
Asymmetry	-0.17(2)		
Lorentzian strain	0.22(5)		
R_p	1.95		
R_{wp}	2.92		
χ	4.06		

To ascertain the site occupancy of Fe in q-Fe_{20} ribbons at room temperature, the actual Rietveld refinement was performed on the neutron diffraction pattern taken at 280 K for q-Fe_{20}. The initial structural model for the

metastable monoclinic Ni_2Al phase is not known and also the volume fraction of the monoclinic phase is found to be less than 3 % (determined by comparing integrated intensity ratio of the peaks of the two phases). For these reasons, the monoclinic Ni_2Al phase was not included in the actual Rietveld refinement. Full pattern refinement method for the austenite B2 phase proceeded first by assuming that all the Fe solute atoms occupy the Al sites. Then, Fe atoms were allowed to occupy either the Ni or Al sites, while keeping thermal parameters fixed. The best fits were obtained (figure 6.6) when the Fe atoms occupied the Al sites. The neutron scattering lengths for Ni (10.3×10^{-12}) and Fe (9.5×10^{-12}) atoms are quite close as compared to that for the Al (3.4×10^{-12}) atom, which makes the determination of Fe population on the Ni site very difficult. However, the forced occupation of Fe atoms on the Ni sites resulted in a negative occupancy with a decline in the goodness-of-fit. The parameter values and the site occupancies are tabulated in Table 6.3. From this exercise, it is clear that most of the Fe atoms are occupied on the Al sites in q-Fe_{20} at 280 K. Similar results were obtained recently from the first principle theoretical calculations [12, 27] and neutron diffraction study [28] in $Ni_{60-x}Al_{40}Fe_x$ with x = 0-10 alloys.

Next, we have analysed the neutron diffraction pattern, taken on the a-Fe_{20} sample at 298 K, using the LeBail fitting, as shown in fig. 6.7. The austenite phase in the a-Fe_{20} sample consists of two majority phases with *bcc* B2 and *fcc* $L1_2$ structures. Inclusion of the monoclinic martensite phase resulted in a little or even no, improvement in the goodness-of-fit. However, as shown in the inset of Fig. 6.7, the low-angle diffraction peaks marked by the symbol '♦' could be accounted for only by the monoclinic phase with P2/m space group. The volume fraction of this phase (when compared to B2 + $L1_2$

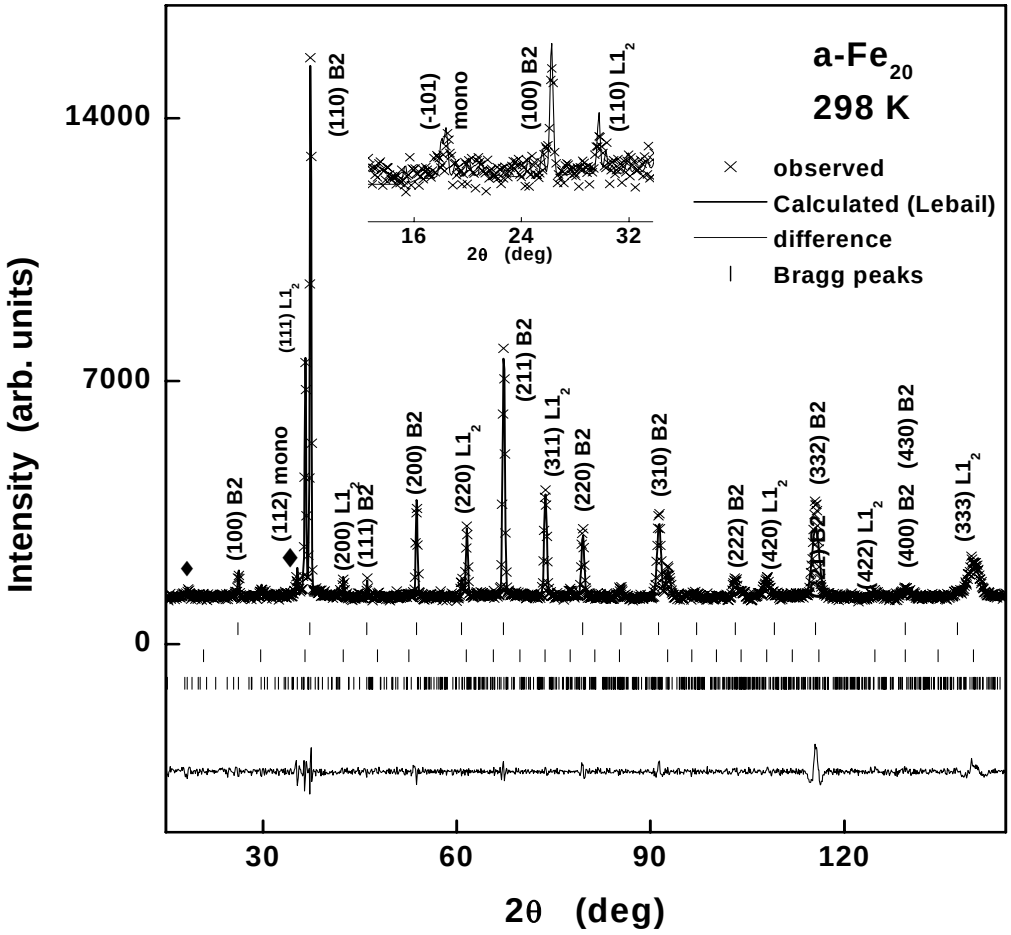

Fig. 6.7: The observed and calculated (LeBail) neutron diffraction pattern of a-Fe_{20} at 298 K. The inset shows low angle Bragg peaks, which indicate the presence of third minor monoclic phase along with both major (B2 and $L1_2$) phases.

phases together) in a-Fe_{20} is even less than that in q-Fe_{20}. The actual Rietveld refinement then proceeds the same way as mentioned earlier in the case of q-Fe_{20} samples. The parameters of the actual refinement are given in table 6.4 and calculated and observed patterns, along with the difference pattern, are shown in figure 6.8.

It is evident from the Table 6.3 and 6.4 that Fe atoms preferentially occupy Al sites in the B2 phase of q-Fe_{20} and a-Fe_{20} samples whereas Fe atoms are nearly equally distributed among Ni and Al sites in the $L1_2$ phase of a-Fe_{20}

at 298 K. The Lorentzian strain parameter is quite large (small) in q-Fe_{20} (a-Fe_{20}) due to the quenched-in stresses and site disorder present in the melt-spun ribbons (annealed strips). The percentage of the Fe (Al) atoms in the B2 phase of q-Fe_{20} is large (small) compared to that in the a-Fe_{20}. R_{wp} and R_p parameters of $L1_2$ phase in a-Fe_{20} have larger values compared to that in the B2 phase. In the $L1_2$ phase, the site occupancies of Fe atoms could not be determined uniquely as a change in the occupation of Fe atoms on both Ni and Al sites has shown no improvement in R_{wp} and goodness-of-fit parameters. The $L1_2$ phase has a preferred orientation in the <111> direction. Thus, at 280 K (298K), q-Fe_{20} (a-Fe_{20}) sample is in the single- (two-) phase state with some traces of minor monoclinic $(NiFe)_2(AlFe)$ phase.

Table 6.4: Rietveld refinement parameters for the ND pattern of a-Fe_{20} taken at T = 298 K.

a-Fe_{20} at 298 K					
Pm3m (B2)			Pm3m ($L1_2$)		
Atoms	Occupancy (%)	Biso ($Å^2$)	Atoms	Occupancy (%)	Biso ($Å^2$)
Ni (0.0,0.0,0.0)	1.0(1)	0.64(7)	Ni (0.0,0.5,0.5)	0.73(1)	0.62(5)
Al (0.5,0.5,0.5)	0.55(3)	0.76(8)	Fe (0.0,0.5,0.5)	0.27(1)	0.62(5)
Fe (0.5,0.5,0.5)	0.45(3)	0.76(8)	Al (0.0,0.0,0.0)	0.76(5)	1.30(9)
			Fe (0.0,0.0,0.0)	0.24(4)	1.30(9)
a(Å) = 2.8690(1)			*a*(Å) = 3.5860(2)		
Loretzian strain (*x*) > 0.01			Loretzian strain (*x*) = 0.28(7)		
			Preff orientation= -1.07(8)		
Volume fraction = 74(2)			Volume fraction = 26(1)		
R_p = 5.78					
R_{wp} = 8.6					
χ = 5.9					

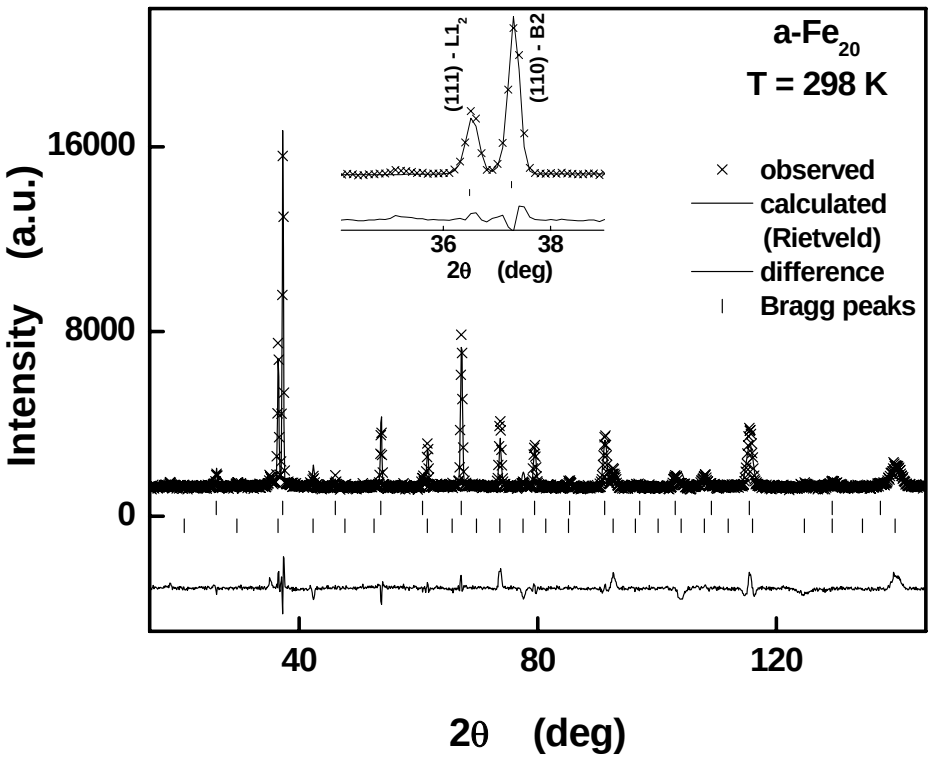

Fig. 6.8: The observed and calculated (Rietveld) neutron diffraction patterns for a-Fe_{20} at 298 K. The inset shows the peaks belonging to the major phases $L1_2$ and B2.

While heating up from 90 K, austenite B2 phase grows at the expense of the monoclinic martensitic phase in q-Fe_{20}, as is clearly seen in Figure 6.2. LeBail profile fitting procedure was employed to low temperature diffraction patterns of q-Fe_{20} and the fits are depicted in figure 6.9(a). The lattice parameters are tabulated in Table 6.5. Figure 6.9(b) shows temperature evolution of the low-angle Bragg peaks of the austenite B2 and the monoclinic martensite phases while heating. Figure 6.9(c) depicts the temperature dependence of the volume fractions of the austenite and martensite phases, across the martensite phase transformation, calculated from the integrated intensities (obtained from the LeBail fit) of the highest intensity Bragg peaks (i.e (-201) of martensite and (110) of austenite phase). The following important observations were made from the analysis. (i) The martensite phase has a monoclinic structure with lattice paramenters a = 4.167 Å, b = 2.630 Å ,

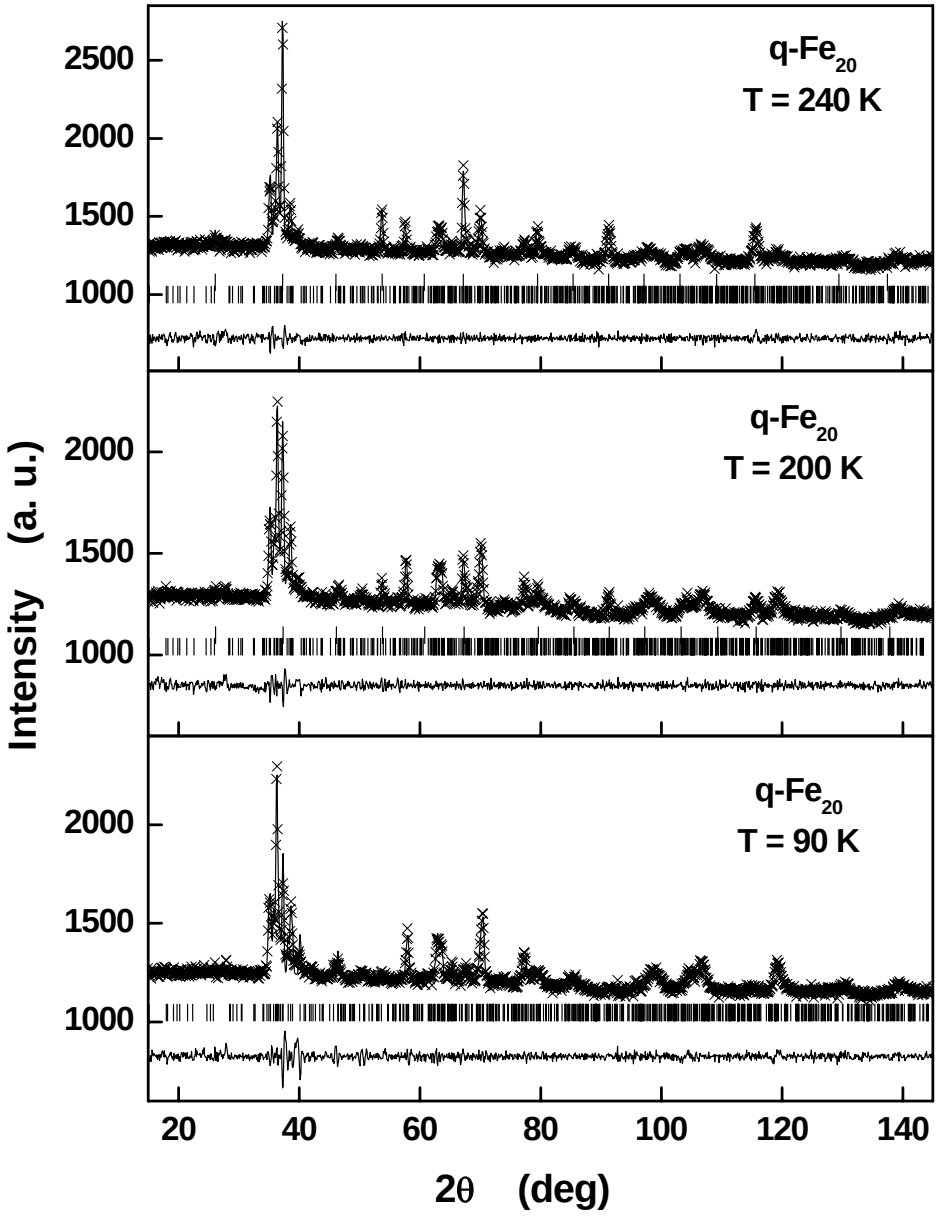

Fig. 6.9(a): The observed and calculated (Lebail) neutron diffraction patterns of q-Fe_{20} at T = 240K, 200K and 90 K, together with difference patterns.

c = 14.79 Å and β = 94.96° at 240 K. (ii) The martensite phase grows rapidly below 240 K so much so that it becomes a majority phase at 200 K, and at 90 K, it is the only phase that exists. (iii) Thus, B2 phase coexists with the monoclinic phase from 240 K to 200 K. (iv) The austenite B2 phase transforms completely to the monoclinic martensite phase at temperatures below 200 K.

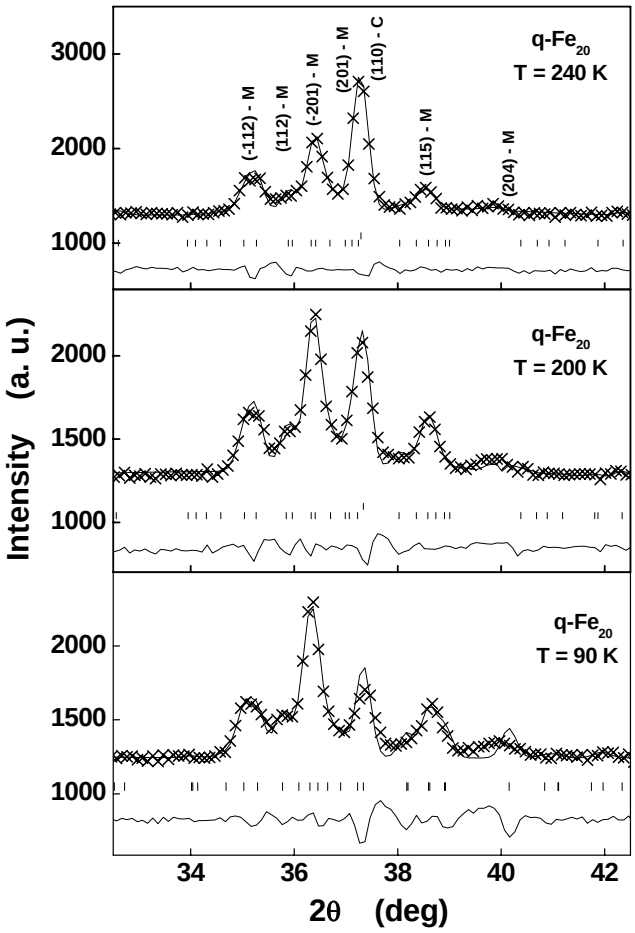

Fig. 6.9(b): Expanded view of the Bragg peaks, appearing at low Bragg angles in the ND patterns displayed in Fig.6.9(a), that highlights the increase of the austenite peak at the cost of the martensite peaks while heating.

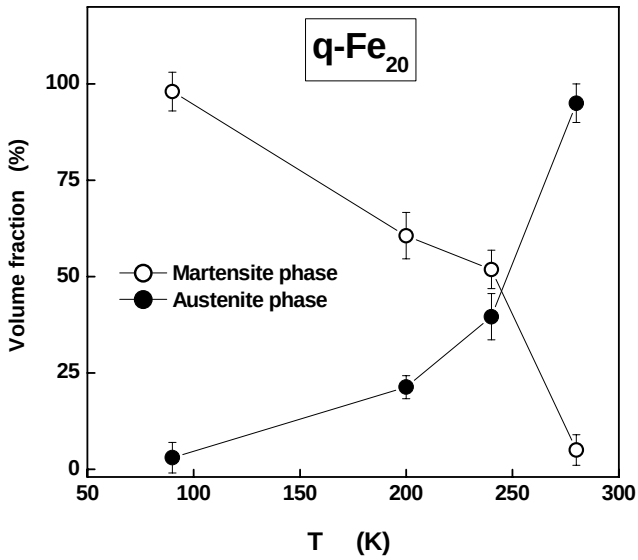

Fig. 6.9(c): Volume fractions of austenite and martensite phases across the martensite transformation of q-Fe_{20}.

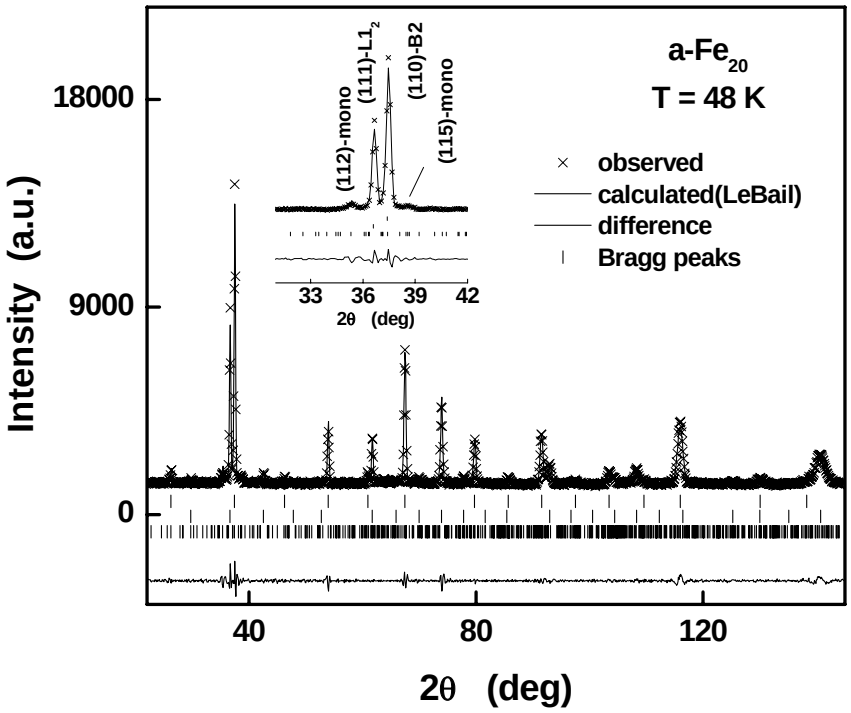

Fig. 6.10(a): The observed and calculated (LeBail) neutron diffraction patterns of a-Fe_{20} at 48 K, together with the difference pattern. Inset shows the Braggs peaks corresponding to all the three phases, viz. B2, $L1_2$ and monoclinic.

Table 6.5: LeBail profile fitting parameters for the ND patterns taken at temperatures T = 240 K, 200 K and 90 K on the q-Fe_{20}.

q-Fe_{20}	**T = 240 K**		**T = 200 K**		**T = 90 K**
	Pm3m(B2)	**P2/m**	**Pm3m(B2)**	**P2/m**	**P2/m**
a (Å)	2.8689(2)	4.1667(3)	2.8653(2)	4.1674(3)	4.1653(4)
b (Å)		2.6305(3)	-	2.6295(2)	2.6203(2)
c (Å)		14.790(1)	-	14.805(1)	14.844(1)
β°		94.962(9)	-	94.897(6)	95.622(7)
R_p	1.05		1.10		1.03
R_{wp}	1.36		1.45		1.47
χ	1.30		2.02		2.12

On the other hand, in a-Fe_{20}, no such drastic phase transformation is observed at T ≥ 48 K. Fig.6.10(a) depicts LeBail fitting of neutron diffraction pattern of a-Fe_{20} taken at 48 K and the lattice parameters from this procedure are given in table 6.6. Figure 6.10(b) shows the Rietveld refinement of the

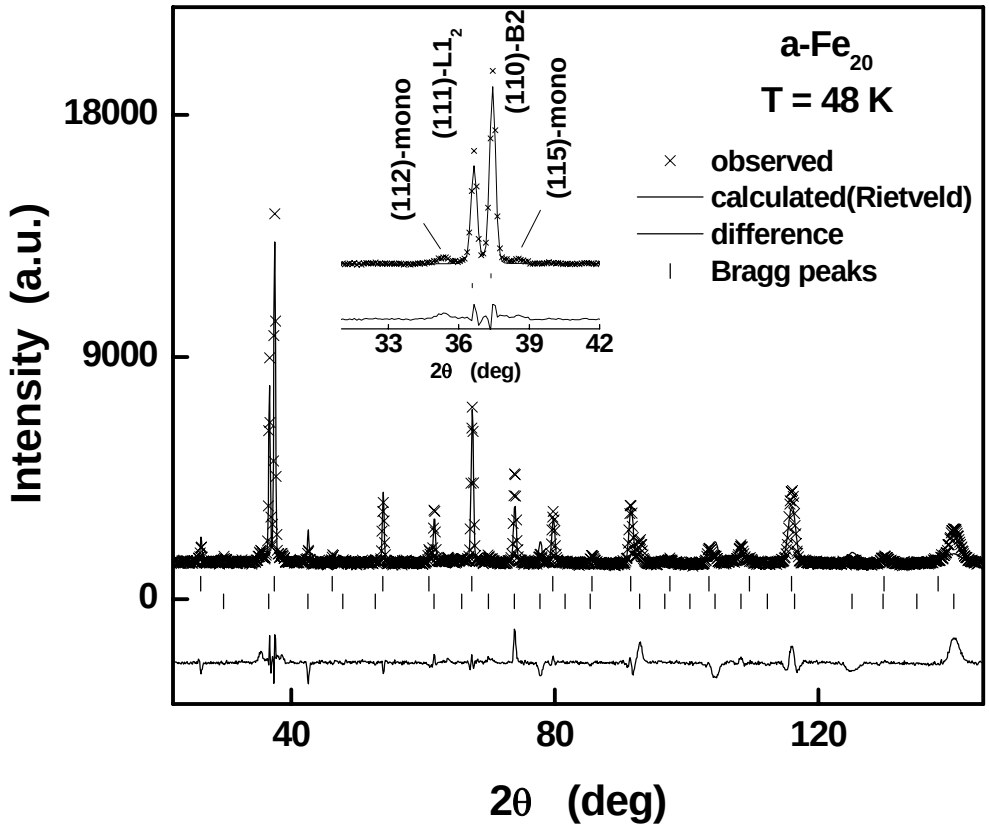

Fig. 6.10b: The observed and calculated (Rietveld) neutron diffraction patterns of a-Fe_{20} at 48K, together with difference pattern. Inset shows the observed Bragg peaks along with the Rietveld fit (continuous curves) for the B2 and $L1_2$ structures only.

Table 6.6: LeBail profile fitting parameters for the neutron diffraction (ND) pattern taken at the lowest measured temperature, T = 48 K, on a-Fe_{20}.

a-Fe_{20} at 48 K	**Pm3m B2**	**Pm3m $L1_2$**	**P2/m monoclinic**
a (Å)	2.8614(2)	3.5780(1)	4.1691(2)
b (Å)	-	-	2.7001(1)
c (Å)	-	-	14.7076 (8)
β°	-	-	94.457(3)
R_p	2.63		
R_{wp}	3.57		
χ	2.55		

neutron diffraction pattern of a-Fe_{20} taken at 48 K. The parameters and volume fraction of the phases obtained from this fitting are given in table 6.7. The volume fraction of the $L1_2$ (B2) phase at 48 K, obtained from Rietveld

analysis, was *almost similar to* (much less than) that at 298 K. Figure 6.11 shows the temperature variation of lattice parameters of B2 phase, over a temperature range of 298 K to 48 K, obtained using the Rietveld method. It is observed that the temperature variation of the lattice parameter, a_{B2}, is not smooth. Instead $a_{B2}(T)$ exhibits periodic undulations with a period of roughly 50 K at temperatures around 250 K, 200 K, 150 K, 100 K and 50 K, as shown in Figure 6.11. It is possible that at these temperature values, some fraction of austenite B2 phase in the sample a-Fe_{20} transforms to the martensite monoclinic phase while cooling. No such a trend with temperature was observed in the of lattice parameters of the $L1_2$ phase. The thermodynamic calculations [14] show that $L1_2$ (Ni_3Al) phase is stable down to 0 K and no thermoelastic martensitic phase transformation occurs in Ni_3Al. Thus, in a-Fe_{20}, B2 phase does not transform completely to the monoclinic martensite phase and $L1_2$ in the austenite phase does not undergo martensitic transformation at all.

Table 6.7: Rietveld refinement parameters for the ND pattern taken at T = 48 K on the sample a-Fe_{20}.

a-Fe_{20} at 48 K					
Pm3m (B2)			Pm3m ($L1_2$)		
Atoms	Occupancy (%)	Biso ($Å^2$)	Atoms	Occupancy (%)	Biso ($Å^2$)
Ni (0.0,0.0,0.0)	1.0(1)	0.38(6)	Ni (0.0,0.5,0.5)	0.73(1)	0.60(5)
Al (0.5,0.5,0.5)	0.55(3)	0.30(9)	Fe (0.0,0.5,0.5)	0.27(1)	0.60(5)
Fe (0.5,0.5,0.5)	0.45(3)	0.30(9)	Al (0.0,0.0,0.0)	0.76(5)	1.75(7)
			Fe (0.0,0.0,0.0)	0.24(4)	1.75(7)
a(Å) = 2.8630(1)			a(Å) = 3.5802(2)		
Loretzian strain (x) > 0.01			Loretzian strain (x) = 0.14(3)		
			Preff orientation= -1.15(7)		
Volume fraction = 66(2)			Volume fraction = 33 (1)		
R_p = 5.96					
R_{wp} = 9.16					
χ = 11.5					

It is important to note that the monoclinic martensite phase was not reported in the earlier studies of Ni-Fe-Al alloys. Instead, these studies [9,10] revealed two phase microstructure (bcc B2 + fcc $L1_2$) in the high temperature austenite phase while low temperature martensite phase was found to be in different low symmetry crystal structures like $L1_0$ body-centered tetragonal or body-centered orthorhombic or a mixture of both the phases depending on the heat treatment and composition of Ni-Fe-Al alloys. However, monoclinic martensite phase was first studied [29] in *stress-induced* martensites of binary B2 Ni_xAl_{100-x} alloys with x = 0.631 at room temperature and the same structure was observed in *thermally-induced* martensites as well, at a similar composition [26]. The long period seven layered structure of the martensite phase can be visualised in the following way. As shown in figure 6.12, the [110] plane of the B2 type structure is taken to be the rigid basal plane and the structure is defined by specifying the stacking sequence of the [110] planes through $<1\bar{1}0>$ directions. Each [110] plane shifts relative to neighbouring planes by $+\Delta u_0$ up to 5^{th} plane by shear and next two planes shuffle by $-\Delta u_0$. The shearing and shuffling of [110] planes of B2 results in 14 M (modulated) martensite monoclinic structure (formerly, 7R or 7M notation [26,29,30]).

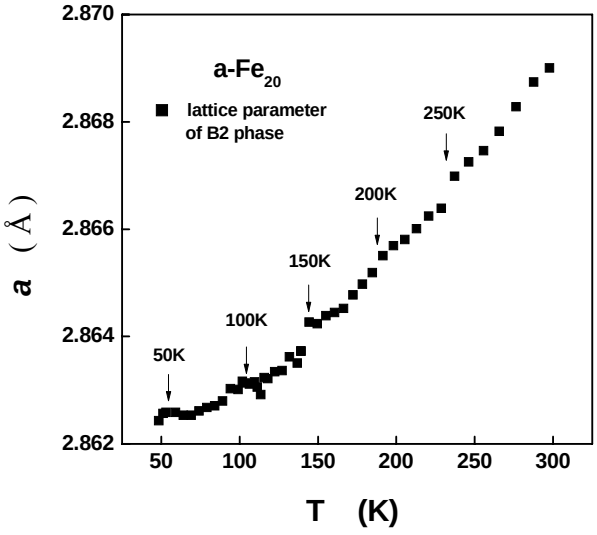

Fig. 6.11: Lattice parameter 'a_{B2}' of the B2 phase as a function of temperature in a-Fe_{20}.

The precise neutron scattering experiments showed that thermally-induced martensite structure of $Ni_{63}Al_{37}$ have incommensurability, in that the anomalous peak broadening and non-integral spacings of superlattice peaks were observed [26]. The reported values of lattice parameters for the monoclinic martensite phase with space group P2/m are a = 4.172 Å, b = 2.690 Å , c = 14.450 Å and β = 94.37°. These values are in good agreement with our results. Based on the results of the TEM studies, Muto et al. [31] have given the detailed crystal structure of this metastable phase. The nucleation of Ni_2Al phase is responsible for the local structural changes in the austenite phase before the occurrence of actual first-order transition (austenite-martensite). This premartensitic behaviour (or precursor effects) is (are) accompanied by an anharmonic coupling of TA_2 phonons modes, generally known as the phonon

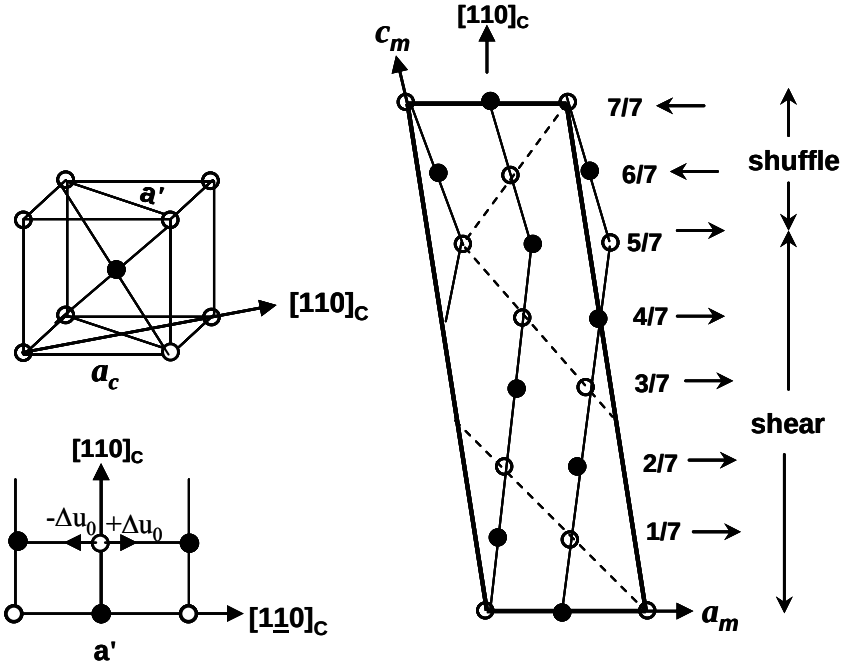

Fig. 6.12: The construction of 7M (5$\underline{2}$) stacking sequence of (110)-B2 planes [26]. At first, all the seven (110)-B2 planes shift relative to neighbouring planes by an amount $+\Delta u_0$ in the (1$\underline{1}$0)-B2 direction. In the next step, the top two planes shuffle by an amount $-\Delta u_0$ to form the monoclinic unit cell,as shown in this figure.

softening [32]. Such a behaviour is indeed observed recently in the dynamic elastic property measurements performed on the q-Fe_{20} samples [33]. The microstructure of the austenite and martensite phases has been studied by Transmission Electron Microscopy (TEM) and the details are given in the next section.

6.3.2 TEM studies

In order to verify the crystal structures of the austenite and martensite phases and to study the microstructure of martensite phase, transmission electron microscopy (TEM) investigation was carried out on the q-Fe_{20} and a-Fe_{20} samples at 300 K and 103 K.

Sample preparation

Quenched $Ni_{55}Fe_{20}Al_{25}$ (q-Fe_{20}) Ribbons

The 'as-prepared' melt-spun ribbons of q-Fe_{20} alloys were having a thickness of the order of ~ 30 μm. TEM discs were punched from the ribbons using a disc-punch machine (Model 659, M/s Gatan, USA). The discs were

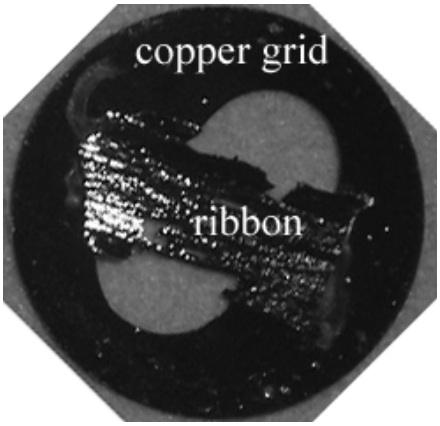

Fig. 6.13: TEM sample of a ribbon, after ion beam thinning. The diameter of the copper grid is about 3 mm.

polished with diamond paste (particle size ~ 3 μm and 1μm) for obtaining a smooth surface. The polished discs were supported on the TEM copper grids (Fig. 6.13) by bonding them to the grids with a fast curing epoxy (Devcon 5-minute epoxy). Enough care was taken so that the epoxy was not spread on the surfaces of the ribbon while bonding. The samples were subjected to argon ion beam thinning, using precision ion polishing system (PIPS, manufactured by M/s Gatan), and beam modulation, for realizing electron-transparent thickness.

Annealed $Ni_{55}Fe_{20}Al_{25}$ ($a\text{-}Fe_{20}$) samples

A strip of $a\text{-}Fe_{20}$ was cut into thin slices of thickness ~ 150 μm, using a low-speed diamond saw (Buehler-make isomet, Model 11-1180). TEM discs (3mm in diameter) were punched using a disk punch. The discs of $a\text{-}Fe_{20}$ were mechanically polished to about 100-120 μm using different grades of emery papers (silicon carbide grinding paper) with grit Nos. 320, 600 and 1200, followed by buffing on a cloth applied with diamond paste with particle size of ~ 3 μm and 1 μm. After this treatment, the sample surface had a mirror polish. The samples were then subjected to electropolishing, using mixed acids (Methanol-78%, H_2SO_4-7%, Lactic acid-10%, HNO_3-3%, and HF-2%; at –30°C, 25V, and 20mA), to realise electron transparent thickness. The electropolished samples were cleaned in AR grade methanol.

Microscopic investigations on quenched $Ni_{55}Fe_{20}Al_{25}$

$q\text{-}Fe_{20}$ at room temperature (300 K)

TEM studies were performed along the ribbon plane. The TEM micrograph, obtained in the bright-field-image-mode and shown in figure 6.14, demonstrates the presence of equiaxed grains along <100> with a grain size of

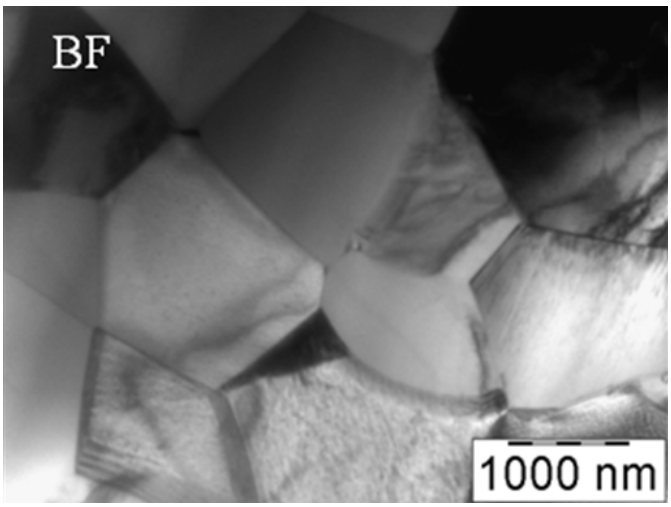

Fig. 6.14: Bright field (BF) TEM micrograph showing equiaxed grains in q-Fe_{20}.

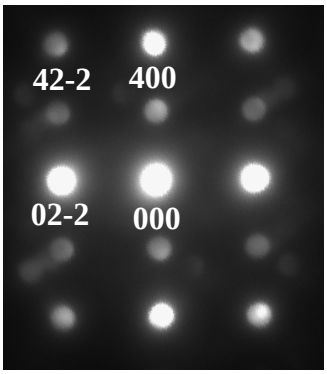

Fig. 6.15: Microdiffraction pattern, along [0-11] zone axis, confirming the B2 structure of the grain. The extra spots are due to the grains that lie below the grain under investigation.

the order of 1 μm. The detailed selected area diffraction (SAD) studies reveal that the grains have B2 (ordered bcc) structure (see, Fig. 6.15).

The Energy Dispersive x-ray Spectroscopy (EDS) studies on ten different grains reveal that the grains consist of Fe, Al and Ni elements (see, figure 6.16). A semi-quantitative analysis yields the composition of the grains as displayed in table 6.8. From the entries in this table, it is evident that the sample is slightly rich in Al and deficient in Ni compared (Fe at % is similar) to its nominal composition. The bold entries in the table serve to illustrate that the local composition fluctuations do exist.

Table 6.8: EDS semi-quantitative analysis of the B2 grains of q-Fe_{20} at room temperature.

Grain No.	Al (at.%)	Fe (at.%)	Ni (at.%)
1	30.2	20.9	48.9
3	29.5	19.7	50.8
4	26.9	21.6	51.5
2	**21.0**	**29.5**	**49.5**
5	27.1	21.6	51.3
6	**24.4**	**22.6**	**53.0**
7	31.8	19.8	48.4
8	26.6	21.8	51.6
9	30.4	18.9	50.7
10	31.5	19.5	49.0
Average	**27.9**	**21.6**	**50.5**
Standard Deviation	**2.1**	**1.1**	**1.3**
Nominal composition	**25**	**20**	**55**

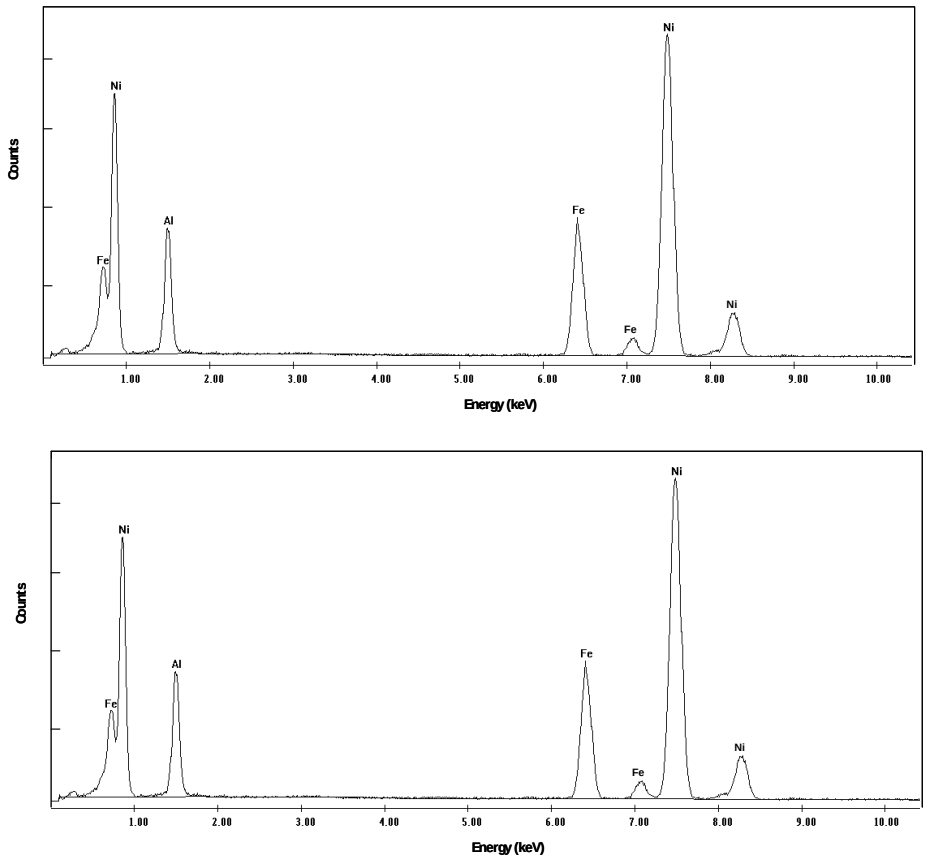

Fig. 6.16: EDS spectrum of a grain demonstrating the presence of Ni, Fe, Al elements.

q-Fe_{20} at cryogenic temperatures (103 K)

The B2 grains were found to undergo thermally-induced martensitic transformation (MT). All the grains observed under the microscope exhibited MT. The representative microstructures of the martensite platelet phase are shown in Fig. 6.17 at different magnifications. The planar faults observed in the martensite variants are due to diffraction contrast arising from the interaction between the electron beam and the internal twins [34]. The internal twins extend from one side of the martensite grain to the other. The martensite

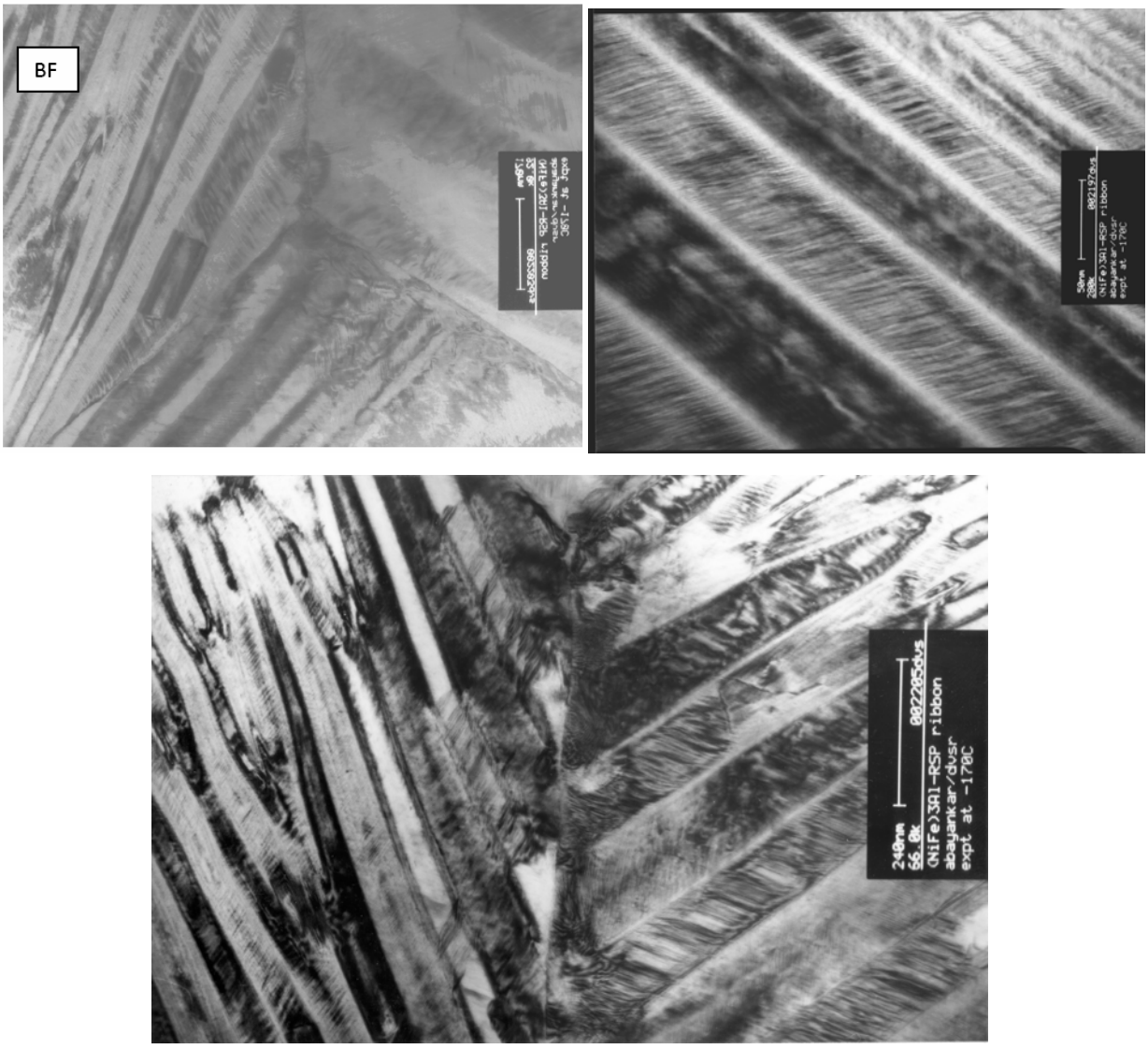

Fig. 6.17: Bright-field TEM micrographs showing martensite lathes at 103 K. The micron markers in figures correspond to 170 nm, 240 nm and 50 nm, respectively.

structure disappeared once the specimen is brought back to the room temperature (Fig. 6.18). The SAD pattern after bringing the specimen back to room temperature was similar to that shown in Fig. 6.15. It confirms the reversible thermoelastic martensitic transformation in melt-spun $Ni_{55}Fe_{20}Al_{25}$ alloy ribbons.

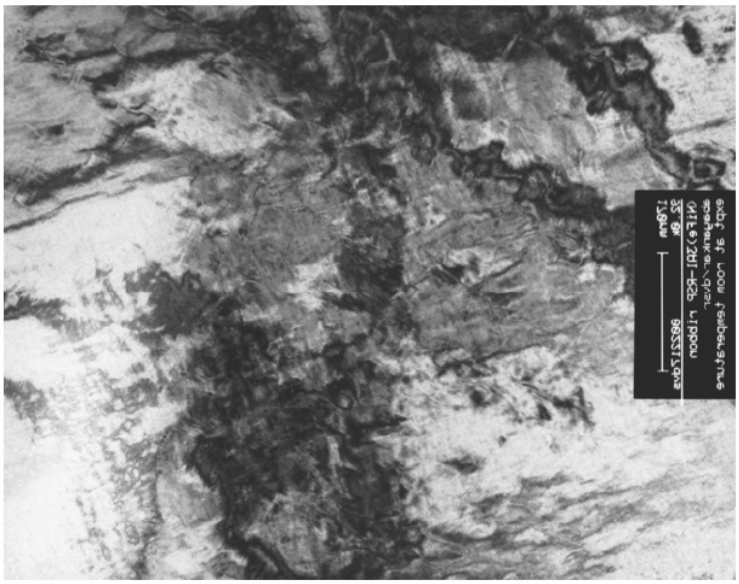

Fig. 6.18: Bright-field TEM micrograph showing the microstructure of the grain (that exhibited martensite structure at 103 K) after bringing the specimen back to room temperature.

Microscopic investigations on annealed $Ni_{55}Fe_{20}Al_{25}$

It has been observed that the electropolishing technique employed for the preparation of the TEM foils developed artefacts in the specimens, viz., appearance of fine particles in the B2 phase of the microstructure. They exhibited no change in contrast with specimen-tilting. The representative microstructures are shown in figures 6.19(a) and 6.19(b). These artefacts were removed almost completely by subjecting the TEM foils to argon ion beam thinning at 4 kV (low-angle milling at 3 degree) for 5 minutes. A representative microstructure without these artefacts is shown in figure 6.19(c).

a-Fe_{20} at room temperatures (300K)

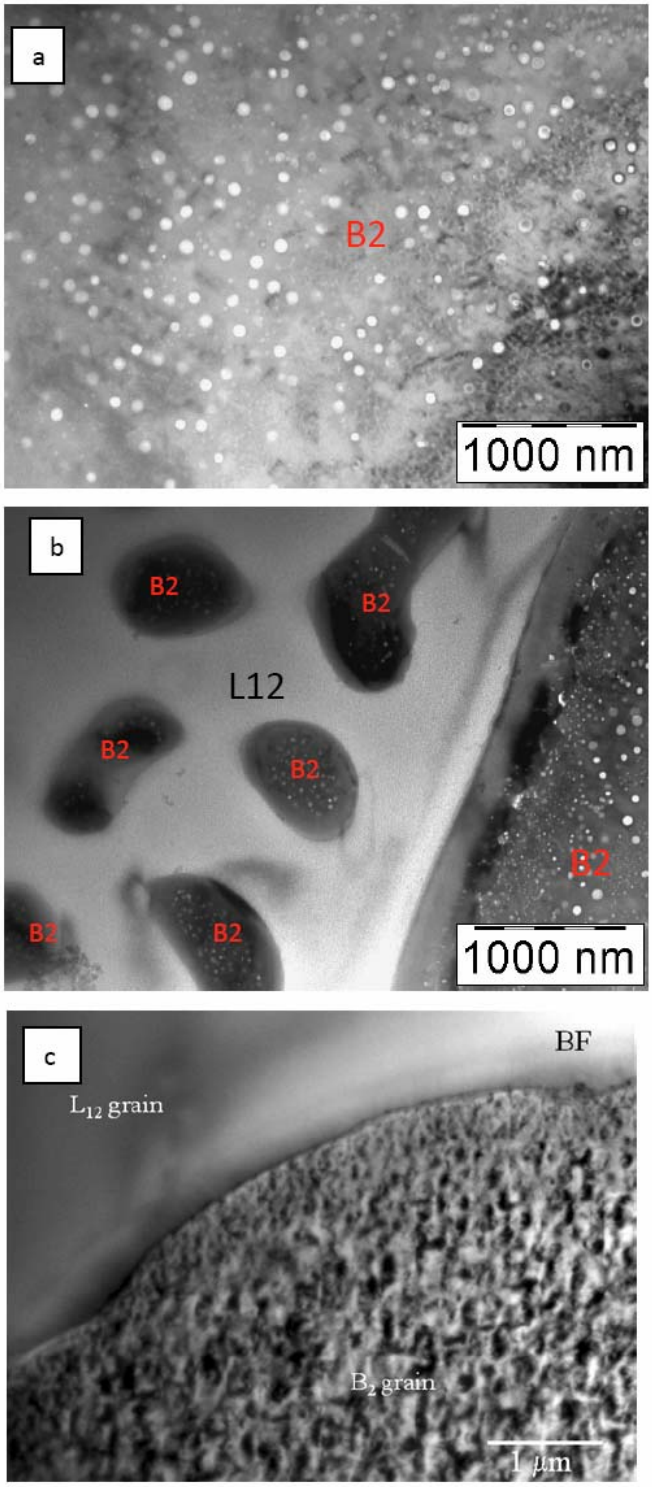

Fig. 6.19: (a,b) BF-TEM micrographs showing artefacts (white circular shape particles) in the B2 phase, that were traced back to the electro-polishing process. These features were removed after ion-beam thinning (Fig.6.19(c)).

The TEM study of the a-Fe_{20} sample at room temperature reveals the presence of grains with $L1_2$ (ordered fcc) and B2 crystal structures. Two types of $L1_2$ grains could be identified based on their distinctly different composition (one rich in Ni and other poor in Ni), as indicated in figure 6.20(a). The electron diffractions patterns, taken at the marked locations, confirm the respective crystal structures of the grains, as is evident from the lower panel of Fig.6.20.

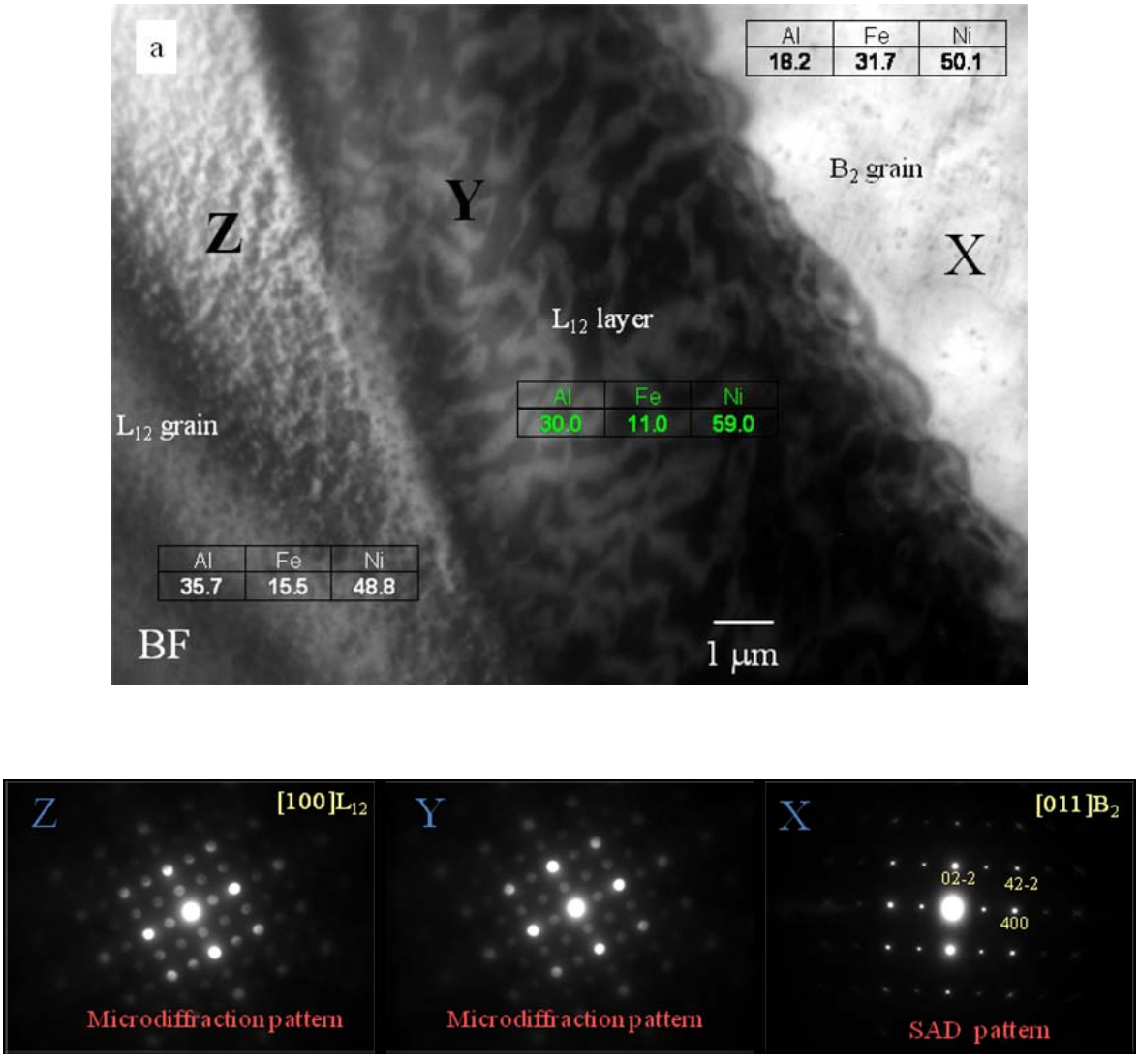

Fig. 6.20: BF-TEM micrographs displaying the B2 and $L1_2$ phases in the annealed sample. The composition (at.%) of these phases is indicated. The corresponding electron diffraction patterns of these phases are also shown in the lower panel.

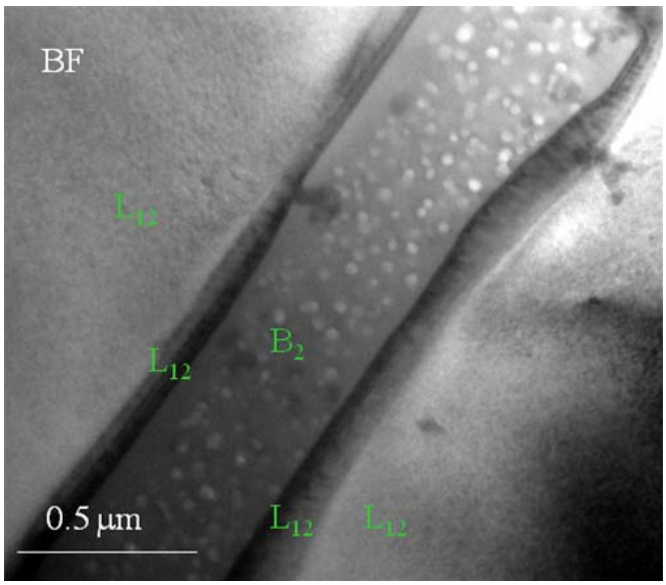

Figure 6.21: BF-TEM micrograph showing the presence of two types of $L1_2$ phases. Note that the width of the $L1_2$ Ni-rich phase between the $L1_2$-B2 grains is about 0.1μm as against 10 μm width in figure 6.20.

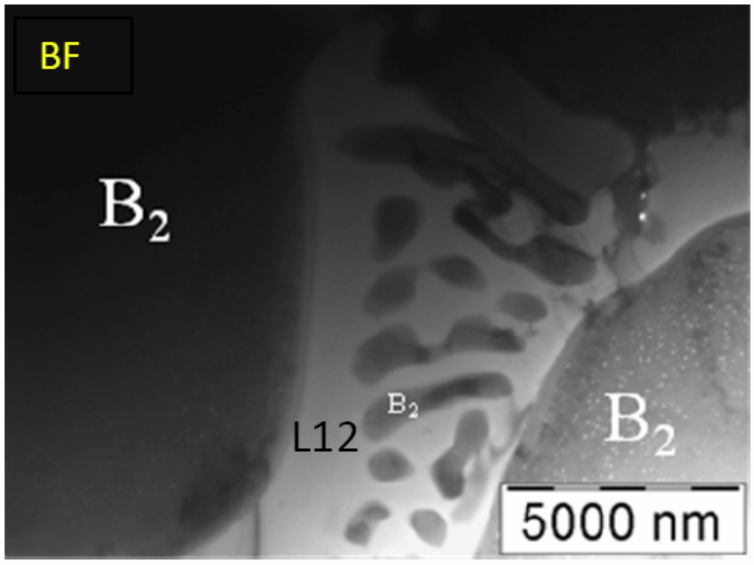

Fig 6.22: BF low-magnification TEM micrograph showing the representative microstructure. The white spots in the B2 region are artefacts due to electropolishing.

The presence of $L1_2$ phases with two different compositions has been confirmed for all the observed grains, even for the relatively smaller grains (Figure 6.21). The other interesting features observed at room temperature are shown in figures 6.22 and 6.23.

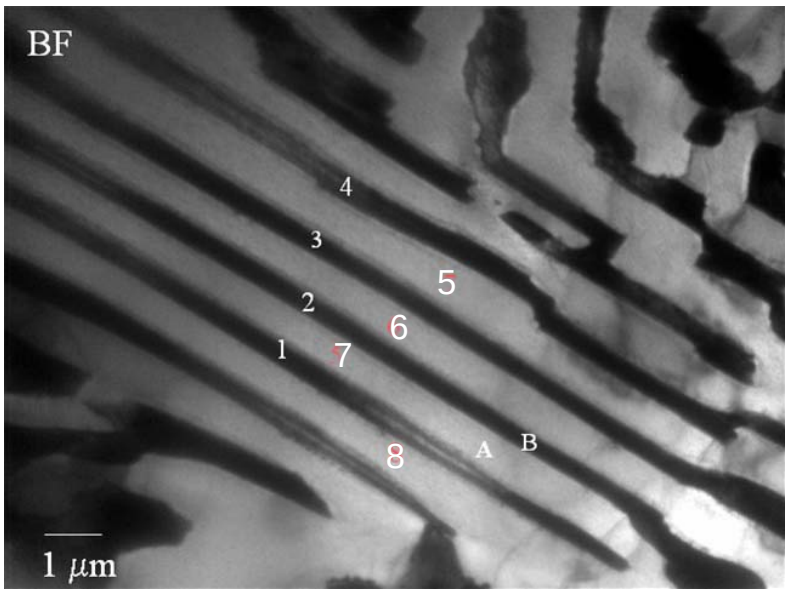

Fig. 6.23: BF-TEM micrograph revealing the formation of the $L1_2$ (region marked as A, corresponding to 5, 6, 7, 8) and B2 (region marked as B, corresponding to 1, 2, 3, 4) phases alternately. The EDS studies (Table 6.9) confirm the compositions.

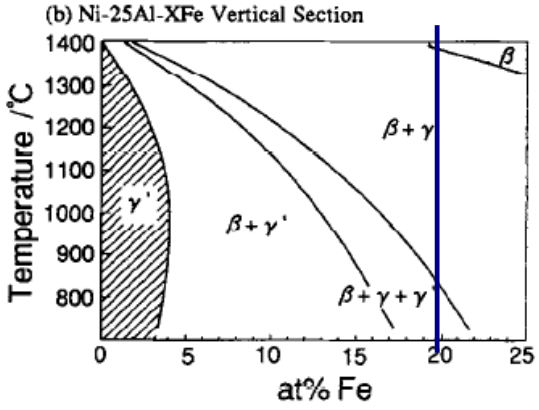

Fig. 6.24: Vertical section of the phase diagram in the Ni-Fe-Al.

The transformation of B2 grains in the $L1_2$ phase can be understood as follows from the vertical section of the Ni-Fe-Al phase diagram, obtained by thermodynamical calculations [10], and shown in figure 6.24. At 20 at.% of Fe, along the vertical line, annealing below 800 °C results in the three phase state namely fcc solid solution of Ni-Al (γ), ordered bcc phase (B2) and ordered fcc phase ($L1_2$). Such a transformation occurs via thermal diffusion of atoms where Al-rich B2 phase stabilizes by transforming into the Fe- or Ni-rich $L1_2$ phase

[35]. The average composition obtained by EDS analysis from regions A (corresponds to the Fe- or Ni- rich $L1_2$ phase) and B (corresponds to Al-rich B2 phase) vindicates this mechanism (see, Table 6.9).

Table 6.9: Average composition (at.%) of the regions A and B in Fig.6.23, obtained from the EDS measurements.

Region	Al	Fe	Ni
A	11.1	36.1	52.8
B	25.7	22.1	52.2
B2	28.2	21.3	50.5
L12	12.6	35.6	51.9

a-Fe_{20} at cryogenic temperatures (103 K)

Detailed TEM studies at 103 K show that only some parts of the B2 grains transform as martensite thin plates whereas the $L1_2$ phase does not exhibit any such transformation. Thus, the martensitic transformation in a-Fe_{20}

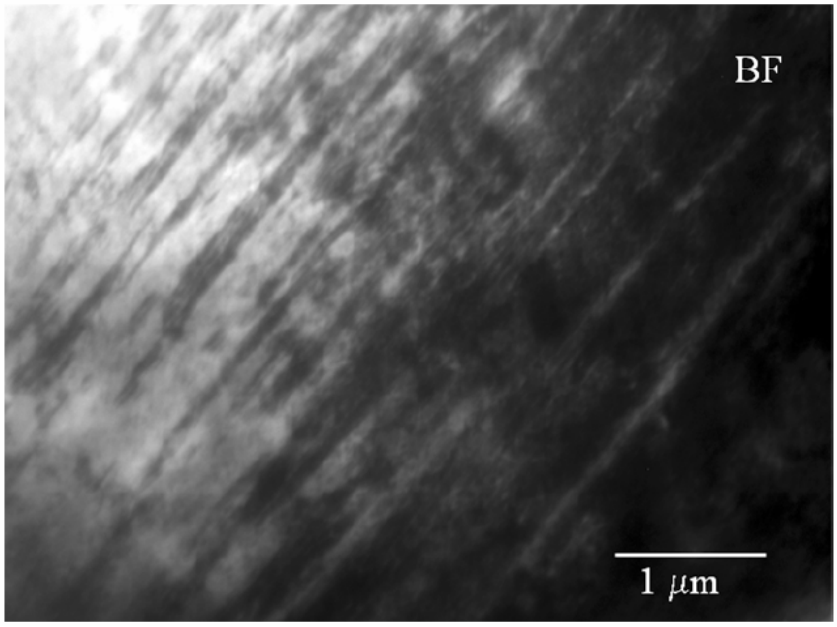

Fig. 6.25: BF-TEM micrograph showing martensite formation due to the cooling of the a-Fe_{20} sample to 103 K. This region exhibited B2 crystal structure at room temperature.

is not complete at T = 103 K whereas a complete MT was observed in the q-Fe_{20} samples. Figure 6.25 depicts the martensite plates embedded in the B2 matrix phase.

We have investigated the structure of martensite platelate phase of a-Fe_{20} at 103 K (which exhibits B2 crystal structure at room temperature), along <100> and <111> orientations. Figure 6.26(*a*) shows the SAD pattern taken from B2 grain at room temperature along the [111] zone axis. The 60° angle between the <220> directions and constant d-spacing confirms the cubic B2 phase with lattice parameter of ~ 0.286 nm. Figure 6.26(*b*) shows the SAD pattern taken from the same region of specimen after cooling down to 103 K. The loss of the cubic symmetry is evident from the distortion of the angles. This has been demonstrated clearly in figure 6.27. In figure 6.27(*a*), a pattern of cubic crystal, simulated in the [111] direction, is overlaid on the experimental pattern at room temperature. The camera length and orientation

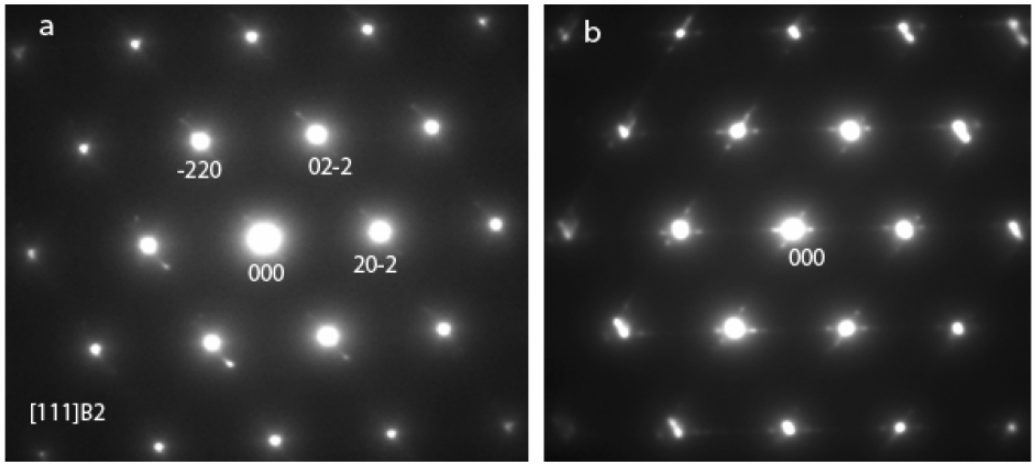

Fig. 6.26: (a) Selected area diffraction pattern obtained from a grain at room temperature along [111] zone axis confirming cubic structure (angles between the <220> directions: 60 degree, constant d-spacing). Detailed studies along [110] zone axis show that this grain has B2 structure (refer Fig. 6.20). (b) On cooling to 103 K, the angles deviate from 60 degree, confirming the loss of the cubic symmetry.

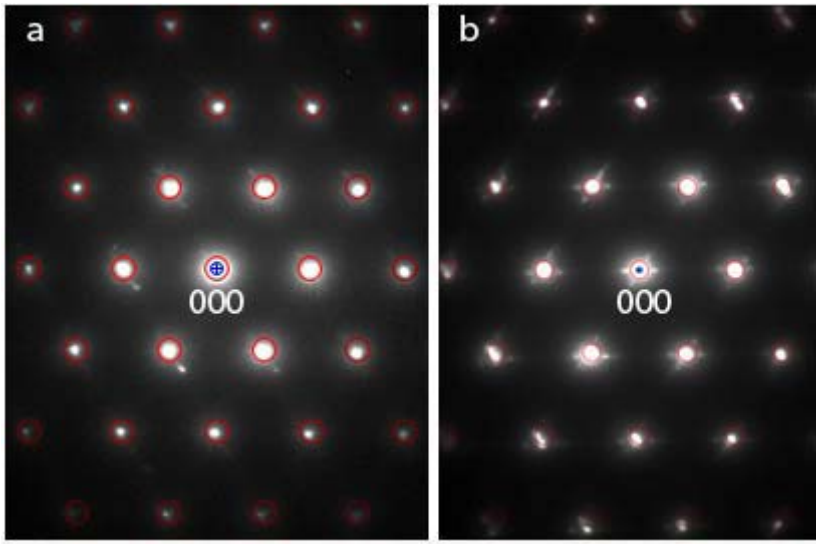

Figure 6.27 : SAD patterns obtained at (a) room temperature, and (b) 103 K. The red circles show an overlay of the diffraction spots (simulated by JEMS software) for cubic crystal along <111> direction. The camera length and orientation were adjusted so as to nearly match with the experimental patterns. A loss of cubic symmetry is seen in (b).

were so adjusted that a best possible match is obtained with the experimental pattern. A good match between the experimental and simulated patterns is obtained at room temperature (see, Fig. 6.27(*a*)) but in a similar attempt, a loss of cubic symmetry is observed in the pattern taken at 103 K (see, figure 6.27(*b*)). The above exercise shows that at 103 K, the cubic structure of the room temperature austenite B2 phase gets distorted due to the MT.

Figure 6.28 depicts convergent beam electron diffraction (CBED) pattern taken from the martensite plates (shown in Fig. 6.17(*c*)) in q-Fe_{20} samples. This pattern has some extra disks, originating from the neighbouring grains. At room temperature, similar pattern (not shown) matched with <100> zone axis of B2 phase. With cooling the four-fold symmetry is lost; suggesting the loss of cubic structure. For a better visualization of this phenomenon, a small portion of this pattern is selected, as shown in figure 6.29, and the selected pattern is overlaid with circular (red colour) grid simulated (using JEMS software) for a

cubic crystal along the <100> zone axis. This grid has been made from the CBED pattern obtained from the B2 phase at room temperature. Another circular grid (blue colour) has been made for the actual disks at low temperatures (103 K) and also overlaid for comparison. Even a cursory examination shows that the lattice has contracted (expanded) by ~ 0.81% (0.02%) approximately along 'a' ('b') direction, assuming the chosen zone axis as [001]. Moreover, the angle between these axes is 88 degree (i.e., $a \neq c$ and one of the angles, $\beta \neq 90$ degree). Considering the possibilities shown in table 6.10, this observation suggests that the crystal is likely to have a modulated monoclinic structure. However, the superstructure peaks corresponding to 14M modulations are not observed in the present investigations. The triclinic structure is another possibility. This needs further examination of the crystal

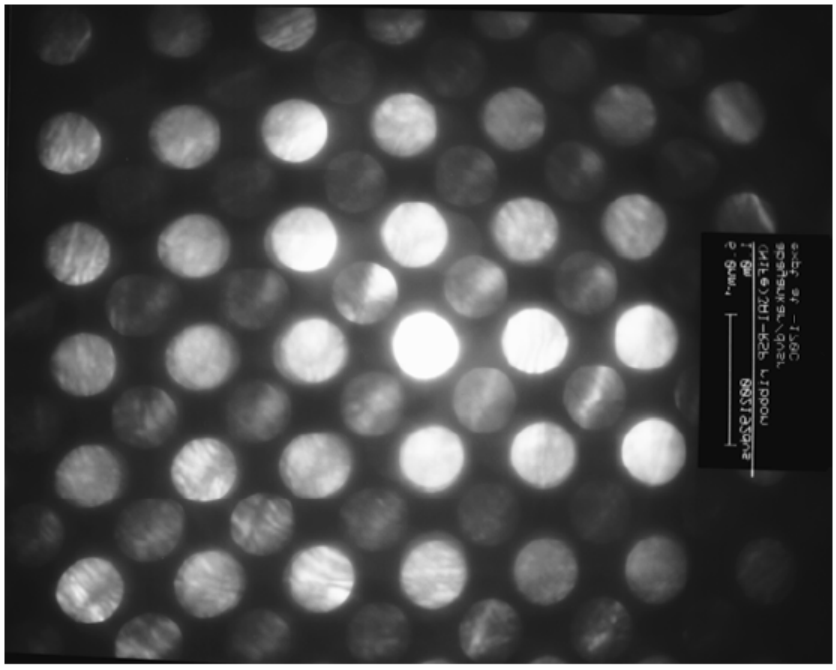

Figure 6.28: Microdiffraction pattern recorded at 103 K from martensite phase. This pattern has some extra disks, originated from neighbouring grains. With cooling, the four fold symmetry is lost, suggesting the loss of cubic structure. For a better visualisation of this phenomenon see Fig. 6.29.

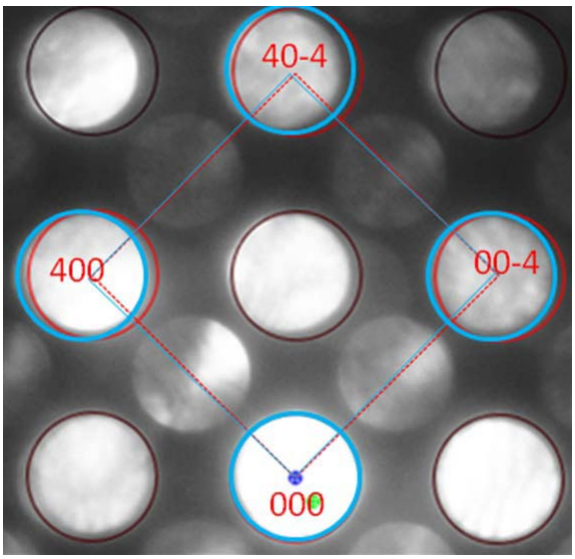

Figure 6.29: A portion of the pattern shown in figure 15, analysed for crystallography

Table 6.10: Bravais lattices Structures

Crystal structure	**Conditions**	**Remarks with reference to present investigations**
Cubic	$a = b = c$, $\alpha = \beta = \gamma = 90^o$	Not possible
Tetragonal	$a = b \neq c$, $\alpha = \beta = \gamma = 90^o$	Not possible
Orthorhombic	$a \neq b \neq c$, $\alpha = \beta = \gamma = 90^o$	Not possible
Rhombohedral	$a = b = c$, $\alpha = \beta = \gamma \neq 90^o$	Not possible
Monoclinic	Unrestricted a:b:c ratios, $\alpha = \gamma = 90^o$, β is unrestricted	Possible
Triclinic	Unrestricted a:b:c ratios, Unrestricted α, β, γ	Possible
Hexagonal	$a = b$, Unrestricted c, $\alpha = \beta = 90^o$, $\gamma = 120^o$	Not possible

along [100] or [001] orientation, which could not be undertaken due to the tilt limitations of the microscope. Our neutron diffraction data confirm the crystal structure of the low-temperature martensite phase in both the samples to be monoclinic (with P2/m space group). Even though it was known that in the

stress-induced [29] as well as thermally-induced [32,36-38] martensite phases, in the binary Ni_xAl_{100-x} alloys with $x < 66$ at.% and off-stoichiometric Ni-Fe-Ga [39] and Ni-Mn-Ga [40] have modulated structures such as 7R or 14M, no such structures were observed in the earlier studies of Ni-Fe-Al system [8,9,10]. The modulated phases arise from a coupling of defect-induced strain fields and anomalous phonon softening in the parent B2 phase [36]. Thus, neutron diffraction and TEM investigations confirm the thermoelastic martensitic transformation from high temperature B2 phase to modulated monoclinic 14M phase in $Ni_{55}Fe_{20}Al_{25}$ alloys. However, the MT is incomplete (complete) in a-Fe_{20} (q-Fe_{20}) samples.

6.3.3 Transport and magneto-transport properties

The temperature dependence of electrical resistivity, $\rho(T)$, in the q-Fe_{20} and a-Fe_{20} samples, measured in the heating and cooling cycles, are shown in figure 6.30. Residual resistivity of melt-spun, q-Fe_{20} samples (~ 118 μΩ-cm at 12 K) is higher than that of annealed, a-Fe_{20} samples (~ 85 μΩ-cm at 12 K). In $\rho(T)$ of q-Fe_{20} and a-Fe_{20}, thermoelastic martensitic (first-order) phase transformation (MT) is evidenced by the thermal hysteresis centred at $T \approx 227$ K and $T \approx 75$ K, respectively. A detailed minor thermal hysteresis loop analysis [41] of the ρ(T) data and the end temperatures, where the major thermal hysteresis loop closes, respectively yield the characteristic temperatures for the beginning, T_{Mb} (T_{Ab}), and end, T_{Me} (T_{Ae}), of the growth of martensite (austenite) phase at the expense of austenite (martensite) phase while cooling (heating) as: $T_{Mb} \approx 260$ K [ill-defined], $T_{Me} \approx 150$ K [<10 K], $T_{Ab} \approx 170$ K [ill-defined] and $T_{Ae} \approx 280$ K [>300 K] for q-Fe20 [a-Fe20]. These temperatures are in excellent agreement with those deduced from the Neutron diffraction patterns. The temperature range over which the martensite and austenite phases

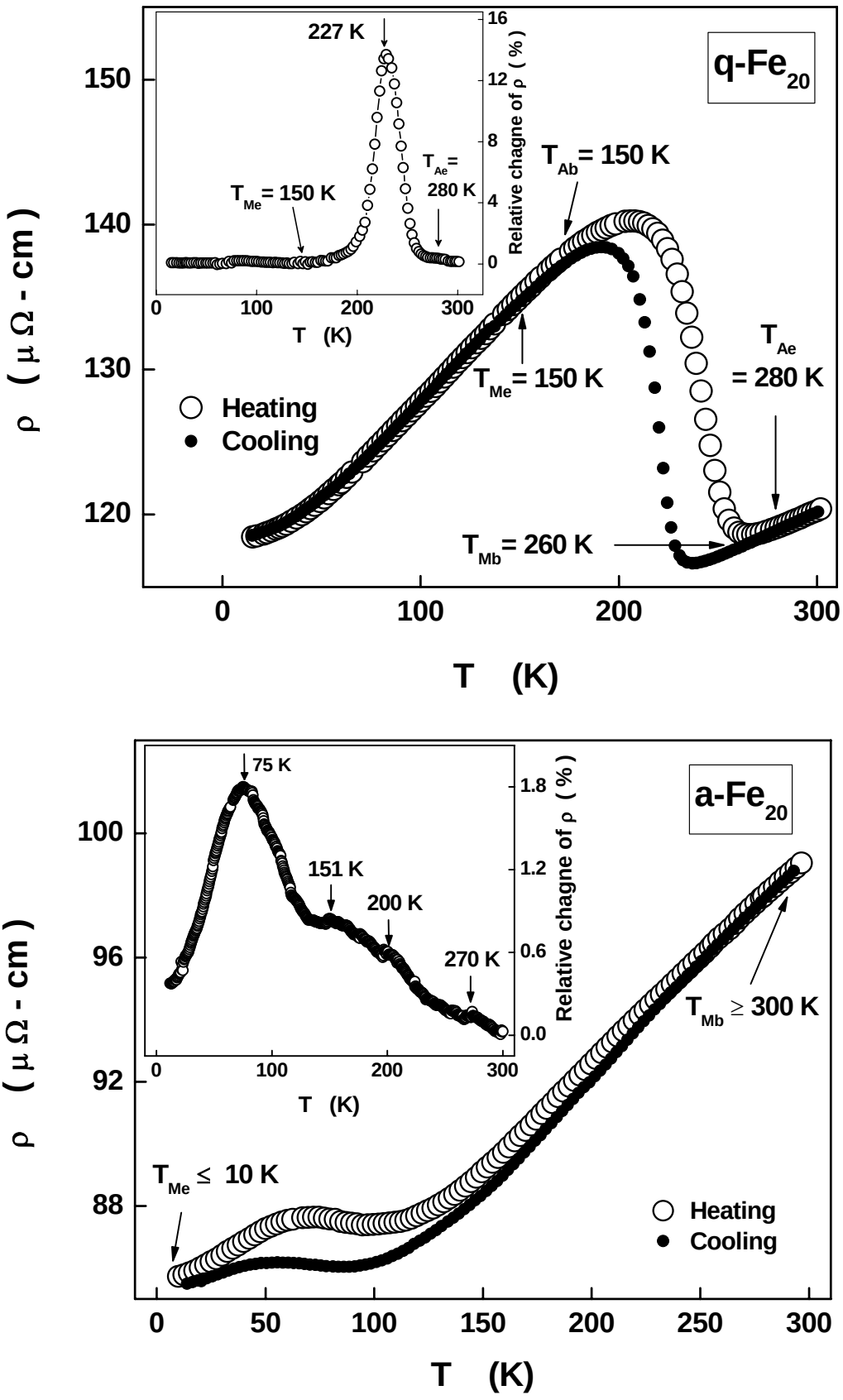

Figure 6.30: Temperature variations of electrical resistivity ρ(T) in the heating (open circles) and cooling (closed circles) cycles for q-Fe_{20} and a-Fe_{20} samples of $Ni_{55}Fe_{20}Al_{25}$ alloy. Insets show the relative change of resistivity (RCR% =[($\rho_{heating}$ -$\rho_{cooling}$)/ $\rho_{heating}$] × 100) during the heating and cooling cycles.

coexist extends from T_{Mb} to T_{Me} on the cooling $\rho(T)$ curve and from T_{Ab} to T_{Ae} on the heating curve. Evidently, the thermal hysteresis in $\rho(T)$ and hence, coexistence region of austenite and martensite phase is narrower by nearly a factor of three in q-Fe_{20} than in a-Fe_{20}. Moreover, the maximum value of the relative change of resistivity, RCR (RCR (%) = $[(\rho_{heating} - \rho_{cooling})/ \rho_{heating}] \times 100$), across the martensitic transition, as shown in the insets of figure 6.30, is ~ 15% in q-Fe_{20}, which is an order of magnitude higher compared to ~ 1.8% in a-Fe_{20}. For both the samples, RCR value peaks at the temperature that coincides with the centre of the thermal hysteresis. It is evident that the martensitic transformation is complete and much sharper (and better-defined) in q-Fe_{20} than in a-Fe_{20}. Another point to note is that the RCR of a-Fe_{20} samples shows a 'step-like' like wavy features in the temperature range 100 K $\leq T \leq$ 300 K whereas no such a features are observed in the RCR of q-Fe_{20}; instead in the latter case, RCR is almost zero except for a pronounced peak in the coexistence region of austenite and martensite phase. The small but finite value, the 'step-like' wavy features of RCR and a thermal hysteresis extending over an extremely broad temperature range 10 K $\leq T \leq$ 300 K in a-Fe_{20} reflects that martensite (austenite) phase nucleation is sparse in the austenite (martensite) matrix phase while cooling (heating). In the case of q-Fe_{20}, two-phase state (austenite + martensite) coexists in the region where the RCR has a finite value and the region where RCR is ~ 0%, on either side of the thermal hysteresis in $\rho(T)$, corresponds to a single-phase state (austenite, T > 280 K and martensite, T < 150 K). Thus, the martensitic transformation is complete in q-Fe_{20} but not in a-Fe_{20}.

In the $\rho(T)$ of off-stoichiometric and as-cast $Ni_{54}Fe_{19}Ga_{27}$ alloys [41], the features such as a large value of RCR (~ 16 %) and thermal hysteresis, with

small width of $\Delta T \sim 10$ K, have been recently observed. By contrast, $\rho(T)$ of the off-stoichiometric and annealed $Ni_{54}Mn_{21}Ga_{25}$ alloys [42] exhibited large values of RCR (~ 15%) and a thermal hysteresis of width as large as ≅ 200 K. In the off-stiochiometric Ni-Mn-Ga, these features are attributed to inter-martensitic transformation from 10M → 14M structures whereas in case of well-annealed Ni-Mn-Ga (where MT is associated with a structural transition from $L2_1$ → non-modulated tetragonal phase), these features are absent. The Ni-Fe-Al and Ni-Fe-Ga are isoelectronic at equal Al/Ga concentrations when the Ni and Fe contents are kept constant. Moreover, the martensitic transformation in Ni-Fe-Ga alloys is associated with a structural transition from a parent B2 → 14M modulated layer structure. Thus, we attribute the features of $\rho(T)$ in q-Fe_{20}, such as a large RCR and well-defined sharp hysteresis to *stress-induced* martensitic transformation from high-temperature cubic Ni-(AlFe) phase (B2) to low-temperature close-packed modulated (14M) monoclinic $(NiFe)_2(AlFe)$ phase. The latter is a long-period structure which results from a combination of shearing and shuffling modes of atoms in the [110] plane of the parent cubic B2 structure (see, Fig.6.12). In the case a-Fe_{20}, annealing at 560 °C causes stress relief and results in the formation of fcc $L1_2$ phase $[(NiFe)_3(AlFe)]$ in the matrix of bcc B2 [Ni-(AlFe)] phase that leads to a very weak nucleation of the monoclinic $(NiFe)_2(AlFe)$ martensite phase over a large temperature range. Thus, the remarkable but distinct transport properties of melt-quenched and annealed $Ni_{55}Fe_{20}Al_{25}$ samples are consistent with the neutron diffraction and TEM results, described in earlier sections.

Figure 6.31 (6.32) displays the $\Delta\rho_{||}/\rho$ versus T ($\Delta\rho_{||}/\rho$ versus H) curves taken on a-Fe_{20} and q-Fe_{20} samples at different but fixed values of magnetic field, H (temperature, T) in the heating cycle. Except at low

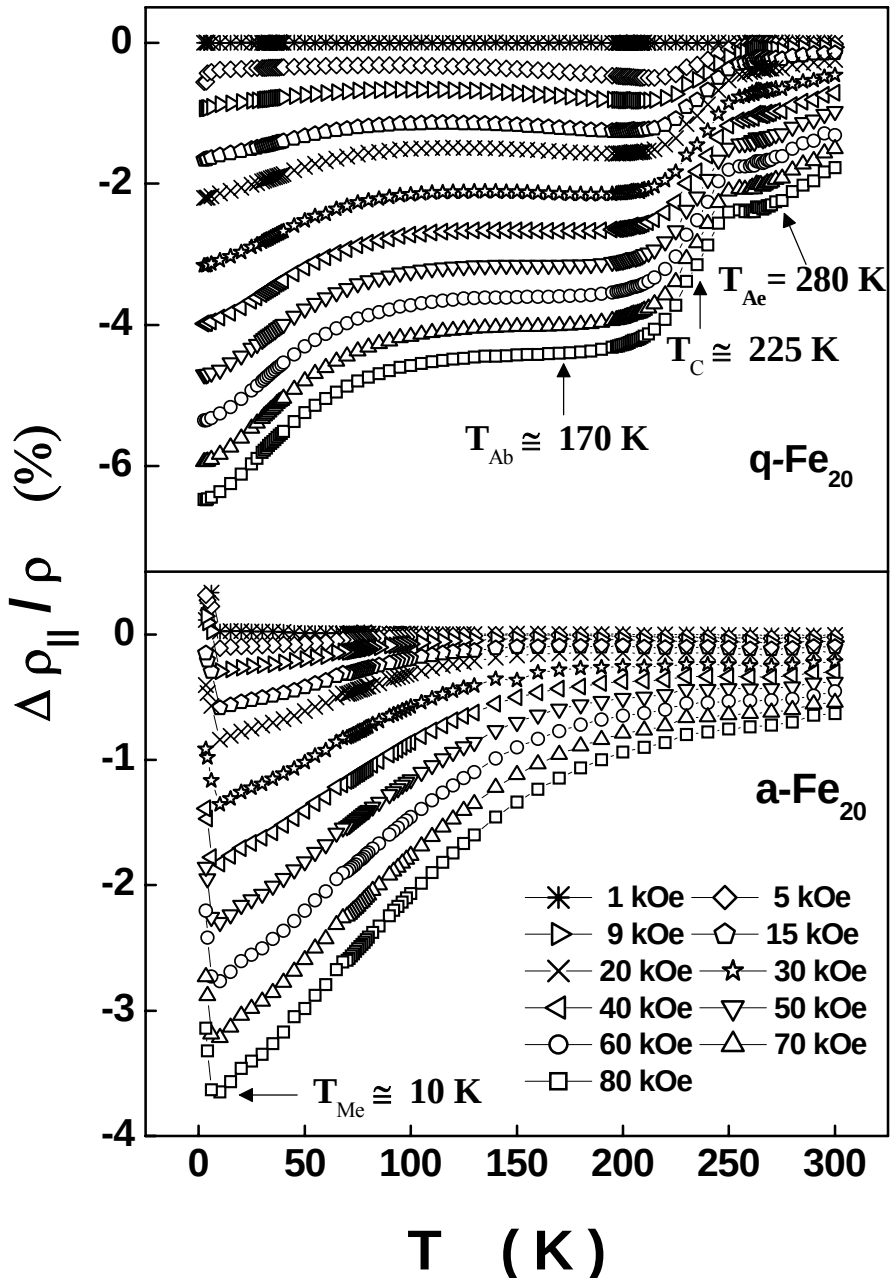

Figure 6.31: Temperature variation of longitudinal magnetoresistance, $\Delta\rho_{\parallel}/\rho$*, at different applied magnetic fields i*(< 1 kOe) and low

magnetic fields (< 1 kOe) and low temperatures (< 10 K), where longitudinal magnetoresistance (MR) is *positive* in the *a*-Fe_{20} sample only, MR is *negative* at all the measuring temperatures and magnetic fields in both a-Fe_{20} and q-Fe_{20} samples. MR at T = 10 K and H = 80 kOe is nearly two times larger in *q*-Fe_{20} than in *a*-Fe_{20}. In q-Fe_{20} at low temperatures, MR varies linearly with H for H < 10 kOe whereas for H > 40 kOe, the variation of MR with H slows down (see lower panel of Fig. 6.32). Above the Curie temperature, T_C, MR

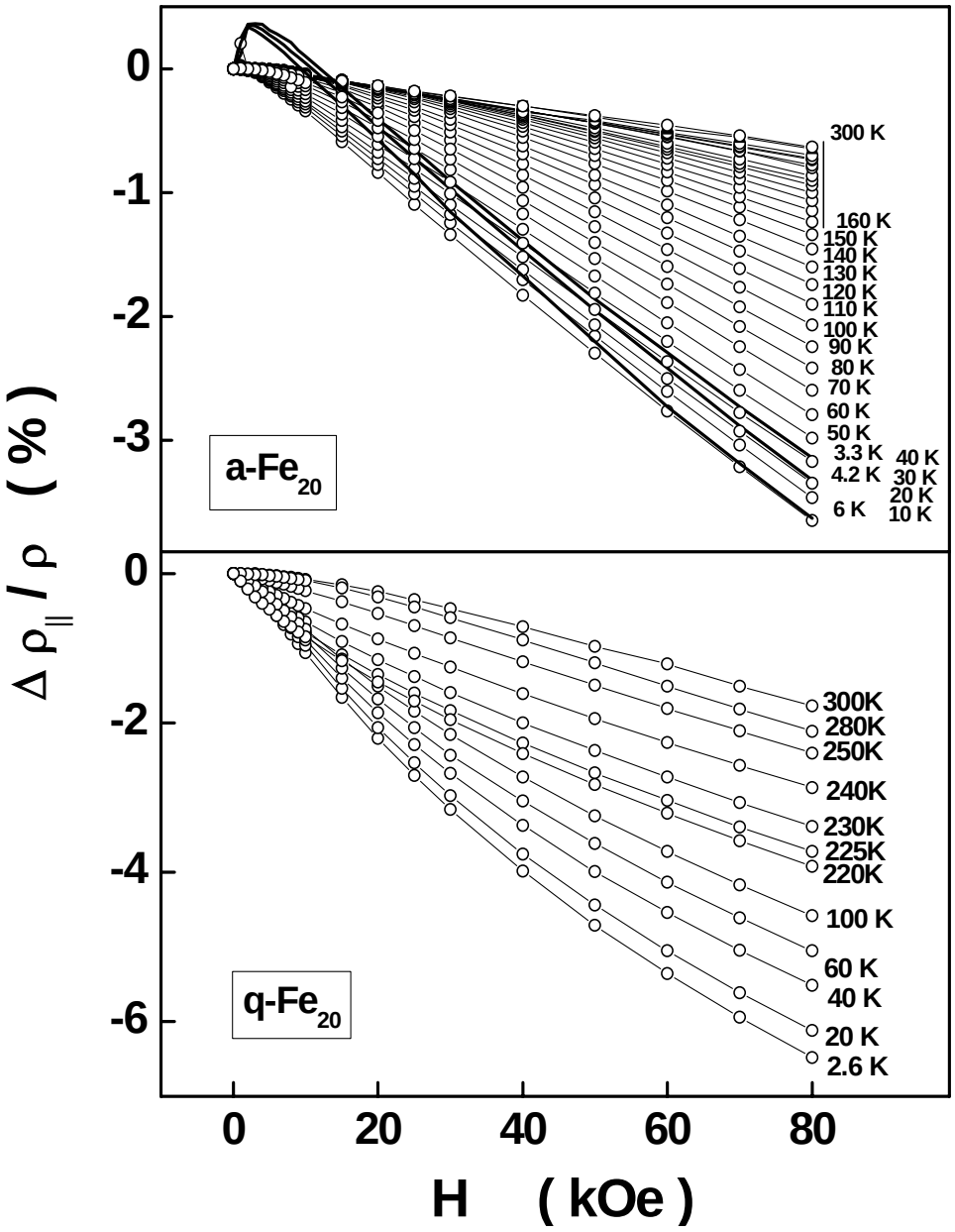

Figure 6.32: Longitudinal magnetoresistance, $\Delta\rho_{||} / \rho$, of a-Fe_{20} and q-Fe_{20} samples, measured in the heating cycle, as a function of magnetic field at a few temperatures ranging from 2.6 K to 300 K.

changes its curvature from concave upward (at low temperatures) to concave downward. These features are reminiscent of a typical weak itinerant-electron ferromagnet. However, negative MR does not peak near T_C and it increases with decreasing temperature, T. These anomalous features are due to the magnetic field-induced martensitic transformation. On the other hand in a-Fe_{20}, MR is *linear* in H over a wide range of measuring fields and temperatures and at a given H, it monotonously decreases with temperature up to 10 K.

Magnetic field seems to promote martensitic transformation in a-Fe_{20} as well. Another important observation is that the temperatures, T_{Ab} and T_{Ae} (or T_{Me}), characteristic of martensitic phase transformation, and even T_C, are *prominently reflected* (Fig.6.32) in the $\Delta\rho_{\|} / \rho$ vs. T curves [43].

6.3.4 Magnetic properties

The thermomagnetic, *M(T, H)*, curves taken in the *heating cycle* at H = 40 Oe (20 Oe), 1 kOe, 10 kOe on q-Fe_{20} (a-Fe_{20}) in the temperature range of 5 K to 300 K are shown in figures 6.33 and 6.34. The characteristic temperatures T_{Ab} and T_{Ae}, determined earlier [17] from 'zero-field' resistivity, are also indicated in this figure. The Curie temperature, T_C, as determined from the dip in the temperature derivative of the *M(T)* curves taken at the lowest field, is $T_C \cong 225$ K for the q-Fe_{20} and $T_C > 300$ K for a-Fe_{20} samples. A steep (gradual) rise in $M(T)$ at H = 40 Oe (20 Oe) in q-Fe_{20} (a-Fe_{20}) as the sample temperature increases from 5 K to T_{Ab} (300 K) essentially reflects the fact that magnetic field, H, becomes more and more effective in polarizing the spins as the magnetocrystalline anisotropy (MCA) associated with the martensite phase decreases with the increasing temperature. The 'step-like' wavy structure in the thermomagnetic curves taken at 1 kOe and 10 kOe on a-Fe_{20} is a remarkable feature not reported in any of the ferromagnetic shape memory alloys (FMSAs) so far. A plausible explanation for this unusual behaviour is as follows [43].

A step-increase in $M(T, H = 1$ kOe) curves normally observed in FSMAs at T_{Ae} upon heating reflects field-induced enhancement in magnetization when the MCA energy or equivalently, the anisotropy field, H_A, suddenly drops as the austenite phase sets in above T_{Ae}. This is true only when $H_A >> H$ (the measuring field) so that even a slight reduction in H_A helps H to increase the

component of magnetization along its own direction. However, in the other extreme case of $H_A << H$, H is unable to take the advantage of a sudden reduction in H_A and M drops to a lower value at T_{Ae} because reduced H_A aids the thermal excitation of spin waves and/or spin fluctuations. In the light of this argument, a 'stair-case-like' decrease in $M(T, H = 1$ kOe, 10 kOe) of a-Fe_{20} (Fig.6.33) would imply that $H_A << H$ and in the present case, H_A drops in regular steps with increasing temperature at a series of local T_{Ae} values where the austenite phase nucleates and grows subsequently as the temperature

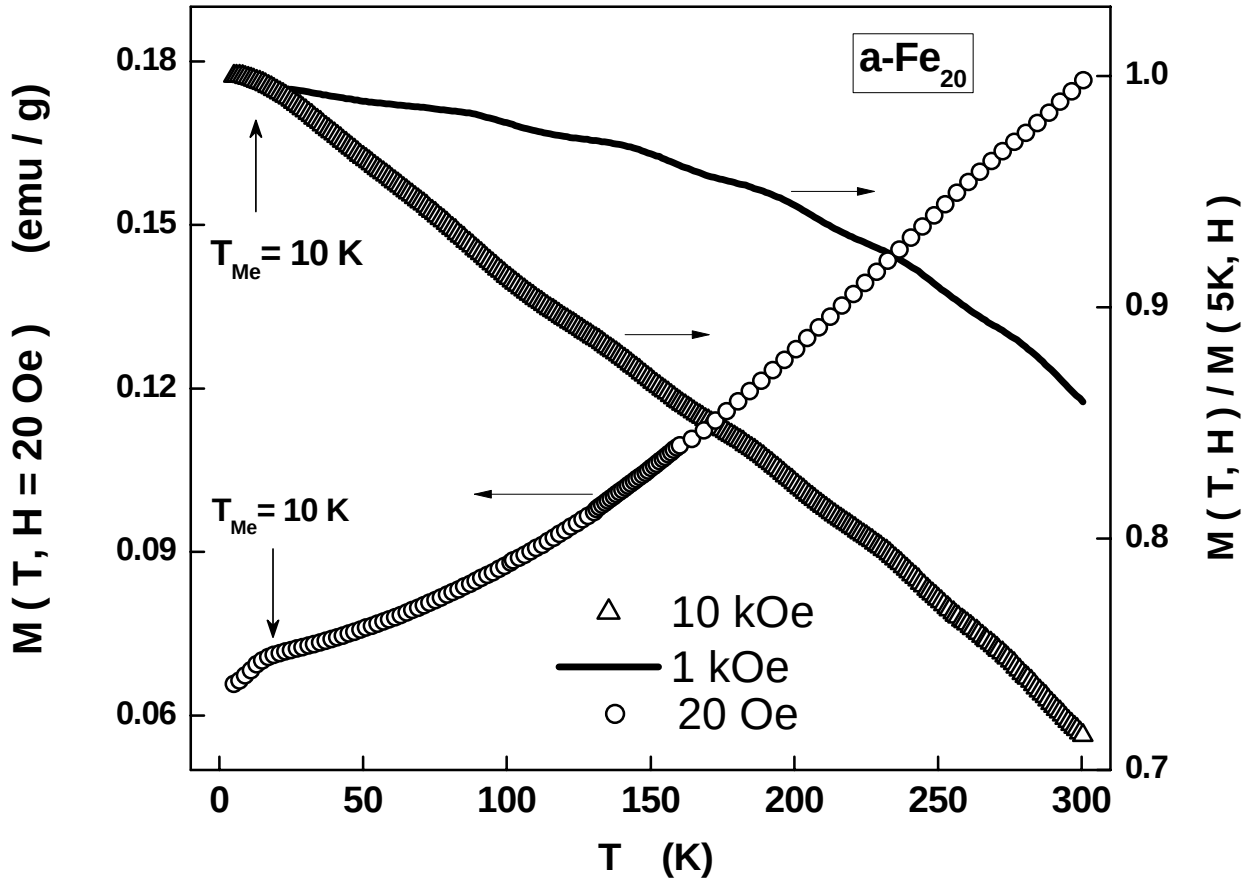

Figure 6.33: Specific magnetization as a function of temperature M(T,H) measured at various fixed magnetic field values in the heating cycle for a-Fe_{20}. The characteristic temperature, T_{Me} determined by $\rho(T)$ is indicated by arrow. To facilitate a comparison between the M(T) curves taken at H = 1 and 10 kOe, M(T) data are normalised to the values of M at 5 K, i.e., to M(T = 5 K, H = 1 kOe) = 23.20 emu/g and M(T = 5 K, H = 10 kOe) = 38.98 emu/g.

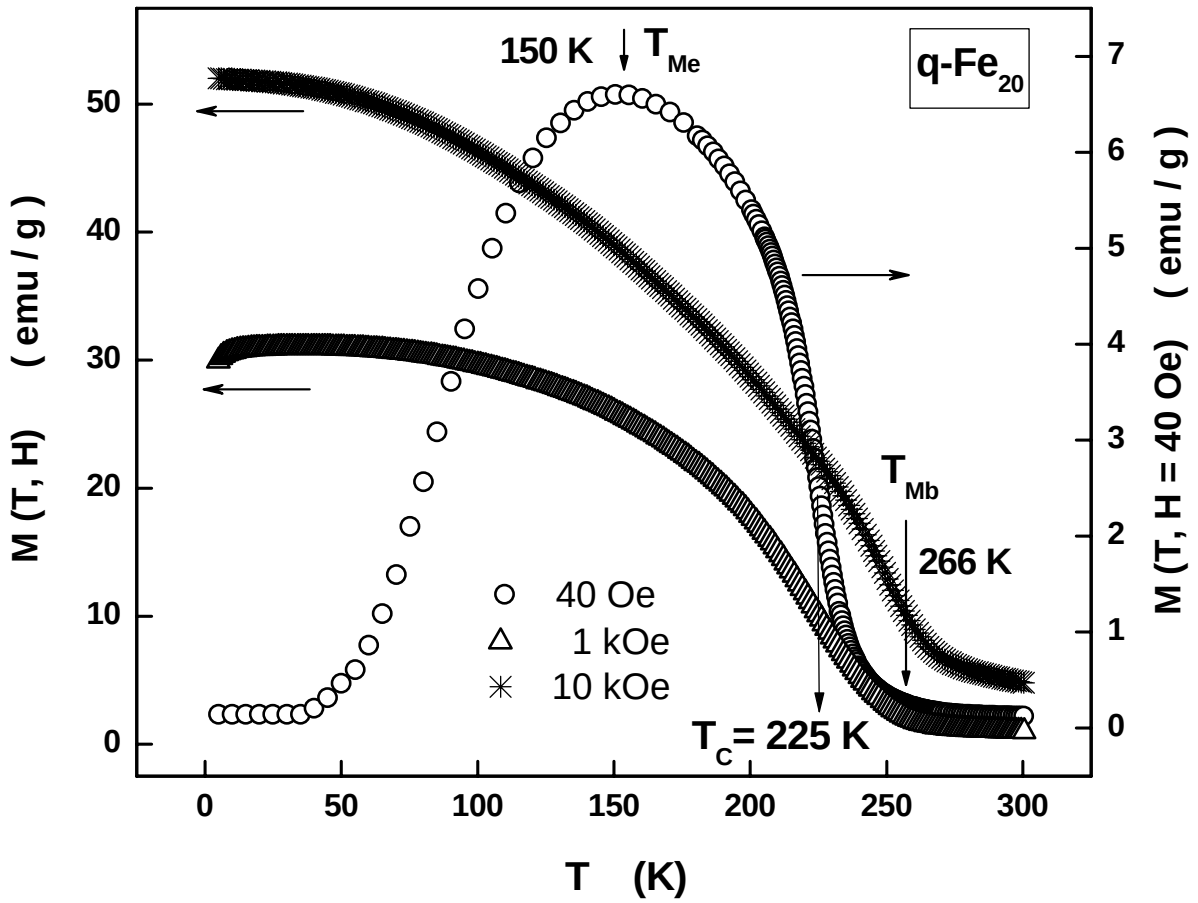

Figure 6.34: Specific magnetization as a function of temperature M(T,H) measured at various fixed magnetic field values in the heating cycle for q-Fe_{20}. The Curie temperature and characteristic temperatures T_{Me} and T_{Mb} determined from $\rho(T)$ and neutron diffraction measurements, are indicated by arrows.

increases. This inference is made more obvious in Figure 6.35 that shows undulations in the dM (T, H = 1 kOe, 10 kOe) /dT curves of a-Fe_{20} samples taken at H = 1 kOe and 10 kOe. Therefore, it is not surprising that T_{Mb} too does not have a unique value and that the phase coexistence temperature region is extremely wide. Thus, in a-Fe_{20}, the nucleation and growth of martensite phase occurs locally and the global growth of martensite phase is hindered due to stress relaxation occurred in the B2 phase during annealing and $L1_2$ phase formation. It is important to note the striking resemblance between the period (50 K) of the 'steps-like' features in the lattice parameter of the B2 phase, a_{B2} and that of the undulations in the dM(T, H = 1 kOe, 10 kOe) / dT curves. Even

in the fields up to H = 10 kOe, the period of the undulations remains the same. The insensitivity of these features to applied external magnetic field suggests that there is strong but local magnetocrystalline anisotropy associated with the nucleation of the martensitic phase in a-Fe_{20}. The 'step-like' jumps in the relative change in resistivity across the martensitic transformation are also symptomatic of the fact that the nucleation and local growth of martensite phase occurs over a wide range of temperature. A consequence of this is that

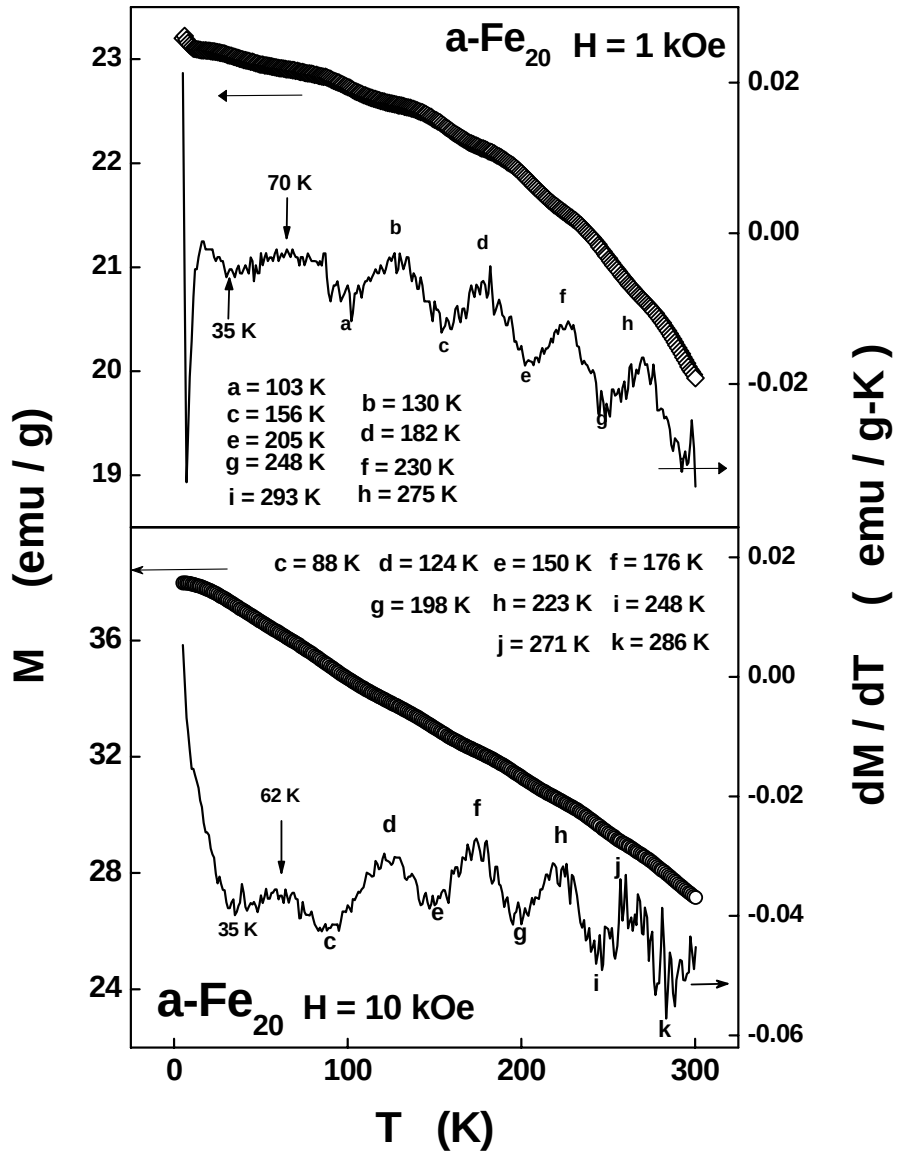

Figure 6.35: dM/dT versus T curves for a-Fe_{20} sample at H = 1 and 10 kOe. The alphabets denote the temperatures corresponding to trough and crest of dM/dT curves.

martensitic transformation in a-Fe_{20} is not complete and is non-thermoelastic. By comparison, dM (T, H = 1 kOe, 10 kOe) /dT as well as relative change in resistivity curves for q-Fe_{20} do not show any such features because $T_{Ae} > T_C$ and H_A of the martensite phase decreases monotonously with increasing temperature and goes to zero before T_C is reached.

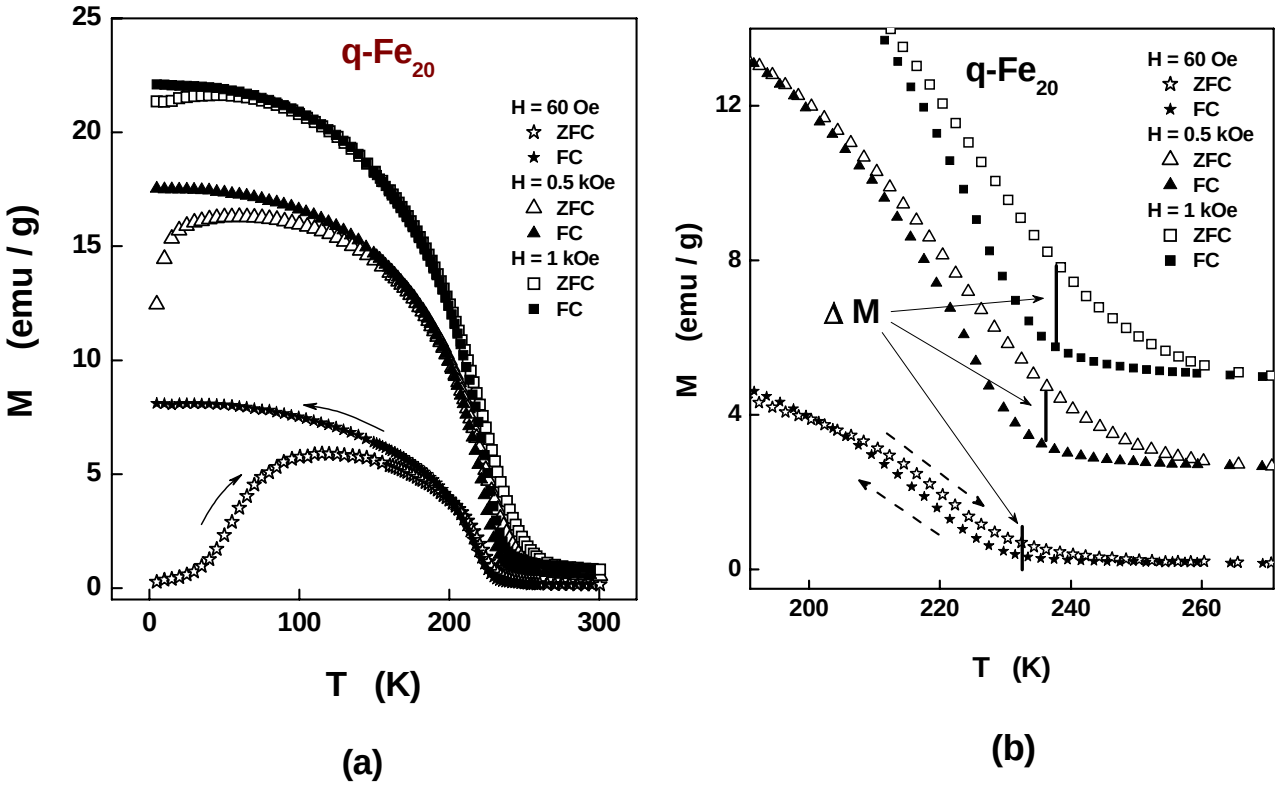

Figure 6.36:(a) ZFC-FC magnetization as a function of temperature at magnetic fields ranging from 60 Oe ≤ H ≤ 1 kOe for q-Fe_{20} samples. (b) Enlarged view of ZFC-FC curves in the temperature range near the martensitic transformation.

To understand the ferromagnetic shape memory behaviour in $Ni_{55}Fe_{20}Al_{25}$, the 'zero-field-cooled' (ZFC) and 'field-cooled' (FC) magnetization measurements were performed on a-Fe_{20} and q-Fe_{20} samples at magnetic fields, H, in the range 60 Oe ≤ H ≤ 1 kOe. Figure 6.36 depicts the ZFC-FC magnetization curves of q-Fe_{20} sample. Irreversibility in the FC-ZFC curves is due to anisotropy of ferromagnetic martensite phase whereas

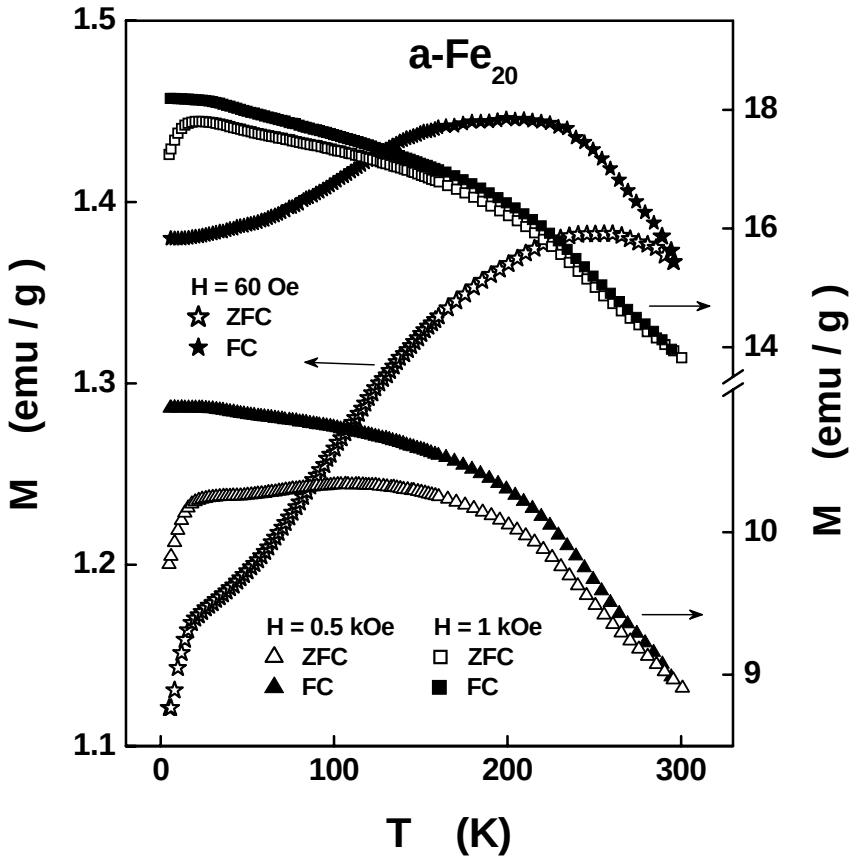

Figure 6.37: ZFC-FC magnetization as a function of temperature at magnetic fields ranging from 60 Oe ≤ H ≤ 1 kOe for a-Fe_{20} samples.

thermal hysteresis observed in the temperature range from ~ 210 K to ~ 260 K is because of first-order thermoelastic martensitic phase transformation. The enlarged view of thermal hysteresis in ZFC-FC magnetization curves in the temperature range, where martensite transformation begins, revealed the following. The change in magnetization, ΔM, across the thermal hysteresis, shown by vertical lines, increases with increasing applied magnetic field. However, the width of thermal hysteresis, ΔT, remains the same at all the measured fields. From these observations it is evident that q-Fe_{20} shows the ferromagnetic shape memory effect. By contrast, the ZFC-FC magnetization curves of a-Fe_{20}, measured at different but fixed magnetic fields, start bifurcating at the highest measuring temperature (300 K) and the bifurcation in the ZFC-FC curves at the lowest temperature (1.7 K) and at a given value of

the field ($H \leq 0.5$ kOe) is at least one order of magnitude less compared to that in q-Fe_{20}. This comparison suggests that the local magnetocrystalline anisotropy is much stronger in a-Fe_{20} than in q-Fe_{20}.

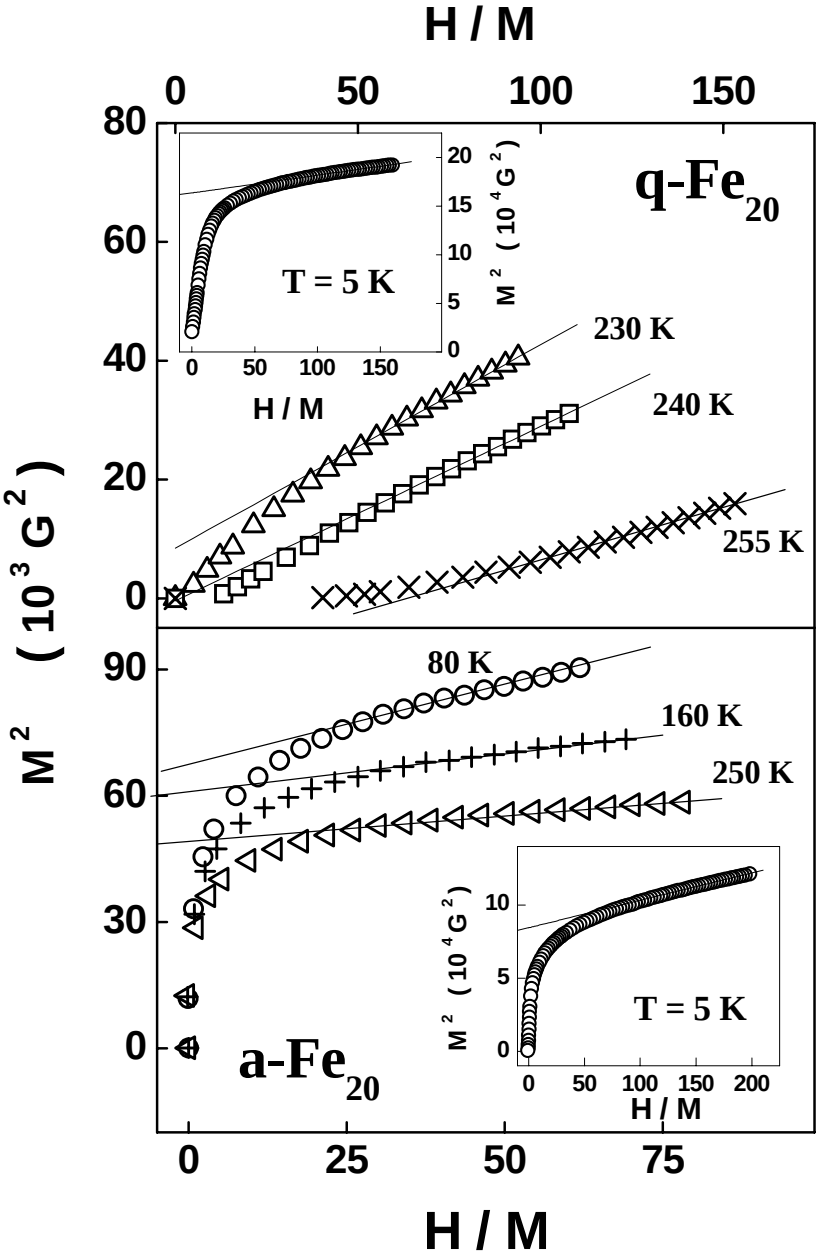

Figure 6.38: Arrott plots (M^2 vs. H/M) at a few representative temperatures.

Another point to note is that the spontaneous magnetization at 5 K, $M_S \equiv M(T = 5\text{ K}, H = 0)$, is larger ($M_S = 404$ G) in q-Fe_{20} than that ($M_S = 290$ G) in a-Fe_{20} even though T_C is considerably higher in a-Fe_{20}. These M_S values are

obtained from the intercepts on the ordinate of the M^2 versus H/M (Arrott) plot at T = 5 K, when the high-field portions of the Arrott plot isotherms are linearly extrapolated to $H = 0$, as shown in insets of figure 6.38. Arrott plots at a few representative temperatures are shown in Fig. 6.38 to highlight that T_C for q-Fe_{20} and a-Fe_{20} samples has the values $T_C \cong 225$ K and $T_C > 300$ K, respectively [43].

6.4 Summary and conclusions

With a view to ascertain the effect of quenched-random site disorder on the martensitic phase transformation in $Ni_{55}Fe_{20}Al_{25}$ alloy; structural, electrical, magneto-transport and magnetic properties of 'quenched' and 'annealed' samples are investigated in detail. Neutron diffraction and TEM studies show that at room temperature, melt-quenching (annealing) $Ni_{55}Fe_{20}Al_{25}$ results in a single-phase (two-phase) state with B2 (B2 + $L1_2$) structure, where Fe atoms preferentially occupy Al sites. Melt-spun ribbons (annealed strips) undergo sharp and complete (sluggish and partial) thermoelastic (non-thermoelastic) martensitic transformation to the monoclinic $(NiFe)_2(FeAl)$ phase at $T < 240$ K (over a wide temperature range 10 K $\leq T \leq$ 300 K). Annealing relieves the quenched-in stress, improves the atomic order by reducing number of the Fe atoms (or increasing Al atoms) on the Al site in the B2 phase (and thus stabilises the B2 phase) and leads to the formation of the $L1_2$ phase. The lattice parameter, a_{B2}, shows undulations with a period of about 50 K in the temperature range 48 K $\leq T \leq$ 300 K. These factors are responsible for a weak martensitic transformation in a-Fe_{20} with thermal hysteresis extending over a wide temperature range.

In q-Fe_{20}, the relative change in resistivity (RCR) across the martensitic transformation is very large (~ 15%) and above and below the narrow coexistence region, RCR is ~ 0% which implies a single-phase state. By contrast, RCR of a-Fe_{20} has a small but finite value and it shows undulations over a wide temperature range. The residual resistivity of a-Fe_{20} samples is lower than that of q-Fe_{20}. At any specified temperature and magnetic field, *negative* magnetoresistance in q-Fe_{20} is *larger* compared to that in the a-Fe_{20} sample.

Spontaneous magnetization, M_s, is higher although Curie temperature, T_C, is lower in q-Fe_{20} compared to that in a-Fe_{20} samples. A sizable reduction of Fe atoms in the Al sublattice is responsible for the diminished value of M_s in a-Fe_{20} since large magnetic moment (2.2 μ_B per Fe atom) bearing Fe atoms are replaced by Ni atom which have roughly 4 times smaller magnetic moment (0.6 μ_B per Ni atom). However, higher T_C in a-Fe_{20} reflects strong exchange interactions mainly in Fe-rich $L1_2$ phase $(NiFe)_3(AlFe)$. The temperature derivative of the $M(T)$ curves taken at H = 1 and 10 kOe in a-Fe_{20} show undulations with a period of 50 K. These undulations in dM/dT, 'step-like' wavy structures of lattice parameter, a_{B2}, and RCR in a-Fe_{20} have common origin in that the martensitic phase nucleates and grows locally in B2 phase over a wide temperature range. These feature are not observed in the q-Fe_{20} sample.

The ZFC-FC $M(T)$ curves taken at different magnetic fields demonstrate the ferromagnetic shape memory effect in q-Fe_{20}, which is not observed in a-Fe_{20} since the martensitic temperature as well as T_C lie well above 300 K. However, the large local anisotropy in a-Fe_{20} is reflected in the bifurcation of

the ZFC-FC $M(T)$ curves. Moreover, in view of the well-known result [13] that a substantial enhancement in the ductility occurs when the ternary addition preferentially substitutes Al sites in the B2 Ni-Al compound, exclusive Al site preference of Fe in the quenched sample results in greater ductility in q-Fe_{20} compared to a-Fe_{20} due to magnetism induced solid softening effect [44].

References

[1] H. Bitterlich, W. lpser, and W. Schultz, J. Phase Equilib. **23**, 301 (2002).

[2] Y. K. Au and C. M. Wayman, Scripta Metall. **6**, 1209 (1972).

[3] A. Inoue, H. Tomioka and T. Masumoto, Metall. Trans. A. **14**, 1367 (1983).

[4] A. Inoue and T. Masumoto, J. Mater. Sci. **19**, 3097 (1984).

[5] S. Furukawa, A. Inoue and T. Masumoto, Mater. Sci. Eng. **98**, 515 (1984).

[6] M. Wallin, P. Johansson and S. Savage, Mater. Sci. Eng. A **133** 307 (1991).

[7] J.A. Juárez-Islas, R. Pérez, and S. Savage, Materials Letter, **14**, 1 (1992).

[8] C. T. Liu, C. J. Sparks, J. A. Horton, E. P. George, and C. A. Carmichael, Mat. Res. Soc. Symp. Proc., **246**, 169 (1992),

[9] E. P. George, C. T. Liu, J. A. Horton, C. J. Sparks, M. Kao, H. Kunsmann and T. King Materials Characterization, **32**, 139 (1994).

[10] R. Kainuma, S. Imano, H. Ohtani, and K. Ishida, Intermetallics **4**, 37 (1996).

[11] D. Goldberg and A. Shevakin, Intermetallics **3**, 293 (1996).

[12] A. J. Duncan, M. J. Kaulfmann, C. T. Lui, and M. K. Miller, Allp. Surf. Sci. **76-77**, 155 (1994).

[13] C. L. Fu, C. T. Liu, Xun-Li Wang, M. Krcmar, and J. Fernandez-Baca, Intermetallics **12**, 911 (2004).

[14] F. Lechermann, M. Fähnle, and J. M. Sanchez, Intermeatallics **13**, 1096 (2005).

[15] B. Annie D'Santhoshini and S. N. Kaul, J. Mag. Mag. Mater. **272-276**, 4930 (2004).

[16] B. Annie D'Santhoshini and S. N. Kaul, J. Phys. : Condens. Matter **15**, 4903 (2003).

[17] S. N. Kaul, B. Annie D'Santhoshini, A. C. Abhyankar, L. Fernández Barquin, and P. Henry, Appl. Phys. Lett. **89**, 093119 (2006).

[18] M. L. Richard, *Thesis submitted* to Massachuetes Institute of Technology, (2005).

[19] R. Ranjan, S. Banik, S. R. Barman, U. Kumar, P. K. Mukhopadhyay, and D. Pandey, Phy. Rev. B **74**, 224443 (2006).

[20] J. Rodriguez-Carvajal, Fullproof Mannual, ILL. CEA-CNRS FRANCE (2001).

[21] V. A. Chernenko, E. Cesari, V. V. Kokorin and I. N. Vitenko, Scr. Metall. Mater. **33**, 1239 (1995); A. N. Vasil'ev, V. D. Buchel'nikov, T. Takagi, V. V. Khovailo, and E. I. Estrin, Phys.-Usp. **46**, 559 (2003).

[22] L. Eleno, K. Frisk and André Schnider, Intermetallics **14**, 1276 (2006).

[23] S. G. Choudhary, R. K. Ray, and A. K. Jena, Scripta Met. Mater. **32**, 1501 (1995).

[24] K. Enami and S. Neno, Mater. Trans. JIM **19**, 571 (1978).

[25] F. Reynauld, J. Appl. Cryst. **9**, 263 (1976).

[26] Y. Noda, S. M. Shapiro, G. Shirane, Y. Yamada, and L. E. Tanner, Phys. Rev. B **42**, 10397 (1990).

[27] C. T. Lui, C. L. Fu, L. K. Pike, and D. S. Easton, Acta. Mater. **50**, 3203 (2002).

[28] L. Yang, X. –L. Wang, C. T. Lui, J.A. Fernandez-Baca, C. L. Fu, J. W. Richardson and D. Shi, Scripta Mater. **56**, 911 (2007).

[29] V. V. Martynov, K. Enami, L. G. Khandros, A. V. Tkachenko, and S. Neno, Scripta. Met. 17, 1167 (1983).

[30] K. Otsuka, T. Ohba, M. Tokonami, and C. M. Wayman, Scripta Metall. **29**, 1359 (1993).

[31] S. Muto, D. Schryvers, N. Merk, and L. E. Tanner, Acta Metall. Mater. **41**, 2377 (1993).

[32] S. M. Shapiro, B. X. Yang, G. Shirane, Y. Noda, and L. E. Tanner, Phys. Rev. Lett. **62**, 1298 (1990); L. Mañosa, A. Planes, J. Zarestky, T. Lagrasso, D. L. Schlagel, and C. Stassis, Phys. Rev. B **64**, 024305 (2001).

[33] P. K. Mukhopadhyay and S. N. Kaul, App. Phys. Lett. **92**, 101924 (2008).

[34] Y. D. Kim and C. M. Wayman, Metall. Trans. **23A**, 2981 (1992).

[35] D. Schryvers, M. Yandouzi, and T. Roth, Thin solid films, **326**, 126 (1998).

[36] L. E. Tanner, D. Schryvers, and S. M. Shapiro, Mater. Sci. Eng. **A127**, 205 (1990).

[37] S. M. Shapiro, B. X. Yang, Y. Noda, L. E. Tanner, and D. Schryvers, Phys. Rev. B **44**, 9301 (1991).

[38] A. S. Murthy and E. Goo, Acta Metall. Mater. **41**, 2135 (1993).

[39] K. Oikawa, T. Ota, T. Ohmori, Y. Tanaka, H. Morito, A. Fujita, R. Kainuma, K. Fukamichi and K. Ishida, App. Phys. Lett. **81**, 5201 (2002).

[40] P. L. Potapov, P. Ochin, J. Pons, and D. Schryvers, Acta Mater. **48**, 3833 (2000).

[41] S. Majumdar, V. K. Sharma, K. J. S. Sokhey, S. B. Roy, and P. Chaddhah, Solid State Commun. **136**, 85 (2005).

[42] V. V. Khovailo, K. Oikawa, C. Wedel, T. Takagi, T. Abe, and K. Sugiyama, J. Phys. : Condens. Matter **16**, 1951 (2004).

[43] A. C. Abhyankar, B. Annie D'Santhoshini, S. N. Kaul, and A. K. Nigam, Adv. Mater. Res. **52**, 77(2008).

[44] C. T. Liu, C. L. Fu, M. F. Chisholm, J. R. Thompson, Maja Krcmar, and X. -L. Wang, Prog. Mater. Sci. **52**, 352 (2007).

Future scope

We have investigated in detail the effect of site- and compositional-disorder, crystallize size and quenched random disorder in the binary Ni_3Al alloy system and in the ternary alloy $Ni_{55}Fe_{20}Al_{25}$. Even such exhaustive and detailed investigations leave scope for further studies on the same or similar systems. For instance,

1. The effect of disorder in melt-quenched ribbons of $NI_{3-x}Al_x$ on the electrical transport and magnetic properties would be interesting.
2. The inelastic-neutron scattering measurements should be performed on the disordered alloys of $NI_{3-x}Al_x$ in order to ascertain the effect of site disorder and compositional disorder on the spin wave/spin fluctuation dispersion relation.
3. Ni_3Ga and Ni_3Al are isostructural compounds and Ni_3Ga system lies near the ferromagnetic instability. The effect of site- and compositional-disorder in this iso-structural compound would be rather interesting.
4. A systematic investigation of the samples with different nanocrystallite sizes in the intermetallic compound Ni_3Al is needed to ascertain the critical sizes at which the long-range ferromagnetic order gets destroyed and the structural transformation occurs.
5. A comparative study of electrical- and magneto-transport properties of 3 nm and 50 nm samples is called for to determine the effect of crystallite size since the transport properties serve as an ideal probe at such length scales.
6. Magnetic field-induced strain measurements are required to verify the ferromagnetic shape effect in melt-spun ribbons of the $Ni_{55}Fe_{20}Al_{25}$ alloy.
7. The composition of the Ni-Fe-Al alloys need to be tuned near $Ni_{55}Fe_{20}Al_{25}$ such that in the melt-quenched state, the Curie temperature as well as the Martensitic transformation temperature are raised above room temperature for these alloys to be useful as Ferro-magnetic Shape Memory Devices .

List of Publications
Papers in refereed Journals:

[1] Effect of off-stoichiometry and site-disorder on the properties of Ni_3Al : I. Electrical- and magneto-transport
A. C. Abhyankar and S. N. Kaul,
J. Phys. : Condens. Matter (2008) at press.

[2] Effect of off-stoichiometry and site-disorder on the properties of Ni_3Al : II. Magnetics
A. C. Abhyankar, A. Semwal and S. N. Kaul,
J. Phys. : Condens. Matter (2008) at press.

[3] Effect of site disorder on martensitic transformation in ferromagnetic $Ni_{55}Fe_{20}Al_{25}$ alloy as inferred from magnetic and magneto-transport measurements
A. C. Abhyankar, B. Annie D'Santhoshini, S. N. Kaul, and A. K. Nigam,
***Advanced Materials Research* 52**, 77 (2008).

[4] Site-disorder-induced non-Fermi liquid behavior of resistivity in Ni_xAl_{100-x} alloys: Effect of magnetic field
A. C. Abhyankar and S. N. Kaul,
***J. Magn. Magn. Mater.* 310**, e310-312 (2007).

[5] Thermoelastic martensitic transformation in ferromagnetic Ni-Fe-Al alloys: Effect of site disorder.
S. N. Kaul, B. Annie D' Santhoshini, **A. C. Abhyankar**, L. Fernández Barquin, Paul F. Henry,
***Appl. Phys. Lett*. 89**, 093119 (2006).

[6] Anomalous positive magnetoresistance at low temperatures in nanocrystalline Ni_3Al.
A. C. Abhyankar and S. N. Kaul,
***Appl. Phys. Lett.* 88**, 193125 (2006).

[7] Microstructure and its correlation to magnetic properties in 2:17 type (Sm, Gd)-Co-Fe-Cu-Zr alloys.
A. C. Abhyankar, R. Gopalan et.al.,
J. Mater. Sci. **36**, 3433 (2004).

Papers presented at National / International conferences / symposia

[1] Effect of site disorder on martensitic transformation in ferromagnetic $Ni_{55}Fe_{20}Al_{25}$ alloy as inferred from magnetic and magneto-transport measurements
A. C. Abhyankar, B. Annie D'Santhoshini, S. N. Kaul, and A. K. Nigam
Presented at International conference on "Ferromagnetic Shape Memory Alloys" at SNBNCBS Kolkata, India (14^{th} to 16^{th} Nov 2007).

[2] Magnetization and Magnetoresistance of shape Memory alloy $Ni_{55}Fe_{20}Al_{25}$
A. C. Abhyankar
Oral presentation at International Conference on Advanced Materials (IUMRS-ICAM), at Bangalore India (8^{th} to 13^{th} Oct 2007).

[3] Site-disorder-induced non-Fermi liquid behavior of resistivity in Ni_xAl_{100-x} alloys: Effect of magnetic field
A. C. Abhyankar and S. N. Kaul
Presented at International Conference of Magnetism 2006, Tokyo, Japan 2006.

[4] Magnetization and Magnetoresistance of a new ferromagnetic shape memory alloy $Ni_{55}Fe_{20}Al_{25}$
B. Annie D'Santhoshini, **A. C. Abhyankar** and S. N. Kaul
Presented at International Conference of Magnetism 2006, Tokyo, Japan 2006.

[5] Thermoelastic martensitic transformation and shape memory effect in crystalline $Ni_{55}Fe_{20}Al_{25}$: Influence of site disorder and magnetic field

B. Annie D'Santhoshini, **A. C. Abhyankar** and S. N. Kaul
Presented at Department of Atomic Energy, Solid State Physics Symposium, at Mumbai India (Dec 2004).
***Proceedings DAE SSPS* 50**, 91 (2005)

[6] Anomalous positive magnetoresistance at low temperatures in nanocrystalline Ni_3Al
A. C. Abhyankar and S. N. Kaul
Presented at Department of Atomic Energy, Solid State Physics Symposium, at Mumbai India (Dec 2004).
***Proceedings DAE SSPS 50**, 223 (2005).*

[7] Effect of Compositional Disorder and Magnetic Field on Spin Fluctuations in Crystalline $Ni_{75 \pm x}Al_{25 \mp x}$ Alloys
Presented at Department of Atomic Energy, Solid State Physics Symposium, at Amritsar India (Dec 2003).
***Proceedings DAE SSPS 49**, 685 (2004).*

[8] Metallurgical and magnetic studies in 2:17 type Sm (CoFeCuZr) alloys with and without Gd addition
A. C. Abhyankar, R. Gopalan, et al.
Presented at 13th AGM MRSI conference, DMRL, Hyderabad (7-9th Feb 2002).